INTERNATIONAL DOCTORAL
SCHOOL OF THE USC

Pablo
Vallet Moreno

PhD Thesis

SYNTHESIS AND PHYSICAL CHARACTERIZATION OF HYBRID IONOGELS OF ELECTROCHEMICAL INTEREST

Santiago de Compostela, 2024

Doctoral Programme in Materials Science

ESCOLA DE DOUTORAMENTO
INTERNACIONAL DA USC

TESIS DOCTORAL

SYNTHESIS AND PHYSICAL CHARACTERIZATION OF HYBRID IONOGELS OF ELECTROCHEMICAL INTEREST

Autor

Pablo Vallet Moreno

Directores: Luís Miguel Varela Cabo
Josefa Salgado Carballo

Tutor/a: Josefa Salgado Carballo

PROGRAMA DE DOCTORADO EN CIENCIAS DE LOS MATERIALES

SANTIAGO DE COMPOSTELA / LUGO

AGRADECIMIENTOS

En primer lugar, me gustaría agradecer a mis directores de tesis Luis Miguel Varela Cabo y Josefa Salgado Carballo por confiar en mi para llevar a cabo este ambicioso proyecto. No cualquiera lo hubiera hecho, y espero que este documento cumpla con sus expectativas. Para mí ha sido un honor poder formar parte de este grupo de investigación. Este pequeño texto no hace justicia al sentimiento de agradecimiento que tengo hacia vosotros. ¡Muchas gracias!

En segundo lugar, aunque no menos importante, a mis compañeros de laboratorio Juan José Parajó Vieito y Antía Santiago Alonso. Habéis hecho un trabajo estupendo aguantando a una persona tan difícil como yo. Solo tengo adjetivos positivos para describir el tiempo que hemos pasado juntos: cuatro años no son nada para toda una vida, pero os habéis ganado un lugar en mi corazón.

No puedo dejar de mencionar a los profesores Joaquim Agostinho y Jean Le Bideau, de las universidades de Porto y Nantes, respectivamente, y también a Francisco Fernández Carretero (Fran para los amigos) de TECNALIA, donde realicé mis estancias de investigación. Gran parte de mi conocimiento se debe a vosotros y no es fácil agradecer la formación que me ofrecisteis. Guardo muy buenos recuerdos de vosotros.

A mi familia. 1000 km de distancia no suponen nada cuando alguien te está apoyando. A mi padre, por su dedicación y educación. Sin él no sería lo que soy ahora. A mi hermano David y mi sobrina Laya, a mi hermana Fanny y sus hijos Aitor y Pablo, y a mi hermano Salva. Tus llamadas mientras conduces al trabajo me han salvado en más de una ocasión.

Al personal de la RIAIDT de la USC, en especial a Manuel Martin, ya que una gran parte de esta tesis lleva su nombre. No tenías por qué hacerlo, pero intentaste enseñarme RMN, y quiero creer que algo conseguiste.

Finalmente, al Ministerio de Ciencia Innovación y Universidades del gobierno de España por permitirme realizar este proyecto por la ayuda PRE2018-084212 enmarcada en el proyecto de investigación MAT2017-89239-C2-1-P.

Pablo Vallet Moreno

RESUMEN

Los nuevos acuerdos alcanzados en la unión europea para reducir las emisiones de dióxido de carbono (CO_2) entre otros gases de efecto invernadero son un hecho, para ello se ha desarrollado un ambicioso plan llamado "*fit for 55*", cuyo objetivo es reducir en, al menos, un 55% las emisiones de dichos gases comparado con los niveles emitidos en el 1990 para el 2030 y llegar a cero emisiones para el 2050. Esto supone un gran desafío para la población europea, y en general, para toda la humanidad. El plan "*fit for 55*" consiste en una serie de propuestas para asegurar que los países miembros están alineados en sus políticas climáticas a través del concilio europeo. Para llevar a cabo este plan, se ha apostado por una transición hacia las energías renovables, pero estas presentan picos de producción que normalmente no coinciden con los picos de demanda de la red eléctrica dificultando la sustitución completa de las fuentes de energía tradicionales. Por este motivo, el almacenamiento de energía se convierte en crucial para poder llevar a cabo este ambicioso plan y la electrificación de los vectores industriales, móviles y económicos de la sociedad. Adicionalmente, y debido a las últimas inestabilidades geopolíticas, la unión europea para hacer frente a la crisis energética ha lanzado la iniciativa REPowerEU, que, entre otras, está ayudando a que los países miembros ahorren energía, produzcan energía limpia y diversifiquen su abastecimiento energético. Gracias a esta iniciativa, se ha conseguido reducir en un 20% el consumo de energía en territorio europeo, reducir la dependencia de combustibles fósiles, introducido un tope a los precios del gas y tope a los precios mundiales del petróleo y se ha duplicado el despliegue adicional de energías renovables.

Hasta la fecha, la demanda energética social era cubierta, en gran medida, por el petróleo y sus derivados, debido a su alta densidad energética (35-45 $GJ\cdot m^{3}$ para la gasolina), pero es bien sabido que la situación actual de cambio climático ha sido provocada por la liberación de gases de efecto invernadero que se producen durante la quema de combustibles fósiles. Esta situación ha provocado que los gobiernos de todo el mundo se movilicen para tomar medidas y paliar, en medida de lo posible, la situación de emergencia climática y realizar una transición hacia fuentes de energías limpias y verdes no contaminantes.

En la presente tesis se analiza desde el punto de vista experimental, la viabilidad de nuevos electrolitos para baterías de Ion-Litio, compuestos por mezclas de Líquidos Iónicos (IL) y sales inorgánicas de interés electroquímico de catión Litio, Magnesio, Calcio y Aluminio y anión común al del líquido iónico. Estas mezclas electroquímicas serán confinadas en matrices de sílice (basadas en enlaces silicio-oxígeno) con el objetivo de obtener un material semisólido electrolítico, conocido como ionogel, para nuevas baterías, con el fin de obtener un material interesante para la industria que impida derramamientos en el ensamblaje de las baterías de ión litio, además de ampliar el conocimiento en baterías de la era post-litio.

Los ILs son compuestos heterogéneos formados por un catión orgánico y un anión orgánico o inorgánico unidos por interacciones electrostáticas. Técnicamente, los ILs son

sales, pero con la peculiaridad de tener el punto de fusión por debajo de los 100 °C. En 1914 por Paul Walden, sintetizó el primer Líquido Iónico, el $[C_2NH_3][NO_3]$ (posteriormente conocido como el EAN), aunque aún en la actualidad sigue siendo material de estudio en la primera línea de investigación. Particularmente, se distinguen los ILs a temperatura ambiente (RTILs por sus siglas en inglés), que son ILs con el punto de fusión por debajo de la temperatura ambiente. Durante las últimas décadas los ILs han suscitado un gran interés tanto en el mundo académico como entre los más diversos sectores tecnológicos e industriales, debido a la infinidad de aplicaciones en la que pueden ser usados. Algunas de sus asombrosas características son presión de vapor casi nula, baja toxicidad (comparados con los cosolventes electrolíticos tradicionales), alta conductividad iónica, amplia ventana electroquímica, no inflamables, alta estabilidad térmica entre otras. Debido a estas propiedades se destaca su alta potencialidad de uso en diversas aplicaciones industriales; ingeniería de materiales, en el sector energético (como por ejemplo electrolitos para células solares, pilas de combustible, baterías de ion litio, fluidos de transferencia de calor, lubricantes o aditivos de lubricantes), en la industria farmacéutica y como alternativa "verde" para evitar/reducir la producción de sustancias peligrosas para el medioambiente. Dependiendo de su ruta de síntesis, los ILs pueden ser divididos en dos grandes grupos, los próticos (PILs por sus siglas en inglés) y los apróticos (APILs). Los PILs son sintetizados vía transferencia protónica mientras que los APILs tienen diferentes métodos de síntesis.

Se estudian cuatro ILs comerciales diferentes, próticos y apróticos, de las familias de cationes más comunes, como son el amonio, el imidazolio y el pirrolidinio. Los aniones correspondientes han sido dos, nitrato (NO_3) y bis(trifluorometilsulfonil)imida (TFSI), estableciendo así las cuatro combinaciones catión-anión de los ILs usados, concretamente nitrato de etilamonio (EAN) y nitrato de 1-etilimidazolio ($[C_2Im][NO_3]$) como líquidos iónicos próticos y 1-butil-1-metilpirrolidinio bis(trifluorometilsulfonil)imida ($[C_4C_1Pyrr][TFSI]$) y 1-etil-3-metilimidazolio bis(trifluorometilsulfonil)imida ($[C_2C_1Im][TFSI]$) como líquidos iónicos apróticos. Como se ha dicho, la sal de interés electroquímico utilizada para la síntesis de las mezclas electrolíticas es seleccionada con anión común con el IL, siendo nitrato de Litio, nitrato de Magnesio, nitrato de Calcio y nitrato de Aluminio las usadas para las combinaciones con EAN y $[C_2Im][NO_3]$ y Litio Bis(trifluorometilsulfonil)imida para las mezclas con $[C_4C_1Pyrr][TFSI]$ y con $[C_2C_1Im][TFSI]$.

Una de las partes más innovadoras de este trabajo ha sido la búsqueda de la ruta de gelificación más adecuada para obtener un electrolito semisólido manipulable. Las rutas de síntesis de gelificación de las mezclas electrolíticas usadas tienen como precursores compuestos basados en silicio y están descritas completamente en este manuscrito. Principalmente, se estudian tres rutas de gelificación diferentes, dos de ellas usan un único precursor de silicio con dos catalizadores diferentes, ácido fórmico y etanol y la tercera hace uso de dos precursores de sílice con ácido fórmico como catalizador. Las dos primeras rutas, denominadas como la ruta del ácido fórmico y la ruta del etanol respectivamente, ya eran conocidas en el grupo de investigación NaFoMat, mientras que la tercera, denominada como la ruta de dos precursores, se desarrolló durante una estancia de investigación en el instituto de materiales Jean Rouxel de la Universidad de Nantes bajo la supervisión del profesor Jean Le Bideau. Cada una de estas rutas tiene unas características y proporciones propias para crear el Ionogel y como resultado se obtienen propiedades diferentes. La ruta de síntesis de ionogeles asume que el IL permanezca inalterable durante la reacción de gelificación, no reaccionando químicamente con ninguno de los componentes usados para formar la matriz de sílice, dando como resultado un material electrolítico semisólido manteniendo las propiedades del IL lo más inalteradas posibles, en otras palabras, la matriz de sílice confina en IL el cual mantiene las propiedades de su forma líquida. Estas afirmaciones se verán confirmadas a lo largo de esta tesis mediante las diferentes técnicas de caracterización experimental utilizadas.

Se estudia el comportamiento térmico, los cambios estructurales, propiedades termo-físicas como la densidad y la viscosidad y comportamiento electroquímico en función de la concentración de sal, del tipo de sal y de la temperatura en el caso de las mezclas en estado líquido. Se analizan también los cambios de estas propiedades y comportamientos como consecuencia del nanoconfinamiento de las mezclas anteriores.

El estudio térmico se realiza por las técnicas como calorimetría diferencial de barrido (DSC) y análisis termogravimétrico (TGA). Las principales observaciones para la DSC han sido que la adición de sal se traduce en una reducción de la cristalinidad para los IL próticos, es decir, los picos de cristalización y fusión característicos de los ILs puros tienden a desaparecer o perder definición a medida que se aumenta la concentración de sal. Con respecto a las mezclas en forma líquida de los ILs apróticos se observa un desplazamiento de los picos de transición de fase hacia temperaturas mayores. El efecto del confinamiento de las mezclas electrolíticas en matrices de sílice no sigue un patrón definido, dependiendo de la ruta de gelificación y del IL, aunque sí se observa una tendencia al aumento del comportamiento amorfo en las muestras. Concretamente, EAN y [C_2Im][NO_3], que han sido gelificados usando las rutas de un único precursor (la ruta del ácido fórmico y la del etanol), muestran resultados diferentes, en el primer caso se observa una completa desaparición de los picos de transición de fase, mientras que para el segundo tenemos un desdoblamiento del pico de fusión y un desplazamiento hacia temperaturas menores del pico de cristalización. Por último, con el nanoconfinamiento del IL [C_4C_1Pyrr][TFSI], realizado por la ruta de dos precursores, no se obtiene un cambio significativo de las transiciones de fase. Estos resultados indican que el tamaño de poro de la red de sílice depende de la ruta seguida y del IL.

La estabilidad térmica de las muestras estudiadas no depende de adición de sal ni del nanoconfinamiento, viene determinada por la estabilidad del propio IL, que como es bien sabido depende mayoritariamente de su anión, otorgando mayor estabilidad térmica el TFSI que el NO_3.

Se analizan los cambios en la estructura de las mezclas electrolíticas por medio de Resonancia Magnética Nuclear (RMN) encontrando que ésta permanece inalterada por la adición de sal, pero se encuentra un desplazamiento de los protones donantes (teoría ácido-base de Lewis) hacia campos magnéticos de mayor energía (up-field), siendo los protones lábiles de los ILs próticos los más afectados por la adición de sal. El confinamiento en matrices de sílice no provoca cambios estructurales significativos en la mezcla electrolítica, aunque se observa una ralentización de la dinámica molecular y un entorno químico diferente entre las moléculas del centro del poro y las cercanas a las paredes de la matriz de sílice.

Las propiedades termofísicas, densidad y viscosidad, de las mezclas líquidas se caracterizan usando las técnicas de denso-viscometría y reometría. Los resultados obtenidos muestran dependencias polinómicas de la densidad con respecto a la concentración de sal (incremento siguiendo un polinomio grado 2 o tendencia cuadrática) y a la temperatura (disminución lineal). En el caso de la viscosidad de las mezclas electrolíticas se ha observado un aumento de ésta con la concentración de sal, como se esperaba, y una disminución con la temperatura siguiendo un comportamiento descrito por el modelo Vogel–Fulcher–Tammann (VFT).

Como parte fundamental de este trabajo, se realizan mediciones electroquímicas usando Espectroscopía Dieléctrica de Banda Ancha (BBDS), la conductividad iónica, espectroscopía de impedancia (EIS), voltametría cíclica (CV) y cargas y descargas galvanostáticas con limitación de potencial (GCPL).

La Espectroscopía Dieléctrica de Banda Ancha (BBDS) se analiza en el régimen interfacial para estudiar la Doble Capa Eléctrica (EDL). El aprendizaje de la BBDS se desarrolló durante una estancia de investigación en la Universidad de Porto, en el Departamento de Física, bajo la supervisión del profesor Agostinho y, posteriormente, se implantó esta técnica experimental y su posterior desarrollo y tratamiento de datos en el grupo de investigación de NaFoMat de la USC. A través de mediciones espectroscópicas de la impedancia se obtiene la constante dielectrica (magnitud compleja) en función de la frecuencia y se ha analizado la ventana frecuencial de los distintos regímenes presentes, en especial la saturación de iones en las vecindades de las paredes o interfase de los electrodos (efecto conocido como Maxwell-Wagner-Sillars, MWS), así como el fenómeno de relajación interfacial. A través de la parte imaginaria de la constante dieléctrica se puede obtener el régimen óhmico de la muestra, derivando de este, con gran exactitud, el rango de frecuencias en que este fenómeno se produce, y con ella determinar la conductividad iónica de la muestra analizada con un alto grado de fiabilidad. Estos estudios se realizan en función de la temperatura, la adición de sal y del nanoconfinamiento. Se observa que tanto la adición de sal como el nanoconfinamiento desplazan la ventana espectroscópica de los diferentes regímenes presentes a frecuencias menores. Esto se traduce en una reducción de la movilidad iónica del "bulk" de la muestra analizada. El efecto de la temperatura es el esperado, la movilidad iónica aumenta cuando la temperatura aumenta. La relajación dieléctrica ha sido un estudio crítico para la selección de un IL para la implantación en una batería funcional de IL, la cual es analizada mediante el diagrama Cole-Cole. Este diagrama representa la parte imaginaria de la constante dieléctrica frente a su parte real, obteniendo un indicativo de cuan relevante es esta relajación y, por lo tanto, se convierte en una cuantificación crucial en el estudio de electrolitos.

La conductividad iónica es uno de los parámetros críticos a determinar cuándo se estudia el comportamiento electroquímico de electrolitos en dispositivos de almacenamiento de energía, como son las baterías. La conductividad iónica de las mezclas electrolíticas estudiadas se obtiene por dos métodos diferentes, una medida directa de esta propiedad por medio de un conductímetro comercial, y por medio de la parte imaginaria de la BBDS cuando se alcanza el régimen óhmico de la muestra, como ya se ha indicado. Es bien sabido que la conductividad iónica es una propiedad de transporte, al igual que la viscosidad (también estudiada en este manuscrito) y ambas propiedades tienen un comportamiento opuesto, así, la conductividad se reduce con adición de sal en todos los casos, mientras que la viscosidad aumenta. Al contrario que la viscosidad, la conductividad iónica de las mezclas electrolíticas aumenta con la temperatura, como se espera, y puede ser bien descrita por el modelo VFT (también utilizado para describir la variación de la viscosidad con la temperatura). Con el confinamiento en matrices de sílice esta propiedad disminuye su valor, aunque la conductividad iónica puede ser modificada dependiendo de la ruta de síntesis de ionogeles utilizada, siendo así una propiedad tuneable para los ionogeles, aunque esta siempre será menor que su homólogo en forma líquida.

Tras el estudio de la BBDS y de la conductividad iónica, se selecciona el IL [C_4C_1Pyrr][TFSI] como potencial candidato para una celda electroquímica de acumulación de energía funcional (batería de ión litio) basada en dicho IL debido a su evidente relajación dielectrica interfacial y su alta conductividad iónica, además de los resultados obtenidos anteriormente como alto rango líquido y una gran estabilidad térmica, tanto en forma líquida como gel. Por lo que se hace un estudio de voltametría cíclica de este IL con el fin de obtener la ventana electroquímica, y estudiar los posibles procesos de descomposición del electrolito y a qué potenciales ocurren estos. Esto es determinante para la selección de los electrodos que se van a usar en la implantación de dicha celda, ya que el potencial de carga-descarga de esta celda va a depender exclusivamente de los electrodos seleccionados. El potencial de carga y descarga debe de estar dentro de la ventana electroquímica para evitar el deterioro de la batería, y de esta manera, comprometer la seguridad del operador y del equipo experimental. Los siguientes estudios se realizaron durante una estancia de investigación en el centro tecnológico privado TECNALIA bajo la supervisión del doctor Francisco Fernández Carretero.

Antes de la implantación del [C_4C_1Pyrr][TFSI] en la celda electroquímica, se analiza la Espectroscopia de Impedancia Electroquímica (EIS) del IL para conocer el comportamiento de esta en función de la temperatura. La impedancia se estudia desde dos representaciones, el Bode Plot y el Nyquist Plot, ambas ampliamente conocidas en la bibliografía. Como es de esperar, el módulo de la impedancia decrece con la temperatura y el comportamiento en general de las impedancias concuerda perfectamente con el de la BBDS. El Nyquist Plot ha sido ajustado con un circuito equivalente para poder dar un significado físico y a su vez, la capacidad diferencial de la muestra también ha sido obtenida y se obtiene la tendencia de aumentar con la temperatura, sorprendentemente, la capacidad diferencial de la muestra gel es mayor que la de la forma líquida.

El estudio final de esta tesis se centra en la implantación del IL puro $[C_4C_1Pyrr][TFSI]$, es decir, sin sal de litio añadida, como electrolito funcional de una celda electroquímica. Para ello se ha ensamblado una celda tipo "coin cell" 2032, una de las más usadas por la bibliografía. El montaje experimental que se ha seleccionado es una configuración de media celda usando Litio-Hierro-Fosfato ($LiFePO_4$ o su forma abreviada LFP) como cátodo y litio metálico como ánodo para el electrolito seleccionado en las formas líquido y gel. El cátodo LFP es un electrodo ampliamente conocido en la bibliografía, el cual posee una capacidad teórica de 170 $mA \cdot h \cdot g^{-1}$, presenta un plató de carga-descarga entrono a 3.5V muy estable, el LFP es un cátodo comercial y una gran parte de las baterías de ion litio actuales lo utilizan, aunque todavía es motivo de investigación por parte de muchos investigadores. El lito metálico posee una alta capacidad teórica de 3860 $mA \cdot h \cdot g^{-1}$, y normalmente, es usado como ánodo debido a su alta capacidad, pero cabe mencionar que el litio metálico conlleva grandes problemas de seguridad puesto que es altamente reactivo con el agua, llegando a provocar incendios al contacto con esta. El litio metálico es usado en experimentos de media celda (o "*half-cell*" en inglés) debido a que este presenta una capacidad mucho mayor que los cátodos usados actualmente (caso conocido como electrodo de exceso en la bibliografía), pudiendo medir el comportamiento del electrodo enfrentado, en este caso, el LFP. Para el montaje en forma líquida como separador se ha usado celgar 2500, mientras que en la forma gel ningún separador ha sido usado ya que la propia matriz de sílice cumple el rol de confinar el líquido iónico y a su vez impedir el contacto entre ánodo y cátodo, actuando así como separador. Como método experimental se ha usado la carga y descarga galvanostática con limitación de potencial (GCPL) a diferentes velocidades. Como velocidades de carga y descarga se han seleccionado C/20, C/10, C/5 y otra vez C/20 para estudiar la reversibilidad y estabilidad de la pila. A pesar de seleccionar un IL en estado puro sin la adición de sal, se ha comprobado que las cargas y descargas se producían de forma estable tras un periodo de, lo que hemos denominado "litiación" del electrolito, y se obtiene una alta eficiencia coulombica, además de alcanzar una capacidad cercana a la teórica presentada por el LFP, aunque esta alta capacidad se produce a bajas velocidades de carga/descarga, disminuyendo rápidamente al aumentarla. Cabe resaltar que para la forma gel, un paso previo al primer ciclado a velocidad muy baja, C/50, ha sido necesario para habilitar las cargas y descargas de la pila en cuestión. Es importante resaltar que a pesar de utilizar un electrolito sin sal de litio añadida para una batería de ión litio, las cargas y descargas han sido posibles. Este interesante resultado, que supone un importante avance en la propuesta de nuevos *Smart-electrolytes*, ya que demuestra que el litio contenido en los electrodos, concretamente en el cátodo LFP, es suficiente para que la batería almacene carga y la libere en sus ciclos de carga y descarga de una batería de iones litio funcional, a pesar de que las cargas y descargas se produzcan a baja velocidad para obtener capacidades competitivas. Sin embargo, antes de una propuesta definitiva y escalable es necesario mejorar las velocidades de carga manteniendo altas capacidades, disminuir la viscosidad y así logar un aumento de la difusión de los iones de litio. Esto podría conseguirse a partir de mezclas ternarias IL + sal de litio + carbonato, por ejemplo.

A modo de conclusión de este resumen inicial, se puede decir que esta tesis que se centra en el análisis de nuevos electrolitos cumple con sus objetivos de ampliar las fronteras de las baterías de Ion-Litio, así como ampliar el conocimiento de las baterías de la era post-litio. Se ha demostrado que las mezclas electrolíticas basadas en líquidos iónicos con una sal de interés electroquímico se pueden nanoconfinar en matrices de sílice, manteniendo propiedades de su forma líquida, para obtener un material manipulable que evite derramamientos durante su implantación a escala industrial. Se han estudiado las transiciones de fase y la estabilidad térmica de estas mezclas electrolíticas, tanto en forma líquida como gel, comprobando que estas presentan un amplio rango de la fase líquida. Se ha comprobado por medio de técnicas de caracterización estructural, como RMN, que la adición de sal, así como el confinamiento, no afectan a la estructura del IL. Propiedades termofísicas, como son la densidad y viscosidad de la forma líquida de dichas mezclas han sido estudiadas en profundidad. Finalmente, una amplia gama de estudios electroquímicos ha sido realizada con el fin de seleccionar un candidato a una pila de ion litio, obteniendo como resultado un electrolito funcional sin sal de litio añadida.

ABBREVIATION LIST

Abbreviation	**Meaning**
AC	Alternating current
APIL	Aprotic ionic liquid
BBDS	Broad band dielectric spectroscopy
CAES	Compressed air energy storage
Cd	Cadmium
CV	Cyclic voltammetry
C/20	C-rate at 20 hours to complete a charge-discharge
C/10	C-rate at 10 hours to complete a charge-discharge
C/5	C-rate at 5 hours to complete a charge-discharge
DC	Direct current
DMDMS	Dimethoxydimethylsilane
DMSO-d6	Dimethyl Sulfoxide-d6
DSC	Differential Scanning Calorimetry
DTG	Derivative Thermogravimetry
EAN	Ethyl ammonium nitrate
EDL	Electric double layer
EES	Electrochemical energy storage
EIS	Electrochemical impedance spectroscopy
EtOH	Ethanol
EU	European union
FA	Formic Acid
GCPL	Galvanostatic charge-discharge with potential limitation
GHG	Greenhouse gases
GJ	Gigajoules
HES	hydrogen energy storage
IL	Ionic liquid
LFP	Lithium iron phosphate

LIB	Lithium-ion battery
LiTFSI	Lithium Bis(trifluoromethylsulfonyl)imide
M_w	Molecular weight
MWS	Maxwell-Wagner-Sillars
Ni	Nickel
NMR	Nuclear magnetic resonance
PIL	Protic ionic liquid
RTIL	Room temperature ionic liquid
SC	Super capacitator
SEI	Solid electrolyte interface
Si	Silicon
TEOS	Tetraethoxysilane
TGA	Thermogravimetry analysis
TMOS	Tetramethyl Ortosilicate
TSP	2,2,3,3-d4-3-(trimethylsilyl)propionic acid
USC	University of Santiago de Compostela
VFT	Vogel-Fulcher-Tammann
$[C_2Im][NO_3]$	1-Ethyl-3-methylimidazolium nitrate
$[C_4C_1Pyrr][TFSI]$	1-Butyl-1-methylpyrrolidinium bis(trifluoromethanesulfonyl)imide
$[C_2C_1Im][TFSI]$	1-Ethyl-3-methylimidazolium bis(trifluoromethylsulfonyl)imide
ρ	Density
η	Dynamic viscosity
σ	Ionic conductivity
δ	Chemical shifting of the NMR signal

Index

1. INTRODUCTION

1. Introduction

1.1 Context, framework and the European Union

The European Union is firmly committed to increasing its climate ambition. With this in mind, the EU have developed the "Fit for 55" plan [1]. This plan aims at reducing net greenhouse gas emissions by at least 55% compared to 1990 levels by 2030 and achieving carbon neutrality and zero greenhouse gas emissions by 2050. This poses one of the greatest challenges humankind is currently facing, especially as the world population continues to grow (reaching a record number of 8 billion in 2022 and wide 9.7 billion expected in 2050), and the demand for energy consequently rises. Additionally, the transition to cleaner, safer, and more efficient energy harvesting systems seems to have accelerated over the past year due to geopolitical tensions causing a substantial increase in energy costs and doubts over its mid-term availability. In this context, electrochemical devices are again essential for the development of novel and efficient energy harvesting and storage methods. Undoubtedly, significant advances in fundamental knowledge are necessary to achieve more mature, competitive, and globally-accepted technologies for energy harvesting and storage during this period.

The EU's commitment to the Fit for 55 plan is clear. But what exactly does this plan entail? The term "Fit for 55" refers to the EU's objective of reducing emissions by at least 55% by 2030. The Fit for 55 plan consists of a set of proposals aimed at reviewing and updating EU legislation, as well as launching new initiatives, to ensure that European policies are aligned with the climate goals agreed upon by the European Council and the European Parliament. The objective of this package of proposals is to guarantee a fair transition, to maintain and reinforce the innovation and competitiveness of the EU industry, and to continue leading the fight against global warming by reducing emissions and achieving climate objectives.

One of the major challenges in the upcoming years is to identify energy production and storage technologies that can uphold three significant parameters: sustainability, performance, and cost-effectiveness. Renewable energy sources can provide a fundamental avenue to meet the energy demands of our society and industrial activities, while concurrently moving towards decarbonization and achieving the EU's climate neutrality targets by 2050. This transition to decarbonization entails direct electrification, a shift from fossil fuels to carbon-free electric vectors, which can be further supplemented by other initiatives such as green hydrogen. These measures are crucial in heavy industrial applications, shipping, aviation, and other sectors where direct substitution of fossil fuels are difficult or not cost-effective.

1.2 Energy sources

Energy is crucial for the human development, affecting well-being on economic, individual, and collective levels, as well as essential for advances in industry. Traditionally, the main energy source to supply society´s demand was based on petroleum and its derivatives due to its high energy density (35-45 GJ per cubic meter for gasoline) and easy storage for later use [2]. But oil and derivate energy sources have a severe impact on the environment due to the GHG emissions as mentioned above. Owing to global warming and climate change, governments around the world are taking serious measures to reduce their emissions and move to renewable sources of energy with a low (or with no) impact on ecosystems.

Nevertheless, this is a major challenge for society worldwide because of the energy density compared with traditional fossil fuels, as will be pointed out next. Traditionally, energy sources are classified into renewable and non-renewable. Conventionally, non-renewable sources of energy are oil, coal, uranium, natural gas and other radioactive minerals. Except uranium, all produce several carbon dioxide emissions contributing to the rise in global temperature with catastrophic and unintended consequences [3–5].

Renewable sources include solar, wind, and geothermal among others. These sources of energy are inexhaustible on a human timescale and the environmental impact is considerably lower than traditional energy sources. Yet, they still challenges such as intermittent production (normally the peak of production does not match the peak in demand), and lower energy density compared to traditional fossil energy sources.

Besides the lower energy density values of renewable energy sources, there are several challenges associated with their deployment:

1. Resistance from the fossil fuel industry: The fossil fuel industry tries to avoid the implementation of renewable energy sources, as they could mean a loss of revenue and market share.
2. High capital costs: The initial investment required to implement renewable energy technologies (CAREX) is often very high and may discourage some consumers and businesses from pursuing this option.
3. Land use: Some renewable energy technologies such as wind turbines and solar farms require large amounts of land, which can be an issue in densely populated areas.
4. Public perception: A part of the public opinion may have reservations about the implementation of renewable energy sources, such as concerns about the visual and/or acoustic impact of wind turbines.
5. Regulatory barriers: Regulations can be a significant barrier in the implementation of renewable energy projects, as they may vary widely by location and can be complex and time-consuming.
6. Intermittency: Many renewable energy sources such as wind and solar power are intermittent and may not always produce power when needed. This can lead to issues with grid stability and energy storage.
7. Storage: The storage of renewable energy can be a challenge, as energy storage technologies are still being developed and can be expensive to implement.

Thus, energy storage becomes crucial for the renewable energy transition and the compliance of the *Fit for 55* plan.

1.3 Energy storage

As demonstrated, energy storage becomes essential when it is intended to carry out the transition to renewable energies. To introduce the reader to existing energy storage systems, there follows a very brief review, focusing on electrochemical accumulation energy systems. But there are many advantages in energy storage for the electrical network such as peak levelling control, frequency adjustment, a softening of energy oscillations, among many others.

Thermal, thermochemical, magnetic, compressed air, hydrogen and electrochemical energy storage systems are summarized below.

a) *Thermal energy storage*

Thermal energy storage can be defined as the temporary storage of thermal energy at high or low temperatures. This concept is not new; it has been used and developed for centuries because it plays an important role in energy management/saving. It typically consists in a heat injection/extraction. Which is accumulated in a storage medium. The storage medium can be a natural structure (for example, an underground cave) or an artificial container with thermal insulating walls preventing heat exchange.

We can thus classify the different ways to store thermal energy as follows:

•sensible heat storage: heating and later cooling liquids and solids.

•latent heat storage: storing heat in a phase-change material

•thermo-chemical heat storage: using reversible endotherm/exotherm chemical reactions with thermochemical materials.

Fig. 1.1 shows the classification of thermal energy storage technologies based on the criterion of the state of the energy storage material.

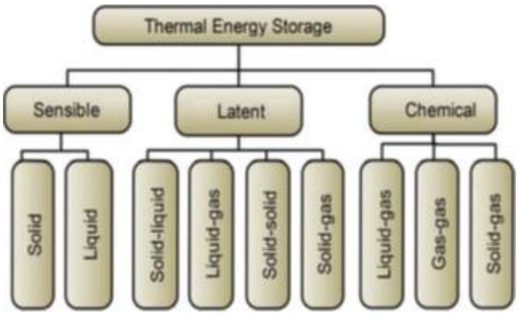

Figure 1.1. Classification of thermal energy storage technology based on the criterion of the state of the energy storage material.

Traditionally, thermal energy storage consists of increasing the temperature of a material (sensible heat). Latent heat energy storage profits from the released/absorbed heat of a substance when there is a phase transition (normally liquid-gas phase transition, but other phase transitions are theoretically available). Latent heat storage presents some advantages with respect to sensible heat storage such as those presented in an isothermal process and higher gravimetric energy density [6].

b) *Thermochemical energy storage*

This energy storage system is based on a chemical reaction that is triggered by heat release or injection. The process can be summarized in three steps: endothermic reaction (energy accumulation), storage of the resultant products, exothermic reaction (energy release). This process is reversible, which means that the entire procedure can be repeated. Thermochemical energy storage presents higher energy density accumulation than sensible and latent thermal energy storage which makes it feasible for higher energy applications in a reduced space and the accumulated energy can be stored long-term [7].

c) *Magnetic energy storage*

It consists of a superconducting coil (kept at low enough temperatures using liquid nitrogen or helium) with, practically, null resistance supporting a DC current which stores energy in the form of a magnetic field. The coil shows almost cero losses by internal resistance, enabling high-efficiency charging and discharging in an almost unlimited cycle. The main application of magnetic energy storage is electrical network stabilization, which includes frequency regulation, peak control, and voltage stability, among others.

d) *Compressed air energy storage*

Compressed air energy storage (CAES) is based on air compression in an artificial structure such as an abandoned mine or a natural structure such as an underground cave. The energy is stored in the form of pressurized air which is released through a turbine which generates electricity by the kinetic energy of moving air. CAES system is interesting due to the versatility of releasing energy and the power to regulate instabilities in the electrical network due to the implantation of renewable energies [8].

e) *Hydrogen energy storage*

Hydrogen energy storage (HES) is based on a chemical reaction that needs a high quantity of energy to produce it. The hydrogen is produced in several ways, such as photoconversion (direct generation of hydrogen) or by electrolytic methods. The produced hydrogen is accumulated for a specific time and is then oxidized to obtain water releasing energy on demand. HES technology has several advantages with respect to electric storage accumulation due to impressive and complementary features. The hydrogen can be used as a mobility vector in combustion engines and fuel cells, and this is a fantastic advantage regarding electrical mobility, especially for heavy duty vehicles, as this is a mature technology and is easily implemented although the current cost of green hydrogen is too high. The expectations placed on hydrogen are so high that authors are describing a full society economy system based on hydrogen implantation, describing the production of the hydrogen, the accumulation or storage and their later distribution and utilization [9,10].

f) *Electrochemical energy storage*

Finally, energy can be stored through electrochemical reactions in two different systems: capacitors and batteries. Electrochemical devices are typically classified in terms of specific energy and specific power. The system used by capacitors and batteries are similar and consist of two electrodes (cathode and anode) where the charge is stored/delivered and an electrolyte where the charge travels through. Capacitors are devices with a high and rapid delivery of energy, making them suitable for a quick exchange of energy. Within capacitors, there is a subgroup which is receiving exceptional attention, the supercapacitors (SC) also known as double layer electrochemical capacitors or ultracapacitors, which are made up of carbonaceous electrodes and an electrolyte.

Electrochemical batteries are highly developed devices with high energy densities and high voltages. There are many different systems for commercial batteries, which are usually classified as primary or secondary batteries. Primary batteries (non-rechargeable batteries) are for single use devices where the energy is delivered by electrode decomposition rendering the electrolyte unusable. This means that the electrochemical reaction is not reversible [11]. Among primary batteries we can find mercury oxide batteries, zinc-air batteries, and silver oxide batteries. These batteries have a high impact on the environment as well as having a high economic cost.

Secondary batteries are based on a reversible redox reaction that reduces the effective cost of electrochemical energy storage (EES). However, the lifespan of secondary batteries depends on the number of cycles of charge/discharge and its conditions. In secondary batteries, the anode undergoes the oxidation reaction during discharge and the reduction reaction during charge, and it is typically referred to as the negative electrode. Conversely, the cathode undergoes the reduction reaction during discharge and the oxidation reaction during charge, and it is referred to as the positive electrode [12]. Secondary batteries are a highly interesting research topic and are garnering attention from researchers. Technologies used for secondary batteries include lead-acid batteries, and nickel-cadmium batteries, among others. However, in the next section we will focus on lithium-ion secondary batteries to delve into the core of this thesis.

1.4 Lithium-ion batteries and the post lithium era

A lithium-ion battery (LIB) is a secondary battery that has revolutionized the field of portable electronics and electric vehicles. They accumulate and release energy by the motion of lithium ions between the two electrodes with opposite polarity through an ionic conductor, the electrolyte. During charge, lithium ions travel through the electrolyte from the cathode to anode, and vice versa during discharge. Reversible redox reactions take place in the electrodes [13]. The first LIB was proposed by M.S. Whittingham in 1976 using titanium sulphide as a cathode and metallic lithium as an anode [14]. But the first LIB was commercialized in 1991 by Sony Co. [15] with a lithium cobalt oxide anode and a carbonaceous material cathode. Since then, the development carried out by companies, and also research centers, has been of such magnitude that in

2003 Li-ion batteries already represented 28% of the market of rechargeable batteries [16] Nowadays, LIBs are still one of the most promising technologies in energy storage and continue to receive a great deal of attention by researchers and industry. LIBs present higher energy densities than other secondary batteries like lead-acid or Cd-Ni batteries, and they also show high coulombic efficiency, low self-discharge and a high operation voltage [17]. However, there are severe limitations of LIB batteries that need to be solved for devices efficient enough to support a fraction of the transition to a decarbonized economy. One of these limitations is safety, related with the use of flammable, toxic and volatile electrolytes usually made up of a mixture of organic solvent (normally consisting of a mixture of carbonates) and lithium salt [18–20]. Another big topic for researchers is the loss of capacity during the Solid Electrolyte Interface (SEI) layer formation which occurs during the first charge/discharge cycles. The SEI layer is the result of the contact between the electrode/electrolyte and is mainly caused by the degradation of the electrolyte, but it has an important role because, at the same time, it acts as protection from electrochemical degradation of the bulk electrolyte. Its formation depends on the selected electrodes and electrolyte. The SEI layer reduces the capacity of the battery but does not prevent its operation since the lithium is capable to travel through and insert itself in the electrodes.

As mentioned above, LIBs are formed by combining the single electrochemical cells which, in turn, are formed by two electrodes with polarity (cathode and anode) where the lithium ions are intercalated in a redox reversible reaction and the electrolyte where the lithium ions travel through. A brief description of the components forming the basic electrochemical cells of a LIB is given below.

- **Positive electrode: Cathode**

Two main parameters are critical when choosing the electrodes, the charge/discharge voltage and the capacity. The capacity (Q), which is directly related with the energy storage in a LIB, is theoretically dependent only of their electrodes, and it is given by this relation:

$$Q = \frac{n \cdot F}{3600 \cdot M_w} \qquad (1.1)$$

measured in mA·h·g^{-1}, where "n" is the the number of charge carrier (in case of lithium n=1), F is the Faraday constant (F=96485.3329 s·A mol^{-1}) and M_w is the molecular weight of the active material used in the electrode. The capacity of the cell is directly related with the power of a fixed voltage in the charge/discharge process.

Another main parameter to characterize an electrochemical cell is the Coulombic efficiency, which is defined as the ratio of the discharge capacity after full charge and the charge capacity of the same cycle. The coulombic efficiency is affected by several factors like electrolyte degradation, irreversibility reactions occurred at the electrodes, electrode degradation, and so on [15].

Whittingham called the highly reversible process of the insertion of the lithium in the ordered layers of the titanium sulphide cathode "intercalation mechanism", observing the minimum structural change in the crystal structure of TiS_2 sheets [14]. The TiS_2 cathode capacity is 240 $mA{\cdot}h{\cdot}g^{-1}$ and charge voltage of 2 V vs Li/Li^+, but this cathode presents several disadvantages such as H_2S toxic gas emission when exposed to ambient conditions as well as the instability of metallic lithium as anode. A few years later, John B. Goodenough, in collaboration with Koichi Mizushima, proposed using $LiCoO_2$ as cathode [21], which has a theoretical intercalation capacity of 274 $mA{\cdot}h{\cdot}g^{-1}$, and presents a charge voltage of between 3.5-4 V vs Li/Li^+ using propylene carbonate as electrolyte. This opened the door to study the lithium-based layered metal oxides ($LiMO_2$ where M is a transition metal for example). This way, cathodes based on layered oxides $LiMO_2$ can be found in the literature, where M can be, besides cobalt, manganese ($LiMnO_2$). Zhu *et al.* [22] report a cathode based on this configuration obtaining a reversible capacity of 254.3 $mA{\cdot}h{\cdot}g^{-1}$ corresponding to 90% of the theoretical capacity of the cathode. Another transition metal used in this lithium layered metal oxides configuration is nickel ($LiNiO_2$), which is cheaper than cobalt oxides, but as H. Arai *et al.* [23] reported, this cathode presents a coulombic efficiency of 80% due to irreversible processes occurring during the first cycle.

Another typical cathode found in the literature is the phospho-olivine $LiFePO_4$, also known as an LFP cathode. It was first reported in 1997 by Pahdi *et al.* [24], and presents a theoretical capacity of 170 $mA{\cdot}h{\cdot}g^{-1}$ with a plane plateau of charge voltage around 3.5 V vs Li/Li^+. Pure LFP has a very low electronic conductivity (~10^{-9} $S{\cdot}cm^{-1}$ at room temperature) [25], but there are some methods to increase the electronic conductivity such as reducing the particle diameter, applying a carbon coat or doping the LFP with activated carbon [26,27].

- **Negative electrode: Anode**

The anode is a crucial element in battery design because it determines battery performance. The first known option in battery design was the above-mentioned metallic lithium by M.S. Whittingham in 1976 [14]. Despite its very high theoretical capacity (3860 $mA{\cdot}h{\cdot}g^{-1}$), metallic lithium shows several safety problems, like flammability and being highly explosive in contact with water. Therefore, it should be manipulated in an inert atmosphere due to high degree of oxidation and dendrite growing while increasing cycle number [28,29]. To avoid dendrite growth with battery aging, the use of low potential intercalation electrodes [30] is recommended. Currently, the two most used anode materials are graphite and lithium alloy metals. In graphite anodes the theoretical insertion capacity is 372 $mA{\cdot}h{\cdot}g^{-1}$ (for LiC_6), safety conditions make graphite anodes one of the most used commercially and the interplanar distance between graphene layers makes lithium insertion [13] feasible. Moreover, graphite is an abundant material making it very affordable. However, graphite anodes have some disadvantages such as low theoretical capacity, a decrease in capacity with battery aging, and dendrite growth due to lithium-ion deposition and the increase of the planar distance.

To overcome the drawbacks of graphite, the researchers are investigating silicon-based (Si) anodes. These show the highest gravimetric and volumetric capacity, and since Si is found in great abundance in nature, this compound is very affordable [13]. But Si-based anodes pose a significant problem when talking about commercial applicability. Namely, the great volumetric expansion when lithium is inserted in the anode structure. The high volumetric expansion of Si-based anodes induces several problems like particle cracking, unstable electrode contacts which causes an ineffective electron transfer. For example, Si alloyed with lithium ($Li_{22}Si_5$) presents a theoretical capacity of 4200 mA·h·g^{-1}, but its volumetric expansion during cyclability is about 310 %. Another Si alloy is $Li_{15}Si_4$ which presents a capacity of 3579 mA·h·g^{-1} and the volumetric expansion when lithium is inserted is 280% at room temperature [31]. Other issues related to volumetric expansion of Si-based anodes are capacity loss during cycle aging, electrode degradation and the continuous SEI formation of Si alloy causes a high drop in capacity when increasing the cycle number of the electrochemical cell which results in reduced coulombic efficiency [32].

- **Electrolyte**

As mentioned above, the theoretical capacity, and therefore, the energy accumulated in a LIB is dependent exclusively of its electrodes, but the electrolyte also plays an important role. An electrolyte is a material that allows ionic transport between the two electrodes. Hence, the most important feature that an electrolyte should present is null electronic conductivity, and high ionic conductivity, which allows for the transport of ionic charge inside [33].

The choice of the electrolyte for a specific LIB depends on the choice of the electrodes for the desired application. But some common reflections can be made for the suitable selection of the electrolyte, such as electrochemical stability in the selected voltage, high thermal stability and the effective cost, among many others.

Electrolyte temperature is a key factor because higher temperatures can reduce battery performance (electrolyte degradation) and safety conditions. Currently, portable devices have battery operation ranges of -20 to 60 ºC [34]. As it is impossible to tune electrode performance for temperature operation, this responsibility belongs to the electrolyte, differentiating between low and high temperature issues in battery malfunction. At low temperatures the main effect is capacity loss, being irreversible if the battery is charged at low temperatures as shown by Petzl *et. al* [35]. The capacity loss at low temperature operation is attached to the increase in the internal resistance. Furthermore, the highest capacity loss for LIBs occurs when the electrolyte crystallizes, which is usually considered a "turning point" [36]. Instead, the consequences of the high temperature could be the degradation and thermal decomposition of the electrolyte and the deterioration of the SEI layer formed at the electrodes, irreversibly damaging the device's performance.

Despite innovations in anodes and to a higher degree, in cathodes (shown previously), electrolytes have remained the same for the last two decades, where lithium salts (normally $LiPF_6$) dissolved in a mixture of organic cosolvent (normally a mixture of carbonates) are the current standard [37–40]. Nonetheless, as it is well known, current carbonate electrolytes are flammable and volatile, and these are major security risks which need improving as we will see in the next section.

As previously mentioned, ion transport inside the electrolyte is one of most important properties of the bulk electrolyte. This means that ionic conductivity should be high enough to allow lithium ions traveling between electrodes and inside the electrolyte. Ionic conductivity is a parameter that quantifies the ionic mobility of the ions inside the electrolyte. In current electrolytes a measure of the ionic conductivity is a direct measure of the mobility of lithium ions of $LiPF_6$ salt. In these electrolytes, the ionic conductivity is given by the lithium salt dissolved in a carbonate cosolvent. So, it is clear that the viscosity of the solvent should be as low as possible to facilitate ion transport, but the solvent should have a high dielectric permittivity to dissolve the lithium salt [39]. This last statement, high dielectric permittivity and low viscosity, is a major challenge in LIB design. The lithium transport number is an important parameter that characterizes the fraction of ionic conductivity that can be made the most of in an electrochemical cell for lithium electrode insertion. But the lithium transport number has some controversial arguments in its measurement [41] and this measurement will not be given any further consideration. The new developments in cathodes, promising higher energy densities (and therefore higher operation voltages), are a reality, but electrolytes of higher electrochemical stability are needed to support high voltages without chemical degradation. Electrolyte solutions must be polar enough to dissolve lithium salts and remain electrochemically stable between 0 - 5 V vs Li/Li^+ [42].

As we have seen before, the SEI is a passivation layer caused by the decomposition of the electrolyte components in the pristine surface of the electrode protecting the electrolyte from further decomposition. It is usually formed during the first cycles. As expected, the formation of the SEI becomes crucial to the performance of the battery since it acts as a limiting factor in the electrode ion transport and intercalation. As in the case of electrolytes, an excessive SEI layer is inconvenient and in LIBs, is responsible for the capacity drop between the first and the second cycle [43].

However, one of the biggest issues of current electrolytes is their liquid state under operating conditions. Liquid electrolytes still possess some difficulties in battery manufacturing which have to be solved, such as spills in industrial assembly processes. On the other hand, solid electrolytes are still problematic due to poor conductivity, high interfacial resistances, and poor contact with the electrodes that demand complex deposition processes or pressure in the cells [44]. The nano-encapsulation in an organic or inorganic matrix (such as silicon-based scaffolds) by spinodal decomposition or sol-gel processes, has proved to be a good alternative to have a solid-like electrolyte preserving the properties of a liquid electrolyte [45]. The interest in solid-like electrolytes began in 1975 when Wright presented a study of electrical conductivity using a poly(ethylene oxide) (PEO) as polymer matrix precursor with sodium iodide and sodium, potassium and ammonium thiocyanates [46]. Since then, many efforts have been devoted to improving these semisolid materials. One of the advantages to having a solid-like electrolyte (*e.g.* ionogel) is that it plays a double role, as the separator and as the electrolyte at the same time. Additionally, ionogels are promising candidates to minimize the risk of short-circuiting due to dendrite formation in stabilizing the lithium anode during the charge/discharge cycle process [47,48]. Many different scaffolds encapsulating a mixture between ILs and a lithium salt have been shown to obtain a solid like electrolyte such as TiO_2 based ionogels [49], metal-organic frameworks (MOFs) [50] and, as used in this thesis, ionogels confined in Si-O frameworks, [51].

1.5 Ionic Liquids as potential electrolytes

Ionic liquids (IL) are heterogeneous compounds formed by an organic cation and an organic/inorganic anion bonded by electrostatic interactions. Strictly speaking, ILs can be considered as molten salts, in the sense that they are formed by ions, with a melting point below 100 ºC, and those with melting points below room temperature are usually called room temperature ionic liquids (RTIL). ILs are nanostructured compounds that constitute a new class of green solvents due to their amazing properties such as, negligible vapor pressure, low toxicity (specifically compared with traditional battery organic electrolytes), high ionic conductivity, and a wide electrochemical window, non-flammability [52], and most relevantly, the possibility of tuning their properties by choosing the appropriate combination of cation and anion from many currently known IL moieties (designer solvents). All these features have attracted the attention of researchers, and they have been used in a plethora of applications, including electrochemistry [53–56].

Depending on their synthesis characteristics, ILs can be divided into two groups, protic ILs (PILs) and aprotic (AILs). PILs are synthetized via proton transfer (neutralization of Brönsted Acid/Base), while AILs are synthetized via different methods such as the quaternization reaction of an imidazole. These differences lead to interesting properties in both groups, since, for example, aprotic ILs present the highest thermal stability and also higher electrochemical stability [57], but the main disadvantage is the high cost and higher toxicity relative to protic ionic liquids (PIL). On the other hand, PILs offer some advantages like costing less and having easier synthesis [58], and they are progressively receiving more attention for their potential in electrochemical applications [59–61].

Among the most promising candidates to replace the currently used electrolytes, as previously pointed out, RTILs and its mix of metal salts are proposed as a good selection for safer chemistries [62]. However, the potential applicability of pure ILs in certain fields has been restricted due to their high viscosity. which hinders their performance within reaction media. Consequently, in the last decade, studies of mixtures of ILs with molecular cosolvent or salts are again opening up possibilities.

In the last decade the number of works concluding with the success of ILs and its mixtures as electrolytes for batteries, supercapacitors, fuel cells, sensors, etc., has exponentially increased [63–67].

Nevertheless, as previously mentioned, their liquid state can be limiting and the confinement of ILs within nano-skeletons is proposed as a clever strategy overcome this problem [68]. Specifically, in an electrochemical field, recent studies suggest the possibility of using sol-gel electrolytes in energy storage devices to improve the safety of the electrolyte and make manipulation easier [64,69,70], although the key properties for this application after gelation have not been thoroughly studied. Garaga *et al*. [71] found an enhancement of ionic mobility of different ILs (protic and aprotics) confined in nanoporous silica networks.

Nanoconfined ILs are a new class of bifasic materials combining the advantages of the key chemistry of ILs and the characteristics of solid matrices. The internal network is cross-linked through weak interactions, such as hydrogen bonds, between the components [64]. Nevertheless, the confinement and the interactions between ILs and walls can lead to changes in physicochemical properties in the restricted space of the ionogel compared to the corresponding bulk systems. This occurs for example in thermal behavior as is shown, in the review by Zhang *et al*. [72].

Despite the interest received by ILs in the last decade, many questions still remain. One such question is, the best way of nanoconfining ILs and their mixtures, and the optimal methodology to make the industrial implantation possible, together with a systematic study of the thermophysical, thermal and electrochemical properties before and after nanoconfinement. The objectives of this thesis aim to contribute to shedding some light on the new 4th generation electrolytes.

1.6 Objectives

The main objective of this thesis is the study of the thermal, structural, and electric properties of mixtures of ILs and inorganic salts of electrochemical interest, both in the liquid state and after nanoconfinement of those systems in a silica scaffold (ionogel) with the aim to propose smart electrolytes that improve the security and durability, reducing the charging time.

With the aim of proposing a new electrolyte that meets all current requirements and fills the current gaps in industry, the three main objectives of this thesis are:

- The systematic characterization of several protic and aprotic ILs and their mixture with lithium, calcium, magnesium, and aluminum salts with common anion with the IL.
- The establishment of nanoconfinement route in silica scaffolds of the previous mixtures to get stable quasi-solid electrolytes and the analysis of the changes of the physical properties due to the confinement.
- The assembly and testing of a battery cell with semi-solid electrolyte and commercial electrodes.

By this aim, this thesis is framed in four different chapters as follows:

1. Introduction: a brief review of the state of art is presented.

2. Materials and methods: sample synthesis is described as well as the experimental used techniques.
3. Results and discussion: the principal results are presented and analyzed.
4. Conclusions: the conclusions of this thesis are presented.

References

[1] S. Schlacke, H. Wentzien, E.-M. Thierjung, M. Köster, Implementing the EU Climate Law via the 'Fit for 55' package, Oxford Open Energy. 1 (2022) 1–13.

[2] B.E. Layton, A COMPARISON OF ENERGY DENSITIES OF PREVALENT ENERGY SOURCES IN UNITS OF JOULES PER CUBIC METER, (n.d.).

[3] L. Hughes, Biological consequences of global warming: is the signal already apparent?, Trends Ecol Evol. 15 (2000) 56–61.

[4] T.K.R. Matthews, R.L. Wilby, C. Murphy, Communicating the deadly consequences of global warming for human heat stress, Proc Natl Acad Sci U S A. 114 (2017) 3861–3866.

[5] M.S. and A.N. P Rowlinson, ed., Livestock and Global Climate Change Livestock and Global Climate Change CAMBRIDGE, Cambridge University Press, Cambridge, 2008.

[6] P. Tatsidjodoung, N. Le Pierrès, L. Luo, A review of potential materials for thermal energy storage in building applications, Renewable and Sustainable Energy Reviews. 18 (2013) 327–349.

[7] N. Rathore, N.L. Panwar, Strategic overview of management of future solar photovoltaic panel waste generation in the Indian context, Waste Management and Research. 40 (2022) 504–518.

[8] M. Budt, D. Wolf, R. Span, J. Yan, A review on compressed air energy storage: Basic principles, past milestones and recent developments, Appl Energy. 170 (2016) 250–268.

[9] C.J. Winter, Hydrogen energy — Abundant, efficient, clean: A debate over the energy-system-of-change, Int J Hydrogen Energy. 34 (2009) S1–S52.

[10] M.A. Rosen, S. Koohi-Fayegh, The prospects for hydrogen as an energy carrier: an overview of hydrogen energy and hydrogen energy systems, Energy Ecol Environ. 1 (2016) 10–29.

[11] S.S. Hosseiny, M. Wessling, Ion exchange membranes for vanadium redox flow batteries, Advanced Membrane Science and Technology for Sustainable Energy and Environmental Applications. (2011) 413–434.

[12] O.S. Burheim, Engineering energy storage, 2017, 1-223.

[13] P.U. Nzereogu, A.D. Omah, F.I. Ezema, E.I. Iwuoha, A.C. Nwanya, Anode materials for lithium-ion batteries: A review, Applied Surface Science Advances. 9 (2022) 100233.

[14] M.S. Whittingham, Electrical Energy Storage and Intercalation Chemistry, Science (1979). 192 (1976) 1126–1127.

[15] M. Li, J. Lu, Z. Chen, K. Amine, 30 Years of Lithium-Ion Batteries, Advanced Materials. 30 (2018) 1800561.

[16] J. Xu, H.R. Thomas, R.W. Francis, K.R. Lum, J. Wang, B. Liang, A review of processes and technologies for the recycling of lithium-ion secondary batteries, J Power Sources. 177 (2008) 512–527.

[17] T. Kim, W. Song, D.Y. Son, L.K. Ono, Y. Qi, Lithium-ion batteries: outlook on present, future, and hybridized technologies, J Mater Chem A Mater. 7 (2019) 2942–2964.

[18] J. Xia, F. Zhu, G. Wang, L. Wang, Y. Meng, Y. Zhang, Synthesis of LiFePO4/C using ionic liquid as carbon source for lithium ion batteries, Solid State Ion. 308 (2017) 133–138.

[19] Q. Wu, W. Lu, J. Prakash, Characterization of a commercial size cylindrical Li-ion cell with a reference electrode, J Power Sources. 88 (2000) 237–242.

[20] J.M. Chen, C.Y. Yao, S.P. Sheu, Y.C. Chiou, H.C. Shih, The study of carbon half-cell voltage in lithium-ion secondary batteries, J Power Sources. 68 (1997) 242–244.

[21] K. Mizushima, P.C. Jones, P.J. Wiseman, J.B. Goodenough, LixCoO2 (0<x<-1): A new cathode material for batteries of high energy density, Mater Res Bull. 15 (1980) 783–789.

[22] X. Zhu, F. Meng, Q. Zhang, L. Xue, H. Zhu, S. Lan, Q. Liu, J. Zhao, Y. Zhuang, Q. Guo, B. Liu, L. Gu, X. Lu, Y. Ren, H. Xia, LiMnO2 cathode stabilized by interfacial orbital ordering for sustainable lithium-ion batteries, Nature Sustainability 2020 4:5. 4 (2020) 392–401.

[23] H. Arai, S. Okada, Y. Sakurai, J.I. Yamaki, Reversibility of LiNiO2 cathode, Solid State Ion. 95 (1997) 275–282.

[24] A.K. Padhi, K.S. Nanjundaswamy, J.B. Goodenough, Phospho-olivines as Positive-Electrode Materials for Rechargeable Lithium Batteries, J Electrochem Soc. 144 (1997) 1188–1194.

[25] S.Y. Chung, J.T. Bloking, Y.M. Chiang, Electronically conductive phospho-olivines as lithium storage electrodes, Nat Mater. 1 (2002) 123–128.

[26] N. Böckenfeld, R.S. Kühnel, S. Passerini, M. Winter, A. Balducci, Composite LiFePO4/AC high rate performance electrodes for Li-ion capacitors, J Power Sources. 196 (2011) 4136–4142.

[27] N. Böckenfeld, T. Placke, M. Winter, S. Passerini, A. Balducci, The influence of activated carbon on the performance of lithium iron phosphate based electrodes, Electrochim Acta. 76 (2012) 130–136.

[28] J.C. Rushing, C.M. Stern, N. Elgrishi, D.G. Kuroda, Tale of a “non-interacting” Additive in a Lithium-Ion Electrolyte: Effect on Ionic Speciation and Electrochemical Properties, Journal of Physical Chemistry C. 126 (2022) 2141–2150.

[29] W. Xu, J. Wang, F. Ding, X. Chen, E. Nasybulin, Y. Zhang, J.G. Zhang, Lithium metal anodes for rechargeable batteries, Energy Environ Sci. 7 (2014) 513–537.

[30] G. Cao, D. Wang, Nanomaterials for energy conversion and storage, (2017) 7-4.

[31] X. Li, F.E. Kersey-Bronec, J. Ke, J.E. Cloud, Y. Wang, C. Ngo, S. Pylypenko, Y. Yang, Study of Lithium Silicide Nanoparticles as Anode Materials for Advanced Lithium Ion Batteries, (2017), 9, 16071-16080.

[32] Y. Jin, B. Zhu, Z. Lu, N. Liu, J. Zhu, Challenges and recent progress in the development of Si anodes for lithium-ion battery, Adv Energy Mater. (2017), 7, 23.

[33] M. Li, C. Wang, Z. Chen, K. Xu, J. Lu, New Concepts in Electrolytes, Chem Rev. 120 (2020) 6783–6819.

[34] L. Chen, H. Wu, X. Ai, Y. Cao, Zhongxue Chen, Z. Chen, Toward wide-temperature electrolyte for lithium–ion batteries, Battery Energy. (2022), 20210006, 1 (2).

[35] M. Petzl, M. Kasper, M.A. Danzer, Lithium plating in a commercial lithium-ion battery – A low-temperature aging study, J Power Sources. 275 (2015) 799–807.

[36] D. Hubble, D.E. Brown, Y. Zhao, C. Fang, J. Lau, B.D. McCloskey, G. Liu, Liquid electrolyte development for low-temperature lithium-ion batteries, Energy Environ Sci. 15 (2022) 550–578.

[37] L.O. Valøen, J.N. Reimers, Transport Properties of LiPF 6-Based Li-Ion Battery Electrolytes, (2005), 152 A882.

[38] C.L. Campion, W. Li, B.L. Lucht, Thermal Decomposition of LiPF 6-Based Electrolytes for Lithium-Ion Batteries, (2005) 152, A2327.

[39] K. Xu, Electrolytes and interphases in Li-ion batteries and beyond, Chem Rev. 114 (2014) 11503–11618.

[40] T. Boulanger, A. Eldesoky, S. Buechele, T. Taskovic, S. Azam, C. Aiken, E. Logan, M. Metzger, Investigation of Redox Shuttle Generation in LFP/Graphite and NMC811/Graphite Cells, J Electrochem Soc. 169 (2022) 040518.

[41] K. Xu, Electrolytes and interphases in Li-ion batteries and beyond, Chem Rev. 114 (2014) 11503–11618.

[42] H. Zhang, H. Zhao, M.A. Khan, W. Zou, J. Xu, L. Zhang, J. Zhang, Recent progress in advanced electrode materials, separators and electrolytes for lithium batteries, J Mater Chem A Mater. 6 (2018) 20564–20620.

[43] K. Xu, Nonaqueous liquid electrolytes for lithium-based rechargeable batteries, Chem Rev. 104 (2004) 4303–4417.

[44] R. Chen, Q. Li, X. Yu, L. Chen, H. Li, Approaching Practically Accessible Solid-State Batteries: Stability Issues Related to Solid Electrolytes and Interfaces, Chem Rev. 120 (2020) 6820–6877.

[45] M. Brachet, D. Gaboriau, P. Gentile, S. Fantini, G. Bidan, S. Sadki, T. Brousse, J. Le Bideau, Solder-reflow resistant solid-state micro-supercapacitors based on ionogels, J Mater Chem A Mater. 4 (2016) 11835–11843.

[46] P. V. Wright, Electrical conductivity in ionic complexes of poly(ethylene oxide), British Polymer Journal. 7 (1975) 319–327.

[47] N. Chen, H. Zhang, L. Li, R. Chen, S. Guo, Ionogel Electrolytes for High-Performance Lithium Batteries: A Review, Adv Energy Mater. 8 (2018) 1702675.

[48] Y. Li, K.W. Wong, K.M. Ng, Ionic liquid decorated mesoporous silica nanoparticles: a new high-performance hybrid electrolyte for lithium batteries, Chemical Communications. 52 (2016) 4369–4372.

[49] X. Li, Z. Zhang, L. Yang, K. Tachibana, S.I. Hirano, TiO2-based ionogel electrolytes for lithium metal batteries, J Power Sources. 293 (2015) 831–834.

[50] K. Fujie, R. Ikeda, K. Otsubo, T. Yamada, H. Kitagawa, Lithium Ion Diffusion in a Metal-Organic Framework Mediated by an Ionic Liquid, Chemistry of Materials. 27 (2015) 7355–7361.

[51] A.I. Horowitz, M.J. Panzer, High-performance, mechanically compliant silica-based ionogels for electrical energy storage applications, J Mater Chem. 22 (2012) 16534–16539.

[52] J. Salgado, M. Villanueva, J.J. Parajó, J. Fernández, Long-term thermal stability of five imidazolium ionic liquids, Journal of Chemical Thermodynamics. 65 (2013) 184–190.

[53] O. Cabeza, J.H. Fernández, F.M. Gaciño, J. Salgado, M. Villanueva, J.A. Nóvoa López, H. Michinel, E.L. Lago, L. Segade, T. Méndez-Morales, L.M. Varela, A.M.A.M. Rubio, F. Tomás-Alonso, J.H. Fernández, A.P. de los Ríos, F.J.H.

Fernández, J. Hernández-Fernández, A. Pérez de los Ríos, F.J. Hernández Fernández, Green Aspects of Ionic Liquids, in: A. Pérez de los Ríos, F.J. Hérnández Fernández (Eds.), Ionic Liquids in Separation Technology, Elsevier, Amsterdam, 2014: pp. 82–93.

[54] J. Salgado, T. Regueira, L. Lugo, J. Vijande, J. Fernández, J. García, Density and viscosity of three (2,2,2-trifluoroethanol+1-butyl-3-methylimidazolium) ionic liquid binary systems, J Chem Thermodyn. 70 (2014) 101–110.

[55] D. Hekmat, D. Hebel, S. Joswig, M. Schmidt, D. Weuster-Botz, Advanced protein crystallization using water-soluble ionic liquids as crystallization additives, Biotechnol Lett. 29 (2007) 1703–1711.

[56] M. Petkovic, J. Ferguson, A. Bohn, J. Trindade, I. Martins, M.B. Carvalho, M.C. Leitao, C. Rodrigues, H. Garcia, R. Ferreira, K.R. Seddon, L.P.N. Rebelo, C. Silva Pereira, Exploring fungal activity in presence of ILs, Green Chemistry. 11 (2009) 889–894.

[57] D.R. McFarlane, J. Sun, J. Golding, P. Meakin, M. Forsyth, High conductivity molten salts based on the imide ion, Electrochim Acta. 45 (2000) 1271–1278.

[58] M. Picquet, I. Tkatchenko, I. Tommasi, P. Wasserscheid, J. Zimmermann, Ionic Liquids, 3. Synthesis and Utilisation of Protic Imidazolium Salts in Homogeneous Catalysis, Adv Synth Catal. 345 (2003) 959–962.

[59] M.S. Miran, T. Yasuda, M.A.B.H. Susan, K. Dokko, M. Watanabe, Electrochemical properties of protic ionic liquids: correlation between open circuit potential for H2/O2 cells under non-humidified conditions and ΔpKa, RSC Adv. 3 (2013) 4141–4144.

[60] L.E. Shmukler, M.S. Gruzdev, N.O. Kudryakova, Y.A. Fadeeva, A.M. Kolker, L.P. Safonova, Thermal behavior and electrochemistry of protic ionic liquids based on triethylamine with different acids, RSC Adv. 6 (2016) 109664–109671.

[61] X. Lu, G. Burrell, F. Separovic, C. Zhao, Electrochemistry of Room Temperature Protic Ionic Liquids: A Critical Assessment for Use as Electrolytes in Electrochemical Applications, (2012).

[62] K. Ghandi, A Review of Ionic Liquids, Their Limits and Applications, Green and Sustainable Chemistry. 4 (2014) 44–53.

[63] M. Cvjetko Bubalo, S. Vidović, I. Radojčić Redovniković, S. Jokić, Green solvents for green technologies, Journal of Chemical Technology and Biotechnology. 90 (2015) 1631–1639.

[64] J. Le Bideau, L. Viau, A. Vioux, Ionogels, ionic liquid based hybrid materials, Chem. Soc. Rev. 40 (2011) 907–925.

[65] P. Hapiot, C. Lagrost, Electrochemical reactivity in room-temperature ionic liquids, Chem. Rev. 108 (2008) 2238–2264.

[66] M. Galiński, A. Lewandowski, I. Stepniak, Ionic liquids as electrolytes, Electrochim Acta. 51 (2006) 5567–5580.

[67] L.M. Varela, J. Carrete, M. García, L.J. Gallego, M. Turmine, E. Rilo, O. Cabeza, Pseudolattice theory of charge transport in ionic solutions: Corresponding states law for the electric conductivity, Fluid Phase Equilib. 298 (2010) 280–286.

[68] T.K.N. Tran, A. Guyomard-Lack, C. Cerclier, B. Humbert, G. Colomines, J.F. Pilard, R. Deterre, J. Le Bideau, E. Leroy, Natural rubber-based ionogels, J Renew Mater. 6 (2018) 251–258.

[69] L. Negre, B. Daffos, V. Turq, P.L. Taberna, P. Simon, Ionogel-based solid-state supercapacitor operating over a wide range of temperature, Electrochim Acta. 206 (2016) 490–495.

[70] S.A.M. Noor, P.M. Bayley, M. Forsyth, D.R. MacFarlane, Ionogels based on ionic liquids as potential highly conductive solid state electrolytes, Electrochim Acta. 91 (2013) 219–226.

[71] M.N. Garaga, L. Aguilera, N. Yaghini, A. Matic, M. Persson, A. Martinelli, Achieving enhanced ionic mobility in nanoporous silica by controlled surface interactions, Physical Chemistry Chemical Physics. 19 (2017) 5727–5736.

[72] S. Zhang, J. Zhang, Y. Zhang, Y. Deng, Nanoconfined Ionic Liquids, Chem Rev. 117 (2017) 6755–6833.

2. Materials and methods

2.1. Background.

The main information of the analysed ionic liquids (ILs) and salts can be found in this section, as well as the employed gelation routes. Additionally, the main characteristics of the experimental techniques and methodologies used in this work are also illustrated. With the aim of helping the reader to understand the approach of this work, this chapter is divided in two parts. The first part describes deeply the preparation of samples and the second part the experimental techniques, together with a summary of their theoretical frameworks. These include:

- Thermal characterization: Thermal behaviour and the liquid range of samples, including phase transitions and thermal degradation are studied by differential scanning calorimetry (DSC) and thermogravimetric analysis (TGA).
- Structural characterization: For this study, the nuclear magnetic resonance (NMR) is described, mainly, to analyse the atomic structure of the samples and its possible changes under salt addition and the nanoconfinement.
- Physicochemical properties: Three physicochemical properties were used during the developing of this thesis, density, viscosity, and speed of sound. These properties are measured with the corresponding experimental equipment to determine intensive and transport properties and their evolution with salt addition and before and after the confinement in a silica scaffold.
- Electrochemical characterization: The electrochemical characterization was carried by different and complementary techniques such as electrochemical impedance spectroscopy (EIS), broad band dielectric spectroscopy (BBDS), AC/DC ionic conductivity, galvanostatic charge/discharge with potential limitation (GCPL). All of them are described in this section.

Part of the information presented in this chapter can be found in the following publications (the publisher authorizations can be found in Annexed material B):

- J. J. Parajó, P. Vallet, M. J. G. Guimarey, A. Santiago, T. Teijera, A. Amigo, L. M. Varela, J. Salgado & M. Villanueva. “Thermophysical properties of n-alkyl-ammonium nitrate ionic liquids (n = 2,3,4) pure and water saturated for energy applications”. Journal of Thermal Analysis and Calorimetry volume 148, pages6699–6714 (2023). DOI:10.1007/s10973-023-12194-1.
- P. Vallet, S. Bouzón-Capelo, T. Méndez-Morales, V. Gómez-González, Y. Arosa, R. de la Fuente, E. López-Lago, J. R. Rodríguez, L. J. Gallego, J. J. Parajó, J. Salgado, M. Turmine, L. Segade, O. Cabeza, L. M. Varela. “On the physical properties of mixtures of nitrate salts and protic ionic liquids”. Journal of Molecular Liquids 350(11):118483. DOI: 10.1016/j.molliq.2022.118483.
- J.J. Parajó, P. Vallet, M. Villanueva, O. Cabeza, F. Fernández-Carretero, A. García Luis, M.E. Di Pietro, A. Mele, F. Castiglione, J. Salgado, L.M. Varela. “Ionogels based on protic ionic liquid - lithium salt mixtures”. Journal of Molecular Liquids, 397(1), 124093. DOI: https://doi.org/10.1016/j.molliq.2024.124093.

- P. Vallet, J.J. Parajó, A. Santiago-Alonso, M. Villanueva, Ó. Cabeza, L.M. Varela, J. Salgado. "Anomalous behaviour of the ionic conductivity of nanoconfined IL - lithium salt mixtures". Journal of Molecular Liquids. In Press, Journal Pre-proof. DOI: 10.1016/j.molliq.2024.124630.

2.2. Chemicals.

The chemicals used for the development of this thesis are ILs, inorganic salts of electrochemical interest and precursor of the ionogels. The main characteristic parameters of all of them can be found in Table 2.1. Specifically, the ILs were two aprotic ionic liquids (AILs) (1-Ethyl-3-methylimidazolium bis(trifluoromethylsulfonyl)imide $[C_2C_1Im][TFSI]$ and 1-Butyl-1-methylpyrrolidinium bis(trifluoromethylsulfonyl)imide) $[C_4C_1Pyr][TFSI]$) and two protic ionic liquids (PILs) (Ethylammonium nitrate [EAN] and 1-Ethyl-3-H-Imidazolium Nitrate $[C_2Im][NO_3]$). The selected inorganic salts for electrochemical purposes are Lithium Nitrate ($LiNO_3$), Magnesium Nitrate Hexahydrate ($Mg(NO_3)_2{\cdot}6H_2O$), Calcium Nitrate Tetrahydrate ($Ca(NO_3)_2{\cdot}4H_2O$), Aluminium Nitrate Nonahydrate ($Al(NO_3)_3{\cdot}9H_2O$) and Lithium Bis(trifluoromethylsulfonyl)imide (LiTFSI). Finally, the, Tetramethyl Ortosilicate (TMOS), Tetraethoxysilane (TEOS) and Dimethoxydimethylsilane (DMDMS) as silica precursors for the ionogel scaffold and Formic Acid (FA) and Ethanol (EtOH) as chemical catalysers to trigger the gelation process.

Table 2.1.-Identification of Chemicals used in this work.

Name	Molecular Weight (g·mol^{-1})	Structure	CAS number	Provenance	Purity
Ethylammonium nitrate	108.097	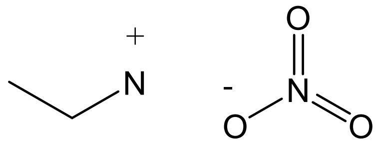	[22113-86-6]	IOLITEC	99.9%[a]
1-Ethyl-3-H-Imidazolium Nitrate	159.14	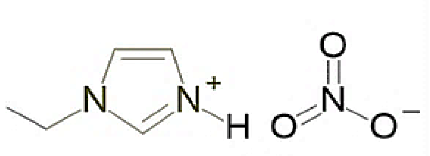	[501693-38-5]	IOLITEC	98%[a]
1-Ethyl-3-methylimidazolium bis(trifluoromethylsulfonyl)imide	391.31	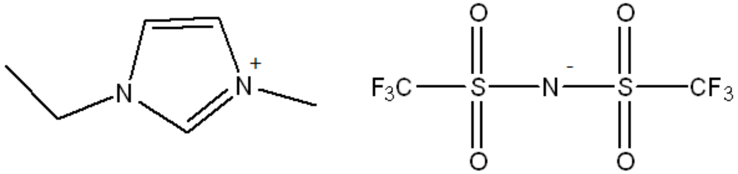	[174899-82-2]	IOLITEC	99%[a]
1-Butyl-1-methylpyrrolidinium bis(trifluoromethylsulfonyl)imide	422.41	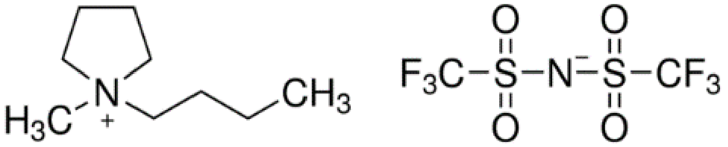	[223437-11-4]	IOLITEC	99%[a]
Lithium Nitrate	68.946	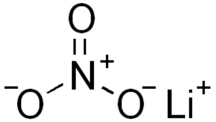	[7790-69-4]	Sigma Aldrich	>0.999[a]

Magnesium Nitrate Hexahydrate	256.41	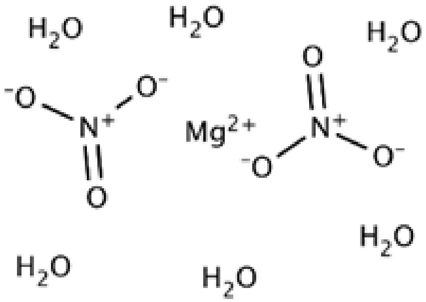	[13446-18-9]	Panreac	>0.98[a]
Calcium Nitrate Tetrahydrate	164.09	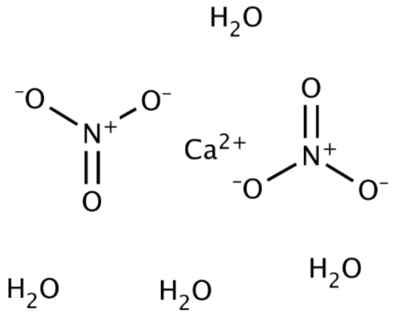	[13446-18-9]	Merck	99.9%[a]
Aluminium Nitrate Nonahydrate	375.13	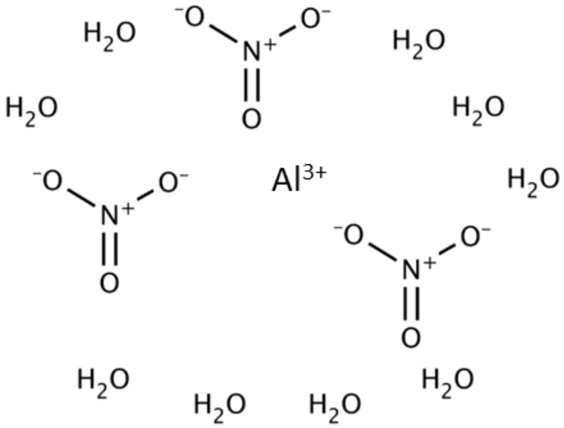	[7784-27-2]	Scharlau	>0.98[a]

Lithium Bis(trifluoromethylsulfonyl)imide	287.09	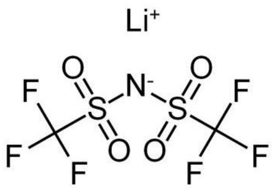	[90076-65-6]	Sigma Aldrich	99%[a]
Tetramethyl Ortosilicate (TMOS)	152.22	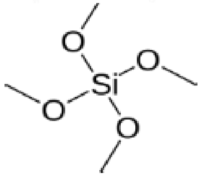	[681-84-5]	Sigma Aldrich	99%[a]
Tetraethoxysilane (TEOS)	208.33	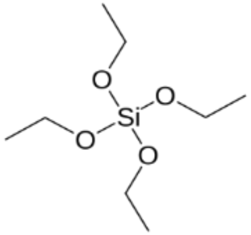	[78-10-4]	Sigma Aldrich	>0.98[a]
Dimethoxydimethylsilane (DMDMS)	120.22	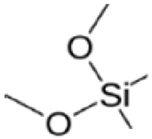	[1112-39-6]	Sigma Aldrich	99.5%[a]
Formic Acid (FA)	46.03	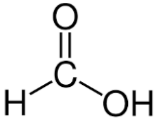	[64-18-6]	Scharlau	98%[a]
Ethanol (EtOH)	46.07	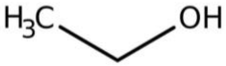	[64-17-5]	Panreac	99.8%[a]

1. [a]Indicated by provider.

2.3. Gelation routes.

One of the main objectives of this thesis is the study of the gelation routes to obtain a semisolid material from a scaffold matrix made by silica and an electrolytic solution (ES, mixtures of IL and metal salt of common anion). In this framework, the **three gelation routes** used for the ionogels synthesis are exposed in the chronological order used in this thesis:

1. <u>Formic acid route</u>: our gelation route is adapted from that of Negre et al. [1]. A solid-like electrolyte (ionogel) is synthetized using TEOS (tetraethylorthosilicate) as silica precursor using formic acid (FA) to trigger the reaction. The synthesis is performed through volumetric ratio ES:TEOS:FA 4:1:2. Firstly the TEOS and the FA are mixed stirring (at 300 rpm) at 40 °C during 18 min, after this, the electrolyte solution (ES), previously prepared following the methodology described elsewhere [2] is added. The pre-gel sample is then stored in sealed containers, and kept at room temperature until complete gelation, and, then, the resulting ionogel is aged for approximately one week.
2. <u>Ethanol route</u>: This gelation route is performed as an adaptation of a methodology previously reported by Garaga et al. [3–5], with volumetric proportions of 1:0.428:3 (ES:TEOS:EtOH). These chemical compounds are stirred for 1 hour. After that, the pre-gel sample is kept into vials in a furnace maintained at 40 °C (lower temperature than the previously reported [3,5,6] due to the formation of cracking in the gel samples if they are kept at higher temperatures due to the insertion of air) for 4 days to evaporate the excess of ethanol.
3. <u>Two silica precursor route</u>: This sol-gel route is performed as an adaptation of that of Brachet et al. [7]. The main modification is the tuning of the ratio between the IL and the silica matrix. The proportions of the gelation route are described, expressed in molar ratio, as follow IL:[silicon matrix]:FA. The silicon matrix is a mixture between two different silicon precursors, TMOS and DMDMS, in the molar ratio 0.7:0.3 respectively. The proportion between IL and silicon matrix is 50% each, which results in a molar ratio of 1:[0.7:0.3] IL:[silicon matrix]. Finally, the proportion of FA to trigger the reaction is given by the rule "one mol of FA to break one mol of $O-CH_3$ bond". So, the molar ratio for the prepared ionogels is 1:[0.7:0.3]:3.4 (IL:[silicon matrix]:FA). Ionogels are synthetised following this method: Stirring the TMOS:DMDMS mixture for 10 minutes. After this, IL is added to the previous mixture and stirred for 10 more minutes and, finally, FA is added to the mixture to trigger the gelation reaction and stirred for 3 more minutes.

   After that, the pre-gel sample is transferred to a Teflon cast and covered for 2 days. Then the cover is removed, and the gelation continued for 4 more days.

Before measurements, the synthetised ionogel is placed in a high vacuum to remove all volatile compounds remaining after the synthesis.

Through routes 1 and 2 the obtained gels present good thermal and electric properties, as will be seen in the results section, but they do not present the desired rigidity for their handling, while route 3 allowed us to obtain a gel more suitable to our objectives, as can be seen in Fig. 2.1.

Figure 2.1. Self-standing ionogel synthetised by two precursors silica route.

The following table shows the optimal gelation methods for the IL/IL+salt mixtures considered in this thesis:

Table 2.2. Used gellification route for each IL/IL+salt.

	Formic Acid Route	*Ethanol Route*	*Two silica precursor route*
EAN	X	X	
$[C_2Im][NO_3]$		X	
$[C_4C_1Pyrr][TFSI]$			X
$[C_2C_1Im][TFSI]$			X

2.4. Thermal characterization.

2.4.1. Differential Scanning Calorimetry (DSC)

A differential scanning calorimeter (DSC Q1000 TA-Instruments) (Fig. 2.2) with hermetically sealed aluminium pans was used to determine the thermal transitions experimented by the pure IL and salt solutions, in liquid and gel conditions, during heating and cooling cycles under nitrogen atmosphere. All the samples were subjected, at least, to four thermal ramps, two in cooling and two in heating modes, with an isothermal step between them: (a) heating from 25 to 120 °C at 20 °C min^{-1}, (b) isothermal step at 120 °C during 45 minutes to remove impurities, free water content and to erase the thermal history of the sample [8], (c) cooling from 120 to -85 °C at 5 °C min^{-1}, (d) isothermal step at -85 °C during 5 minutes and (e) heating from -85 °C to 100 °C at 10 °C min^{-1} and (f) cooling from 100 °C to -85 °C at 5 °C min^{-1}. Transition temperatures were determined from the DSC curves, as the onset points of the different peaks, during the reheating and re-cooling steps following the methodology described elsewhere [2,9].

Figure 2.2. DSC Q1000 TA-Instruments used in the thermal characterization of this thesis.

2.4.2. Thermogravimetric Analysis (TGA)

A thermogravimetric analyser TGA/DSC1 from Mettler Toledo (Fig. 2.3) operating in the dynamic mode under nitrogen atmosphere was used to study the thermal stability of the pure ILs and their mixtures in the liquid and gel states. Samples ranging from 3 to 5 mg were placed in an open platinum pan. Experiments were performed at temperatures from 100 to 800 C, with a temperature ramp of 10 °C min^{-1} and with a purge gas flow of 20 cm^3 min^{-1}. Each ramp was repeated three times. Curie points of alumel, nickel and perkalloy were used for temperature calibration.

Figure 2.3. TGA/DSC1 Mettler Toledo used in the thermal characterization of this thesis.

2.5. Structural characterization: NMR.

A Bruker NEO-750 (Fig. 2.4) spectrometer of 17.6 T (proton resonance 750 MHz) and a DRX-500 spectrometer of 11.7 T (proton resonance 500 MHz), belonging to the *Infrastructure Network to Support Research and Technological Development* of USC (RIAIDT) were used to obtain NMR spectra at 313.15 K. The NEO-750 spectrometer was equipped with a PA-TXI 1H/13C/15N triple resonance probe, with shielded PFGz-gradient capability. The DRX-500 spectrometer was equipped with a BBI 1H/BB double resonance probe with shielded PFGz-gradient. The spectrometer used to measure each type of spectrum is indicated below [10].

NMR samples were prepared in 5 mm standard tubes. An external capillary containing a 5 mM solution of 2,2,3,3-d4-3-(trimethylsilyl)propionic acid (TSP) in Dimethyl Sulfoxide-d6 (DMSO-d6) was inserted coaxially in the 5 mm NMR tube containing the sample for deuterium lock and external chemical shift reference. The peak of TSP appearing in the ^{1}H and ^{13}C NMR spectra was referenced as $\delta^{1H} = 0$ ppm and $\delta^{13C} = 0$ ppm, respectively.

The 1D ^{1}H spectrum was obtained (NEO-750, pulse sequence “zg” of Bruker library) under quantitative conditions using a low excitation tilt pulse angle of only 5 degrees, 64 scans with an inter-scan delay (d1) of 4 s and an acquisition time (aq) of 2.88 s.

The 1D ^{13}C spectrum was obtained (NEO-750, pulse sequence “zgpg30” of Bruker library) with 256 scans, with a relaxation delay (d1) of 2s and a fid acquisition time (aq) of 0.72 s. The ^{13}C hard pulse was applied with a low tilt angle of 30 degrees. Broad-band 1H decoupling was applied during the relaxation and free induction decay (fid) acquisition time periods with a Waltz-16 decoupling sequence applied with field strength of 8.33 kHz. The fid was acquired with 64 k complex data points and was processed with zero-filling and FT to obtain a spectrum with 128 k data points.

Figure 2.4. Bruker NEO 750 NMR spectrometer.

2.6. Physicochemical properties.

Three different experimental equipment were used to determine the thermophysical properties of the analysed samples during this thesis.

To ensure the Newtonian regime in viscosity determinations, the dynamic viscosity of EAN and water content saturated EAN were firstly measured using a rheometer TA Instruments, and the results were compared with those obtained with the denso-viscosimeter. AR2000 (Fig. 2.5) stress control, with a Peltier cooling device that controls the temperature value. Geometry of cone and plate with a diameter of 60 mm, an angle of 1° and a truncation of 28 μm was employed. Both, the sample and the geometry, were covered with a lid to avoid the exchange of atmospheric water with the environment. The temperature ranges of the experiment were (283.15 to 338.15) K. Viscosity values were obtained with temperature sweep stepped tests with a temperature increment of 5 K and 3 min of equilibration time before each measurement, 10 Pa of oscillatory stress and a frequency of 1 Hz.

Figure 2.5. Rheometer TA Instruments AR2000.

Density and speed of sound were continuously, simultaneously, and automatically measured for a temperature interval from 288 K to 313 K using a DSA 5000 Anton Paar density and sound velocity analyser (Fig. 2.6). The densimeter was calibrated with dry air and distilled water at known pressure and temperature. This apparatus is equipped with a latest-generation vibrating tube for density measurement and a stainless-steel cell connected to a sound velocity analyser with resolutions of $\pm 10^{-6}$ g·cm^{-3} and 10^{-2} m·s^{-1}, respectively. Both, the speed of sound and density are extremely sensitive to temperature, so the latter was controlled to within $\pm 10^{-3}$ K by means of a Peltier module. The reproducibility of the density and ultrasound measurements was $\pm 10^{-5}$ g·cm^{-3} and 10^{-1} m·s^{-1}, respectively.

Figure 2.6. DSA 5000 densimeter Anton Paar.

Additionally, as it was previously pointed out, to perform a comparison, density and viscosity of the EAN pure IL, and its saturated water content samples were also measured, at atmospheric pressure, with a rotational automated viscometer Anton Paar Stabinger SVM3000 (Fig. 2.7), that allows, according to the manufacturer, density, dynamic and kinematic viscosity measurements over the temperature range from 243.15 to 378.15 K, and in the viscosity range from 0.2 to 20 Pa s. The apparatus was calibrated by the manufacturer, using several density and viscosity standard reference fluids. The uncertainty of the temperature measurement is 0.02 K, the uncertainty of the dynamic viscosity is 1%. The apparatus is also equipped with a vibrating-tube that allows measurements of the densities with an uncertainty of 0.0005 g cm^{-3}.

Figure 2.7. Anton Paar Stabinger viscodensimeter SVM3000.

2.7. Electrochemical Characterization.

The electrochemical characterization is one of the key studies of this thesis since it is one of the necessary parts for the development of electrolytes for energy storage. At the same time, ionic conductivity is one of the most important parameters in the design and implantation of the electrolytes for energy storage purposes.

Two different experimental techniques are used to determine the ionic conductivity (σ), exposed in this section (conductimeter and broad band dielectric spectroscopy, BBDS). Similarly to dynamic viscosity determination, the different experimental techniques to obtain the ionic conductivity are used to ensure that the given value by the conductimeter is the correct ionic conductivity, and its frequency measuring regime is the optimal.

The conductimeter used is a GLP31 CRISON conductimeter, with a resolution better than 1% of the measured value (with a minimum resolution of 2×10^{-6} mS cm^{-1}). All data are measured at least twice in different samples to ensure its reproducibility, which is better than 5% in absolute value. The measuring cells are formed by two parallel plane plates covered with platinum oxide, and are used to measure conductivities in both forms, liquid and semisolid (ionogel).

A deeper analysis of the electrical properties through complex impedance spectroscopy in the frequency range of 20 Hz to 1 MHz in the temperature interval of 288K- 338K is performed by using a RLC HP 4284A precision meter from Agilent (Fig. 2.8), working with 8610 selectable frequencies between the selected frequency range. The basic accuracy of HP 4284 A is better than 0.05% [11].

A Swagelok cell (Fig. 2.9) with two parallel electrodes of stainless steel (4 mm radius and 1 mm of thickness) is used for these experimental measurements. The short circuit compensation of the cell and its correction coefficient are considered to eliminate the effect of stray capacitance during the evaluation of the frequency dependent values of complex dielectric function [12].

A calibrated Julabo F25 thermostat is used to control the temperature of the sample in both, conductivity and impedance measurements; the uncertainty of the temperature is lower than 0.1 K. It is important to note that all measurements are performed isothermally; so, the sample is kept for 15 min at constant temperature before any single measurement is performed, while at the phase transition that interval is increased to at least 30 min.

Figure 2.8. HP 4284 A for Agilent technologies

Figure 2.9. Swagelok cell.

The theoretical framework to obtain the dielectric spectroscopy through impedance measurements is as follows. The admittance of a conductive sample can be defined as:

$$Y = \frac{1}{Z} = G + jB, \tag{2.1}$$

where $\boldsymbol{Z}$ is the impedance, $\boldsymbol{G}$ the conductance, $\boldsymbol{B}$ the susceptance and $\boldsymbol{j}$ the imaginary unit ($\boldsymbol{j^2 = -1}$). The conductance $\boldsymbol{G}$ and the susceptance $\boldsymbol{B}$ are measured with the RLC HP 4284A experimental equipment, and respectively related with the capacity of the sample ($\boldsymbol{C}$) and the dissipation factor ($\boldsymbol{D}$) by the following mathematical relations:

$$B = 2\pi f C \tag{2.2}$$

$$D = \frac{G}{|B|}, \tag{2.3}$$

Where $\boldsymbol{f}$ is the frequency. On the other hand, the complex dielectric permittivity is defined as:

$$\varepsilon = \varepsilon' - j\varepsilon'', \tag{2.4}$$

where $\boldsymbol{\varepsilon'}$ and $\boldsymbol{\varepsilon''}$ are the real and imaginary parts, respectively, of the dielectric permittivity. The negative sign in the imaginary part is due to the negative character of the imaginary part of the capacitive impedance. If the sample is placed in an electric capacitator, the real and the imaginary part of the sample can be obtained as:

$$\varepsilon' = \frac{C}{C_0} \tag{2.5}$$

$$\varepsilon'' = \frac{C \cdot D}{C_0}, \tag{2.6}$$

where $\boldsymbol{C_0}$ is the vacuum capacitance, defined as:

$$C_0 = \varepsilon_0 \frac{A}{h}, \tag{2.7}$$

where $\boldsymbol{\varepsilon_0}$ is the vacuum dielectric permittivity, $\boldsymbol{A}$ the cross-sectional area of the capacitator and $\boldsymbol{h}$ the width of the holding sample.

The conductive regime of the sample is given by the linear part of $\boldsymbol{\varepsilon''}$ against frequency in a double logarithmic scale (x and y axis), this linear regime can be described by pure Ohmic conduction by the following model:

$$\varepsilon'' = \frac{\sigma}{\varepsilon_0 \omega}, \tag{2.8}$$

where $\boldsymbol{\sigma}$ is the conductivity and $\boldsymbol{\omega}$ the angular frequency. For data analysis the region where the slope is -1.00 ± 0.02 on log $\boldsymbol{\varepsilon''}$ *vs* log $\boldsymbol{\omega}$ representation, was selected, and the conductivity can be obtained from a linear fitting of the parameters.

2.7.1. Electrochemical Impedance Spectroscopy (EIS) and Galvanostatic Charge/discharge with Potential Limitation (GCPL).

To improve the quality of the measured impedance parameters, and extend the electrochemical measurements to impedance studies, a research collaboration with TECNALIA Research Center took place during this thesis. A VMP3 Multichannel Potentiostat from BioLogic with impedance module incorporated at a frequency range of 1 MHz to 5 mHz was used during this collaboration (the main difference between this experimental equipment and the RLC HP 4284A is a wider low frequency measuring range). The perturbation AC voltage was set at 100 mV for electrochemical impedance spectroscopy (EIS) and the selected temperature range was 298 K – 333 K with 30 minutes step of stabilization at each temperature. EIS measurement was performed in a two-electrode configuration (stainless steel both) with Swagelok cell with the aim to study the Nyquist plot, Bode plot, and the dielectric constant in the ionic relaxation regime.

Temperature is controlled by a Heraeus T6 laboratory oven with 0.1 K measurement uncertainty.

For galvanostatic cycling potential limitation (GCPL) the selected coin cell is 2032 type and the experience is performed at room temperature. Metallic Lithium is used as anode while lithium iron phosphate (LFP) is used as cathode (170 mAh·g^{-1} theoretical capacity for one electron transfer) in a *sandwich* configuration, performing a half cell. In the case of liquid samples, a conditioning step at C/20 (5 cycles) is performed, followed by 5 cycles of C/10, C/5, and C/20 again. For gel samples a pre-conditioning step of one cycle at C/50 is performed to allow the charge and discharge, after that, a conditioning step at C/20 is executed during 5 cycles, followed by 5 cycles of C/10, C/5, and C/20 again.

An interesting representation of the impedance measurements is the Bode plot, which is used to study the frequency response of a system. It allows analysing the gain and phase shift of the system over a wide range of frequencies. Bode plots are commonly used in circuit design, filter design, and control system design. They provide a clear and concise way to visualize the behaviour of a system and to optimize it for specific applications. A Bode plot summarizes two plots: amplitude plot and phase plot of the impedance. The magnitude plot is a logarithmic graph that shows the impedance module as a function of frequency. The phase plot shows the phase shift between the input and output signals as a function of frequency in degrees as it is shown in Fig. 2.10.

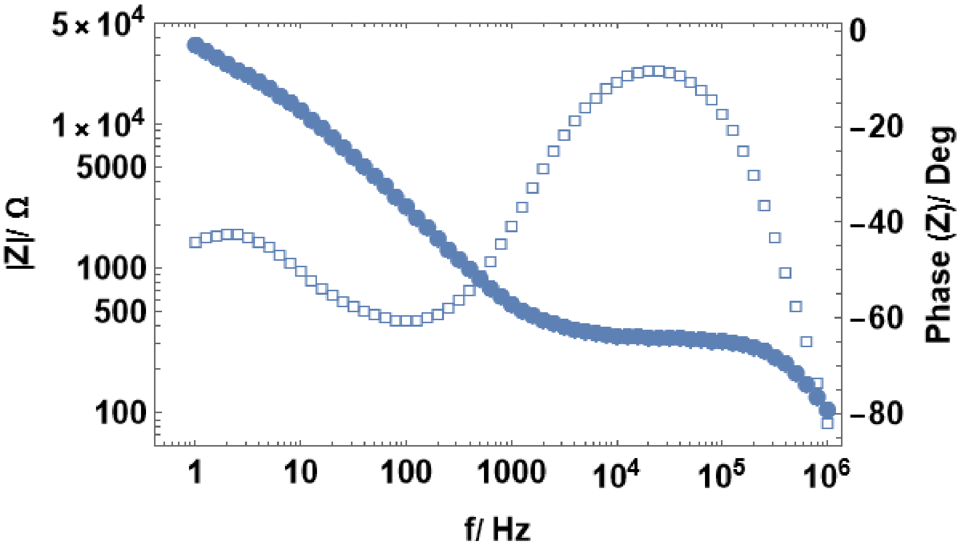

Figure 2.10. Bode Plot at 298 K of [C_4C_1Pyrr][TFSI] in liquid state. Impedance module (filled dots) and phase (empty dots)

The C-rate is defined as the speed at which the battery is fully charged. For example, 1C refers to the battery is fully charged in 1 hour at its theoretical capacity. The C-rate is defined in function of the intensity applied when charging/discharging, because the voltage at which the charge/discharge is fixed by the electrode material. The theoretical capacity of a battery is defined as:

$$C_{theo} = \frac{nF}{3600M_w}, \tag{2.9}$$

where n is the number of charge carriers (in case of lithium $n = 1$), F is the Faraday constant and M_w is the molecular weight of the active materials of the electrodes. So, the C is the rate at which the battery reaches its theoretical capacity. As mentioned before, the operating voltage of battery charging/discharging is fixed by the electrode's material, the parameter that sets the velocity of charge/discharge is the intensity, which is calculated as:

$$i = \frac{C_{theo} \cdot m_{active}}{t}, \tag{2.10}$$

where C_{theo} is the theoretical capacity, m_{active} is the active mass of the electrode, and t is the time at which the battery is fully charged.

For cyclic voltammetry (CV) a two-electrode configuration was selected. Swagelok cell (Fig. 2.9) for CV measurements was used with stainless steel working electrode (WE) and metallic lithium as counter electrode and reference electrode (CE+RE) at 298 K.

2.8. Dielectric relaxation, analysis, and parametrization.

This section reviews the theoretical framework in which the dielectric permittivity will be analysed and parametrised during this thesis; all this information can be found elsewhere [13]. The dielectric behaviour at a fixed temperature can be characterised by the complex dielectric permittivity (ε^*) as a function of frequency. The complex dielectric permittivity, defined in eq. (2.4) can be written as [14,15]:

$$\varepsilon^* = \varepsilon' - j\varepsilon'' = \sum_{j=1}^{l} S_j \, \tilde{F}_j(\omega) + \varepsilon_\infty, \tag{2.11}$$

where S_j is the relaxation amplitude, $\tilde{F}_j(\omega)$ is the spectral distribution of the jth mode of the dielectric relaxation (in this thesis, the interfacial relaxation), and ε_∞ is the dielectric constant at high enough frequency. The real part of the dielectric permittivity is related with the storing charge capacity, whereas the imaginary part is attributed to the loss of energy inside the material [16]. The function $\tilde{F}_j(\omega)$ can take different forms depending on the selected relaxation model for the analysed sample, in this thesis is considered as follows:

$$\tilde{F}_j(\omega) = \frac{1}{1 + j\omega\tau_j}, \tag{2.12}$$

two different models have been used to fit the dielectric behaviour of the electrolyte mixtures (IL or IL + metal salt) used in this thesis. These models are Debye and Cole-Cole models, which are briefly described below.

2.8.1. Debye relaxation model.

In this case the complex dielectric permittivity is defined by:

$$\varepsilon^*(\omega) = \frac{\varepsilon_\infty + \varepsilon_s}{1 + j\omega\tau} + \varepsilon_\infty, \tag{2.13}$$

where ε_∞ is the dielectric permittivity at high enough frequency, ε_s is the static dielectric permittivity and τ is the relaxation time [17]. Eq. (2.13) can be decomposed in the real part, ε', (related with the dispersion of the sample, or the storing charge capacity as mentioned above), and the imaginary part, ε'', (related with the energy dissipation or energy losses)[14,18].

Eq. (2.13) can be expressed in terms of $(\varepsilon'' = f(\varepsilon'))$ for a better visualization of the relaxation [13]:

$$\varepsilon''(\omega) = [\varepsilon'(\omega) - \varepsilon_\infty]\sqrt{\frac{\varepsilon_\infty + \varepsilon_S}{\varepsilon'(\omega) - \varepsilon_\infty} - 1}, \tag{2.14}$$

this relation can be used to easily fit the Cole-Cole plot (Fig. 2.11) and the ε_∞ and ε_S are fitting parameters that can be obtained for each studied temperature. This Cole-Cole plot is named after R. H. Cole and A. D. Cole, who developed it for describing the frequency-dependent behaviour of complex materials. It is especially important to highlight that another dielectric relaxation, known as Maxwell-Wagner- Sillars (MWS) effect, can occur at low frequencies (right part of the Cole-Cole plot) in the inner dielectric boundary layer. This MWS effect leads to a separation of charges in a mesoscopic scale, resulting in a contribution in the dielectric constant orders of magnitude higher than the dielectric respond of the sample due to the molecular fluctuations. In this case, only the first half part of the semicircle is considered for the fitting, considering that the aim of this work is to study the molecular dielectric polarization, and that is the reason MWS effect is discarded to obtain the relaxation time of the interfacial polarization in the Debye approximation. The criteria to discard the MWS affected data is to extrapolate the straight line obtained in the Cole-Cole plot until the cross with the x-axis (corresponding to the real part of the dielectric constant). All data located within the quadrant in which the MWS effect is still present are discarded.

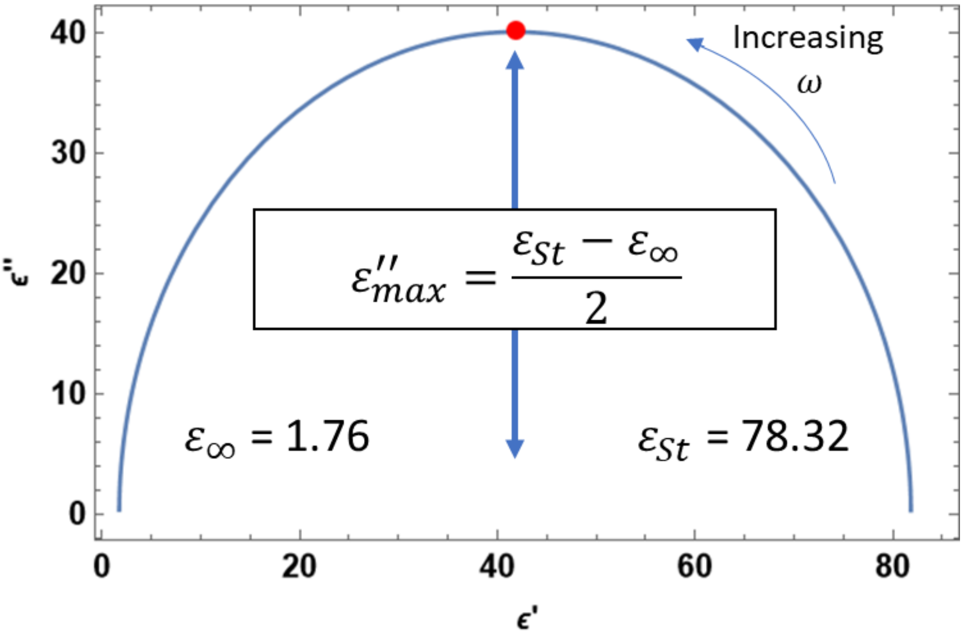

Figure 2.11. Cole-Cole plot for the Debye dielectric permittivity.

The obtained parameters ε_S and ε_∞ in the Cole-Cole framework are used to fit the dielectric spectroscopy obtaining the relaxation time τ at the studied temperature.

This model presents a different limitation such as suppose one single relaxation time, to generalize this model, the Cole-Cole model is considered to analyse the studied samples in this work.

2.8.2. Cole-Cole relaxation model.

The Cole-Cole relaxation gets a wider description in quantitative analysis, and it is considered in this work, to complete the previous analysis. The Cole-Cole relaxation is described as:

$$\varepsilon^*(\omega) = \frac{\varepsilon_\infty + \varepsilon_s}{1 + (i\omega\tau)^{1-\alpha}} + \varepsilon_\infty = \varepsilon^*(\omega) = \frac{\varepsilon_\infty + \varepsilon_s}{1 + (i\omega\tau)^{\beta}} + \varepsilon_\infty, \tag{2.15}$$

where $1 - \alpha = \beta$ is a term that characterises the flattening of the Cole-Cole semicircle (Fig. 2.12). In a theoretical framework the Cole-Cole model is developed for a molecule which dipole moment is not aligned with the long of molecular axis, in consequence, the dispersion presented by these liquids is much broader with the maximum lower than the Debye relaxation model. These broadening is explained by a distribution in the relaxation times since it is seen like a continuous function instead of considering just one relaxation like the Debye model.

This is based in the assumption that the molecule is randomly oriented relative to the applied field. If the molecule is perfectly oriented with the field only the longitudinal part of the dipole is active, while if the molecule is perpendicular to the field, the transversal component is active. This model assumes that the molecules are randomly oriented between these two extreme cases presenting a continuous distribution in the relaxation time.

The data is analysed upon all frequency range, considering two Cole-Cole relaxation, one corresponding to MWS effect (low frequency relaxation) and the higher frequency region, corresponding to the interfacial relaxation. The critical parameter analysed in this study was $\beta = 1 - \alpha$, which determines how close to a Debye process is the high frequency relaxation.

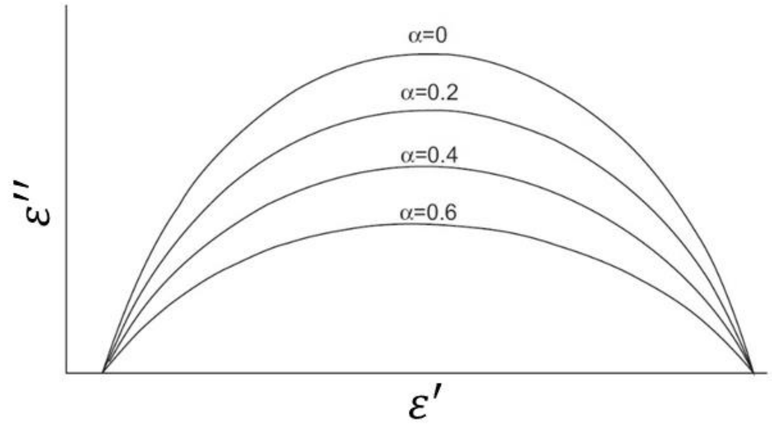

Figure 2.12. Cole-Cole plot for the Cole-Cole model at different α values. Figure from Mehrotra book [13].

It is important to highlight that the Cole-Cole model is mainly applied to visualize the deviation of the dielectric behaviour of the sample analysed from the Debye model, which assumes only one relaxation process with a single relaxation time. The deviation from the Debye model is usually most evident at low frequencies, where the relaxation time distribution of the material becomes important.

As it was pointed out above, the Cole-Cole plot for a typical Cole-Cole relaxation (Fig. 2.12) is typically a semi-circle with its centre located above the real axis.

References:

[1] L. Negre, B. Daffos, V. Turq, P.L. Taberna, P. Simon, Ionogel-based solid-state supercapacitor operating over a wide range of temperature, Electrochim Acta. 206 (2016) 490–495.

[2] J. Salgado, J.J. Parajó, M. Villanueva, J.R. Rodríguez, O. Cabeza, L.M. Varela, Liquid range of ionic liquid – Metal salt mixtures for electrochemical applications, J Chem Thermodyn. 134 (2019) 164–174.

[3] M.N. Garaga, L. Aguilera, N. Yaghini, A. Matic, M. Persson, A. Martinelli, Achieving enhanced ionic mobility in nanoporous silica by controlled surface interactions, Physical Chemistry Chemical Physics. 19 (2017) 5727–5736.

[4] N. Andersson, B. Kronberg, R. Corkery, P. Alberius, Combined Emulsion and Solvent Evaporation (ESE) synthesis route to well-ordered mesoporous materials, Langmuir. 23 (2007) 1459–1464.

[5] S.A.M. Noor, P.M. Bayley, M. Forsyth, D.R. MacFarlane, Ionogels based on ionic liquids as potential highly conductive solid state electrolytes, Electrochim Acta. 91 (2013) 219–226.

[6] N. Andersson, B. Kronberg, R. Corkery, P. Alberius, Combined Emulsion and Solvent Evaporation (ESE) synthesis route to well-ordered mesoporous materials, Langmuir. 23 (2007) 1459–1464.

[7] M. Brachet, D. Gaboriau, P. Gentile, S. Fantini, G. Bidan, S. Sadki, T. Brousse, J. Le Bideau, Solder-reflow resistant solid-state micro-supercapacitors based on ionogels, J Mater Chem A Mater. 4 (2016) 11835–11843.

[8] J. Salgado, J.J. Parajó, M. Villanueva, J.R. Rodríguez, O. Cabeza, L.M. Varela, Liquid range of ionic liquid – Metal salt mixtures for electrochemical applications, J Chem Thermodyn. 134 (2019) 164–174.

[9] J.J. Parajó, M. Villanueva, P.B. Sánchez, J. Salgado, Liquid window of some biologically-active ionic liquids, Journal of Chemical Thermodynamics. 126 (2018) 1–10.

[10] V. V. Matveev, A. V. Ievlev, M.A. Vovk, O. Cabeza, J. Salgado-Carballo, J.J. Parajó, J.R. Rodríguez, R. de la Fuente, E. Lähderanta, L.M. Varela, NMR

investigation of the structure and single-particle dynamics of inorganic salt solutions in a protic ionic liquid, J Mol Liq. 278 (2019) 239–246.

[11] Hewlett Packard, Operation manual, Operation Manual. HP 4284A Precision LCR METER. (1998).

[12] R.J. Sengwa, S. Choudhary, S. Sankhla, Low frequency dielectric relaxation processes and ionic conductivity of montmorillonite clay nanoparticles colloidal suspension in poly(vinyl pyrrolidone)-ethylene glycol blends, Express Polym Lett. 2 (2008) 800–809.

[13] S. Mehrotra, A. Kumbharkhane, A. Chaudhari, Theoretical and Experimental Aspects of Time Domain Permittivity Spectroscopy, Binary Polar Liquids (2017), 1-43.

[14] C. Daguenet, P.J. Dyson, I. Krossing, A. Oleinikova, J. Slattery, C. Wakai, H. Weingärtner, Dielectric response of imidazolium-based room-temperature ionic liquids, Journal of Physical Chemistry B. 110 (2006) 12682–12688.

[15] J. Hunger, A. Stoppa, S. Schrödle, G. Hefter, R. Buchner, Temperature dependence of the dielectric properties and dynamics of ionic liquids, ChemPhysChem. 10 (2009) 723–733.

[16] K.M. Batoo, S. Kumar, C.G. Lee, Alimuddin, Study of dielectric and ac impedance properties of Ti doped Mn ferrites, Current Applied Physics. 9 (2009) 1397–1406.

[17] S. Mehrotra, A. Kumbharkhane, A. Chaudhari, Theoretical and Experimental Aspects of Time Domain Permittivity Spectroscopy, 2017.

[18] R. Khalil, F. Salman, R. Khalil, H. Hazaa, Dielectric studies and Cole-Cole plot analysis of silver-ion conducting glasses Magnesium Batteries View project Dielectric studies and Cole-Cole plot analysis of silver-ion conducting glasses, 3 (2014) 1–9.

3. Results and discussion

3. Results and Discussion

3.1. Background

This section summarizes the results of this work. They are grouped by experimental techniques to compare the differences between the ILs and the effect of the doping salt before and after the nano-confinement in the silica scaffolds, with the aim to expand the frontiers of knowledge regarding electrolytes for 4th generation batteries.

Part of the information presented in this chapter can be found in the following publications (authorizations on behalf of the publisher can be found in the Annexed Material B):

- J. J. Parajó, P. Vallet, M. J. G. Guimarey, A. Santiago, T. Teijera, A. Amigo, L. M. Varela, J. Salgado & M. Villanueva. "Thermophysical properties of n-alkyl-ammonium nitrate ionic liquids (n = 2,3,4) pure and water saturated for energy applications". Journal of Thermal Analysis and Calorimetry volume 148, pages 6699–6714 (2023). DOI:10.1007/s10973-023-12194-1.
- P. Vallet, S. Bouzón-Capelo, T. Méndez-Morales, V. Gómez-González, Y. Arosa, R. de la Fuente, E. López-Lago, J. R. Rodríguez, L. J. Gallego, J. J. Parajó, J. Salgado, M. Turmine, L. Segade, O. Cabeza, L. M. Varela "On the physical properties of mixtures of nitrate salts and protic ionic liquids". Journal of Molecular Liquids 350 (11):118483. DOI: 10.1016/j.molliq.2022.118483.
- J.J. Parajó, P. Vallet, M. Villanueva, O. Cabeza, F. Fernández-Carretero, A. García Luis, M.E. Di Pietro, A. Mele, F. Castiglione, J. Salgado, L.M. Varela. "Ionogels based on protic ionic liquid - lithium salt mixtures". Journal of Molecular Liquids, 397(1), 124093. DOI: https://doi.org/10.1016/j.molliq.2024.124093.
- P. Vallet, J.J. Parajó, A. Santiago-Alonso, M. Villanueva, Ó. Cabeza, L.M. Varela, J. Salgado. "Anomalous behaviour of the ionic conductivity of nanoconfined IL - lithium salt mixtures". Journal of Molecular Liquids. In Press, Journal Pre-proof. DOI: 10.1016/j.molliq.2024.124630

3.2. Thermal characterization

3.2.1. Differential scanning calorimetry (DSC)

3.2.1.1. Pure Ionic Liquids

DSC curves of pure ILs, EAN (a), $[C_2Im][NO_3]$ (b), $[C_4C_1Pyr][TFSI]$ (c) and $[C_2C_1Im][TFSI]$ (d) in cooling and heating ramps at 5 °C/min using nitrogen atmosphere can be found in Fig. 3.1. All studied ILs present a clear tendency to crystallization, characterized by freezing (exothermic) and melting (endothermic) peaks in cooling and heating ramps, respectively, except for $[C_4C_1Pyr][TFSI]$ which presents two exothermic peaks in the heating ramp due to cold crystallization process. The behavior of each IL individually is described below.

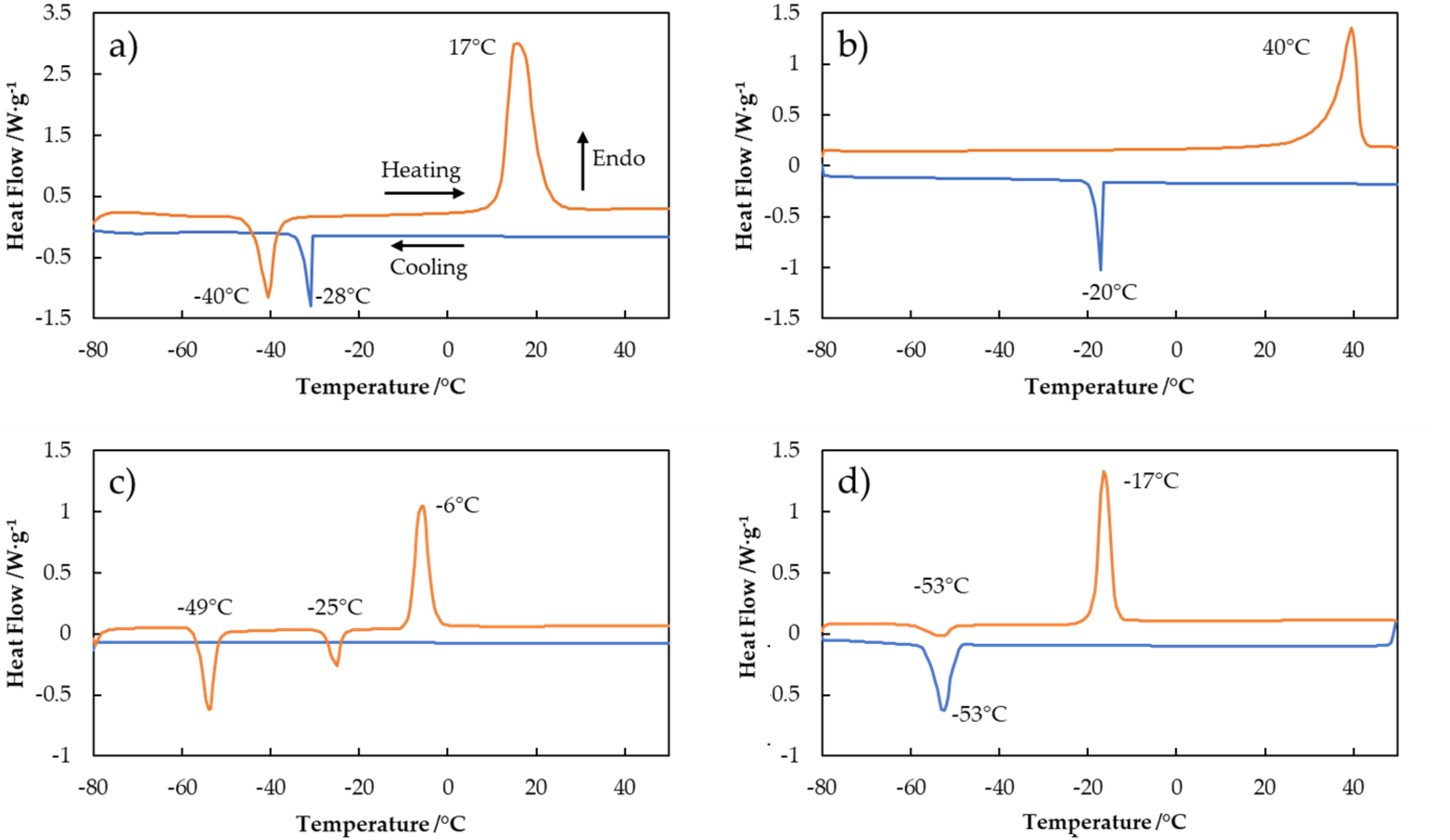

Figure 3.1. DSC (5 °C/min) curves of pure a) EAN, b) $[C_2Im][NO_3]$, c)$[C_4C_1Pyr][TFSI]$ and d) $[C_2C_1Im][TFSI]$ for heating (orange line) and cooling (blue line) ramps. Endo up.

The obtained thermal behavior of EAN (Fig 3.1 a) is similar to that previously reported in the literature [1,2], characterized by an exothermic peak clearly visible at -28 °C which suggests a process of crystallization upon cooling. An additional exothermic peak starting at -44 °C, and with its maximum at -40 °C is also found upon heating due to cold crystallization [3], which is a process consisting in the reordination of the amorphous structure presented in the sample after a cooling at high enough rates that prevent total (or partial) crystallization. At those low temperatures the molecular mobility is strongly reduced, but when the temperature increases, basically above the glass temperature, small crystals can be formed at relatively low temperatures releasing heat. While increasing the temperature, an endothermic peak with onset at 12 °C and maximum at 17 °C, attributed to melting is found. As previously pointed out, these values are in very good agreement with most previously contributed works, with a reported EAN melting temperature between 12–13 °C [4–9]; although a remarkable exception is that of Greaves et al. [37], who found T_m = 9 °C. Discrepancies, besides differences in experimental conditions, can be probably due to the different impurities contents, which is much lower in our case (100 ppm (0.01%) against 0.22% for water content of these authors). No glass transition can be found for pure EAN, probably because it is out of the studied temperature range, or maybe because the signal associated to the amorphous regions is too small in comparison with the endo and exothermic process.

As is well known, the scanning rate has important influence on thermal behavior, and to look at this question more thoroughly, Fig. 3.2 presents the heating ramp of the EAN at 5 °C·min^{-1} after the cooling at two different rates 5 °C/min and 50 °C·min^{-1} (quenching) to frustrate the crystallization of the sample resulting in an amorphous phase transition. The curves in Fig. 3.2 show a decrease of the peak area of about 20% corresponding to a melting phase transition and a glass transition at -41 °C (inset Fig. 3.2) for the quenched sample. Then, the main effect of the different heating rates is the existence of the cold crystallization of the sample, being well defined at low heating rates, while at higher ones a quenched amorphous material is formed, being softened before the melting, and thus reducing the amount of heat needed for the solid-liquid transition.

Pure $[C_2Im][NO_3]$ (Fig. 3.1 b) shows an exothermic peak in the cooling ramp with an onset temperature at -15 °C (maximum at -20 °C) associated to the crystallization of the sample, and a single endothermic peak with onset at 34 °C and maximum at 40 °C is observed, related to the melting process of the IL upon heating ramp. Similarly to other ILs an important supercooling effect has been observed [10,11]. This IL presents a strong tendency to form crystals under these conditions, and no evidence of an amorphous phase has been observed in the liquid state in the studied temperature range. Up to our knowledge no data of the thermal behavior of this IL have been previously published.

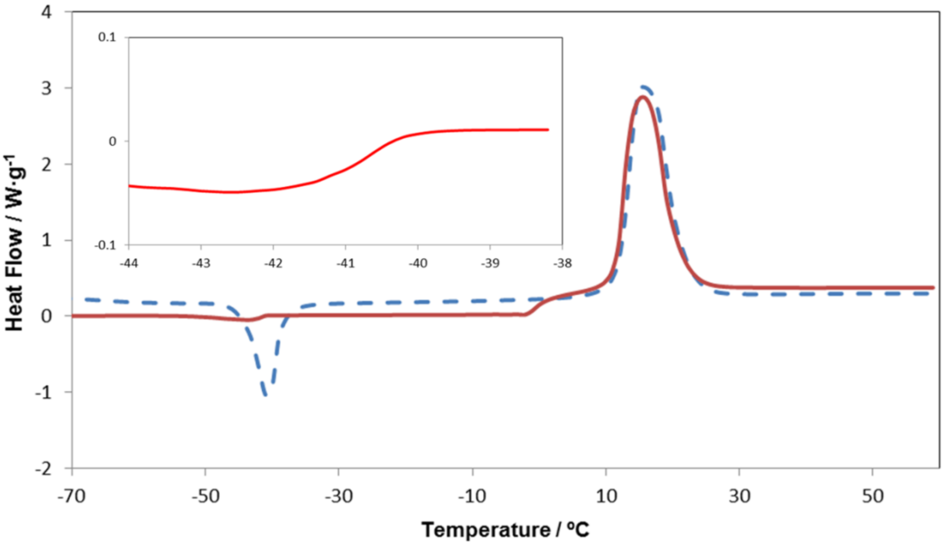

Figure 3.2. Effect of cooling rate (Red solid line is the signal recorded after the quenching and blue dashed line signal after cooling at 5 °C min^{-1}) on the DSC curves in heating ramp at 5 °C/min of pure EAN. Endo up.

No phase transitions have been observed upon cooling for $[C_4C_1Pyrr][TFSI]$ (Fig 3.1 c), as pointed out previously, but two exothermic peaks upon heating are observed, which correspond to two cold crystallization processes associated to two different polymorphic states. The first peak is registered at -53 °C (onset temperature), with a minimum at -49 °C, and the second peak lies at -27 °C (minimum at -25 °C) followed by the endothermic melting peak at -9 °C (onset temperature) whose maximum is formed at -6.8 °C. The fact that no phase transition is detected upon colling ramp is due to the well-known circumstance that TFSI based ILs are good glass formers [12] and the transition temperature, probably a glass transition one, should be present at lower temperatures.

On the other hand, Fig 3.1 d shows a clear exothermic peak associated to crystallization, with onset temperature at -50 °C (minimum at -53 °C) upon cooling for $[C_2C_1Im][TFSI]$. Additionally, another exothermic peak with an onset temperature at -59 °C (minimum at -53 °C) is detected upon heating. Finally, an endothermic melting point is clearly visible with onset at -19 °C and maximum at -16 °C. The exothermic peak in the heating ramp corresponds to a cold crystallization due to the dynamic nature of the experiment. Total crystallization of the sample has not been achieved upon cooling and, therefore, a part of it falls in an amorphous state that crystallizes upon heating. This is also confirmed by the DSC curves of this IL at a lower scanning rate, 2 °C·min^{-1} (see Fig. 3.3). A single peak can be observed in every ramp, that is, in the cooling ramp a clear freezing exothermic peak is found with onset at -46 °C (maximum at -46 °C), while in the heating ramp the exothermic peak (cold crystallization) is completely absent, and only an endothermic peak, corresponding to the melting is observed at -18 °C (onset temperature) with a maximum at -17 °C.

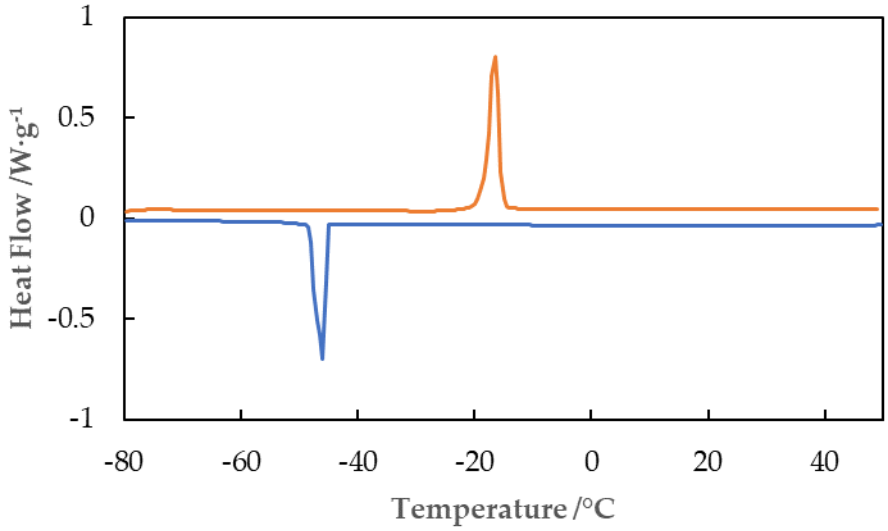

Figure 3.3. DSC curves of pure $[C_2C_1Im][TFSI]$ for heating (orange) and cooling (blue) ramps at 2 °C·min^{-1}. Endo up.

Besides a clear tendency to crystallize, another important finding in all these ILs is the supercooling effect, i.e., the difference between crystallization and melting temperatures. This feature is common behavior in pure ILs, as is usually reported in the literature [13,14].

The tendency observed for the melting temperatures of these ILs is $[C_2C_1Im][TFSI]$ (-17 °C) < $[C_4C_1Pyr][TFSI]$ (-6 °C) < EAN (17 °C) < $[C_2Im][NO_3]$ (40 °C), which clearly indicates that aprotic ILs studied in this work present lower melting temperature than protic ILs, that is it $T_m^{aprotic} < T_m^{protic}$ for the ILs studied in this work.

3.2.1.2. Mixtures of ILs and inorganic salts. Effect of salt addition.

The effect of the addition of salts of electrochemical interest for our studied ILs will be analyzed in this subsection. It should be considered that the salts used are commercially available, and due to sharing the anion with the IL, mono, di and tri-valent nitrate salts could be used, but only lithium salt with a TFSI cation was commercially accessible.

Figs. 3.4 and 3.5 show the DSC experiences of EAN and $[C_2Im][NO_3]$ and its mixtures with common anion metal salts (lithium nitrate, magnesium nitrate, calcium nitrate and aluminum nitrate) at different concentrations, respectively.

The main parameters obtained from the DSC profiles, such as onset temperatures and enthalpies for phase transitions, are summarized in Table 3.1 for protic studied IL mixtures. The melting point is clearly shifted to lower temperatures, and becomes broader when salt concentration increases, and the peaks corresponding to first order phase transitions (freezing and melting) disappear for the saturated samples. Instead, a glass transition appears at -65 °C and -73 °C for saturated mixtures of EAN with magnesium and calcium salts, respectively. Similarly, mixtures of $[C_2Im][NO_3]$ with these salts show a tendency to reduce the crystallinity upon salt addition, although because it accepts more salt, the broadening and the vanishing of the phase transition peaks is observed slowly and in more detail, beginning by the disappearance of the crystallization peak in cooling ramp and the appearance of cold crystallization in heating ramp at intermediate concentrations, and with the complete disappearance of melting and freezing peaks and a clear glass transition for all saturated samples.

These behaviors, the decrease in the temperature of melting after salt addition and the presence of the glass transition have been reported for different families of ILs [15,16].

On the other hand, the melting temperature decrease is linked with the loss in definition, and is ascribed to a disorder in the ionic equilibrium when the sample is in the solid phase before reaching the melting point [17]. Owing to this interesting property, these mixtures can be used, in addition to the energy accumulation, in refrigerators as cooling refrigerant fluids due to the phase transition vanishing.

Since ate the melting point $\Delta G_m = 0$, we have:

$$\Delta S_m = \frac{\Delta H_m}{T_m}, \tag{3.1}$$

wich allows the estimation of ΔS_m from DSC measurements. According to this equation, the melting temperature decrease upon salt addition can be attributed to a simultaneous increase in the melting entropy and a decrease in the melting heat as table 3.1 shows.

The melting entropy and enthalpy variations follow the trend $Li^+ > Ca^{2+} > Mg^{2+} > Al^{3+}$, leading to the conclusion that the entropy and enthalpy variations are linked to the electrostatic potential of the salt anion, calculated by Gómez-González *et al.* [18].

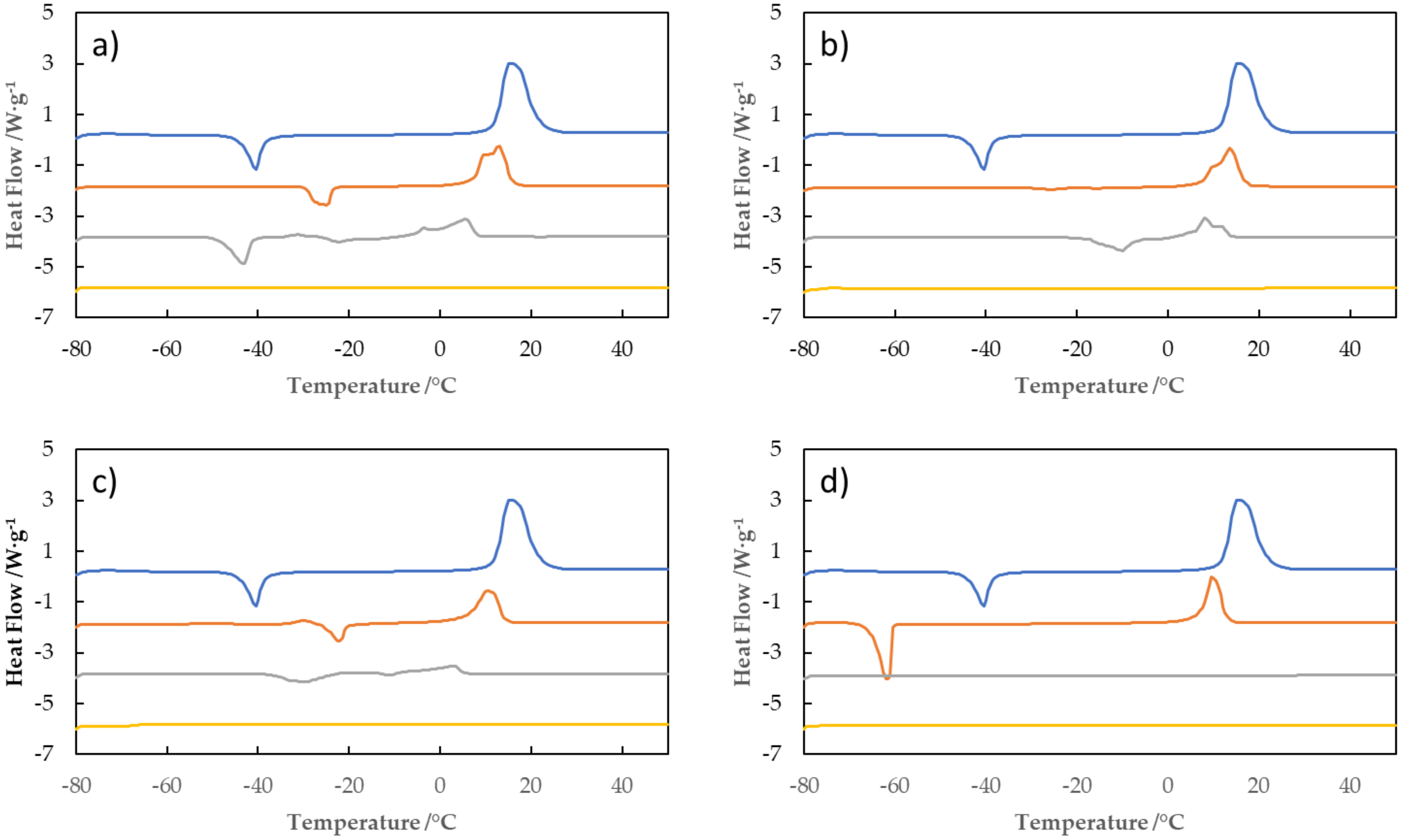

Figure 3.4. DSC curves for heating ramp of the pure IL EAN (blue line) and its mixtures with salt: (a) orange line correspond to $Li(NO_3)$ 0.1m, grey line to 1m, yellow line 2m, (b) orange line to $Ca(NO_3)_2$ 0.1m, grey line to 0.75m, yellow line to 1m, (c) orange line to $Mg(NO_3)_2$ 0.1m, grey line to 1m, yellow line to 2m, (d) orange line to $Al(NO_3)_3$ 0.1m, grey line to 1m, yellow line to 1.5m. Endo up.

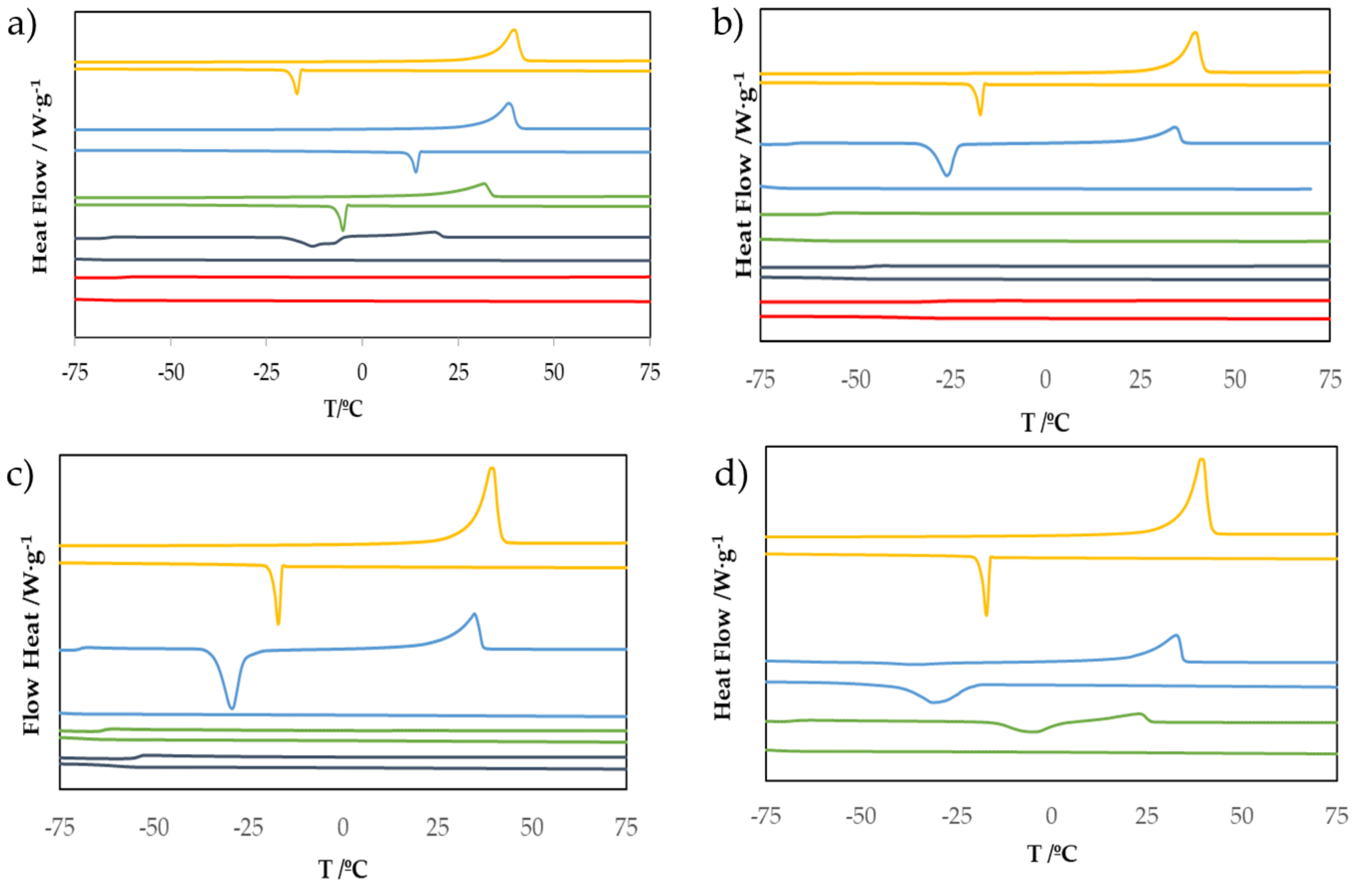

Figure 3.5. DSC of 6 $[C_2Im][NO_3]$ with a) lithium salt, b) calcium, c) magnesium and d) aluminum. Yellow line represents pure IL, blue 0.5 mol·kg^{-1} salt addition, green 1 mol·kg^{-1}, dark grey 2 mol·kg^{-1} and red 3 mol·kg^{-1}. Upper line represents the heating, while lower line represents the cooling. Endo up.

Table 3.1. Temperature, enthalpy and entropy of melting (T_m, ΔH_m and ΔS_m), temperature and enthalpy of freezing (T_f and ΔH_f), temperature of cold crystallization (T_{cc}) and temperature of glass transitions (T_g) of pure EAN + inorganic salt mixtures.

	T_m / °C	T_f / °C	T_{cc} / °C	T_g/ °C	ΔH_m/ J.g^{-1}	ΔH_m/ kJ.mol^{-1}	ΔH_f/ J.g^{-1}	ΔH_{cc}/ J.g^{-1}	ΔS_m/ J. °C^{-1} g^{-1}	ΔS_m/ J. °C^{-1} mol^{-1}
Pure EAN	12	-27	-42	--	122	13.2	76	30	0.43	46
EAN + $LiNO_3$ 0.1m	8	-40	-30	--	122	13.2	68	37	0.43	46
EAN+ $LiNO_3$ 1m	-5	--	-48	--	59	6.2	--	55	0.22	23
EAN+ $LiNO_3$ 2m	--	--	--	--	--	--	--	--		--
EAN+ $Ca(NO_3)_2$ 0.1m	8	-38	--	--	110	12.0	81	--	0.39	43
EAN + $Ca(NO_3)_2$ 0.75m	6	--	-14	--	49	5.7	--	50	0.18	21
EAN + $Ca(NO_3)_2$ 1m	--	--	--	-73	--	--	--	--		--
EAN + $Mg(NO_3)_2$ 0.1m	6	-46	-25	--	100	11.0	57	41	0.36	40
EAN + $Mg(NO_3)_2$ 1m	-9	--	-37	--	28	3.4	--	35	0.11	14
EAN+$Mg(NO_3)_2$ 2m	--	--	--	-65	--	--	--	--		--
EAN + $Al(NO_3)_3$ 0.1m	7	--	-64	--	100	11.1	--	74	0.36	40
EAN + $Al(NO_3)_3$ 1 m	1	--	--	--	7	0.9			0.03	4
EAN+$Al(NO_3)_3$ 2 m	--	--	--	--	--	--	--	--		--
Pure $[C_2Im][NO_3]$	34	-14	---	---	82.7	13.2	82.2	---	0.27	43.0
$[C_2Im][NO_3]$ + $LiNO_3$ 0.5m	32	16	---	---	74.8	12.3	81.6	---	0.25	41.2
$[C_2Im][NO_3]$ + $LiNO_3$ 1m	21	-3	---	---	51.3	8.7	63.9	---	0.17	28.9

$[C_2Im][NO_3] + LiNO_3$ *2m*	20	---	-15	-65	18.6	3.6	---	39.6	0.06	11.5
$[C_2Im][NO_3] + LiNO_3$ *3m*	---	---	---	-69	---	---	---	---	---	---
$[C_2Im][NO_3] + Ca(NO_3)_2$ *0.5m*	27	---	-30	-65	45.4	7.8	---	52.6	0.15	25.8
$[C_2Im][NO_3] + Ca(NO_3)_2$ *1m*	---	---	---	-59	---	---	---	---	---	---
$[C_2Im][NO_3] + Ca(NO_3)_2$ *2m*	---	---	---	-47	---	---	---	---	---	---
$[C_2Im][NO_3] + Ca(NO_3)_2$ *3m*	---	---	---	-30	---	---	---	---	---	---
$[C_2Im][NO_3] + Mg(NO_3)_2$ *0.5m*	28	---	-34	-68	51.5	8.8	---	56.7	0.17	29.1
$[C_2Im][NO_3] + Mg(NO_3)_2$ *1m*	---	---	---	-65	---	---	---	---	---	---
$[C_2Im][NO_3] + Mg(NO_3)_2$ *2m*	---	---	---	-58	---	---	---	---	---	---
$[C_2Im][NO_3] + Al(NO_3)_3$ *0.5m*	24	-21	-50	---	41.2	7.3	42.7	14.1	0.14	24.7
$[C_2Im][NO_3] + Al(NO_3)_3$ *1 m*	11	---	-15	-70	14.4	2.8	---	20.1	0.05	9.7

Expanded uncertainties are U(t) = 6 K and $U_r(\Delta H)$ = 4% (0.95 level of confidence (k=2))

DSC measurements of mixtures of the aprotic IL [C_4C_1Pyrr][TFSI] with lithium TFSI salt at different concentrations are shown in Fig. 3.6. Melting, freezing, cold crystallization and glass transition temperatures and their respective enthalpies and entropies can be found in Table 3.2. In contrast with the previously analyzed PILs, the melting temperature firstly decrease with the lowest concentration of salt addition (blue line in Fig. 3.6) but if the salt concentration increases melting temperature rises to higher values. The lowest concentration of salt (0.1 mol·kg^{-1}) leads to a reduction of the melting temperature from -8 °C (pure IL) to -22 °C, but the behavior of the mixtures of 0.5 mol·kg^{-1}and 1 mol·kg^{-1}, is completely different, characterized, firstly, by a double melting peak at -12 °C and 4 °C for the concentration of 0.5 mol·kg^{-1} and -12 °C and 19 °C for the 1.0 mol·kg^{-1}, indicating the existence of a double population in the mixture. This observation agrees with the results of Martinelli et al. [19] who pointed out the existence of more than one phase for high concentrations of salt in this mixture. Finally, for the saturation concentration a single melting point is presented at 19 °C. As already pointed out, although important differences were observed in the behavior of PILs with salt addition, a common aspect must be highlighted: the tendency to reduce the degree of crystallinity of the sample with the concentration of the salt, which is evident in this case with the appearance of glass transition for the highest concentrations.

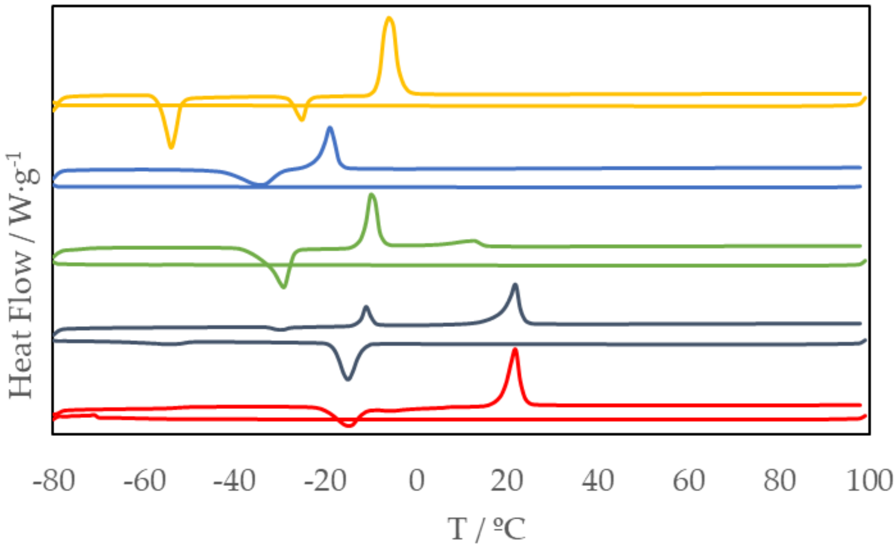

Figure 3.6. DSC curves for [C_4C_1Pyrr][TFSI] with LiTFSI salt at different concentrations. yellow line represents pure IL, blue 0.1 mol·kg^{-1} salt addition, green 0.5 mol·kg^{-1}, dark grey green 1 mol·kg^{-1} and red 1.5 mol·kg^{-1}. Upper line represents the heating, while lower line represents the cooling. Endo up.

Table 3.2. Temperature, enthalpy and entropy of melting (T_m, ΔH_m and ΔS_m) , temperature and enthalpy of freezing (T_f and ΔH_f), temperature of cold crystallization (T_{cc}) and temperature of glass transitions (T_g) of $[C_4C_1Pyrr][TFSI]$ with LiTFSI salt mixtures.

	T_m / °C	T_f/ °C	T_{cc}/ °C	T_g/ °C	ΔH_m/ $J.g^{-1}$	ΔH_m/ $kJ.mol^{-1}$	ΔH_f/ $J.g^{-1}$	ΔH_{cc}/ $J.g^{-1}$	ΔS_m/ $J.$ °C^{-1} g^{-1}	ΔS_m/ $J.$ °C^{-1} mol^{-1}
Pure $[C_4C_2Pyrr][TFSI]$	-8	---	-57 / -28	---	48.2	20.4	---	27.5 / 10.6	0.18	76.0
$[C_4C_2Pyrr][TFSI]$ *+ LiTFSI 0.1m*	-22	---	-43	---	23.4	10.2	---	21.6	0.09	39.1
$[C_4C_2Pyrr][TFSI]$ *+ LiTFSI 0.5m*	-12 / 4	---	-34	---	26.1 / 5.8	11.6 / 2.6	---	31.0	0.08 / 0.02	35.5 / 8.9
$[C_4C_2Pyrr][TFSI]$ *+ LiTFSI 1m*	-12 / 19	-15/ -50	-33	---	7.2 / 24.8	3.4 / 11.6	22.9 / 3.9	1.7	0.03 / 0.08	14.0 / 37.4
$[C_4C_2Pyrr][TFSI]$ *+ LiTFSI 1.5m*	19	---	-20	-53	30.4	14.4	---	24.9	0.10	47.3

Expanded uncertainties are U(t) = 6 K and $U_r(\Delta H)$ = 4% (0.95 level of confidence (k=2))

In summary, in this subsection the thermal behavior as a function of salt concentration was analyzed. The main findings were:

-Protic ILs show a clear tendency to shift the melting point to lower temperatures with increasing salt concentration. This behavior is only observed for the lowest concentration of lithium salt in the aprotic IL.

-Primary phase transitions completely disappear in saturated IL-salt mixtures for protic ILs.

-Glass transitions appear at the lowest temperatures for all studied saturated samples, except for EAN + $LiNO_3$ and EAN + $Al(NO_3)_3$, probably, because the glass transition temperature is out of the measuring range.

3.2.1.3 Effect of nanoconfinement of pure ILs and salt mixtures

i Pure ionogels

In this subsection the effect of the nanoconfinement of the previous samples, both pure ionic liquids and its mixtures with inorganic salts, is analyzed. Fig. 3.7 shows the DSC curves of silica-based gels of pure ILs. Fig 3.7 a) shows the heating ramps of the gel of EAN by the two selected synthesis routes, ethanol (EtOH) and formic acid (FA) (see materials and methods) and the comparison with the pure IL in liquid state. Where the liquid sample presents a clear tendency to crystallize, the gel samples do not present any relevant transitions in the studied temperature interval, which is in good agreement with previous results of the bibliography [20,21] and due to the small available space inside the gel pores frustrating crystallization. Fig. 3.7 b) and 3.7 c) show the cooling and heating ramps at 5 °C·min^{-1} of silica based gels of pure [C_2Im][NO_3] (by EtOH route) and [C_4C_1Pyrr][TFSI] (by two precursors route), respectively. In these cases, the gel sample also shows, in general, similar peaks to those of the liquid sample, but shifted to lower temperatures and broader, in all the cases. Thus, the gelation of [C_2Im][NO_3] reduces the temperature of the freezing by approximately 30 °C which is related to the tendency to hinder crystallization after gelation. Additionally, the melting peak is split into two wider and less defined peaks, associated to two different sizes of the crystals formed during gelation, as Göbel *et al.* [22] suggested. Similarly, [C_4C_1Pyrr][TFSI] in gel state do not show either a crystallization peak or a glass transition in the temperature interval studied in cooling ramp, as was observed for the liquid state (see figure 3.6). Interestingly, the gel sample presents a peak of cold crystallization at -51 °C and a melting process at -13 °C, both in good agreement with the process observed in the liquid sample. Moreover, it is noteworthy that the heat released and absorbed in the exo and endothermic peaks, which are lower than those corresponding to the liquid sample, are similar to each other. That fact indicates that the confined IL crystallizes and melts in a unique step whereas two steps are needed in liquid state. This is due to two main reasons. Firstly, the gel sample presents less IL than in liquid state for the same volume and, on the other hand, the silica matrix scaffolding must have a pore size large enough to allow crystallization of the IL. Consequently, the endothermic peak observed at -29 °C in gel sample must be a solid-solid transition, usual transition in this kind of fluids.

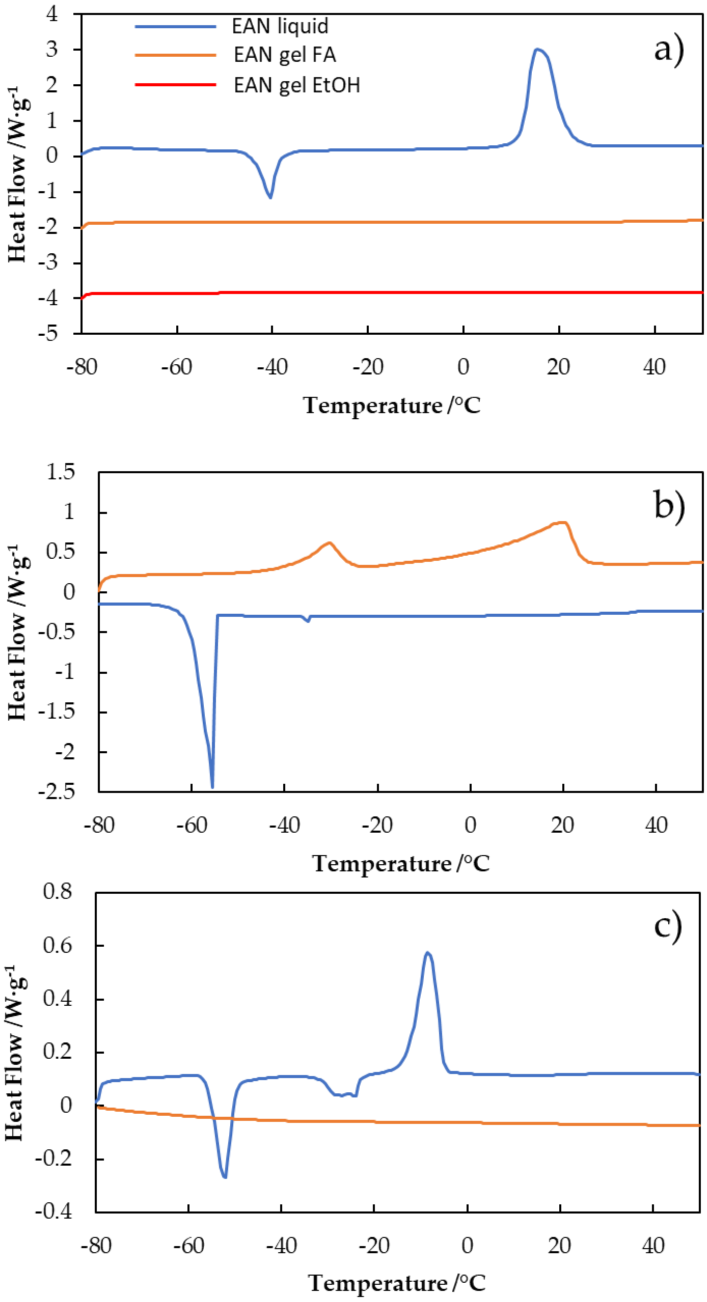

Figure 3.7. DSC curves at 5 °C·min^{-1} of a) on heating ramp for EAN in pure liquid and gel states synthesized by EtOH and FA route, b) curves in heating (blue line) and cooling (orange line) ramps of pure [C_2Im][NO_3] in the gel state synthesized by EtOH route and c) curves in heating (blue line) and cooling (orange line) ramps of pure [C_4C_1Pyrr][TFSI] in the gel state synthesized by two precursors route. Endo up.

ii Ionogels of EAN and [C_2Im][NO3] with lithium salt

With regard to the effect of both salt addition and gelation, Fig. 3.8 and Fig 3.9 show the DSC profiles of the mixtures of EAN +lithium nitrate and [C_2Im][NO_3] + lithium nitrate after nanoconfinement in silica scaffolds, respectively. Similar to pure ILs, gelation does not significantly change the thermal behavior in comparison with the liquid mixtures. Indeed, no crystalline behavior is observed either upon heating or upon cooling for EAN + $LiNO_3$ mixtures. Furthermore, confinement of mixtures of $[C_2Im][NO_3]$ + $LiNO_3$ in the silica network enhances the reduction of the supercooling effect and degree of crystallinity observed as a consequence of salt addition. Thus, only the DSC curves at the lowest concentration of Li salt present freezing and melting peaks in both cooling and heating ramps respectively; mixture $[C_2Im][NO_3]$ + $LiNO_3$ 1 mol·kg^{-1} shows a cold crystallization peak at -53 °C followed by a broader melting peak in heating ramp, which is indicative of crystallization frustration upon salt addition, and verified by the absence of peaks (only the glass transition can be observed) in the DSC curves at the higher salt concentrations (2 and 3 mol·kg^{-1}).

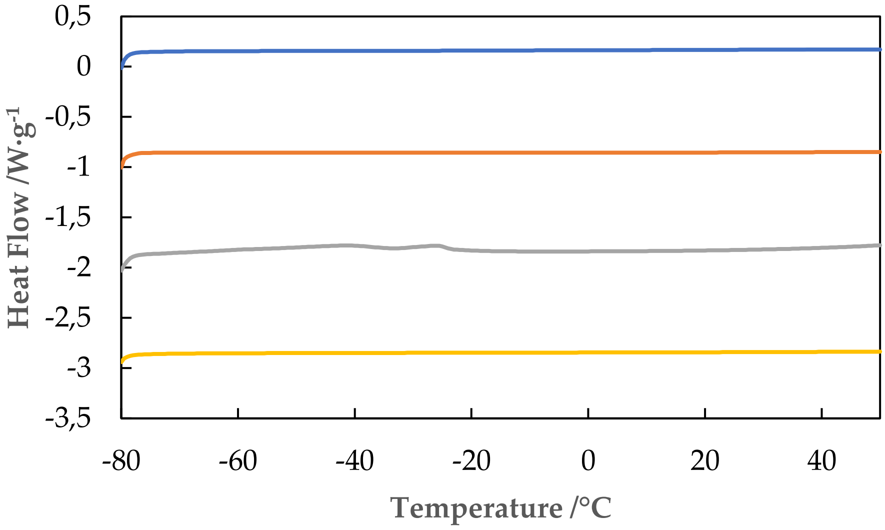

Figure 3.8. DSC curves on heating ramp at 5 °C·min^{-1} of gel samples EAN + $LiNO_3$ synthesized by ethanol route. Blue line represents pure EAN gel, orange EAN + $LiNO_3$ 0.1 mol·kg^{-1}, grey EAN + $LiNO_3$ 1 m and yellow EAN + $LiNO_3$ 2 mol·kg^{-1}. Endo up.

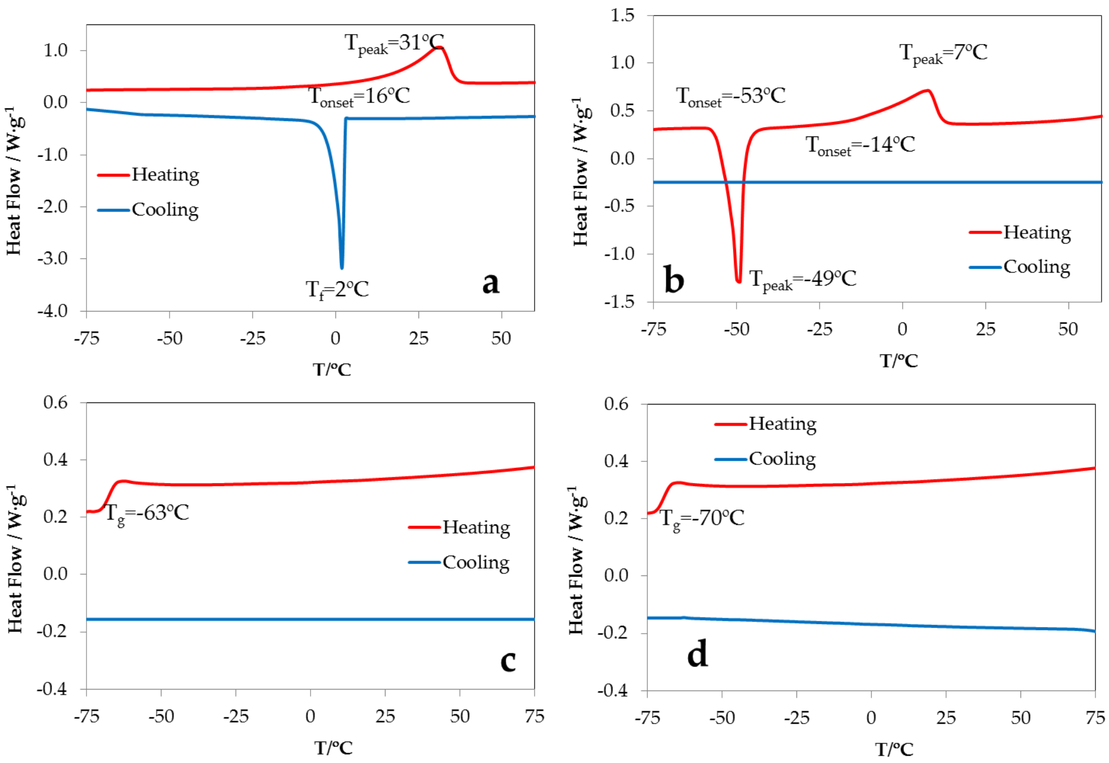

Figure 3.9. DSC curves of $[C_2Im][NO_3]$ + $LiNO_3$ metal salt solutions at different concentrations (5 °C·min^{-1}) in gel states, heating (red line) and cooling (blue line) ramp, (a) 0.5 m salt addition, (b) 1 m, (c) 2 m and (d) 3 m. Exo down.

In summary, the nano-confinement in silica matrix does not significantly change the liquid behavior inside the organic matrix, allowing some phase transitions observed previously in the liquid samples, although gelation accentuates the reduction of crystallinity already initiated with the addition of salt. This could be due to the space assigned to the liquid mixture inside the gel pore (water and some other impurities created during gelation process also, restrict the space see *Structural Characterization – NMR*) being small and does not allow for transitions, forcing the liquid to remain in an amorphous state.

3.2.2 Thermogravimetric analysis (TGA)

In this subsection the thermal stability of ionic liquids, mixtures and ionogel is analyzed using the thermogravimetric technique. The first objective planned was to determine of the best experimental procedure to do it. The effect of the atmosphere was studied to the thermogravimetric experiences in nitrogen and air. The TG and DTG curves are for pure EAN presented in Fig. 3.10. No significant differences can be found, suggesting that a common oxygen-independent mechanism (evaporation) is behind this process [23].

The effect of the heating rate was also studied for the pure EAN and the TGA curves at different heating rates (1 to 20 °C·min^{-1}) in a N_2 atmosphere, and is presented in Fig. 3.11. From these curves, onset temperature (T_{onset}), peak temperature (T_{peak}) and the percentage of mass loss at T_{onset} (W_{onset}) were obtained and presented in Table 3.3

following the methodology specified in the materials and methods chapter. As can be seen, the temperatures associated to the degradation process increase with the heating rate, which means, as is well known, the heating rate is a crucial parameter in the thermal stability studies using this technique [24,25]. As several studies indicate, T_{onset}, determined by TGA dynamic studies, cannot be considered as the limit temperature at which the sample is able to work properly for the desired application [26,27], but additional studies are needed and new realistic parameters such as the maximum operation temperature (MOT) must be determined.

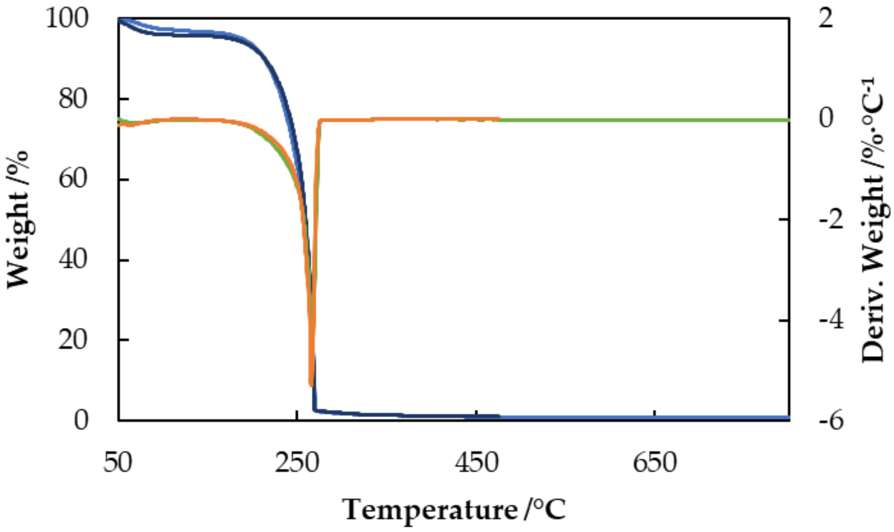

Figure 3.10. TG curves under nitrogen (blue) and air (black) atmospheres and DTG curves under nitrogen (green) and air (orange) atmospheres of pure EAN at a heating rate of 10 °C min^{-1}

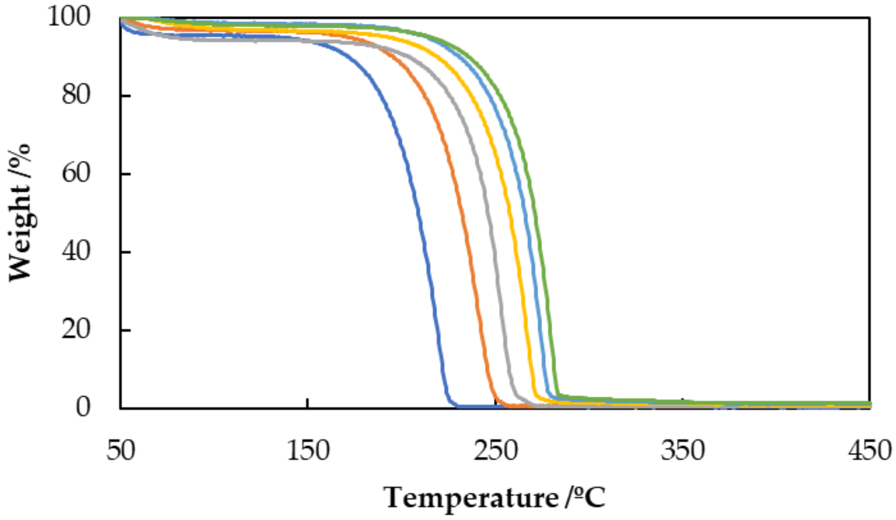

Figure 3.11. TG curves of pure EAN at different heating rates [1 °C min^{-1} (dark blue), 3 °C min^{-1} (orange), 5 °C min^{-1} (grey), 10 °C min^{-1} (yellow), 15 °C min^{-1} (clear blue) and 20 °C min^{-1} (green)] under nitrogen atmosphere.

Table 3.3: Onset (T_{onset}) and peak (T_{peak}) temperatures and relative mass loss at onset temperature (W_{onset}) determined from TG and DTG curves at the different heating rates under nitrogen atmosphere. Experiments were performed at a 1008 ± 10 hPa of atmospheric pressure, and relative humidity of 55 ± 10%.

Heating rate/ ºC min^{-1}	t_{onset} / °C	t_{peak} / °C	W_{onset} / %
1	196	219	78
3	217	241	77
5	236	252	75
10	247	266	74
15	253	273	74
20	260	278	73

Expanded uncertainties are U(t) = 6 °C and U(W) = 2% (0.95 level of confidence (k=2))

Due to these results, dynamic scans at 10 °C·min^{-1} were selected to study the thermal stability of the bulk ILs.

3.2.2.1 Pure Ionic Liquids

The TG and DTG curves under nitrogen atmosphere and heating rate of 10 °C/min of the pure ILs, [C_2Im][NO_3], [C_4C_1Pyrr][TFSI] and [C_2C_1Im][TFSI] are presented in Fig. 3.12 and compared with the previously exposed EAN.

DTG and TG signals of all the ILs exhibit a unique loss step (endothermic peak) at the same temperature interval indicating that vaporization is the main mechanism of degradation of the ILs. For nitrate anion (Fig. 3.12 a and b), an initial mass loss is found up to 110 °C, corresponding to the release of water and some volatile synthesis precursors due to the hygroscopic character of the nitrate anion. This contrasts with the plateau at low temperatures for [C_4C_1Pyrr][TFSI] and [C_2C_1Im][TFSI], where no initial mass loss is observed.

For EAN (Fig. 3.12 a), evaporation occurs between 190 – 270 ºC where an 85% mass loss with a peak temperature presented at 266 ºC. In case of [C_2Im][NO_3] (Fig. 3.12 b) the highest mass loss step (85% loss) appears between 160 and 226 ºC with a maximum rate at 207 ºC. For [C_4C_1Pyrr][TFSI] (Fig. 3.12 c) the onset temperature (T_{onset} = 426 °C) was determined, the temperature at which 10% of the initial mass has been lost (T_{90} = 416 °C). For the last studied IL (Fig. 3.12 d), [C_2C_1Im][TFSI], from the tangent method to determine the onset temperature, T_{onset} = 447 °C and the peak temperature found was T_{peak} = 470 °C. Thermal Stability follows the trend [C_2Im][NO_3] < EAN < [C_4C_1Pyrr][TFSI] < [C_2C_1Im][TFSI]. It is clearly seen that the [TFSI]$^-$ anion confers greater thermal stability than [NO_3]$^-$, associated in the literature with low thermal stability [28]. Additionally, the DTG of [NO_3]$^-$ ILs is much more pronounced than the [TFSI]$^-$ ILs, this is due because the mass loss is produced in a lower temperature interval for [NO_3]$^-$ anion compared to [TFSI]. Additionally, protic ILs frequently show lower thermal stabilities than aprotic ILs, due to the proton transfer from the salt form to the precursor acid/base pairs [29].

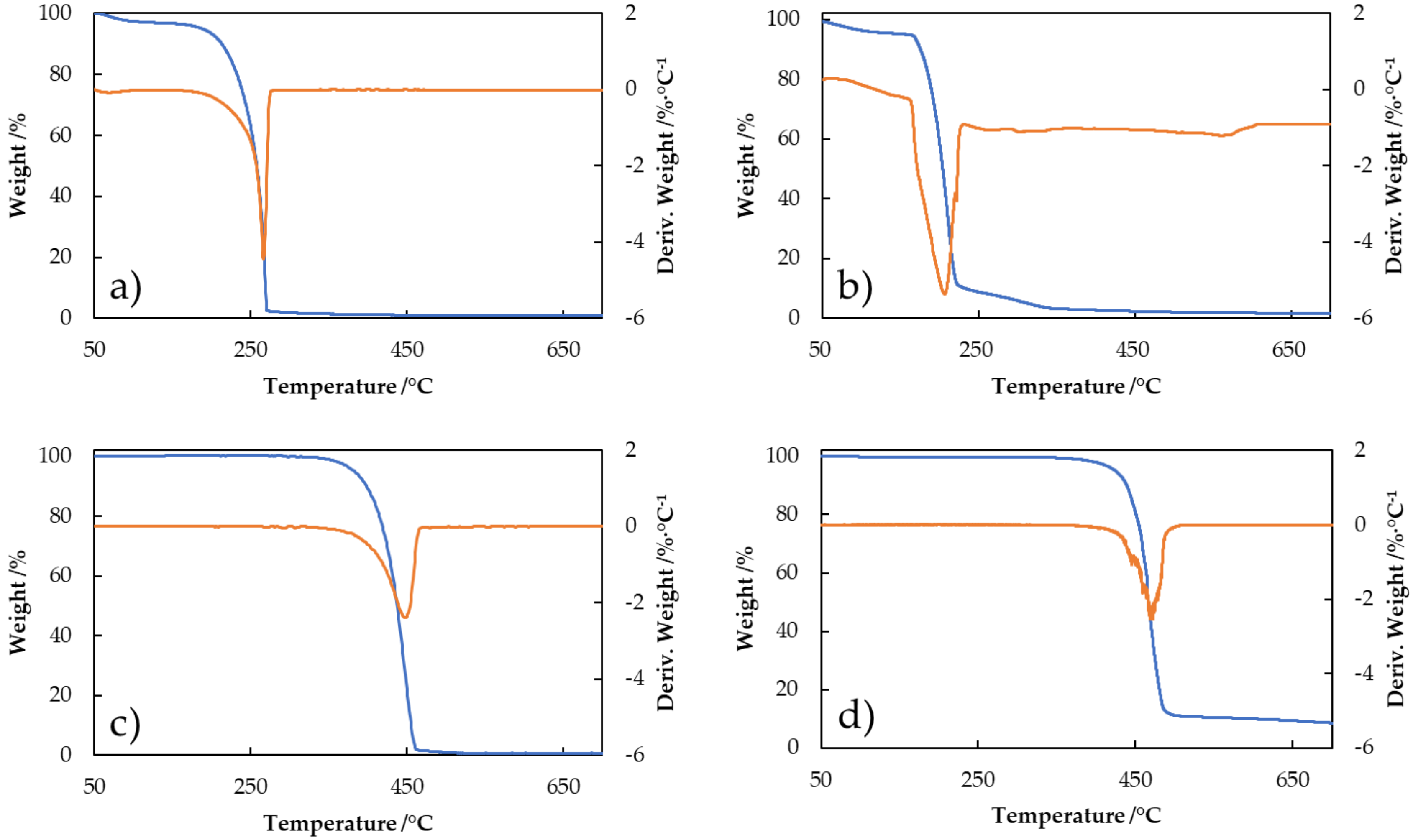

Figure 3.12. TG (blue line) and DTG (orange line) curves at 10 °C min^{-1} in nitrogen atmosphere of a) EAN, b) [C_2Im][NO_3] c) [C_4C_1Pyrr][TFSI] and d) [C_2C_1Im][TFSI].

From a bibliographical point of view, no reported data for $[C_2Im][NO_3]$ were found to compare with results reported here. It is important to note that long-term thermal stability of ILs is much lower than the decomposition temperatures obtained by step-tangent TG analysis, and, although it is not the aim of this work to analyze it thoroughly, a good way to estimate it [30] is using the method of Wooster *et al.* [31] and Baranyai *et al.* [32]. Following this criterion, a value of 130 °C was obtained for this pure IL.

Bibliographic data for $[C_4C_1Pyrr][TFSI]$ has been found for this experimental technique [33–35]. The reported results agree relatively well with those reported here, taking into account the dependence of the thermal analysis results on the experimental conditions (atmosphere, scanning speed, sample mass, etc.) [36]. As mentioned above, thermal stability depends, to a large extent, on the IL anion. $[TFSI]^-$ is the one that confers the highest thermal stability, with values of T_{onset} above 400 °C [37].

Bibliographic data coincide with the obtained results for $[C_2C_1Im][TFSI]$ [36,38] taking into account different experimental setups. The $[C_4C_1Pyrr][TFSI]$ and $[C_2C_1Im][TFSI]$ share the same anion, but for this experience, an imidazolium cation confers higher thermal stability than pyrrolidinium.

Thermal stability of ILs is strongly dependent on the former anion, and it is clearly seen in Fig. 3.12 that the $[TFSI]^-$ anion confers greater thermal stability than $[NO_3]^-$. Additionally, the DTA of $[NO_3]^-$ ILs is much more pronounced than the $[TFSI]^-$ ILs, this is due to a high mass ratio loss in $[NO_3]^-$ anion than in $[TFSI]^-$.

3.2.2.2 Mixtures of ILs and inorganic salts. Effect of salt addition.

TGA analysis for EAN, its mixtures with nitrate salt (lithium, magnesium, calcium and aluminum) and the pure salts are presented in Fig. 3.13. Thermogravimetric curves (TG) and its corresponding derivative curves (DTG) of $[C_2Im][NO_3]$ plus lithium, magnesium and aluminum salt mixtures are shown in Fig. 3.14, and Fig 3.15 shows the thermogravimetric analysis of $[C_4C_1Pyrr][TFSI]$ mixtures with lithium salt at saturation concentration.

The TGA curves were obtained under inert nitrogen atmosphere with a scan rate of 10 $°C \cdot min^{-1}$. Table 3.4 shows the T_{onset}, T_{peak} as well as a bibliographic study of the onset temperature ($T_{onset}^{Bibliographic}$) of the pure EAN and the pure studied salts, and as can be seen, a good agreement between this work values and bibliographic ones is obtained. No bibliographic values for the studied IL + salt mixtures were found. Zhang et al [39] have reported that the thermal stability of 1-ethyl-2, 3-dimethylimidazolium nitrate, is almost 100 ºC higher than our IL. This can be explained by the two extra methyl groups on the IL analyzed by Zhang et al. that confer higher thermal stability to the IL [37].

Although the pure ILs showed an unique step in the TG curves, as previously pointed out, mixtures of $[C_2Im][NO_3]$ and nitrate salts present a second peak related to a second step mass loss process (Fig. 3.14) [23].

Another interesting fact for nitrate salts is the decrease of the onset temperature of the pure salt with increasing valency of the salt cation (Fig. 3.13), where the obtained thermal stability temperatures for pure salt is found as $LiNO_3 > Ca(NO_3)_2 > Mg(NO_3)_2 > Al(NO_3)_3$. This behavior could be caused by the hydration water present in the Mg, Ca and Al [40]. But the salt thermal behavior seems to not affect the IL + salt mixture nor in the mass loss with respect to pure EAN at its T_{onset}. But at 400 °C, the remaining mass at EAN + salt mixtures are, approximately, 10% of the total mass, while for pure EAN the remaining mass at this temperature is practically 0%. This could be due to residual traces of the doping salt. In the case of $[C_2Im][NO_3]$ (Fig. 3.14), looking at the onset temperature values in Table 3.4, it can be seen how the mass loss temperature practically remains constant with lithium and magnesium salts. However, a decrease of 40 °C is observed in the case of aluminum salt, it could be related with the lower thermal stability of this salt, 136 °C [41]. A mass loss before reaching 200 °C can also be observed in the case of magnesium and aluminum mixtures. This mass loss is related to the hydration water of the nitrate salts, since the pure salts present six and nine hydration water molecules, respectively. For $[C_4C_1Pyrr][TFSI]$ (Fig. 3.15) the onset temperatures (T_{onset}) for the saturated salt mixture lies at 420 °C while for pure IL the T_{onset} is found as 426 °C, concluding that thermal stability is not affected by lithium salt addition. This is in fairly good agreement with previous results found by other authors [42]. No significant decrease in mass is found below 120 °C, so it follows that no traces associated with free water are present in the samples.

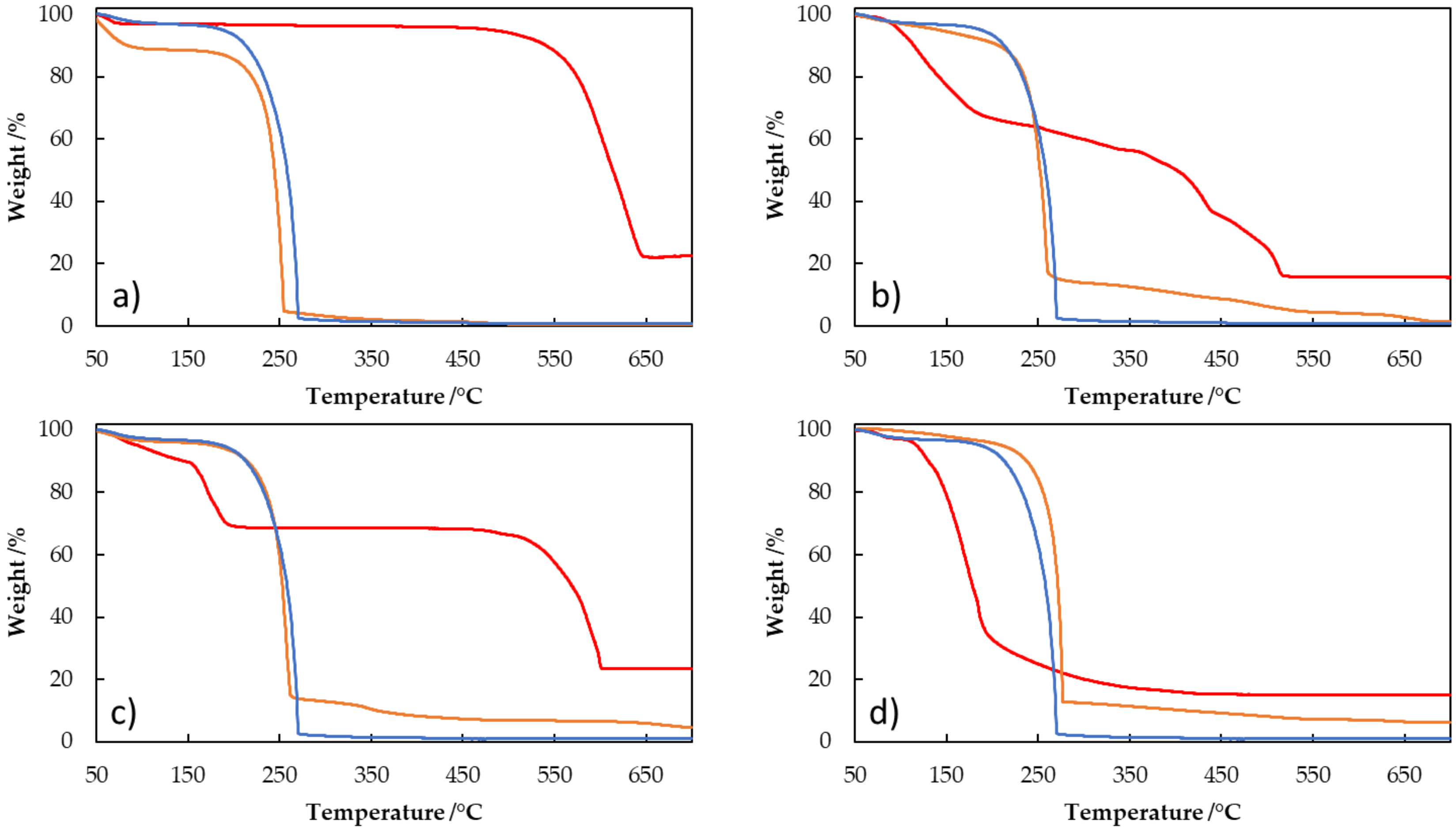

Figure 3.13. TG of pure EAN (blue line), pure salt (red line) and saturated mixture of EAN plus salt (orange line) of a) $LiNO_3$ b) $Mg(NO_3)_2$, c) $Ca(NO_3)_2$ and d) $Al(NO_3)_3$

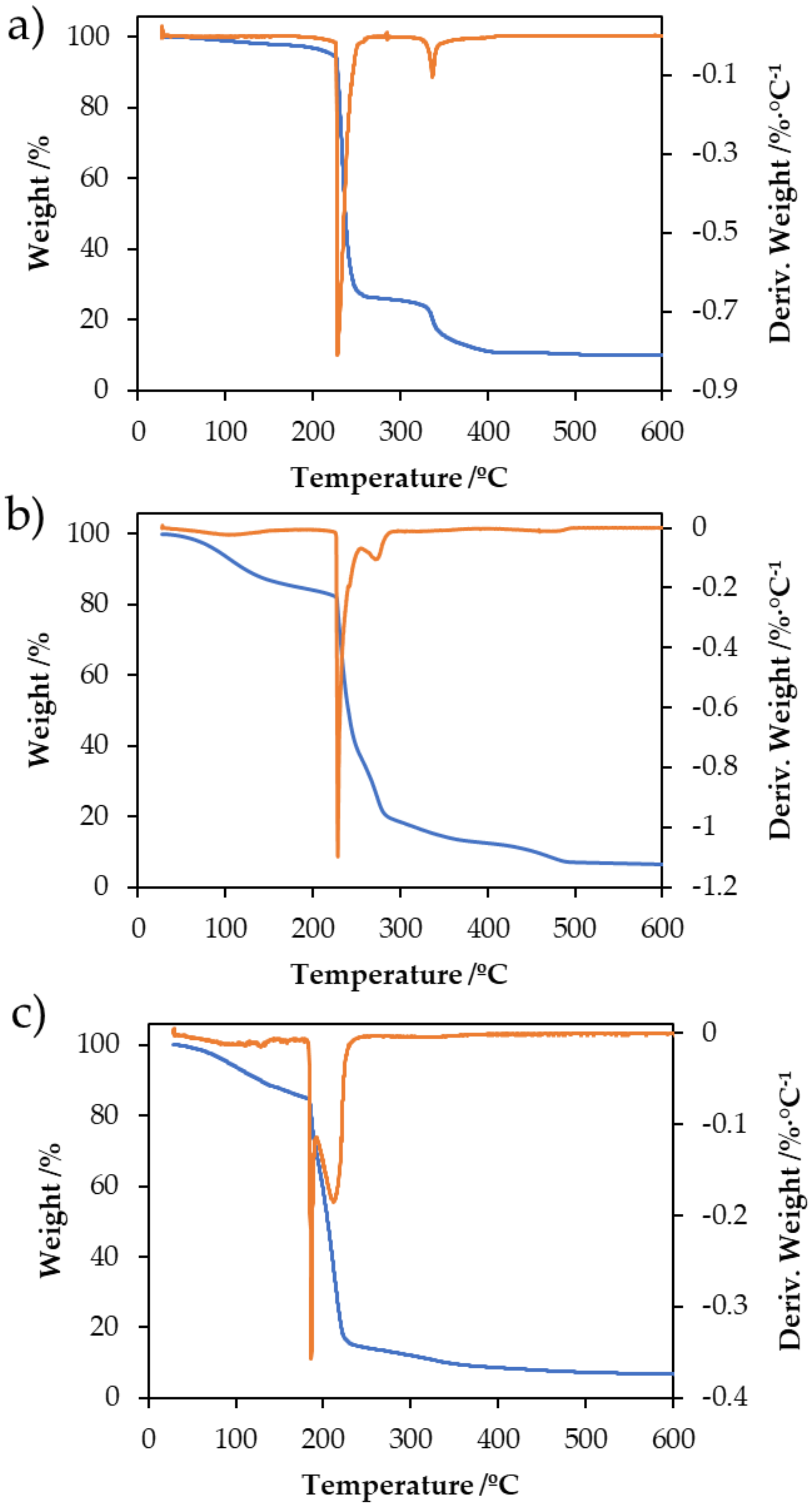

Figure 3.14. TG (blue line) and DTG (orange lines) curves of mixtures of [C$_2$Im][NO$_3$] with b) LiNO$_3$, c) Mg(NO$_3$)$_2$ and d) Al(NO$_3$)$_3$ salt at saturation concentration.

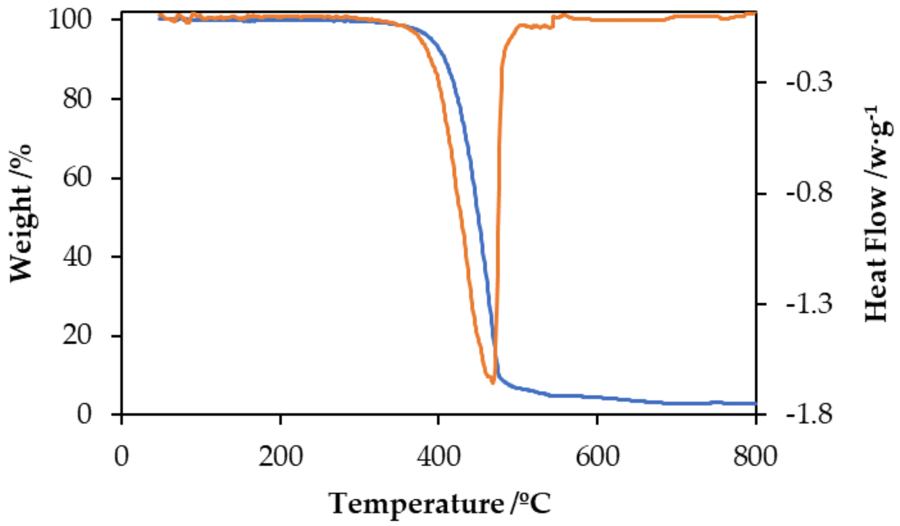

Figure 3.15. TGA (blue line) and DTG (orange line) of [C_4C_1Pyrr][TFSI] + LiTFSI 1.5 mol·kg^{-1}.

Table 3.4. Onset temperatures (T_{onset}) and DTG peak temperatures (T_{peak}) and weight at onset (W_{onset}) and at 400 °C ($W_{400\,°C}$) of mixtures of IL+inorganic salt.

Sample	T_{onset} / ºC	$T_{onset}^{Bibliographic}$	T_{peak} / ºC
EAN	*247*	*240*[43]	*265*
Li(NO$_3$)	*567*	*600*[44]	*627*
Ca(NO$_3$)$_2$	*555*	*561*[45]	*597*
Mg(NO$_3$)$_2$	*361*	*330*[45]	*433*
Al(NO$_3$)$_3$	*136*	*135*[45]	*186*
Saturated mixtures EAN + Nitrate salts			
EAN+ LiNO$_3$ 2m	*237*	---	*252*
EAN + Ca(NO$_3$)$_2$ 1m	*250*	---	*270*
EAN+Mg(NO$_3$)$_2$ 2m	*244*	---	*258*
EAN+Al(NO$_3$)$_3$ 2m	*250*	---	*272*
Saturated mixtures [C$_2$Im][NO$_3$] + nitrate salts			
[C$_2$Im][NO$_3$]+ LiNO$_3$ 3m	*223 / 325*	---	*230 / 333*
[C$_2$Im][NO$_3$]+ Mg(NO$_3$)$_2$ 2m	*222 / 263*	---	*228 / 268*
[C$_2$Im][NO$_3$]+ Al(NO$_3$)$_3$ 1m	*181 / 190*	---	*185 / 202*
Saturated mixtures [C$_4$C$_1$Pyrr][TFSI] + Lithium TFSI salts			
[C$_4$C$_1$Pyrr][TFSI] + LiTFSI 1.5 m	*420*	---	*470*

Expanded uncertainties are U(t) = 6 °C and U(W) = 2% (0.95 level of confidence (k=2))

3.2.2.3 Effect of nanoconfinement of pure ILs and salt mixtures

A. Pure ionogels

To understand the effect of gelation on thermal decomposition, a thermogravimetric study of gelled samples of pure EAN liquid and gels by EtOH and FA routes (Fig. 3.16 a), pure $[C_2Im][NO_3]$ liquid and gel by EtOH route (Fig. 3.16 b) and pure $[C_4C_2Pyr][TFSI]$ liquid and gel (Fig 3.16 c) was performed.

An important mass loss of up to 150 °C took place due to evaporation of free water and volatile precursors of the gelation in all cases, but especially remarkable in the ethanol route. TG curves are characterized by a step starting at 175 °C and finishing at 275 °C with a single peak in the corresponding DTG curve, this is an indicator that the decomposition is triggered by one single step as in the case of pure ILs. The onset temperature of gelled samples is slightly lower than that of the pure ILs, suggesting that the confinement in the silica scaffold does not significantly affect the thermal stability of the IL. Table 3.5 summarizes the onset temperature; mass loss occurs between 150 °C and 450 °C of all these samples.

With the aim to check if the residual volatiles from gelling process can be removed Fig. 3.17 shows the TG curves of EAN gel before and after vacuum procedure. The results indicate that the onset temperature is not dependent on the way the gel is prepared, and it is the same as that of pure ILs. Our results are in good agreement with those of previous researchers [46–48]. The only difference is that the first step disappeared with the gelation under vacuum, and a subsequent heating at 80 °C, as can be expected because the most volatile substances evaporate before the TG experiments (see structural characterization). These gelled samples were later used for measurements of the electrical conductivity to avoid any relevant influence of spurious volatiles (See section 3.5.- Electrochemical characterization).

After this experimental setup, it can be concluded that the thermal stability of the IL is not affected by the nanoconfinement in the different silica scaffold analyzed, where the thermal degradation temperature in liquid and gel states coincide. Additionally, the thermal decomposition of the ionogels takes place in one single step, as in the case of bulk liquid samples.

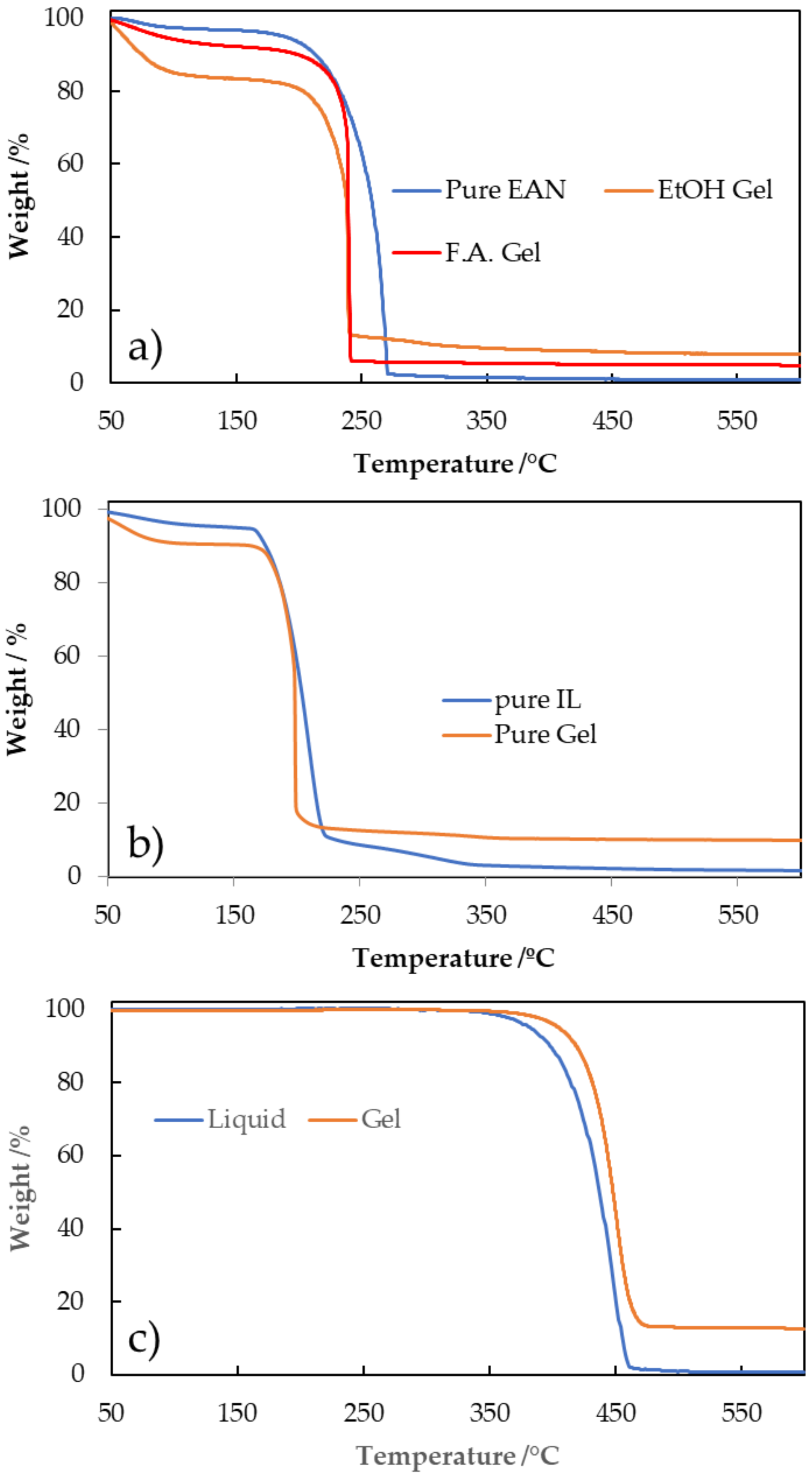

Figure 3.16. TGA of a) pure EAN (Blue line), EAN gel by EtOH route (orange line) and EAN gel by F.A., b) pure [C$_2$Im][NO$_3$] liquid (blue line) and gel by EtOH route (orange line) and c) [C$_4$C$_1$Pyrr][TFSI] liquid (blue line) and gel by two precursors route (orange line).

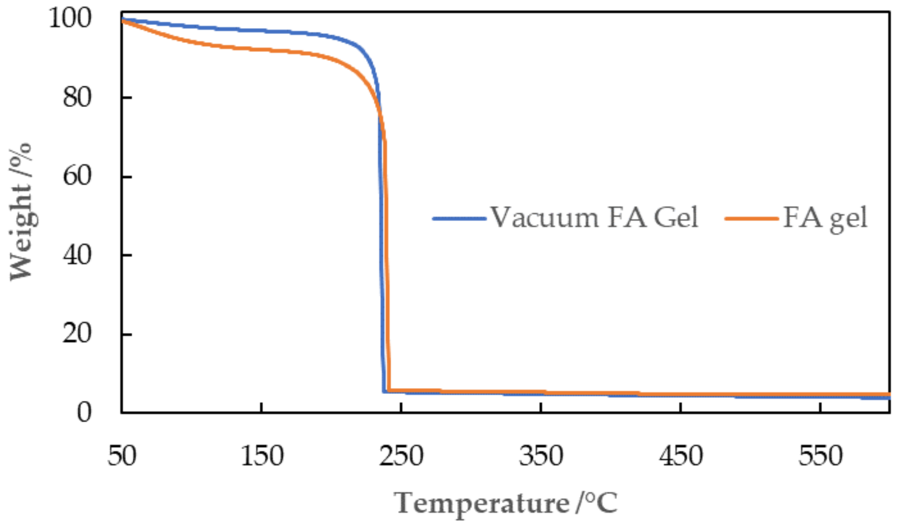

Figure 3.17. TG curves of gels of EAN by formic acid route before (orange line) and after (blue line) vacuum process.

Table 3.5. Onset temperature (T_{onset}) and mass loss at 150 °C (Δm(150 °C)) and 450 °C (Δm(450 °C)) for the different samples of pure IL, mixtures IL+$LiNO_3$ in the liquid and gel states. All the experiments were performed in a nitrogen atmosphere.

	T_{onset} /ºC	*Δm(150 ºC) /%*	*Δm(450 ºC) /%*
Liquid			
EAN	*245*	*3*	*100*
Gel			
EAN gel (Ethanol)	*226*	*17*	*92*
EAN gel (FA)	*237*	*8*	*95*
EAN gel vacuum (FA)	*234*	*3*	*96*

ΔU (*T_{onset}*)= 6ºC, ΔU (Δm)=1%

B. Ionogels of EAN with lithium salt

Regarding the effect of the lithium salt, Fig. 3.18 shows the corresponding TG curves. The onset temperature and mass loss at 150 °C and 450 °C were also indicated in Table 3.6. The salt addition has no appreciable effect on the onset temperature, as happened in the liquid mixtures reported in a previous work [23]. Only a reduction in mass loss (in %) at 150 °C, due to the evaporation of water and ethanol is observed. An increase of mass loss at 450 °C due to salt residue at this temperature is visible, and was also observed in liquid mixtures [23].

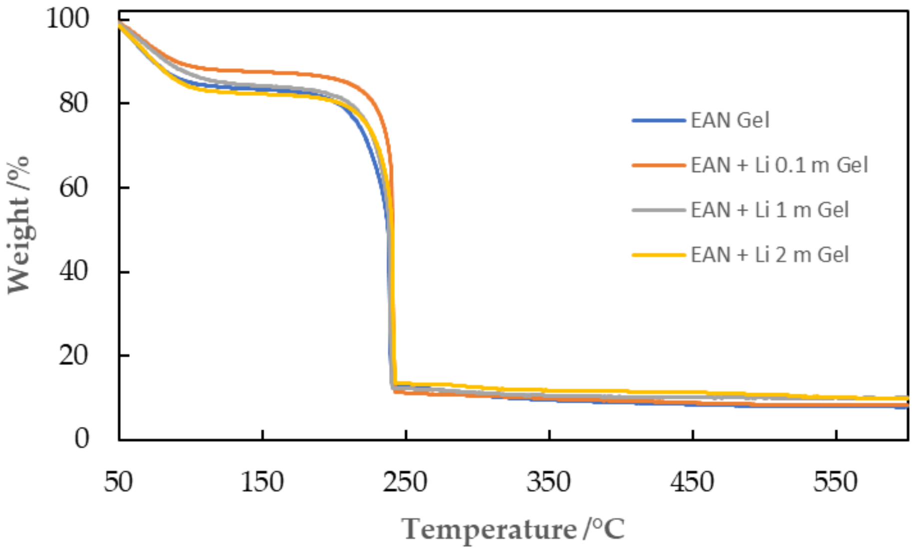

Figure 3.18. TG curves of EAN gel doped with different concentrations of Li salt, prepared by the ethanol route.

Table 3.6. Onset temperature (T_{onset}) and mass loss at 150 °C (Δm(150 °C)) and 450 °C (Δm(450 °C)) for the different samples of mixtures IL+$LiNO_3$ in gel states. All the experiments were performed in nitrogen atmosphere.

	T_{onset} /°C	*Δm(150 °C) /%*	*Δm(450 °C) /%*
EAN+$LiNO_3$ 0.1m (Ethanol)	231	12	91
EAN+$LiNO_3$ 1.0 m (Ethanol)	230	15	90
EAN+$LiNO_3$ 2.0m (Ethanol)	230	16	87

3.3. Structural Characterization: Nuclear Magnetic Resonance (NMR)

In this section, the structural arrangement of the ILs and their mixtures with doping salts is analyzed, in both liquid and gel states. Different experimental NMR techniques are used such as 1-D ^1H and ^{13}C NMR, and to study some of the synthesized semisolid ionogels, a magic angle spinning NMR (MAS-NMR) was used to achieve a resolution similar to that for liquid samples.

3.3.1. Pure Ionic Liquids

The NMR of the liquid samples of pure ILs, EAN, [C_2Im][NO_3], [C_4C_1Pyrr][TFSI] and [C_2C_1Im][TFSI] are shown in Fig. 3.19. For a better understanding, the proton signals are labelled in the same way than the numbered atoms in the inset of each figure. The signals were referenced using TSP/D_2O as deuterated solvent.

Nitrate based ILs are formed by a protic cation, which means that the labile proton signal is present downfield in both spectra. In the case of EAN, the signal corresponding to NH_3 is located at 7.79 ppm (FWHM = 51.08 Hz) while for [C_2Im][NO_3] the NH peak is located at 14.48 ppm (FWHM = 122.52 Hz). Specifically, the NH_3 of EAN are composed of three labile protons, so the measured signal is the average chemical shift for this chemical species. This is the reason for the large widening and low intensity of the obtained signal. For $[C_2Im][NO_3]$ the proton signal corresponding to the N-H bond is the least shielded (downfield) of all obtained signals, and at the same time, is the widest and the least intense. This is due to the labile character of the N-H proton. Although no previous studies were found for this IL, this experimental study is in agreement with that of other authors, for example Zhu *et al.* [49] analyzing the 1-methyl-3H-imidazolium triflate and Takao and Tsubomura [50] for 1-methyl-3H-imidazolium tetrafluoroborate. The differences in this peak position found between our results and the results of these articles, especially those in [50], can be explained in terms of hydrogen bond formation between imidazolium cations and the oxygen of the different anions. In the work of Takao and coworkers, they found a low field signal at 11.39 ppm associated to the labile proton of the molecule $[C_1Im][BF_4]$ impurities found during the synthesis process of $[C_2C_1Im][BF_4]$. The upper-field shifting for the labile proton of the IL $[C_2Im][NO_3]$ indicates that N-H proton is more deshielded, indicating that the NO_3 anion has higher influence in the polar region of the imidazolium ring due to the formation of hydrogen bonds.

With regards to the aprotic ILs ($[C_4C_1Pyrr][TFSI]$ and $[C_2C_1Im][TFSI]$), the relative shifting of the recorded proton signals are much more shielded than the protic ILs, due to the nonexistence of labile protons which means a lower relative shifting of the proton signal. For $[C_4C_1Pyrr][TFSI]$ the number of recorded peaks coincides with previously published works [51,52]. No deuterated reference was used to record the spectra of $[C_2C_1Im][TFSI]$, so the CH_3 of the ethyl alkyl chain was referenced using this previously published manuscript [53] at 1.41 ppm. As in the case of $[C_4C_1Pyrr][TFSI]$, the shifting of the obtained proton signals is significantly lower than those obtained for PILs, except for proton number 3 of $[C_2C_1Im][TFSI]$ (inset Fig. 3.19 d), the downfield signal of this proton can be explained in terms of the electronegative surrounding nitrogens (atoms number 2 and 4).

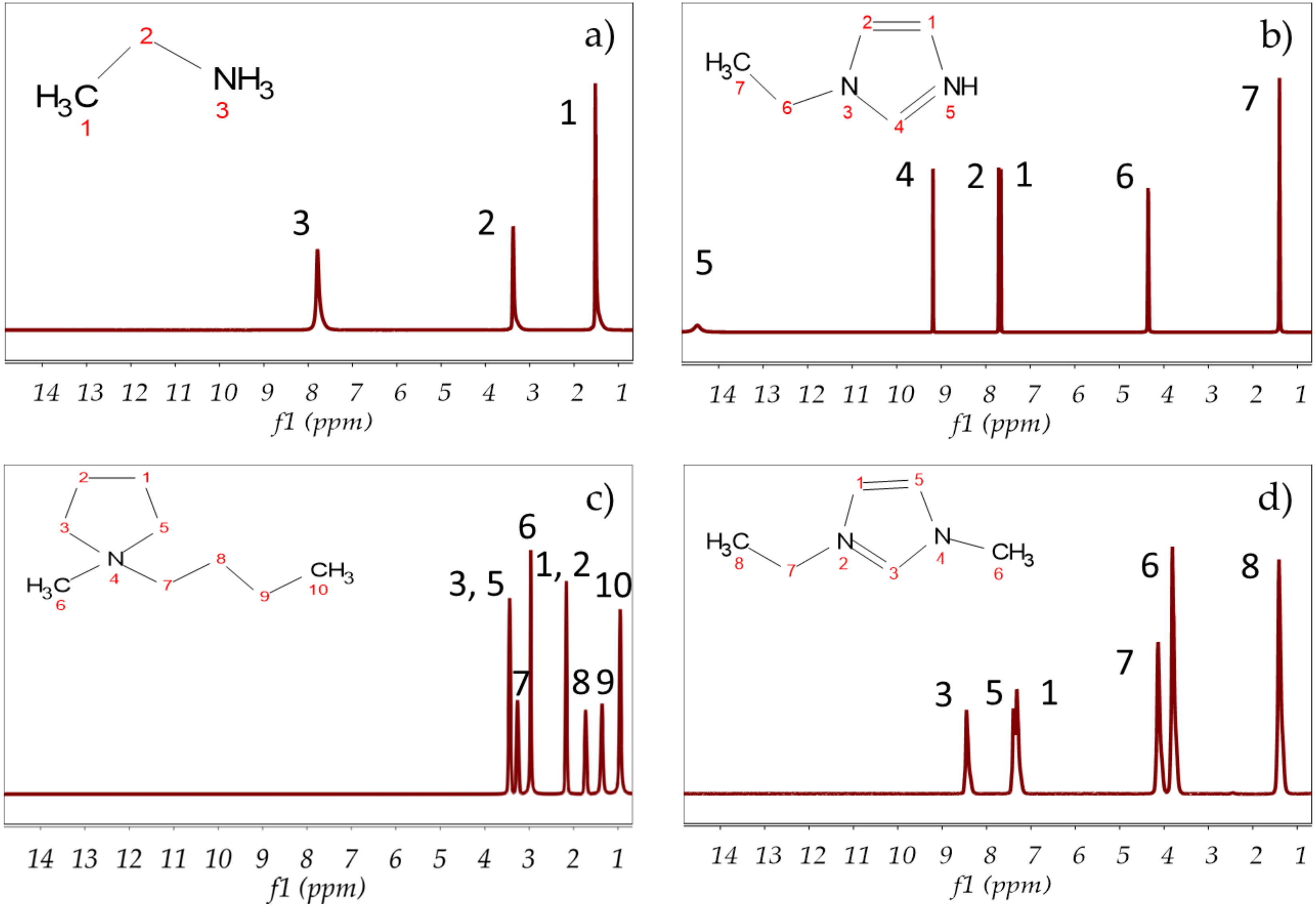

Figure 3.19. ^{1}H NMR spectra of pure ILs a) EAN b) [C_2Im][NO_3] c) [C_4C_1Pyrr][TFSI] and d) [C_2C_1Im][TFSI]

3.3.2. Mixtures of ILs and inorganic salts. Effect of salt addition.

The effect of the salt addition in the different studied ILs will be discussed by each IL, due to the individual importance of each result, and later a joint compilation will be made to highlight the common results and the possible differences between them. Firstly, the influence of the addition of different metallic salts (mono, di and trivalent) in the protic ILs (NO_3^- anion) is studied. For this experimental study, NMR measurements are made at the saturation concentration used for each added salt.

Hydrogen spectra (^{1}H) of EAN mixtures with lithium, calcium, and magnesium nitrate salts are shown in Fig. 3.20. ^{1}H and ^{13}C NMR spectra of [C$_2$Im][NO$_3$] pure, and with lithium, magnesium, and aluminum nitrate salts are shown in Figs. 3.21 and 3.22, respectively. The chemical shift of the CH$_3$ group of EAN for all samples was established at 1.52 ppm, as Matveev and co-workers found [54], notwithstanding, for [C$_2$Im][NO$_3$] spectra were refenced using TSP/D$_2$O as deuterated disolvent.

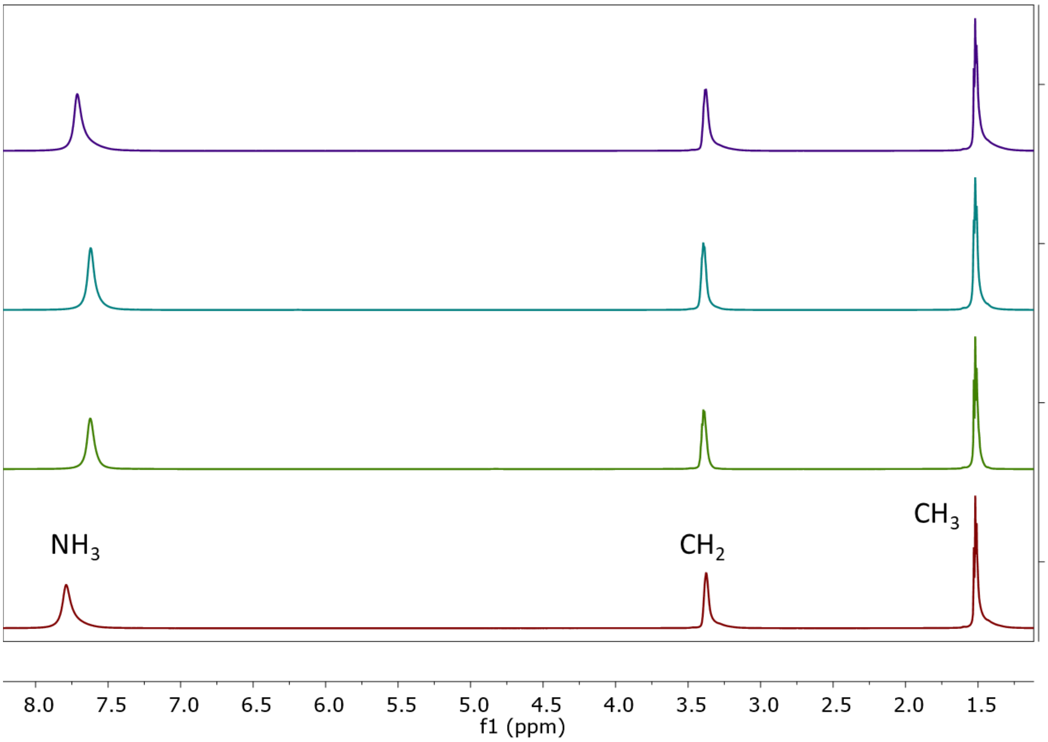

Figure 3.20. ^{1}H RMN of EAN pure (red line), LiNO$_3$ at 2 mol·kg^{-1}(green line), Mg(NO$_3$)$_2$ at 1 mol·kg^{-1} (blue line) and Ca(NO$_3$)$_2$ at 0.5 mol·kg^{-1} (purple line).

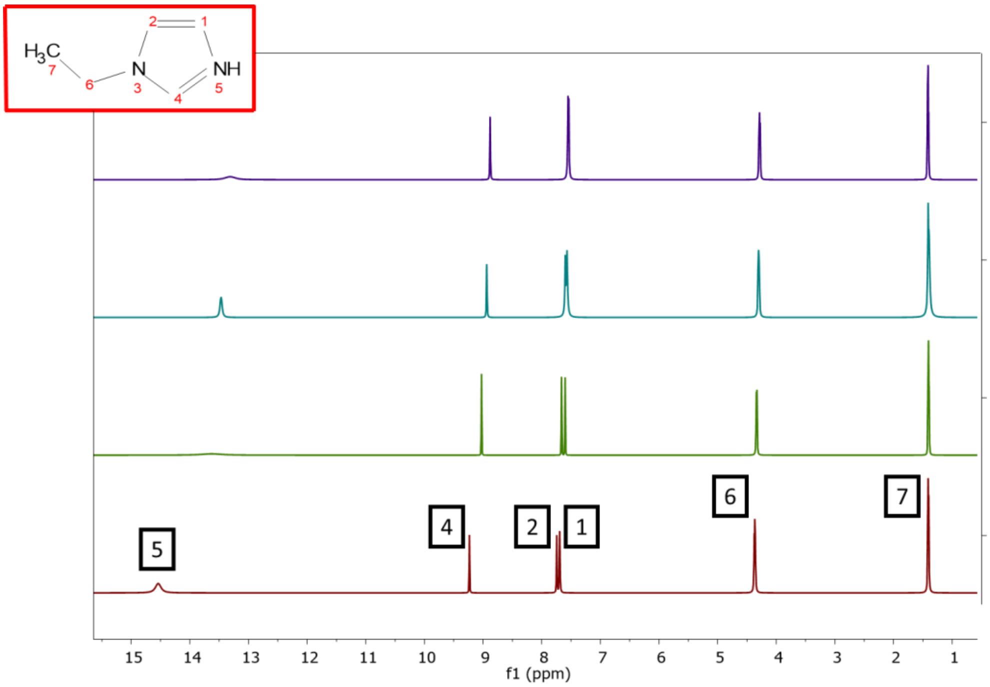

Figure 3.21. ^{1}H RMN of [C_2Im][NO_3] mixtures with different salts at saturation concentrations (liquid form). Pure IL (red line), $LiNO_3$ at 3 mol·kg^{-1} (green line), $Mg(NO_3)_2$ at 2 mol·kg^{-1} (blue line) and $Al(NO_3)_3$ at 1 mol·kg^{-1} (purple line). Inset shows the IL cation.

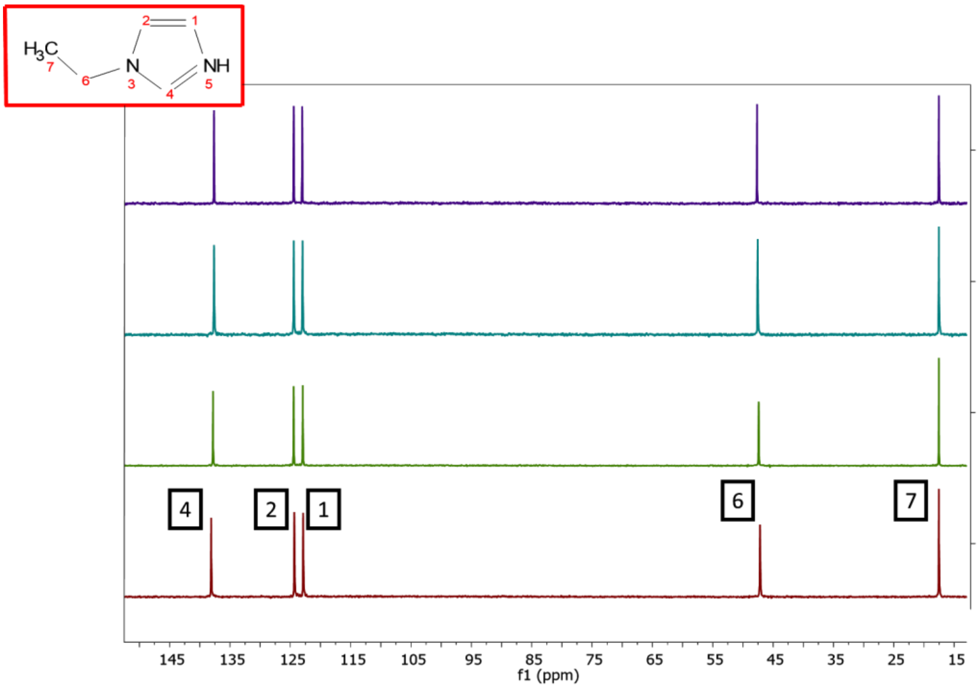

Figure 3.22. ^{13}C RMN of [C_2Im][NO_3] mixtures with different salts at saturation concentrations (liquid form). Pure IL (red line), $LiNO_3$ at 3 mol·kg^{-1} (green line), $Mg(NO_3)_2$ at 2 mol·kg^{-1} (blue line) and $Al(NO_3)_3$ at 1 mol·kg^{-1} (purple line). Inset shows the IL cation.

For both ILs + salt mixtures no significant differences were found for the alkyl chain with salt addition, and the most affected peak with salt addition is the N-H peak (7.79 ppm for pure EAN and 14.48 ppm for pure [C_2Im][NO_3]), being shifted up-field for all studied samples, which makes sense due to the labile character of this amine proton. After this, for [C_2Im][NO_3] the most affected protons by salt addition are 4, 2 and 1 respectively, due to the H-bond donor character of these acidic protons in the Lewis acid/base framework. They tend to form hydrogen bonds (HB) with the anion [55], and after salt addition they are distorted and weakened, causing this up-field shifting. It is well known that the HB network of the EAN is usually compared to that of water [56,57], where the PILs play a crucial role in the generation of the 3-D HB network due to the proton donor/acceptor role played by the cation/anion in the Brønsten acid/base framework. Thus, the initial idea is that the HB network, formed by NH···O interactions, is perturbed by salt addition displacing the NH signal up-field (Table 3.7 and Table 3.8), which leads to the assumption that the hydrogen nucleus in the N-H bond for both ILs is more shielded due to a partial HB network breaking and/or weakening after salt addition.

Table 3.7. ^{1}H RMN shifting of recorded signals in ppm.

Sample	δ_{CH_3}	δ_{CH_2}	δ_{NH_3}
EAN pure	*1.52*	*3.38*	*7.79*
EAN + $LiNO_3$ 2m	*1.52*	*3.39*	*7.62*
EAN + $Mg(NO_3)_2$ 1m	*1.52*	*3.40*	*7.62*
EAN + $Ca(NO_3)_2$ 0.5m	*1.52*	*3.38*	*7.71*

Table 3.8. Peak shift (in ppm) of ^{1}H spectra and ^{13}C for liquid mixtures [C_2Im][NO_3] + Nitrate salts.

	Sample	*7 (CH_3)*	*6 (CH_2)*	*1 (CH)*	*2 (CH)*	*4(CH)*	*5(NH)*
LIQUID	***^{1}H spectra***						
	Pure IL	*1.4 (T)*	*4.35 (Q)*	*7.66 (S)*	*7.71 (S)*	*9.19 (S)*	*14.48 (S)*
	IL + $LiNO_3$ 3m	*1.4 (T)*	*4.33 (Q)*	*7.60 (S)*	*7.66 (S)*	*9.03 (S)*	*13.63 (S)*
	IL + $Mg(NO_3)_2$ 2m	*1.4 (T)*	*4.30 (Q)*	*7.57 (S)*	*7.60 (S)*	*8.94 (S)*	*13.47 (S)*
	IL + $Al(NO_3)_3$ 1m	*1.4 (T)*	*4.28 (Q)*	*7.54 (S)*	*7.55 (S)*	*8.88 (S)*	*13.31 (S)*
LIQUID	***^{13}C spectra***						
	Pure IL	*17.54*	*47.19*	*124.36*	*122.9*	*138.13*	*X*
	IL + $LiNO_3$ 3m	*17.47*	*47.33*	*124.39*	*122.88*	*137.76*	*X*
	IL + $Mg(NO_3)_2$ 2m	*17.54*	*47.56*	*122.98*	*124.43*	*137.64*	*X*
	IL + $Al(NO_3)_3$ 1m	*17.54*	*47.67*	*123.02*	*124.43*	*137.64*	*X*

S: singlet, T: triplet, Q: quadruplet. For carbon spectra, all detected signals were identified as a singlet.

On the other hand, the effect of salt concentration in the mixture IL + salt has been analyzed. For this purpose, the ILs [C_2Im][NO_3] and [C_4C_1Pyrr][TFSI] and the corresponding lithium salt have been selected.

Fig. 3.23 shows a systematic study of the chemical shift of the ^{1}H proton spectra of the IL [C_2Im][NO_3] mixtures with lithium salt at different concentrations. The signal was referenced using TSP/D_2O as deuterated dissolvent. The most remarkable change regarding salt addition corresponds to a proton signal of N-H, which is up-fielded from 14.48 ppm for pure liquid to 13.66 ppm at the highest doped concentration sample due to a hydrogen bond break in presence of the lithium salt (Fig. 3.23). Since $[C_2Im][NO_3]$ is considered a protic ionic liquid (PIL) due to the N-H bond (proton 5 inset Fig. 3.23), which could be forming H-bonds due to donor character in the framework of Brönsted-Lowry acid/base theory.

The FWHM of this N-H peak for all the samples is more than 10 times higher than the rest of the peaks of the spectra (except for IL + $LiNO_3$ at 1.5 and 2 molal samples), as it can be seen in Figure 1 and Table 4. This broadening is typically observed in substances with –OH groups due to intermolecular exchange capacity of the –OH protons with protons of the protic solvents [58,59]. In our case, the broadening of this single peak can be associated to the exchangeable character of the proton of hydrogen 5, which provokes the generation and vanishing of different species, with different signals, at a too high speed to be recognized independently by the NMR, as other authors also pointed out previously [60,61].

Additionally, with the aim to compare the signal intensity of this NH peak (hydrogen number 5), the ratio between the intensities of this proton and CH_3 proton (hydrogen 7, used as reference intensity) of every ^1H spectra are presented in Table 3.11. It can be seen that the IL + lithium salt at 1.5 and 2 m shows the highest values of this ratio, and, interestingly, these two mixtures show the smallest FWHM values of the N-H signal (Table 3.10). This could be understood considering that Li^+ cations are tetrahedrally coordinated by $[NO_3]^-$ anions, as previously reported to EAN solutions with $LiNO_3$ [62]. Indeed, upon salt addition a competition between Li^+ cation and $[C_2Im]^+$ cation to coordinate with $[NO_3]^-$ anions takes place. To clarify this statement, number of moles of $[NO_3]^-$ per Li^+ mole in the studied mixtures of IL-$LiNO_3$ were calculated and presented in Table 3.12. The stoichiometric concentration of anions corresponds to 2 m mixture, and an excess of $[NO_3]^-$ anions can be observed for mixtures with lower salt concentration, so a distorted coordination takes place in the polar nanoregions.

At the lowest salt concentration ($LiNO_3$ 0.5 molal sample) the Li^+ cation is strongly coordinated to the $[NO_3]^-$ anion from $[C_2Im][NO_3]$, and some quantity of the remaining $[NO_3]^-$ could be reacting with $[C_2Im]^+$ to form HNO_3 exchanging the N-H proton at higher velocity than NMR resolution spectra, widening the peak and increasing the FWHM. This phenomenon is known as chemical exchange [63]. Similar observations were found by Zhu *et al.* [64] in mixtures of 1-methyl-3H-imidazolium triflate with DMSO or with D_2O. Then, a FWHM reduction is observed with the increasing salt concentration until the mixture IL + $LiNO_3$ 2m, which corresponds to the tetrahedral coordination limit [65], the Li^+ is surrounded by four $[NO_3]^-$, narrowing the peak and the minimum of the FWHM of this peak is therefore achieved (Table 4). Finally, for the mixture IL + $LiNO_3$ 3 m, exceed the tetrahedral coordination, the ordered phases are not possible and disordered configurations are recorded again with the consequent increase in the width of the peak.

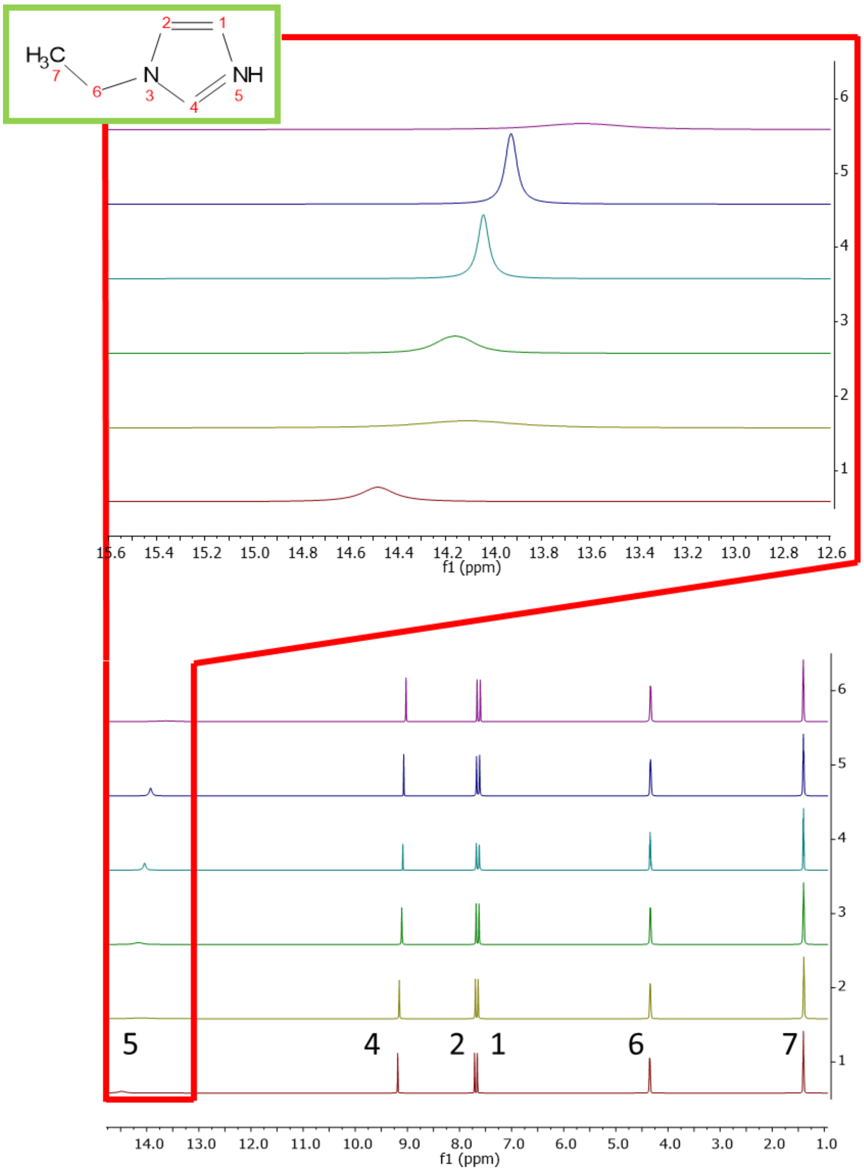

Figure 3.23. ^1H RMN of $[C_2Im][NO_3]$ mixtures with $LiNO_3$ salt at different concentrations (liquid form). Pure IL (red line), 0.5 mol·kg^{-1} (yellow line), 1 mol·kg^{-1} (green line), 1.5 mol·kg^{-1} (light blue line), 2 mol·kg^{-1} (dark blue line) and 3 mol·kg^{-1} (purple line). Squared area shows a magnification of the N-H peak for a better visualization. Inset shows the IL cation.

It is interesting to see that the salt addition does not affect the ^{13}C NMR spectra (Fig. 3.24): This contributes to confirm the hypothesis that the salt is located in the polar regions of the mixture IL + salt.

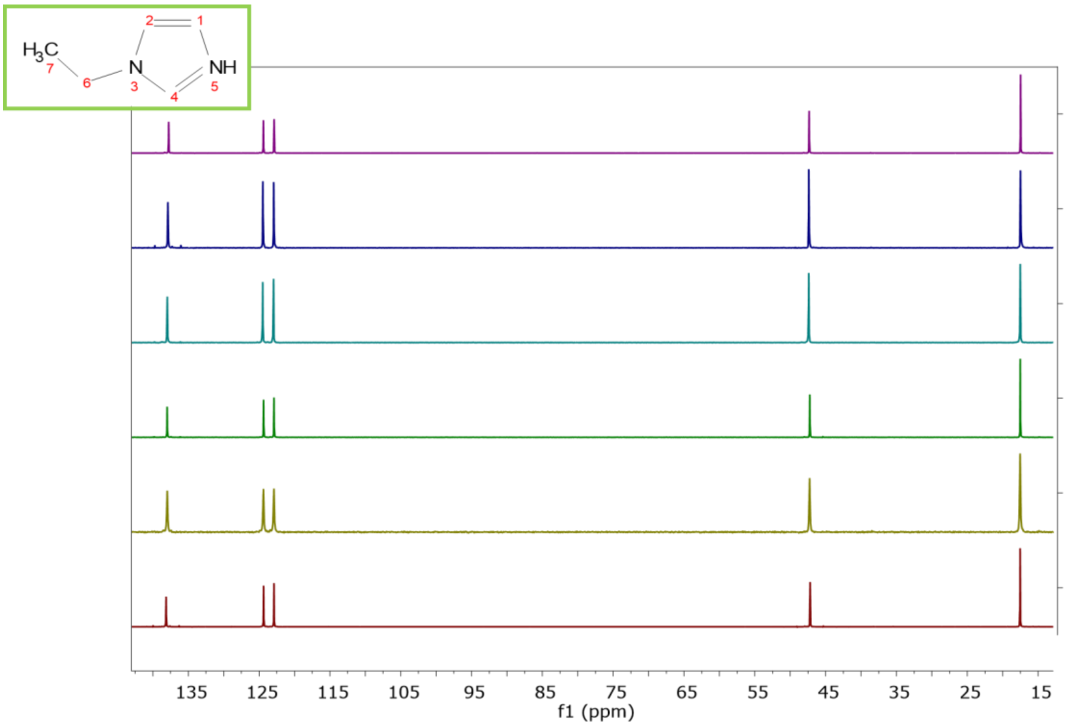

Figure 3.24. ^{13}C RMN of $[C_2Im][NO_3]$ mixtures with $LiNO_3$ salt at different concentrations (liquid form). Pure IL (red line), 0.5 mol·kg^{-1} (yellow line), 1 mol·kg^{-1} (green line), 1.5 mol·kg^{-1} (light blue line), 2 mol·kg^{-1} (dark blue line) and 3 mol·kg^{-1} (purple line). Inset shows the IL cation.

Table 3.9. Peak shift (in ppm) of ^{1}H spectra and ^{13}C for liquid and gel mixtures $[C_2Im][NO_3]$ + $LiNO_3$ salt.

	Sample	*7 (CH_3)*	*6 (CH_2)*	*1 (CH)*	*2 (CH)*	*4(CH)*	*5(NH)*
	^{1}H spectra						
LIQUID	***Pure IL.***	*1.4 (T)*	*4.35 (Q)*	*7.66 (S)*	*7.71 (S)*	*9.19 (S)*	*14.48 (S)*
	Mixture 0.5 m	*1.4 (T)*	*4.35 (Q)*	*7.64 (S)*	*7.7 (S)*	*9.16 (S)*	*14.11 (S)*
	Mixture 1 m	*1.4 (T)*	*4.34 (Q)*	*7.63 (S)*	*7.68 (S)*	*9.11 (S)*	*14.16 (S)*
	Mixture 1.5 m	*1.4 (T)*	*4.34 (Q)*	*7.62 (S)*	*7.68 (S)*	*9.09 (S)*	*14.04 (S)*
	Mixture 2 m	*1.4 (T)*	*4.34 (Q)*	*7.61 (S)*	*7.67 (S)*	*9.07 (S)*	*13.93 (S)*
	Mixture 3 m	*1.4 (T)*	*4.33 (Q)*	*7.6 (S)*	*7.66 (S)*	*9.03 (S)*	*13.66(S)*
	^{13}C spectra						
LIQUID	***Pure IL.***	*17.54*	*47.19*	*124.36*	*122.9*	*138.13*	*X*
	Mixture 0.5 m	*17.54*	*47.27*	*124.39*	*122.91*	*137.97*	*X*
	Mixture 1 m	*17.52*	*47.24*	*124.37*	*122.9*	*137.99*	*X*
	Mixture 1.5 m	*17.52*	*47.38*	*124.49*	*122.96*	*137.96*	*X*
	Mixture 2 m	*17.49*	*47.38*	*124.47*	*122.94*	*137.88*	*X*
	Mixture 3 m	*17.47*	*47.33*	*124.39*	*122.88*	*137.76*	*X*

S: singlet, T: triplet, Q: quadruplet. For carbon spectra, all detected signals were identified as a singlet.

Table 3.10. Fitted FWHM (in Hz) of ^1H and ^{13}C spectra for liquid and gel samples shown in Fig. 3.23. For triplet and quadruplet is presented each fitted FWHM of the peak forming multiplet.

	Sample	*7 (CH_3)*	*6 (CH_2)*	*1 (CH)*	*2 (CH)*	*4 (CH)*	*5 (NH)*
			^1H spectra				
LIQUID	***Pure IL.***	*5.31; 7.06; 6.67*	*8.97; 5.69; 6.28; 4.80*	*6.87*	*6.88*	*6.87*	*122*
	Mixture 0.5m	*6.75; 9.02; 6.21*	*7.08; 7.25; 7.07; 6.86*	*7.55*	*7.67*	*7.81*	*356*
	Mixture 1m	*6.31; 9.02; 6.31*	*5.98; 8.42; 6.04; 9.73*	*8.09*	*8.09*	*9.16*	*143.68*
	Mixture 1.5m	*3.11; 4.75; 5.68*	*3.76; 2.54; 5.62; 5.45*	*7.53*	*8.26*	*7.56*	*50.02*
	Mixture 2m	*8.30; 7.97; 4.87*	*7.65; 7.37; 6.21; 4.68*	*7.62*	*7.15*	*6.8*	*42.98*
	Mixture 3m	*6.07; 4.34; 4.01*	*4.74; 4.20; 3.75; 3.53*	*7.32*	*7.36*	*7.4*	*325*
			^{13}C spectra				
LIQUID	***Pure IL***	*7.8*	*19.89*	*7.3*	*6.7*	*10.39*	*X*
	Mixture 0.5m	*10.39*	*25.24*	*26.86*	*27.53*	*27.45*	*X*
	Mixture 1m	*8.4*	*8.5*	*7.4*	*6.8*	*9.9*	*X*
	Mixture 1.5m	*11.58*	*10.8*	*10.7*	*10.7*	*15.4*	*X*
	Mixture 3m	*5.87*	*6.78*	*11.55*	*7.08*	*7.83*	*X*

Table 3.11. Relative intensity of NH signal versus CH_3 signal proton spectra.

	Sample	I_{N-H}/I_{CH3}
LIQUID	***Pure IL.***	*0.028*
	Mixture 0.5m	*0.013*
	Mixture 1m	*0.034*
	Mixture 1.5m	*0.112*
	Mixture 2m	*0.141*
	Mixture 3m	*0.012*

Table 3.12. Number of $[NO_3]^-$ mol per Li^+ mol in IL + Li salt samples

Sample	*$[NO_3]^-$ /mol (for each added Li^+ mol)*
$LiNO_3$ 0.5 molal Liq.	*13.4*
$LiNO_3$ 1 molal Liq.	*7.3*
$LiNO_3$ 1.5 molal Liq.	*5.2*
$LiNO_3$ 2 molal Liq.	*4.0*
$LiNO_3$ 3 molal Liq.	*2.1*

The ^1H and ^{13}C spectra of $[C_4C_2Pyrr][TFSI]$ mixtures with lithium salt can be found in Figs. 3.25 and 3.26, respectively. No deuterated solvent was used to reference the obtained spectra, so the CH_3 signal of the alkyl chain was referenced using previously published results by Pavel et. al. [66]. Regarding multiplet information (Zeeman effect [67]) of the different present peaks, the resolution reached was not enough to exactly determine what kind of splitting is present. Peak shift can be found in Table 3.13. As can be seen, salt addition keeps the peak position (shift) at a similar value compared to the pure IL, indicating that the structure remains constant without a significant change to the structural arrangement.

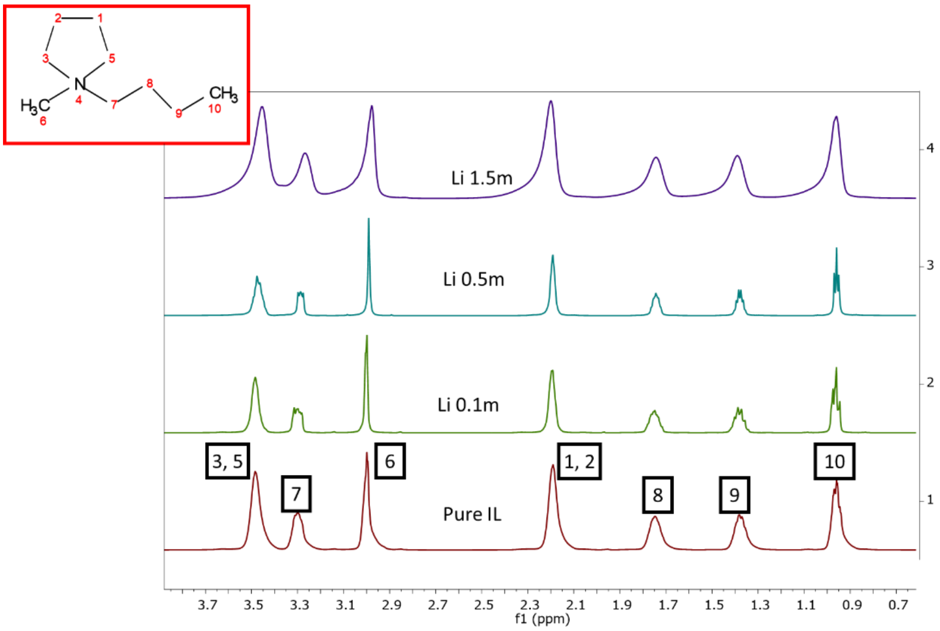

Figure 3.25. ^{1}H NMR of [C_4C_1Pyrr][TFSI] mixtures with lithium at 293K. Pure IL (red line), LiTFSI 0.1 mol·kg^{-1} (green line), LiTFSI 0.5 mol·kg^{-1} (blue line) and LiTFSI 1.5 mol·kg^{-1} (purple line).

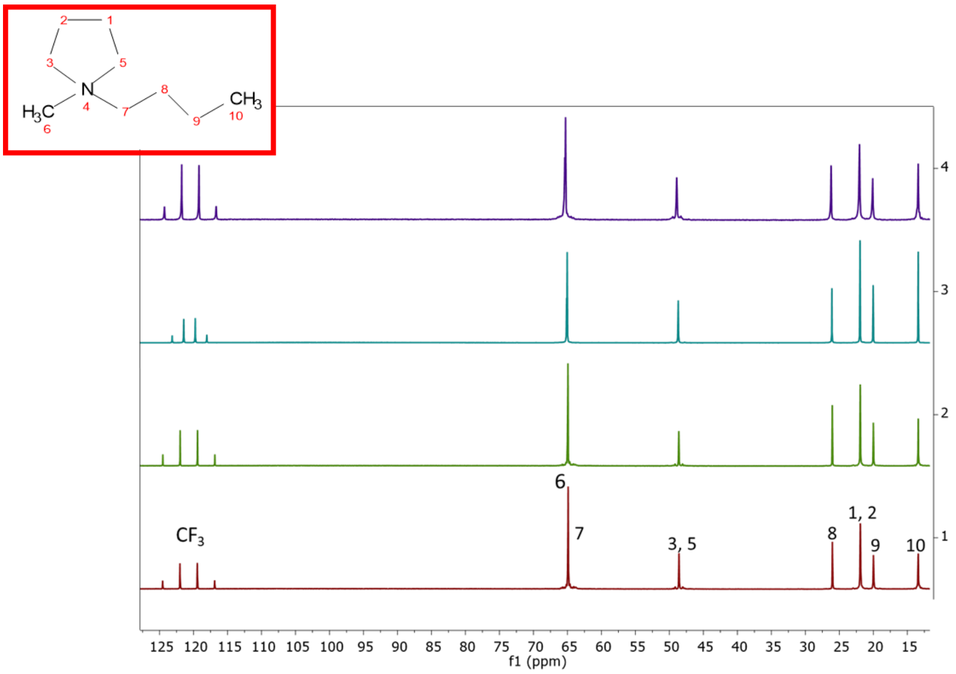

Figure 3.26. ^{13}C NMR of [C_4C_1Pyrr][TFSI] mixtures with lithium at 293K. Pure IL (red line), LiTFSI 0.1 mol·kg^{-1} (green line), LiTFSI 0.5 mol·kg^{-1} (blue line) and LiTFSI 1.5 mol·kg^{-1} (purple line). Inset show the IL cation.

Table 3.13. Peak shift (in ppm) of ^{1}H spectra and ^{13}C for liquid mixtures of [C_4C_2Pyrr][TFSI] + LiTFSI salt.

	Sample	*10 (CH_3)*	*9 (CH_2)*	*8 (CH_2)*	*1,2 (CH)*	*6(CH_3)*	*7(CH_2)*	*3,5(CH)*
				^1H spectra				
LIQUID	***Pure IL.***	*0.96*	*1.38*	*1.75*	*2.19*	*3.00*	*3.30*	*3.48*
	Mixture 0.1 m	*0.96*	*1.38*	*1.75*	*2.19*	*3.00*	*3.30*	*3.48*
	Mixture 0.5 m	*0.96*	*1.37*	*1.74*	*2.19*	*2.99*	*3.29*	*3.48*
	Mixture 1.5 m	*0.96*	*1.39*	*1.75*	*2.20*	*2.98*	*3.27*	*3.45*
				^{13}C spectra				
LIQUID	***Pure IL.***	*13.40*	*19.99*	*26.03*	*21.92*	*64.90*	*64.95*	*48.59*
	Mixture 0.1 m	*13.40*	*20.00*	*26.04*	*21.93*	*64.93*	*64.99*	*48.62*
	Mixture 0.5 m	*13.40*	*20.03*	*26.10*	*21.96*	*65.04*	*65.12*	*48.70*
	Mixture 1.5 m	*13.40*	*20.11*	*26.22*	*22.05*	*65.28*	*65.38*	*48.93*

3.3.3. Effect of nanoconfinement of pure ILs and salt mixtures

To study the EAN mixtures with $LiNO_3$ with higher resolution than traditional NMR, magic angle spinning (MAS) NMR was used. This study was performed in collaboration with the team of Prof. Andrea Mele from the Politecnico di Milano, Italy. The MAS NMR is commonly used to analyze solid samples that show broader peaks impossible to analyze with traditional liquid NMR. The other studied systems (gellified IL) were performed with a traditional liquid NMR technique, since the obtained resolution was enough to prove that the confined IL inside the silica scaffold was still in liquid state.

With regards to the gelation effect, firstly it is interesting to indicate that the reference capillary (containing the deuterated dissolvent) was not used for gel samples due quasi-solid state of the samples, and it was presumed that CH_3 signals were located at similar values to those obtained in the liquid state.

3.3.3.1. Pure ionogels

Fig. 3.27 shows the ^1H MAS NMR spectra at 305 K of gel of pure EAN (prepared by the ethanol route) and pure liquid EAN. This figure immediately reveals that in the gel sample, next to the three signals corresponding to the $[EA]^+$ cation, there are also signs of methylene and methyl protons from the residual ethanol as well as a residual water peak. It can be estimated that the EtOH and water content in the ionogel are ca. 3 wt% and 4 wt%, respectively. Enlarged areas in Fig. 3.27 are shown to a better visualization of the reached definition by this experimental technique, where the Zeeman effect is clearly appreciable in the gel samples.

These non-negligible amounts of water and ethanol, residues of the sol-gel process, can be the cause of the high values of conductivity in gel samples, especially the water content, as different authors have previously reported [68,69] as will be discussed later in the electrochemical characterization (section 3.5).

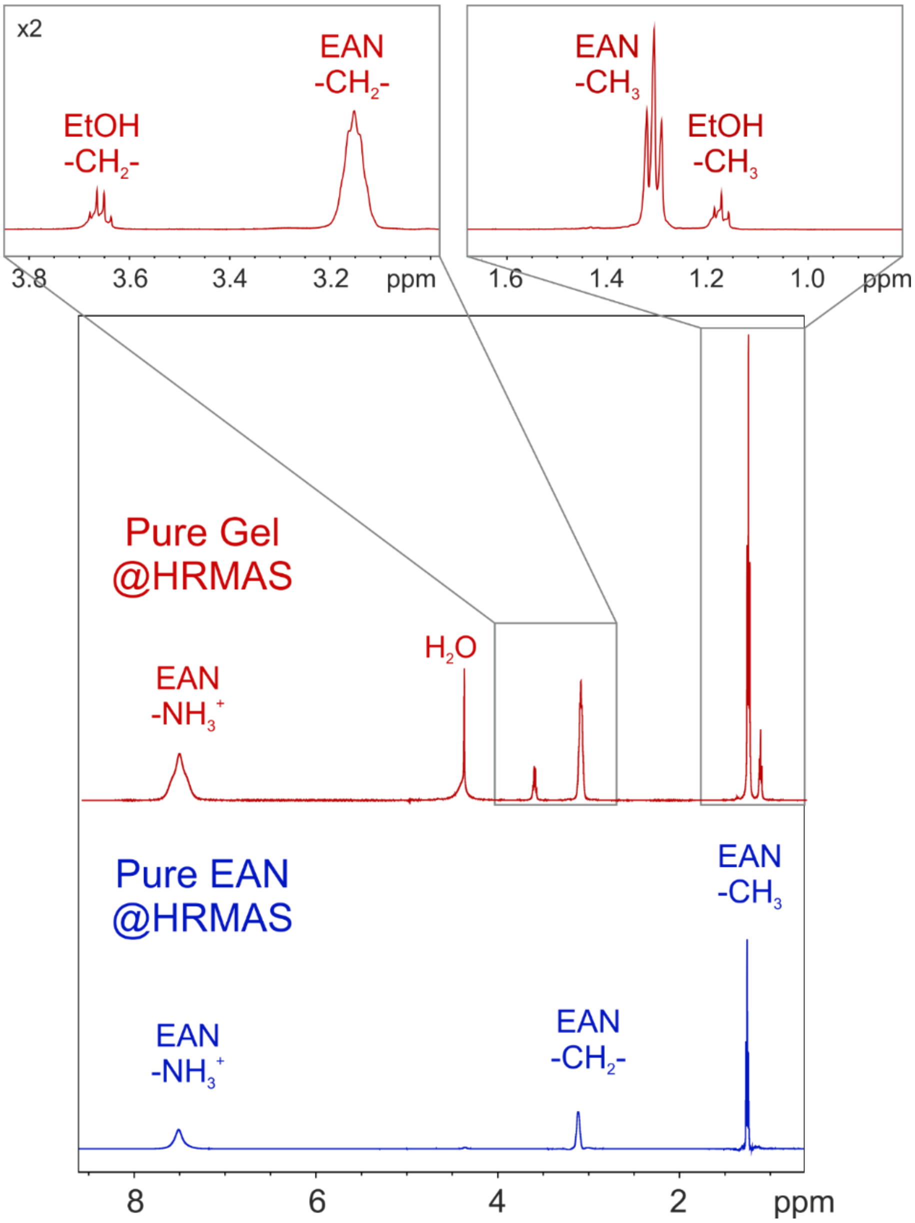

Figure 3.27. 1D ^{1}H HRMAS NMR spectra of the gel of pure EAN measured at 305 K. Enlargement of the regions corresponding to the methylene and methyl protons are shown for the sake of clarity.

As a kind reminder to the reader, each IL is nanoconfined by a different gelation route, which are described individually in the second chapter of this thesis (see materials and methods).

The NMR spectra for gellified samples of [C_2Im][NO_3] by EtOH route, [C_4C_1Pyrr][TFSI] by two precursors route, and [C_2C_1Im][TFSI] by two precursors route can be seen in Fig. 3.28 a), b) and c) respectively. Additionally, a systematic study of the gelation effect of [C_2C_1Im][TFSI] varying the ratio of IL/silica of the scaffold is also presented.

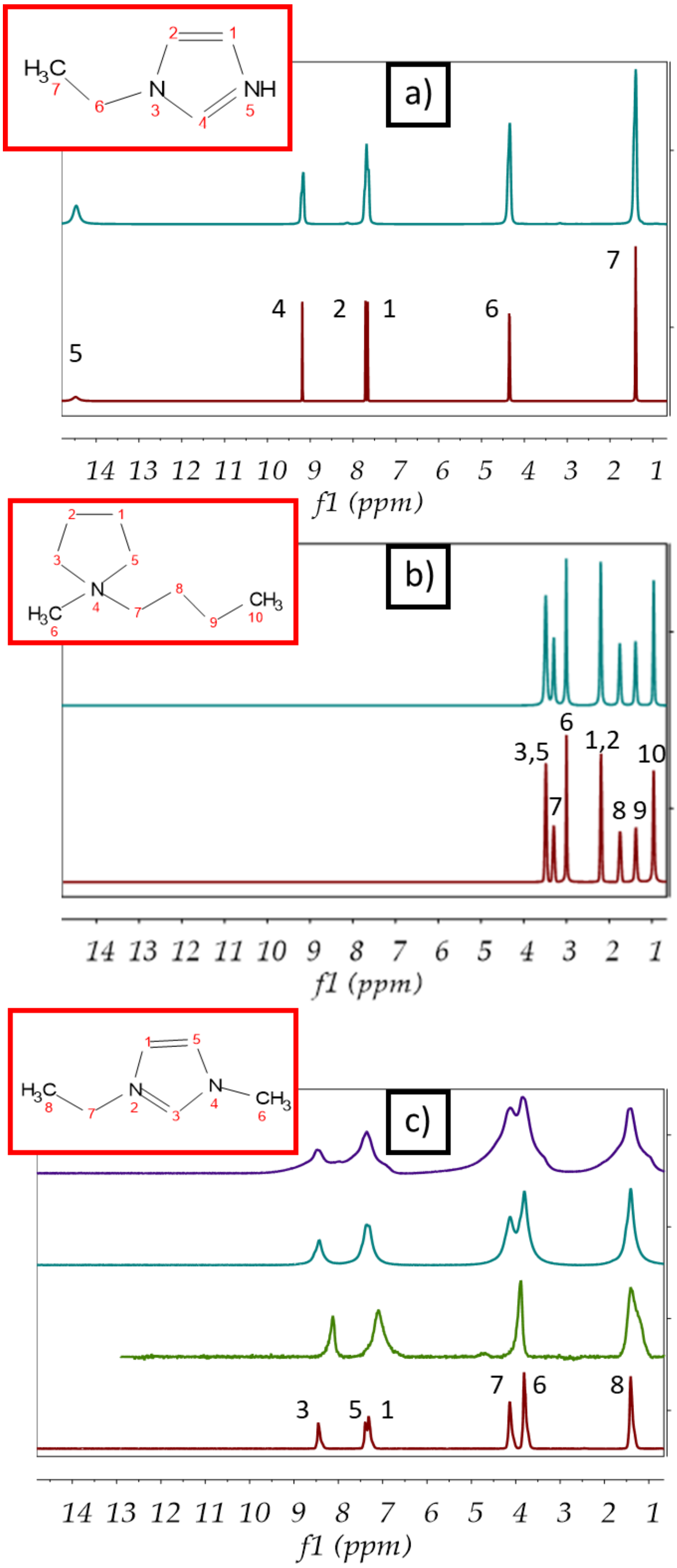

Figure 3.28. ^{1}H NMR spectra of a) [C$_2$Im][NO$_3$] at 313 K in liquid (red line) and ionogel (prepared by EtOH route) (blue line), b) [C$_4$C$_1$Pyrr][TFSI] at 293 K in liquid (red line) and ionogel (prepared by two precursors route) (blue line) and c) [C$_2$C$_1$Im][TFSI] at 293K in liquid (red line), 0.5:[0.3:0.7] ionogel (green line), 0.6:[0.3:0.7] ionogel (green line) and 07:[0.3:0.7] ionogel (purple line).

For all the studied samples, the peaks are presented at the same positions as those in the liquid state and defined enough to consider them as indicative of a liquid-like behavior, except for [C_2C_1Im][TFSI], for which the studied samples show an evident widening for all recorded proton signals. This unusually defined signals for a quasi-solid phase in [C_2Im][NO_3], and specially for [C_4C_1Pyrr][TFSI], were already detected in NMR spectra by Le Bideau and collaborators [21,70], suggesting that the recorded signal is similar to a liquid phase. The broadening of the recorded signals is due to a slowing down in the molecular dynamics of the IL and a difference in the chemical environment of the IL molecules situated in the pore center and those located near the walls of the silica scaffold [71].

Regarding the obtained spectra of [C_2C_1Im][TFSI], the widening of the obtained proton signals increases as the quantity of nanoconfined IL increases as can be seen in Fig. 3.28 d), this is due to a highly reduced mobility of the nanoconfined ions, being close to solid state behavior.

3.3.3.2. Gels of IL +Lithium salt mixtures

With the aim to jointly analyze the effect of salt addition and gelation, mixtures of protic ILs and lithium salt were selected. NMR studies using the high-resolution magic angle spinning (HRMAS) technique were performed in liquid and gel samples (by ethanol route) of pure EAN and mixtures of EAN + $LiNO_3$ at 0.1 m concentration. As mentioned previously, this NMR technique, uncommon and special, makes it possible to achieve liquid-like (i.e., high resolution) spectra from gellified samples [72]. The dramatic increase in resolution obtained with HRMAS NMR applied to gel of EAN can be seen in Fig. 3.29.

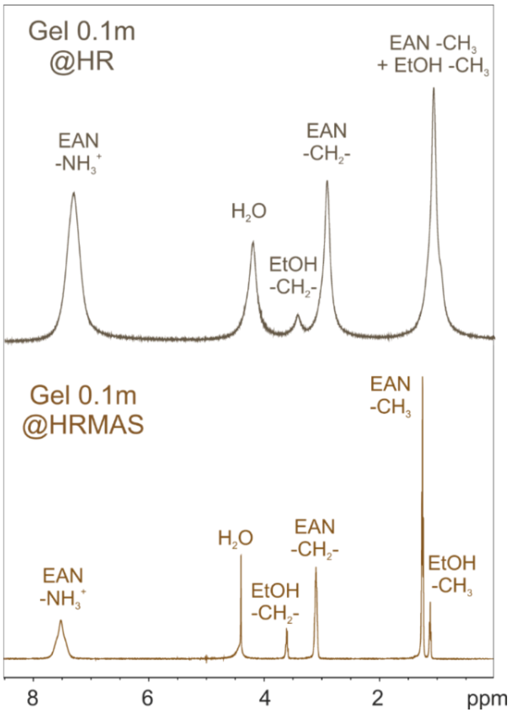

Figure 3.29. 1D ^{1}H spectra of gel of EAN + $LiNO_3$ 0.1m at 305 K obtained by using HR NMR (top) and HRMAS (bottom) NMR (4kHz spin rate).

Figs. 3.30 and 3.31 show the ^1H and ^{13}C spectra for $[C_2Im][NO_3]$ mixtures with lithium salt gel form respectively. For all the samples, except for 0.5 m, a slight slowing down in the molecular dynamics and a difference in the molecular environment between the IL molecules that are in the middle of the pore and those near the walls is observed, and this is associated to peak broadening, which is broader than in liquid state but sharp enough to distinguish the signal without magic angle spinning (MAS) NMR. The peaks appear at a similar position than liquid state but a clear broadening occurs in all signals recorded [71]. For IL + $LiNO_3$ 3 m sample, two additional peaks, corresponding to ethanol impossible to evaporate from the sample, are still present after gelation. This affirmation is corroborated by the NMR ^{13}C spectrum (Fig. 3.31). The most interesting effect after gelation is the broadening of all signal peaks of the $LiNO_3$ 0.5 m sample both ^1H and ^{13}C spectra, this behavior is very close to a solid behavior (due to the important broadening of the recorded signals). This broadening is wide enough to hide some details, such as the signals of peaks 1 and 2, which have been overlapped and it is impossible to distinguish between the two proton signals. So, in this case, the molecular motion of the $[C_2Im]^+$ slows down to a greater extent than in the other samples.

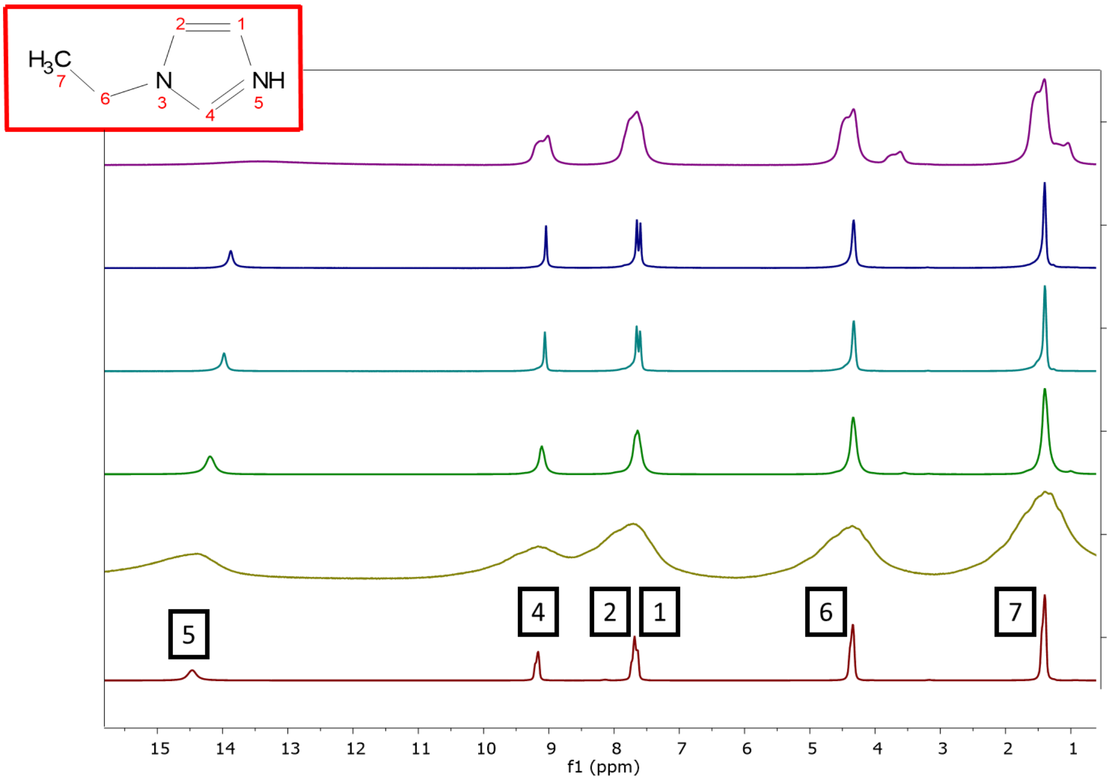

Figure 3.30. ^1H RMN of $[C_2Im][NO_3]$ mixtures with $LiNO_3$ salt at different concentrations (gel form). Pure IL (red line), 0.5 mol·kg^{-1} (yellow line), 1 mol·kg^{-1} (green line), 1.5 mol·kg^{-1} (light blue line), 2 mol·kg^{-1} (dark blue line) and 3 mol·kg^{-1} (purple line).

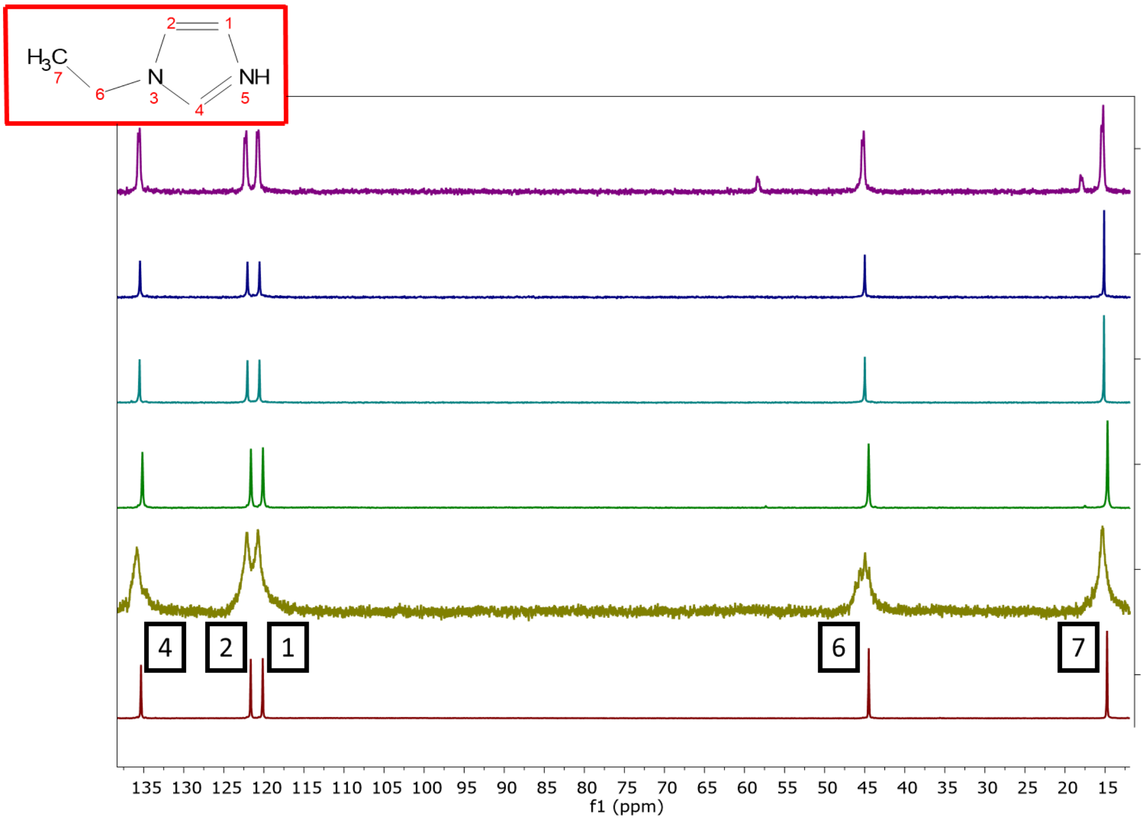

Figure 3.31. ^{13}C NMR of gel mixtures, prepared by EtOH route, of $[C_2Im][NO_3]$ with $LiNO_3$ salt at different concentrations. Pure IL (red line), 0.5 mol·kg^{-1} (yellow line), 1 mol·kg^{-1} (green line), 1.5 mol·kg^{-1} (light blue line), 2 mol·kg^{-1} (dark blue line) and 3 mol·kg^{-1} (purple line). Inset shows the IL cation.

Table 3.14. Peak shift (in ppm) of ^1H spectra and ^{13}C and gel mixtures $[C_2Im][NO_3]$ + $LiNO_3$ salt.

	Sample	*7 (CH_3)*	*6 (CH_2)*	*1 (CH)*	*2 (CH)*	*4(CH)*	*5(NH)*
				^1H spectra			
GEL	***Pure IL***	*1.4 (S)*	*4.34 (S)*	*7.64 (S)*	*7.69 (S)*	*9.16 (S)*	*14.47 (S)*
	Mixture 0.5 m	*1.4 (S)*	*4.35 (S)*	*7.71 (S)*		*9.16 (S)*	*14.37 (S)*
	Mixture 1 m	*1.4 (S)*	*4.34 (S)*	*7.64 (S)*	*7.69 (S)*	*9.11 (S)*	*14.19(S)*
	Mixture 1.5 m	*1.4 (S)*	*4.33 (S)*	*7.60 (S)*	*7.65 (S)*	*9.06 (S)*	*13.98 (S)*
	Mixture 2 m	*1.4 (S)*	*4.33 (S)*	*7.60 (S)*	*7.65 (S)*	*9.04 (S)*	*13.88(S)*
	Mixture 3 m	*1.4 (T)*	*4.30 (Q)*	*7.55 (S)*	*7.64 (S)*	*9.01 (S)*	*UNDEFINED*
				^{13}C spectra			
GEL	***Pure IL***	*17.54*	*47.29*	*124.43*	*122.94*	*138.13*	*X*
	Mixture 0.5 m	*17.54*	*47.23*	*124.32*	*122.76*	*137.84*	*X*
	Mixture 1 m	*17.54*	*47.36*	*124.47*	*122.96*	*138.01*	*X*
	Mixture 1.5 m	*17.54*	*47.38*	*124.45*	*122.96*	*137.92*	*X*
	Mixture 2 m	*17.54*	*47.41*	*124.47*	*122.96*	*137.89*	*X*
	Mixture 3 m	*17.54*	*47.32*	*124.46*	*122.88*	*137.70*	*X*

Table 3.15. Fitted FWHM (in Hz) of ^{1}H and ^{13}C spectra for gel samples shown in Figure 1. For triplet and quadruplet is presented each fitted FWHM of the peak forming multiplet.

	Liquid	*7 (CH_3)*	*6 (CH_2)*	*1 (CH)*	*2 (CH)*	*4 (CH)*	*5(NH)*
	^{1}H spectra						
GEL	***Pure IL.***	*58.89*	*58.87*	*45.31*	*32.57*	*32.79*	*117.76*
	Mixture 0.5m	*468*	*454*	*501*		*501*	*501*
	Mixture 1m	*77.79*	*78.15*	*74.75*	*55.48*	*72.27*	*114.36*
	Mixture 1.5m	*24.31*	*28.67*	*17.83*	*16.31*	*16.12*	*38.37*
	Mixture 2m	*24.5*	*29.38*	*15.25*	*17.33*	*14.2*	*34.3*
	Mixture 3m	*31.81*	*27.31*	*21.12*	*21.72*	*20.93*	*UNDEFINED*
	^{13}C spectra						
GEL	***Pure IL.***	*14.79*	*15.96*	*16.03*	*16.45*	*16.45*	*X*
	Mixture 0.5m	*117*	*246.8*	*155.1*	*241.5*	*183.2*	*X*
	Mixture 1m	*22.7*	*26.7*	*24.5*	*24.5*	*25.1*	*X*
	Mixture 1.5m	*6.2*	*10.6*	*11.3*	*11.3*	*10.6*	*X*
	Mixture 2m	*6.5*	*11.1*	*14.1*	*13.8*	*12.4*	*X*
	Mixture 3m	*14.2*	*11.3*	*10.3*	*10.7*	*16.2*	*X*

Table 3.16. Relative intensity of NH signal versus CH_3 signal proton spectra.

	Sample	I_{N-H}/I_{CH3}
GEL	***Pure IL.***	*0.119*
	Mixture 0.5m	*0.295*
	Mixture 1m	*0.208*
	Mixture 1.5m	*0.205*
	Mixture 2m	*0.202*
	Mixture 3m	*UNDEFINED*

3.3.4. General conclusions for NMR results

As a conclusion for this section, salt addition does not significantly affect the structural arrangement of ILs, but HB networks are perturbed and weakened. This is clearly seen in the labile proton of the protic ILs by up-field shifting of the corresponding signal.

Gelation does not significantly affect the structural arrangement of the IL, but the molecular dynamics are slowed down, and the chemical environment is distorted to a widening of the proton signals. Nevertheless, this widening is not significant enough to consider the nano encapsulated IL as a solid, but the liquid properties inside the silica scaffold are seen to be kept.

3.4. Thermophysical properties

3.4.1. Density and thermal expansion coefficient

3.4.1.1. Pure Ionic Liquids

The initial analysis of the density is a systematic study of the effect of environmental water absorbed by EAN exposed to the open atmosphere, compared to purified EAN by vacuum to eliminate spurious volatiles. This initial evaluation is performed to highlight the importance of the purification step of the ILs.

Density values for dried and water saturated EAN in the temperature range from 288 to 368 K are shown in Fig. 3.32. As can be seen, density decreases linearly (with similar negative slope for pure and saturated water content) with temperature, as can be expected [73,74]. Density values were fitted to the following equation:

$$\rho = a + bT \tag{3.2}$$

Fitting parameters are shown in Table 3.17 indicating that the Eq. (3.2) describes the density of these samples very well. Due to the lowest value of the density of the water, the density of the mixture EAN + water presents lower density than the pure IL as expected. Thus, for example at 298 K, density of EAN shows a decrease of 2.97%, calculated relative to the density values of the dried IL at 298 K.

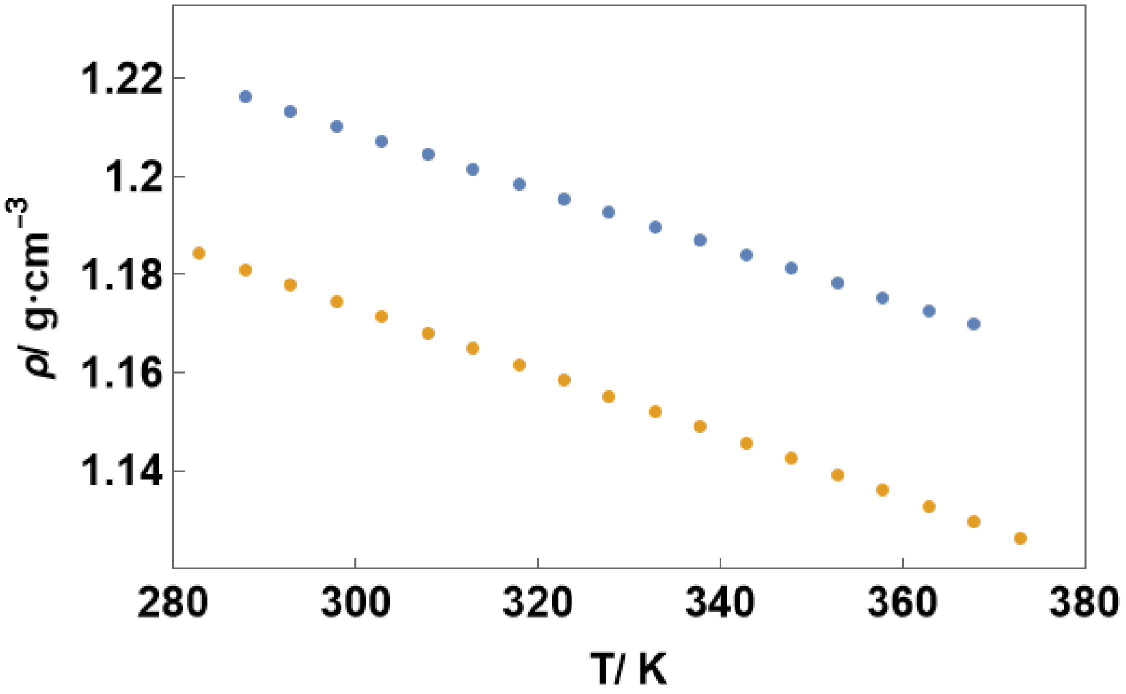

Figure 3.32. Density of pure EAN (blue dots) and EAN saturated water content (orange dots) between 288 and 368 K.

Table 3.17. Linear fitting parameters for density of pure ILs.

	a /g·cm^{-3}	b /g·cm^{-3}·K^{-1}	R^2
EAN	1.3838 ± 0.0005	(5.831 ± 0.017)·10^{-4}	0.9999
EAN saturated	1.36619 ± 0.00019	(6.439 ± 0.009)·10^{-4}	0.99998
[C_2Im][NO_3]	1.4686 ± 0.0006	(6.920 ± 0.017)·10^{-4}	0.99997
[C_4C_1Pyrr][TFSI]	1.6548 ± 0.0002	(8.785 ± 0.006)·10^{-4}	0.999994
[C_2C_1Im][TFSI]	1.8167 ± 0.0003	(10.022 ± 0.008)·10^{-4}	0.999992

From density measurements, the thermal expansion coefficient can be determined as in Eq. (3.3):

$$\alpha_p = -\frac{1}{\rho}\left(\frac{\partial \rho}{\partial T}\right)_p \tag{3.3}$$

Fig. 3.33 presents the values of the thermal expansion coefficient (Eq. (3.3)) for pure and saturated water content IL. Saturated EAN shows higher values of the thermal expansion coefficient than pure IL, indicating a reduction of hydrogen bonds, possibly associated to the fact that the water solvates the anion forming clusters and increasing the coulombic forces in the structure of the ILs [75,76].

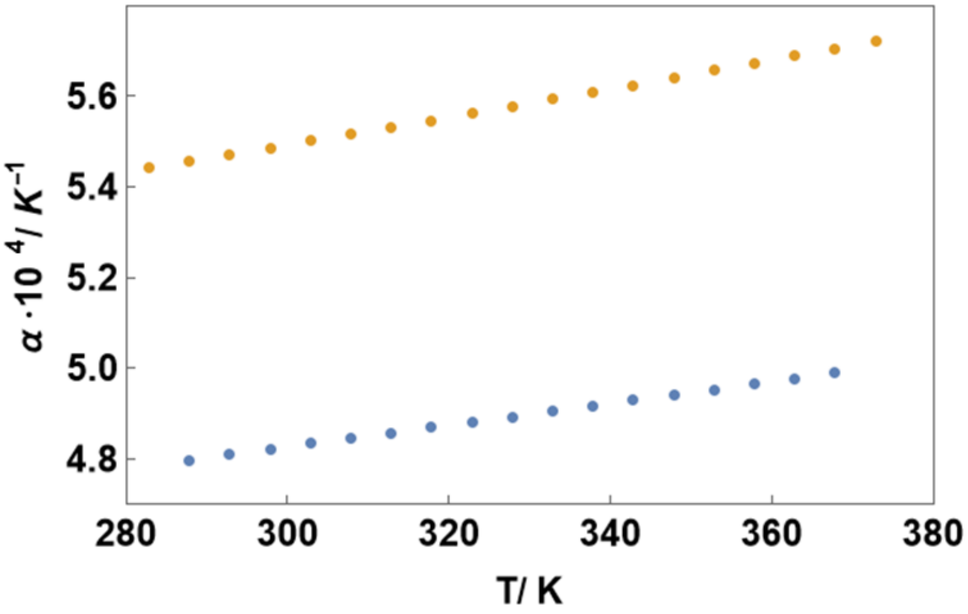

Figure 3.33. Thermal coefficient expansion of pure and water content saturated EAN between 288 and 368 K

Moreover, relatively good agreement with previously reported results can be found for the density of water saturated ILs. Thus, Zarrougui et al. [77] determined the dependence of density for the mixture EAN-water at different molar fractions, obtaining a density value of 1169.4 kg m^{-3} at 298 K for a molar fraction of 0.4210, which is next to our value for saturated EAN of 1174.2 kg m^{-3} (which corresponds to a EAN mole fraction of 0.426). Segade et al. [78] studied mixtures containing alkylammonium nitrates and water at 298.15 K obtaining values of 1163 and 1191 kg m-3 for 0.3394 and 0.6031 molar fractions of EAN, respectively, at the same temperature, in good agreement with our results.

After this preliminary study of the water effect on the density of an IL, the ILs were placed under vacuum to eliminate possible volatile impurities and water.

Density values for EAN, $[C_2Im][NO_3]$, $[C_4C_1Pyr][TFSI]$ and $[C_2C_1Im][TFSI]$ are shown in Fig. 3.34. As can be expected once again, density decreases linearly with increasing temperature for all studied ILs.

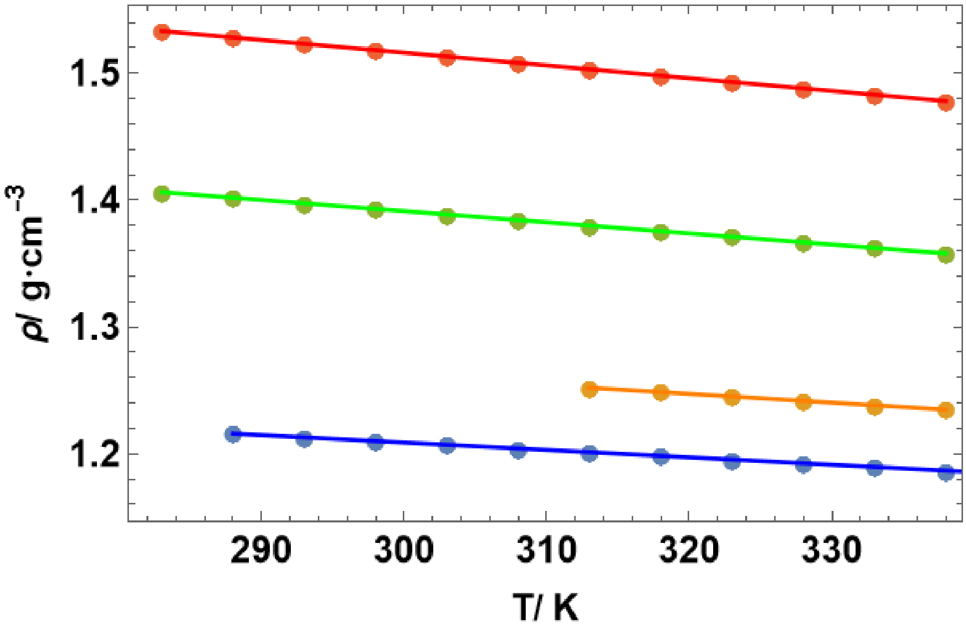

Figure 3.34. Density vs temperature of EAN (blue dots), $[C_2Im][NO_3]$ (orange dots), $[C_4C_1Pyr][TFSI]$ (green dots) and $[C_2C_1Im][TFSI]$ (red dots). Lines represent the obtained linear fitting (Eq. (3.2)).

Density of EAN at 298 K is found as 1210.1 kg·m^{-3} while Canongia et al. found 1212.4 kg·m^{-3} at the same temperature [79], and Zarrougui et al. 1206 kg·m^{-3} [80].

For $[C_2Im][NO_3]$ the density of the pure IL at 313 K is 1.2521 g·cm^{-3}, and no reference values were found in literature, but Rodrigues et al. found the density of $[C_2Im][TFSI]$ to be 1.547 g·cm^{-3} [81], Chen et al reported the $[C_2Im][TFSI]$ density at 313 K as 1.556 g·cm^{-3} [82]. This is in good agreement with the hypothesis that the anion's molecular weight has a strong influence on the density of imidazolium based PILs, where the higher the density, the higher the molecular weight of the anion [83,84].

The density of $[C_4C_1Pyrr][TFSI]$ at 298 K is 1393 kg·m^{-3}, which is also in good agreement with previous results of 1395 kg·m^{-3} [85] and 1394.9 kg·m^{-3} [86]. Similarly, $[C_2C_1Im][TFSI]$ yielded a density of 1518 kg·m^{-3}, while Souckova et. al found 1519.5 kg·m^{-3} [87].

So, the obtained tendency of density for the studied ILs is $[C_2C_1Im][TFSI]$ > $[C_4C_1Pyrr][TFSI]$ > $[C_2Im][NO_3]$ > EAN.

The thermal expansion coefficient gives information about the volumetric behavior with temperature at constant pressure. Fig. 3.35 shows the isobaric coefficient of thermal expansion of the studied samples. As expected, this coefficient increases with increasing temperature, which means that the volumetric expansion increases with temperature, due to the decrease of density.

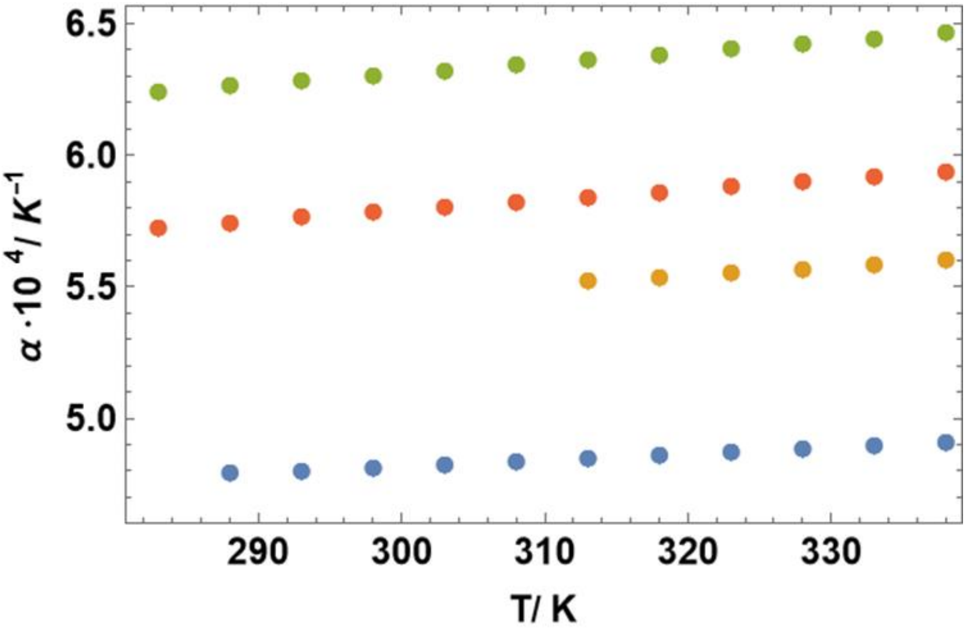

Figure 3.35. Thermal coefficient expansion of EAN (blue dots), [C_2Im][NO_3] (orange dots), [C_4C_1Pyr][TFSI] (green dots) and [C_2C_1Im][TFSI] (red dots).

3.4.1.2 Mixtures of ILs and inorganic salts. Effect of salt addition.

Density of mixtures of [C_2Im][NO_3] with lithium, magnesium and aluminum salt with common anion at different concentrations are shown in Fig. 3.36. [C_4C_1Pyrr][TFSI] mixtures with lithium at different concentrations are presented in Fig. 3.37. Density, once again, decreases linearly with increasing temperature, in the studied temperature range, and increases with salt addition for all studied samples, both protic and aprotic IL, as reported previously [88–92]. The density dependence on salt concentration for [C_2Im][NO_3], 1 molal of Li, Mg and Al nitrate salt are compared at 313 K, whose recorded values are 1.2810 g·cm^{-3}, 1.3141 g·cm^{-3} and 1.3310 g·cm^{-3} respectively. This leaves the trend $\rho_{Al} > \rho_{Mg} > \rho_{Li}$, clearly increasing with increasing molecular weight of added salt.

The density values against temperature were also fitted to a linear equation and the parameters obtained are presented in Table 3.18. Both parameters increase with salt addition.

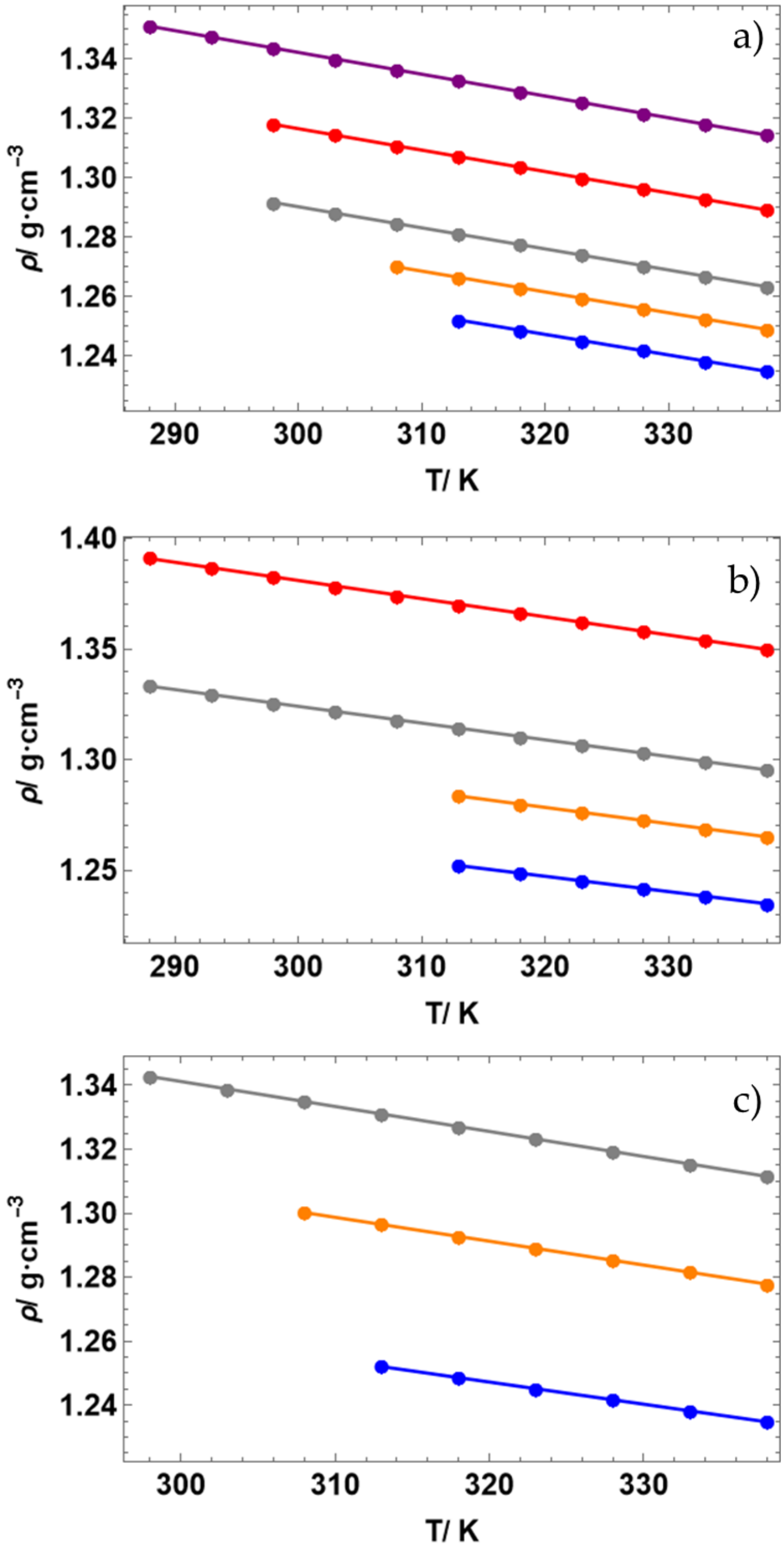

Figure 3.36. Density vs Temperature of a) [C_2Im][NO_3] + $LiNO_3$, b) [C_2Im][NO_3] + $Mg(NO_3)_2$ c) [C_2Im][NO_3] + $Al(NO_3)_3$. Blue dots correspond to the pure IL, orange dots 0.5 mol·Kg^{-1}, gray dots 1 mol·Kg^{-1}, red dots 2 mol·Kg^{-1} and purple dots 3 mol·Kg^{-1} mixtures. Lines represent the linear fitting (Eq. (3.2)).

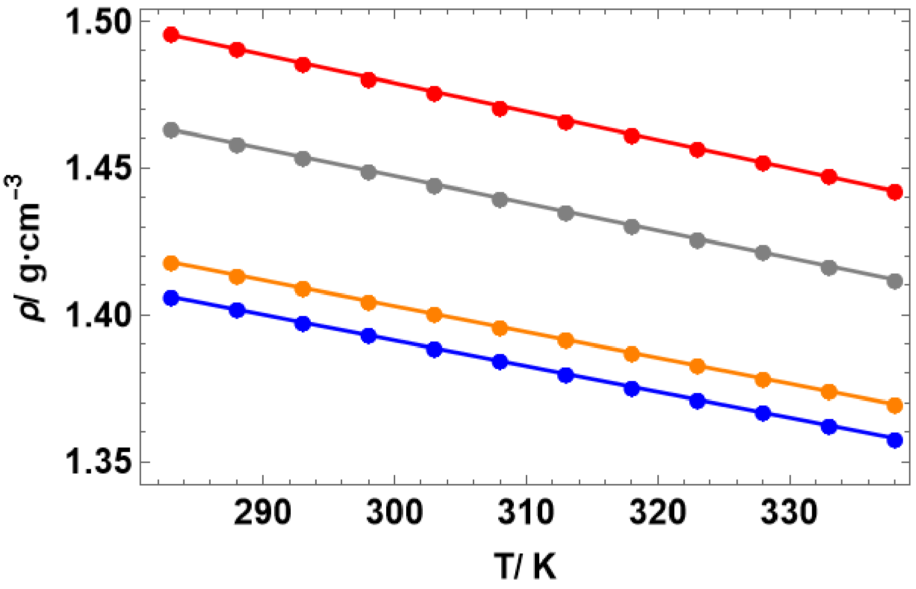

Figure 3.37. Density vs Temperature of $[C_4C_1Pyrr][TFSI]$. Blue dots correspond to the pure IL, orange dots 0.1 mol·Kg^{-1}, gray dots 0.5 mol·Kg^{-1}, red dots 1 mol·Kg^{-1}. Lines represent the linear fitting (Eq. (3.2)).

Table 3.18. Calculated fitting parameters of Eq. (3.2) to the analyzed samples.

Sample	a /g·cm^{-3}	$b \cdot 10^3$ /g·cm^{-3}·K^{-1}	R^2
Pure $[C_2Im][NO_3]$	1.4687 ± 0.0006	-0.6920 ± 0.0017	0.99996
$[C_2Im][NO_3]$ + Li 0.5 m	1.4862 ± 0.0004	-0.7021 ± 0.0012	0.99998
$[C_2Im][NO_3]$ + Li 1 m	1.5032 ± 0.0003	-0.7100 ± 0.0011	0.99998
$[C_2Im][NO_3]$ + Li 2 m	1.5332 ± 0.0003	-0.7223 ± 0.0008	0.99998
$[C_2Im][NO_3]$ + Li 3 m	1.5625 ± 0.0005	-0.7342 ± 0.0017	0.99994
$[C_2Im][NO_3]$ + Mg 0.5 m	1.5152 ± 0.0009	-0.740 ± 0.002	0.99993
$[C_2Im][NO_3]$ + Mg 1 m	1.5511 ± 0.0006	-0.7569 ± 0.0019	0.99993
$[C_2Im][NO_3]$ + Mg 2 m	1.6274 ± 0.0016	-0.821 ± 0.005	0.9996
$[C_2Im][NO_3]$ + Al 0.5 m	1.5299 ± 0.0004	-0.7457 ± 0.0013	0.99998
$[C_2Im][NO_3]$ + Al 1 m	1.5756 ± 0.0002	-0.7813 ± 0.0008	0.999992
Pure $[C_4C_1Pyrr][TFSI]$	1.6548 ± 0.0002	-0.8785 ± 0.0006	0.999994
$[C_4C_1Pyrr][TFSI]$ + Li 0.1 m	1.66742 ± 0.00017	-0.8815 ± 0.0006	0.999995
$[C_4C_1Pyrr][TFSI]$ + Li 0.5 m	1.7263 ± 0.0009	-0.930 ± 0.003	0.9998
$[C_4C_1Pyrr][TFSI]$ + Li 1 m	1.7698 ± 0.0017	-0.969 ± 0.005	0.9997

For a better understanding of the effect of salt addition, Fig. 3.38 (a) shows the density versus salt concentration for EAN mixtures with $LiNO_3$, $Mg(NO_3)_2$, $Ca(NO_3)_2$ and $Al(NO_3)_3$ at room temperature. The same plot can be found in Fig. 3.39 for $[C_2Im][NO_3]$ with $LiNO_3$ and $Mg(NO_3)_2$, and in Fig. 3.40 for $[C_4C_1Pyrr][TFSI]$ with Li TFSI. The mixture $[C_2Im][NO_3]$ + $Al(NO_3)_3$ is not shown because only three concentrations were considered for this study and the fitting procedure wasn't reliable. An increase of density with salt concentration is obtained, and experimental values have been fitted according to Kadyan et al. [93], who proposed a quadratic relation (Eq. (3.4)):

$$\rho = a + b\chi_{salt} + c\chi_{salt}^2 \tag{3.4}$$

Fitting parameters are shown in Table 3.19. Density of EAN and $[C_2Im][NO_3]$ mixtures increases, at constant molar fraction, as the molecular weight and the charge of the salt cation increases. For EAN mixtures with salt the density follows the tendency $\rho_{Al} > \rho_{Ca} \approx \rho_{Mg} > \rho_{Li}$. For $[C_2Im][NO_3]$ the followed trend is $\rho_{Al} > \rho_{Mg} > \rho_{Li}$.

The density vs molar fraction fitting parameters for multivalent salt (Mg^{2+}, Ca^{2+} and Al^{3+}) with EAN seems to not follow a quadratic relation (see error bars of c parameter in Table 3.19). This could be due to the hydrated water present in the nitrate multivalent salts.

Fig. 3.38 b) and c) shows the velocity of sound (VOS) and the adiabatic compressibility of the studied samples, respectively. Adiabatic compressibility is obtained by the well-known Laplace equation (Eq. (3.5)):

$$k_s = \frac{1}{\rho v^2}, \tag{3.5}$$

where v is the VOS. The adiabatic compressibility decreases with the valency of the salt cation, indicating that the addition of those salts with cations of larger valences leads to more densely packed and more compact mixtures. This effect is more pronounced the larger the valency and comes from the formation of compact ionic clusters. Moreover, as was previously reported [94], the network of directed hydrogen bonds in EAN is more strongly distorted the greater the charge density of the salt cations, which leads to a stronger molecular reorientation that breaks the liquid network of hydrogen bonds inducing a structural transition in the mixture which makes it more compact and difficult to be compressed.

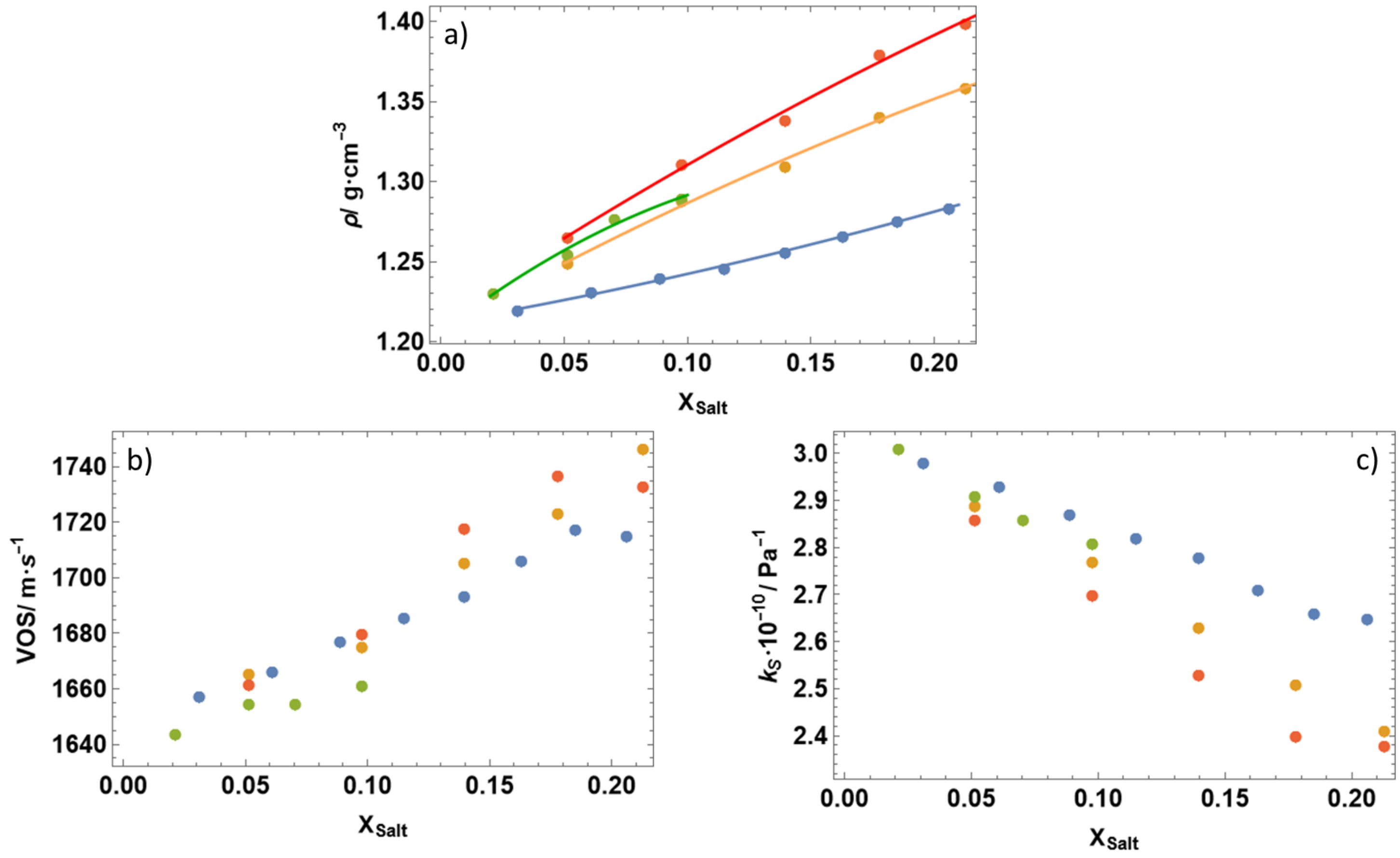

Figure 3.38. Concentration dependence (molar fraction) of the density (a), the speed of sound (b) and the adiabatic compressibility of (c) EAN mixtures with $LiNO_3$ (blue dots), $Mg(NO_3)_2$ (orange dots), $Ca(NO_3)_2$ (green dots) and $Al(NO_3)_3$ red dots) at 298.15K. Lines in the density plot correspond to quadratic fit (Eq. (3.4)). Supersaturated values are shown for Li, Mg and Al mixtures.

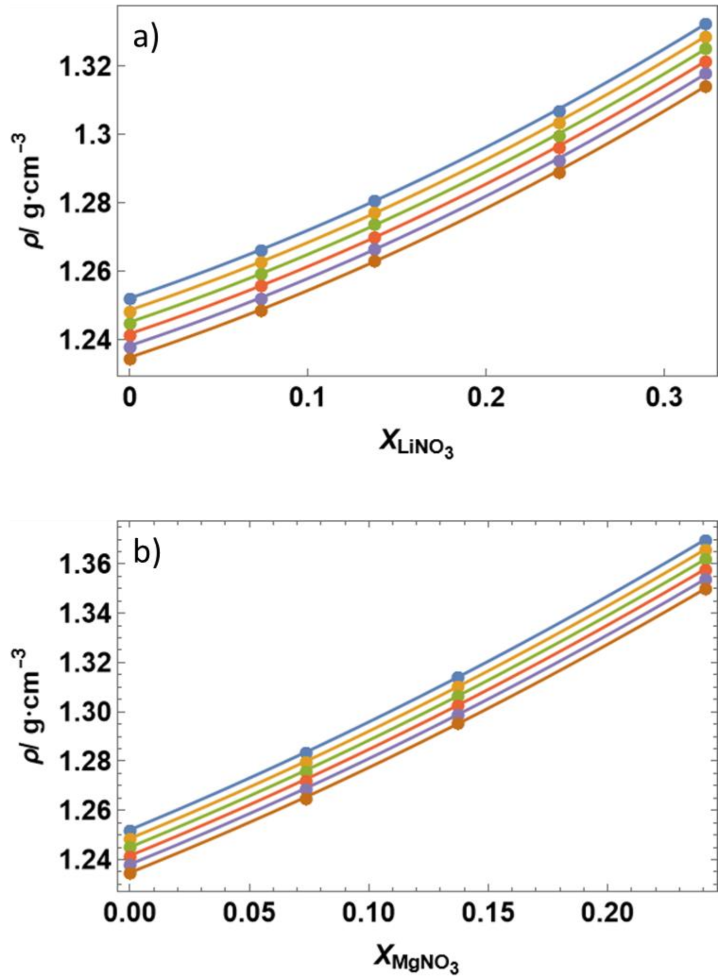

Figure 3.39. Density vs salt concentration of of a) [C_2Im][NO_3] + $LiNO_3$, b) [C_2Im][NO_3] + $Mg(NO_3)_2$. Blue dots represent 313 K, orange dots 318 K, green dots 323 K, red dots 328 K, purple dots 333 K and brown 338 K. Lines represent the quadratic fitting (Eq. (3.4)) at a constant temperature.

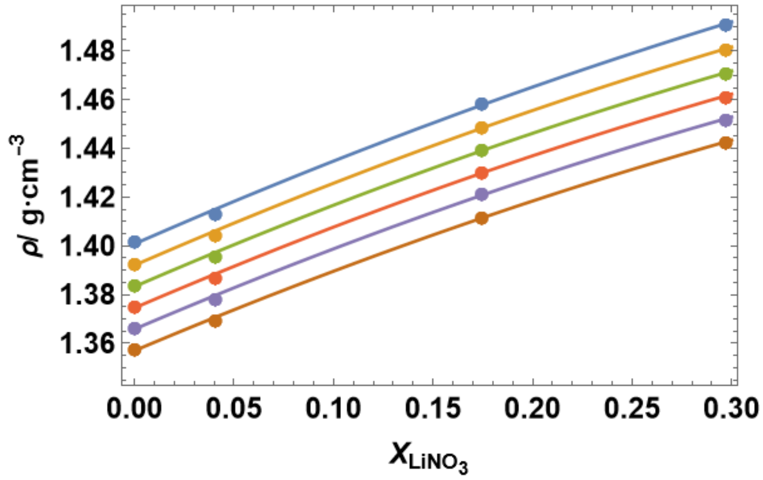

Figure 3.40. Density vs salt concentration of [C_4C_1Pyrr][TFSI] + Li TFSI. Blue dots represent 288 K, orange dots 298 K, green dots 308 K, red dots 318 K, purple dots 328 K and brown 338 K. Lines represent the quadratic fitting (Eq. (3.4)) at a constant temperature.

Table 3.19. Obtained fitting values of Eq. (3.4) to the analyzed samples

	a / *g·cm*$^{-3}$	*b* / *g·cm*$^{-3}$	*c* / *g·cm*$^{-3}$	*R*^{2}
EAN + Li(NO_3)	1.212 ± 0.002	0.26 ± 0.04	0.41 ± 0.16	0.999999
EAN +Mg(NO_3)$_2$	1.208 ± 0.011	0.86 ± 0.19	-0.7 ± 0.7	0.999995
EAN + Ca(NO_3)$_2$	1.206 ± 0.012	1.2 ± 0.44	-3 ± 3	0.999996
EAN + Al(NO_3)$_3$	1.215 ± 0.015	1.0 ± 0.25	-0.7 ± 0.9	0.999993
[C_2Im][NO_3] + LiNO_3				
313 K	1.2522 ± 0.0005	0.176 ± 0.007	0.22 ± 0.02	0.999999
318 K	1.2487 ± 0.0004	0.176 ± 0.007	0.22 ± 0.02	0.999999
323 K	1.2452 ± 0.0005	0.176 ± 0.007	0.22 ± 0.02	0.999999
328 K	1.2418 ± 0.0004	0.174 ± 0.007	0.22 ± 0.02	0.999999
333 K	1.2383 ± 0.0004	0.174 ± 0.007	0.22 ± 0.02	0.999999
338 K	1.2349 ± 0.0005	0.173 ± 0.007	0.22 ± 0.02	0.999999
[C_2Im][NO_3] + Mg(NO_3)$_2$				
313 K	1.25209 ± 0.00006	0.4013 ± 0.0012	0.365 ± 0.004	0.999999
318 K	1.24856 ± 0.00015	0.398 ± 0.003	0.370 ± 0.012	0.999999
323 K	1.2450 ± 0.0002	0.397 ± 0.005	0.368 ± 0.018	0.999999
328 K	1.2416 ± 0.0003	0.394 ± 0.007	0.370 ± 0.03	0.999999
333 K	1.2381 ± 0.0004	0.392 ± 0.008	0.370 ± 0.03	0.999999
338 K	1.2347 ± 0.0004	0.389 ± 0.008	0.370 ± 0.03	0.999999
[C_4C_1Pyrr][TFSI] + Li TFSI				
288 K	1.4008 ± 0.0017	0.36 ± 0.03	-0.18 ± 0.11	0.999998
298 K	1.3920 ± 0.0016	0.36 ± 0.03	-0.19 ± 0.11	0.999998
308 K	1.3833 ± 0.0016	0.36 ± 0.03	-0.20 ± 0.10	0.999998
318 K	1.3745 ± 0.0015	0.35 ± 0.03	-0.20 ± 0.10	0.999998
328 K	1.3658 ± 0.0015	0.35 ± 0.03	-0.20 ± 0.10	0.999998
338 K	1.3570 ± 0.0014	0.35 ± 0.03	-0.19 ± 0.09	0.999999

Figure 3.41 and 3.42 shows the isobaric coefficient of thermal expansion (Eq. (3.3)) of the mixtures of [C_2Im][NO_3] + nitrate salts and [C_4C_1Pyrr][TFSI] + LiTFSI salt, respectively. A different behavior can be found for the different IL mixtures. Thus, for mixtures of [C_2Im][NO_3] + LiNO_3 (Fig. 3.41 a) and considering the uncertainties of the results, the thermal expansion coefficient is practically independent of the concentration of the lithium salt of these mixtures, as demonstrated by V. Gómez-González and coworkers through the unaltered molecular volume of a mixture IL-salt [95]. Nevertheless, in mixtures of [C_2Im][NO_3] with the divalent (magnesium) and trivalent (aluminum) salts, the thermal expansion coefficient clearly increases with the concentration of the salt, probably due to the presence of hydrated water in salts that cannot evaporate after vacuum procedure. Finally, for the aprotic IL, [C_4C_1Pyrr][TFSI], mixture with the LiTFSI

salt (Fig. 3.42) the behavior is the opposite, the thermal expansion coefficient decreases as salt concentration increases.

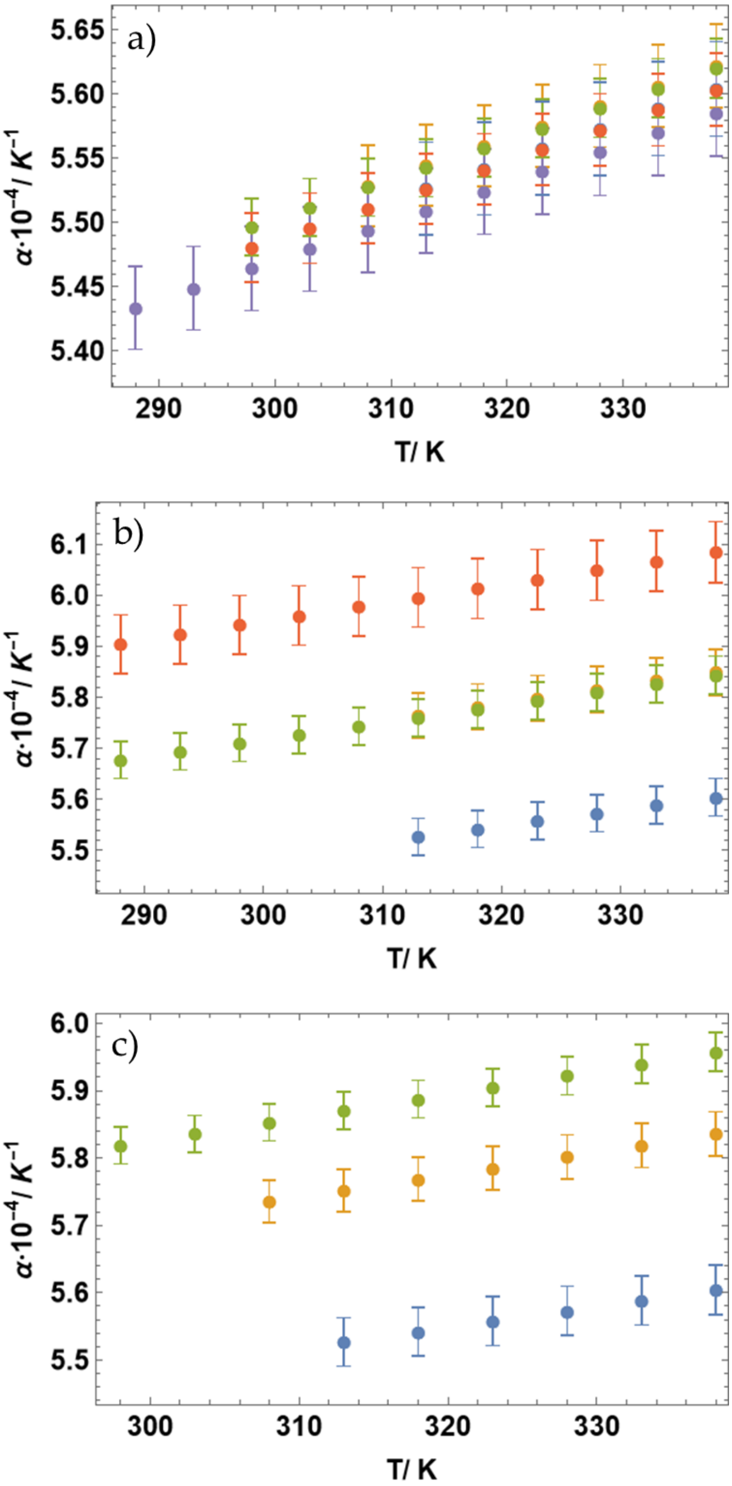

Figure 3.41. Thermal Expansion of a) $[C_2Im][NO_3]$ + $LiNO_3$, b) $[C_2Im][NO_3]$ + $Mg(NO_3)_2$ c) $[C_2Im][NO_3]$ + $Al(NO_3)_3$. Blue dots represent pure compound, orange dots 0.5 mol·Kg^{-1} salt addition, green dots 1 mol·Kg^{-1}, red dots 2 mol·Kg^{-1} and purple dots 3 mol·Kg^{-1}.

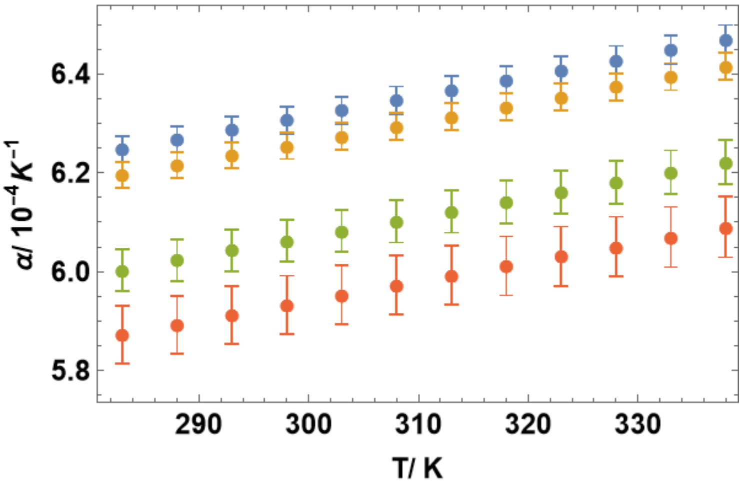

Figure 3.42. Thermal Expansion of [C_4C_1Pyrr][TFSI] + LiTFSI mixtures. Blue dots represent pure IL, orange dots 0.1 mol·Kg^{-1} salt addition, green dots 0.5 mol·Kg^{-1} and red dots 1 mol·Kg^{-1}.

3.4.2. Viscosity

3.4.2.1. Pure Ionic liquids

As with the density study, a comparison between dried and water content saturated EAN was performed first to analyze the water effect on the ionic liquid viscosity.

Two experimental techniques were used for this study, Anton Paar Stabinger SVM3000 and a rheometer from TA Instruments model AR 2000, as mentioned in the materials and methods section.

Fig. 3.43 shows the temperature dependence of the dynamic viscosity. Small discrepancies were found between the rheometer and the Stabinger viscometer probably because both samples have different water contents attributed to differences in measuring conditions. Although to reduce the absorption of water from the environment during the rheometer measurement, the measurements were taken in the ambient atmosphere and the inert conditions were not achieved, water absorption was minimized by covering the sample during the measurement. In the viscometer the sample is kept in a closed tube, preventing water absorption during the measurement.

As it can be seen in Fig. 3.43, the largest differences were obtained for water saturated EAN. The effect of water is much less important at high temperatures (low viscosities), as was previously pointed out by Jacquemin et al. [96]. The differences for water saturated EAN with the two used experimental techniques are probably due to fluctuations in the water content on the saturated samples, which can easily change with small alterations on environmental humidity. In the case of purified samples, the differences between the two experimental techniques are much smaller and decrease as the temperature increases.

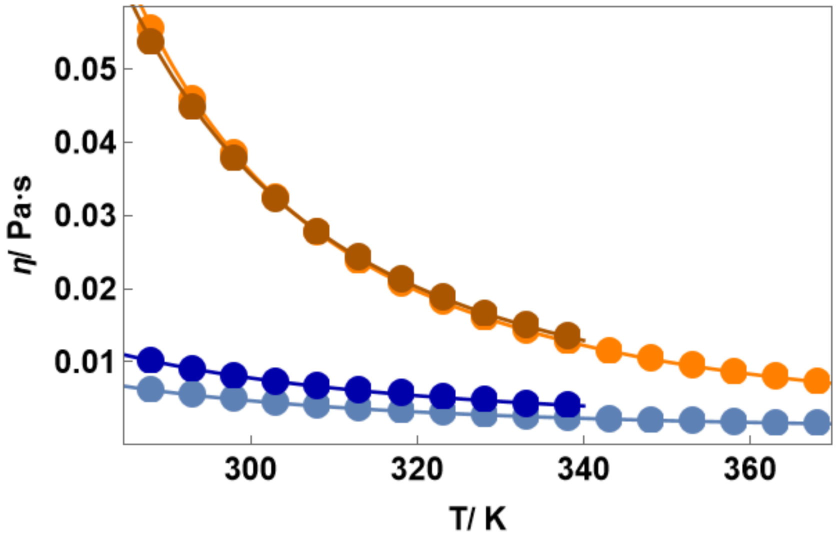

Figure 3.43. Comparison of dynamic viscosities obtained from viscosimeter (lighter dots) and rheometer (darker dots) experiments for dried (orange) and water saturated (blue) EAN. Lines represent the corresponding VFT fitting.

Several studies in the literature, comprising protic and aprotic ILs, show that these fluids do not follow Arrhenius law, due to the glass forming of ILs, including their mixtures with water [97]. As is well known [98], the Vogel-Fulcher-Tamman equation, (Eq. (3.6)) (also known as VFT), is the best approximation to describe the transport properties of the majority of ILs:

$$\eta = \mathrm{A} \cdot \exp\left(\frac{B}{T-C}\right), \tag{3.6}$$

where $A = \eta_0$ (the viscosity at infinitum temperature), $B = \frac{E_a}{R} = \frac{E'_a}{k_B}$, where the activation energy can be given in J·mol^{-1} (E_a) or in eV per particle (E'_a) and $C = T_g$ (the ideal glass transition temperature). These are fitting parameters summarized in Table 3.20. R is the ideal gas constant and k_B the Boltzmann constant.

Table 3.20. Fitting parameters of experimental viscosity data (RHEO: rheometer, STAB: Stabinger) of the studied ILs to Vogel-Fulcher-Tamman (Eq. (3.6)) and those reported in Canongia-Lopes et al. for dried samples [99].

		$H_0 \pm s(\eta_0)$/mPa·s	*$E_a \pm s(E_a)$ /J mol^{-1}*	*$T_g \pm s(T_g)$ /K*	*R^2*
EAN	*RHEO*	*0.285± 0.016*	*6050 ± 140*	*149 ± 2*	*0.99993*
	STAB	*0.2061 ± 0.0087*	*6157 ±115*	*148 ± 1*	*0.9994*
	Canongia	*0.2199*	*6362*	*148.5*	
EAN SAT	*RHEO*	*0.19 ± 0.13*	*5580 ± 2169*	*119 ± 36*	*0.999992*
	STAB	*0.063 ± 0.019*	*7167 ±1046*	*100 ± 15*	*0.99994*

The dynamic viscosity of pure EAN, [C_2Im][NO_3], [C_4C_1Pyrr][TFSI] and [C_2C_1Im][TFSI] is shown in Fig. 3.44. The viscosity dependence with temperature was fitted with VFT (Eq. (3.6)), and the resulting parameters can be found in Table 3.21.

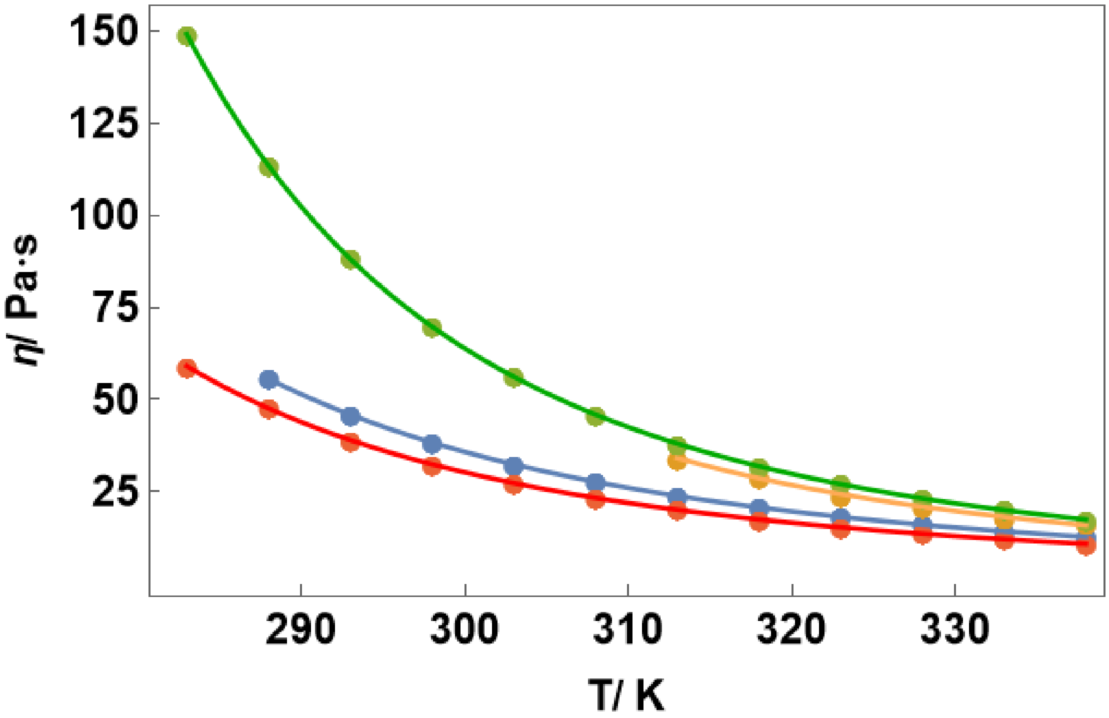

Figure 3.44. Dynamic viscosity of EAN (blue dots), [C_2Im][NO_3] (orange dots), [C_4C_1Pyr][TFSI] (green dots) and [C_2C_1Im][TFSI] (red dots). Lines represent the corresponding VFT fitting.

Table 3.21. Fitting parameters to Eq. (3.6) of experimental dynamic viscosity data of the pure ILs.

	η_0 /mPa·s	$E_a \cdot 10^{-3}$ /eV	T_0 /K	R^2
EAN	0.189 ± 0.018	70 ± 3	145 ± 3	0.999996
[C_2Im][NO_3]	0.28 ± 0.05	50 ± 40	180 ± 60	0.9998
[C_4C_1Pyrr][TFSI]	0.165 ± 0.006	70.1 ± 0.8	163.5 ± 0.8	0.999999
[C_2C_1Im][TFSI]	0.266 ± 0.002	56.0 ± 0.2	162.8 ± 0.3	0.99999

No previous results for dynamic viscosity of [C_2Im][NO_3] were found in the literature. Nevertheless, comparing our measured value for pure IL dynamic viscosity at 313 K, 38.848 mPa·s., with results reported by Rodrigues et. al. [81] for the IL [C_2Im][TFSI] at the same temperature, 32.014 mPa·s, the difference between both can be explained considering that the labile proton of the [C_2Im] forms strong hydrogen bonds with oxygen atoms from nitrate anions which increases the viscosity. Seddon et al. [100] presents a dynamic viscosity value of 33.8 mPa·s for the IL [C_2C_1Im][NO_3] at 313K, which is still lower than that obtained for this work, reinforcing the idea that the labile proton of the PILs form stronger hydrogen bonds than the AILs.

For [C_4C_1Pyrr][TFSI] the obtained dynamic viscosity at 298 K is 69.74 mPa·s and Zarrougui et al. reported 68.1 mPa·s [101], while Warminska and coworkers [102] found a dynamic viscosity for this IL of 70.124 mPa·s.

With regard to $[C_2C_1Im][TFSI]$, Tariq and coworkers [103] reported a dynamic viscosity at 298 K of 33 mPa·s , similar to Seki and coworkers [104], who obtained 32.7 mPa·s, both in good agreement with our result at this temperature (32.423 mPa·s).

Finally, from the comparison of the results of the dynamic viscosity of the four measured pure ILs the following trend is obtained:

$$\eta_{EAN} > \eta_{[\mathrm{C_4C_1Pyrr}][\mathrm{TFSI}]} > \eta_{[\mathrm{C_2Im}][\mathrm{NO_3}]} > \eta_{[\mathrm{C_2C_1Im}][\mathrm{TFSI}]}.$$

3.4.2.2. Effect of salt addition on viscosity.

Below, the main results for the dynamic viscosities of the IL + salt mixtures are shown. Firstly the nitrate anion based ILs + nitrate salt mixtures will be analyzed, and finally the $[C_4C_1Pyrr][TFSI]$ + Li TFSI mixture will also be studied and compared with previous mixtures.

Figs. 3.45, 3.46 and 3.47 show the dynamic viscosities of mixtures of EAN with lithium, magnesium, calcium and aluminum nitrate, mixtures of $[C_2Im][NO_3]$ with lithium, magnesium and aluminum nitrate and mixture of $[C_4C_1Pyrr][TFSI]$ + Li TFSI for different salt concentrations, respectively. This property decreases with increasing temperature and increases with salt concentration for all studied systems IL+ Salt.

The VFT model well describes dependence of IL viscosity-temperature (Eq. (3.6)) [105,106], and this is the case of the mixtures here studied (see Table 3.22), although the model used to fit the mixtures of EAN with the multivalent salts (magnesium, calcium and aluminum nitrate) is Arrhenius' law. This is probably due to large differences between the studied temperature range and the ideal glass transition temperature of the sample. In these cases, the VFT law leads to Arrhenius' law. In other words, these discrepancies in the temperature dependence between EAN with multivalent salts mixtures and the other ILs mixtures could be due to a large decrease of the Vogel temperature (or ideal glass transition as introduced before) with the multivalent salt addition which causes the behavior of VFT not to be observed in the studied temperature range.

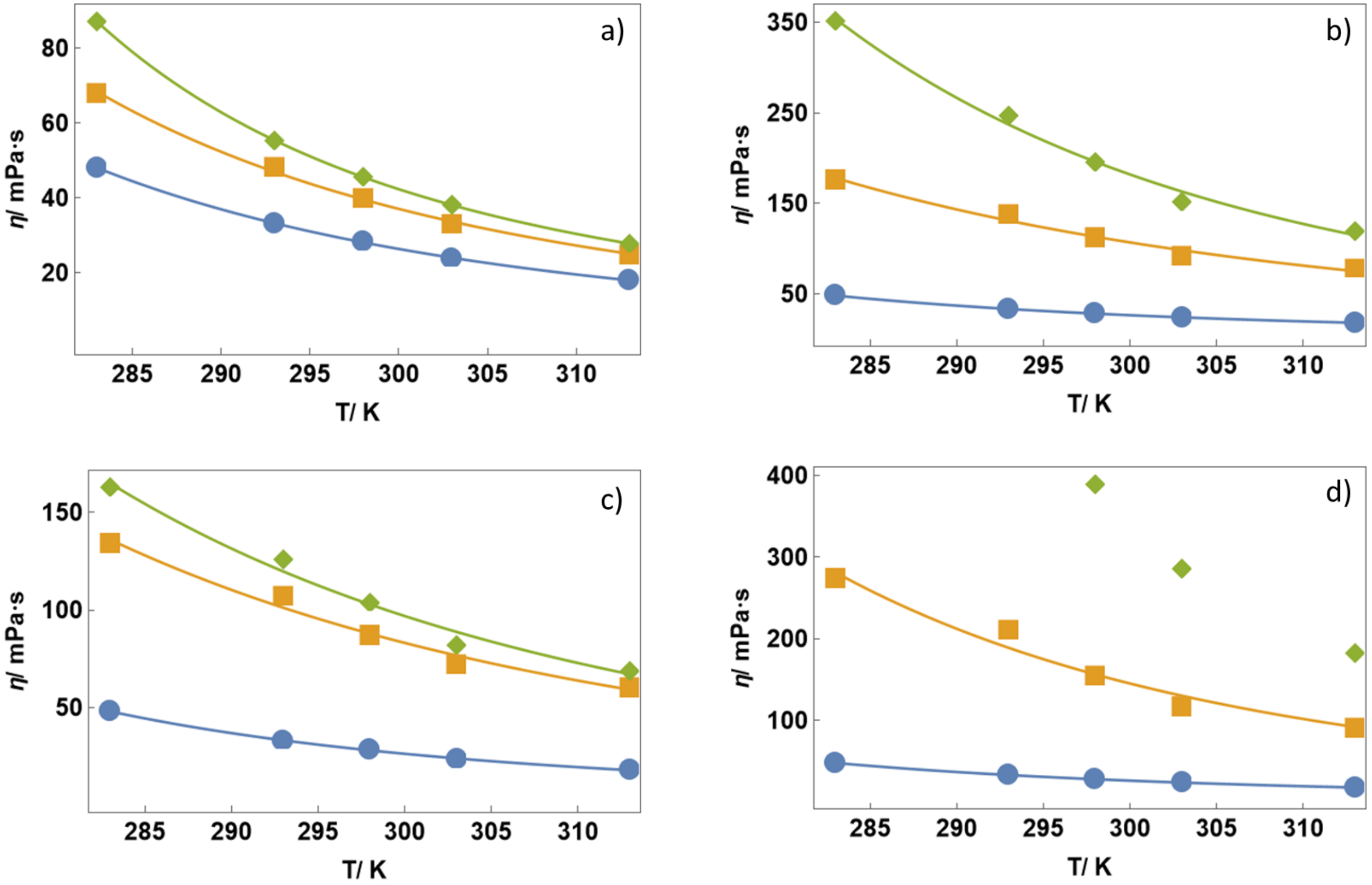

Figure 3.45. EAN+ nitrate salt mixtures: a) Lithium Nitrate salt (Blue dots pure EAN, orange squares 1 mol·kg^{-1} and green diamonds 2 mol·kg^{-1}), b) Magnesium Nitrate salt (Blue dots pure EAN, orange dots 1.5 mol·kg^{-1} and green dots 2.5 mol·kg^{-1}), c) Calcium Nitrate salt (Blue dots pure EAN, orange dots 0.5 mol·kg^{-1} and green dots 1 mol·kg^{-1}) and d) Aluminum Nitrate (Blue dots pure EAN, orange dots 1.5 mol·kg^{-1} and green dots 2.5 mol·kg^{-1}). Lines represent the corresponding fitting (VFT for lithium salts and Arrhenius for multivalent salts).

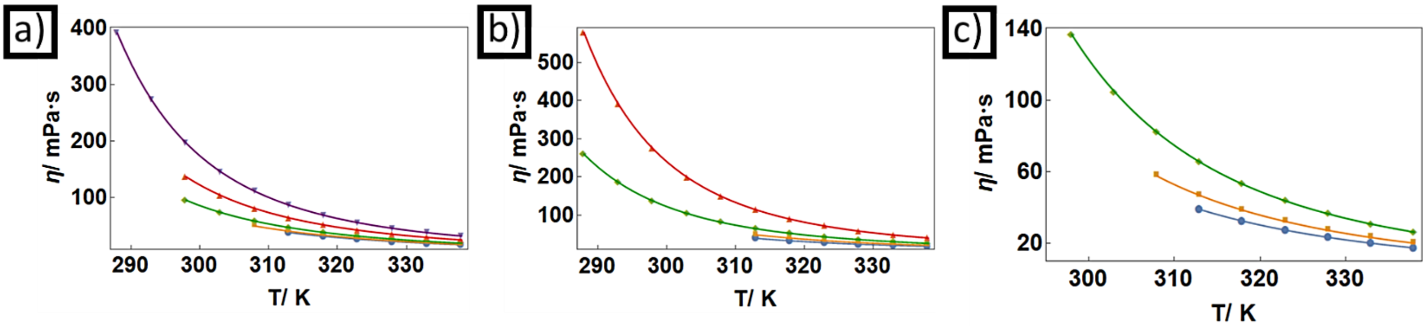

Figure 3.46. Viscosity of a) $[C_2Im][NO_3] + LiNO_3$, b) $[C_2Im][NO_3] + Mg(NO_3)_2$ c) $[C_2Im][NO_3] + Al(NO_3)_3$. Blue dots represent pure compound, orange dots 0.5 mol·Kg^{-1} salt addition, green dots 1 mol·Kg^{-1}, red dots 2 mol·Kg^{-1} and purple dots 3 mol·Kg^{-1}. Lines represent the corresponding VFT fitting.

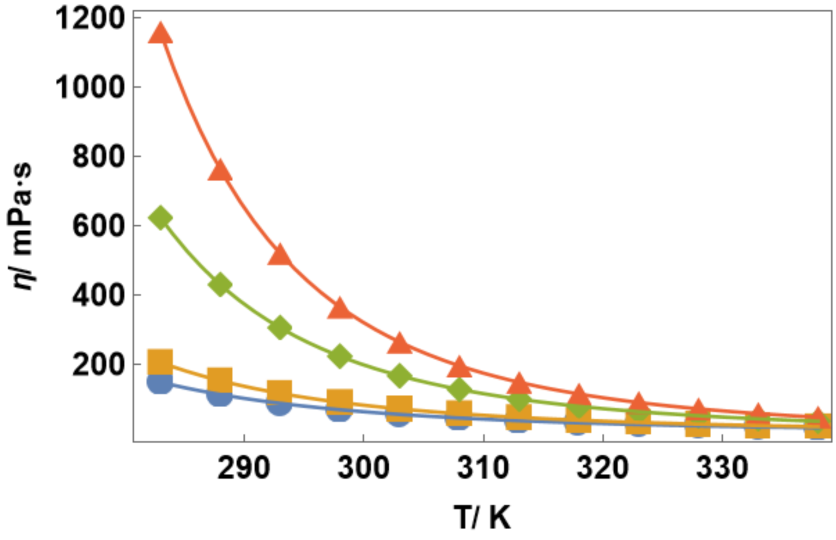

Figure 3.47. Viscosity of $[C_4C_1Pyrr][TFSI]$ + Li TFSI. Blue dots represent pure compound, orange dots 0.1 mol·Kg^{-1} salt addition, green dots 0.5 mol·Kg^{-1} and red dots 1 mol·Kg^{-1}. Lines represent the corresponding VFT fitting.

Table 3.22. Fitting parameters of viscosity of IL + Nitrate salts to VFT equation.

EAN + Li salt (VFT fitting)

	η_0 /mPa·s	*$E_a \cdot 10^{-3}$ /eV*	*T_0*	*R^2*
Pure EAN	*0.12 ± 0.17*	*80 ± 40*	*130 ± 40*	*0.99992*
EAN + $LiNO_3$ 1m	*0.14 ± 0.06*	*80 ± 30*	*130 ± 70*	*0.9993*
EAN + $LiNO_3$ 2m	*0.71 ± 0.11*	*40 ± 3*	*187 ± 4*	*0.999996*

EAN + Mg, Ca and Al salts (Arrhenius fitting)

	η_0 /mPa·s	*$E_a \cdot 10^{-3}$ /eV*	*R^2*
EAN + $Mg(NO_3)_2$ 1.5 m	*0.021 ± 0.014*	*220 ± 17*	*0.997*

EAN + $Mg(NO_3)_2$ 2.5 m	*0.0028 ± 0.0017*		*286 ± 15*	*0.998*
EAN + $Ca(NO_3)_2$ 0.5 m	*0.023 ± 0.015*		*211 ± 17*	*0.997*
EAN + $Ca(NO_3)_2$ 1 m	*0.014 ± 0.010*		*229 ± 18*	*0.997*
EAN + $Al(NO_3)_3$ 1.5 m	*0.002 ± 0.003*		*284 ± 30*	*0.992*
$[C_2Im][NO_3]$ + Li, Mg and Al salts (VFT fitting)				
	η_0 /mPa·s	*$E_a \cdot 10^{-3}$ /eV*	*T_0*	*R^2*
Pure $[C_2Im][NO_3]$	*0.18 ± 0.02*	*66 ± 2*	*171 ± 3*	*1*
$[C_2Im][NO_3]$ + Li salt 0.5m	*0.13 ± 0.03*	*75 ± 6*	*161 ± 7*	*0.999997*
$[C_2Im][NO_3]$ + Li salt 1m	*0.297 ± 0.002*	*54.40 ± 0.14*	*188.72 ± 0.16*	*1*
$[C_2Im][NO_3]$ + Li salt 2m	*0.31 ± 0.02*	*56.2 ± 1.4*	*191.1 ± 1.5*	*0.999998*
$[C_2Im][NO_3]$ + Li salt 3m	*0.323 ± 0.008*	*57.1 ± 0.5*	*194.6 ± 0.4*	*0.999999*
$[C_2Im][NO_3]$ + Mg salt 0.5m	*0.22 ± 0.02*	*62 ± 3*	*179 ± 3*	*1*
$[C_2Im][NO_3]$ + Mg salt 1m	*0.307 ± 0.002*	*55.47 ± 0.14*	*192.50 ± 0.13*	*1*
$[C_2Im][NO_3]$ + Mg salt 2m	*0.303 ± 0.002*	*59.29 ± 0.12*	*196.94 ± 0.11*	*1*
$[C_2Im][NO_3]$ + Al salt 0.5m	*0.21 ± 0.03*	*62 ± 3*	*179 ± 3*	*0.999999*
$[C_2Im][NO_3]$ + Al salt 1m	*0.241 ± 0.010*	*62.2 ± 0.9*	*184.1 ± 0.9*	*0.999999*
$[C_4C_1Pyrr][TFSI]$ + Li salt (VFT fitting)				
	η_0 /mPa·s	*$E_a \cdot 10^{-3}$ /eV*	*T_0 /K*	*R^2*
Pure $[C_4C_1Pyrr][TFSI]$	*0.165 ± 0.006*	*70.1 ± 0.8*	*163.5 ± 0.8*	*0.999999*
$[C_4C_1Pyrr][TFSI]$ + Li TFSI 0.1 m	*0.172 ± 0.003*	*70.1 ± 0.3*	*168.0 ± 0.3*	*1*
$[C_4C_1Pyrr][TFSI]$ + Li TFSI 0.5 m	*0.126 ± 0.005*	*80.2 ± 0.9*	*173.5 ± 0.7*	*0.999999*
$[C_4C_1Pyrr][TFSI]$ + Li TFSI 1 m	*0.101 ± 0.006*	*85.8 ± 1.1*	*176.4 ± 0.8*	*0.999999*

Although ILs are glass formers and, therefore VFT describes viscosity behavior very well, if the temperature range is much higher than the ideal glass transition temperature, an Arrhenius approximation can be performed to understand the effect of the salt addition on the viscosity and its thermodynamic activation parameters. In this approximation, proposed by Mukherjee et al. [107], the viscosity can be written as Eq. (3.7), ΔG^* being the activation energy for the viscous flow, and the thermodynamic relationship between the Gibbs free energy and the enthalpy (ΔH^*) and the entropy (ΔS^*) [107]:

$$\eta = \left(\frac{hN}{v}\right) e^{\frac{\Delta G^*}{RT}} = \left(\frac{hN}{v}\right) e^{\frac{\Delta H^*}{RT}} e^{-\frac{\Delta S^*}{R}}, \qquad (3.7)$$

where h, N and v are Planck's constant, Avogadro number and the molar volume calculated as $v = \frac{M_w}{\rho}$, respectively.

$$ln\,\eta = \left\{ln\left(\frac{hN}{v}\right) - \frac{\Delta S^*}{R}\right\} + \frac{\Delta H^*}{RT}. \qquad (3.8)$$

The derivative of Eq. (3.8) vs temperature can be written as

$$\frac{d\,ln\,\eta}{dT} = -\frac{\Delta H^*}{RT^2}. \qquad (3.9)$$

Focusing our attention on Fig. 3.48, the natural logarithm of the viscosity can be fitted by a quadratic function as in Eq. (3.10), where the obtained fitting parameters can be found in Table 3.23

$$ln\,\eta = a + bT + cT^2. \qquad (3.10)$$

Combining Eq. (3.9) and (3.10), the enthalpy can be written as:

$$\Delta H^* = -RT^2(b + 2cT). \qquad (3.11)$$

On the other hand, the heat capacity change is obtained as:

$$\Delta C_p^* = \frac{d\Delta H^*}{dT} = -2RT(b + 3cT). \qquad (3.12)$$

The free energy of activation can be obtained from Eq. (3.7):

$$\Delta G^* = RT\left\{ln\left(\frac{\eta v}{hN}\right)\right\}, \qquad (3.13)$$

and finally, the entropy variation is obtained as:

$$\Delta S^* = \frac{\Delta H^* - \Delta G^*}{T} \qquad (3.14)$$

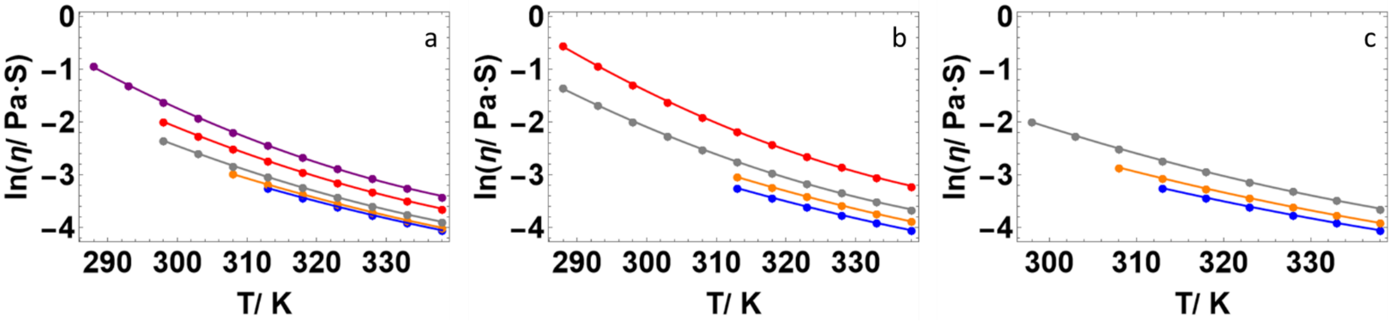

Figure 3.48. *ln η* vs T of a) [C$_2$Im][NO$_3$] + LiNO$_3$, b) [C$_2$Im][NO$_3$] + Mg(NO$_3$)$_2$ c) [C$_2$Im][NO$_3$] + Al(NO$_3$)$_3$. Blue dots represent pure IL, orange dots 0.5 mol·Kg^{-1}, gray dots 1 mol·Kg^{-1}, red dots 2 mol·Kg^{-1} and purple dots 3 mol·Kg^{-1}. Lines represent the quadratic fitting (Eq. (3.10)).

Table 3.23. Fitting parameters in Eq. (3.10) for [C$_2$Im][NO$_3$] with Li, Mg and Al nitrate salts.

Sample	*a*	*b /K^{-1}*	*C · 10^{-6} /K^{-2}*	*R^2*
Pure [C$_2$Im][NO$_3$]	28.4 ± 0.8	-0.165 ± 0.005	(205 ± 8)	0.999999
[C$_2$Im][NO$_3$] + Li salt 0.5m	30.2 ± 0.4	-0.175 ± 0.003	(219 ± 4)	0.999999
[C$_2$Im][NO$_3$] + Li salt 1m	39.2 ± 1.1	-0.229 ± 0.007	(299 ± 11)	0.999998
[C$_2$Im][NO$_3$] + Li salt 2m	44.1 ± 0.9	-0.255 ± 0.006	(336 ± 9)	0.999998
[C$_2$Im][NO$_3$] + Li salt 3m	54.0 ± 1.7	-0.312 ± 0.011	(420 ± 18)	0.99997
[C$_2$Im][NO$_3$] + Mg salt 0.5m	31.2 ± 0.4	-0.180 ± 0.003	(224 ± 4)	0.999999
[C$_2$Im][NO$_3$] + Mg salt 1m	49.3 ± 1.5	-0.287 ± 0.010	(385 ± 15)	0.99998
[C$_2$Im][NO$_3$] + Mg salt 2m	59.6 ± 1.9	-0.342 ± 0.012	(462 ± 19)	0.99996
[C$_2$Im][NO$_3$] + Al salt 0.5m	32.5 ± 1.2	-0.188 ± 0.008	(236 ±12)	0.999999
[C$_2$Im][NO$_3$] + Al salt 1m	40.7 ± 1.2	-0.233 ± 0.008	(302 ± 12)	0.999997

The previously-described fitting parameters have been summarized in Figs. 3.49-3.51, grouped by doping salt addition. As expected, ΔH^* decreases with increasing temperature, corresponding to a process with heat absorption. Regarding salt addition, the variation of the activation enthalpy increases its slope which increases the salt concentration. The decrease in the enthalpy variation is the cause of the negative values of the heat capacity variation (ΔC_p^*) which decreases with increasing temperature. All the obtained values for the activation energy (ΔG^*) were positive, which correspond to a non-spontaneous process with a potential barrier that must be overcome to trigger the viscous flow process. The activation energy increases with salt addition significantly, which indicates that triggering the viscous flow is difficult when the salt concentration increases. For all studied samples a change in the slope of ΔG^* is observed, since ΔG^* goes through a minimum, and this is why the entropy variation (ΔS^*) presents a crossover from positive to negative values, and the reason why the entropy variation becomes smaller when temperature rises.

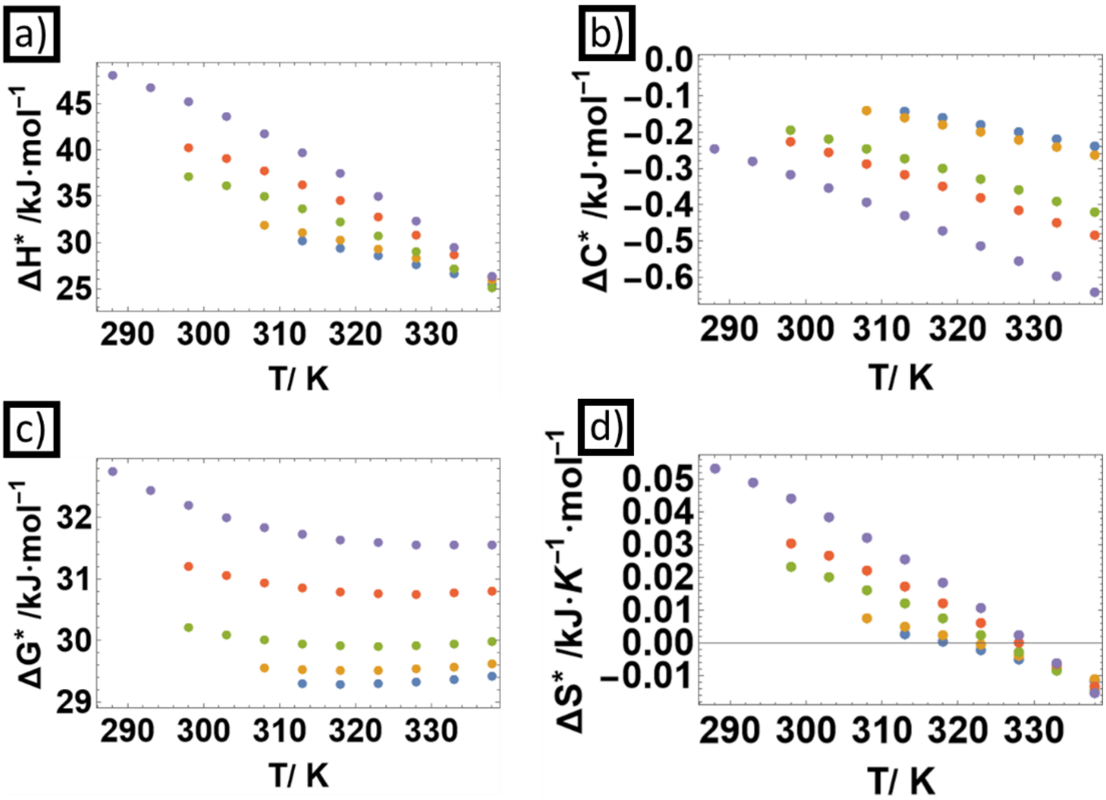

Figure 3.49. Thermodynamic activations parameters for $[C_2Im][NO_3]$ + $LiNO_3$. Blue dots represent pure IL, orange dots 0.5 mol·Kg^{-1}, green dots 1 mol·Kg^{-1}, red dots 2 mol·Kg^{-1} and purple dots 3 mol·Kg^{-1}

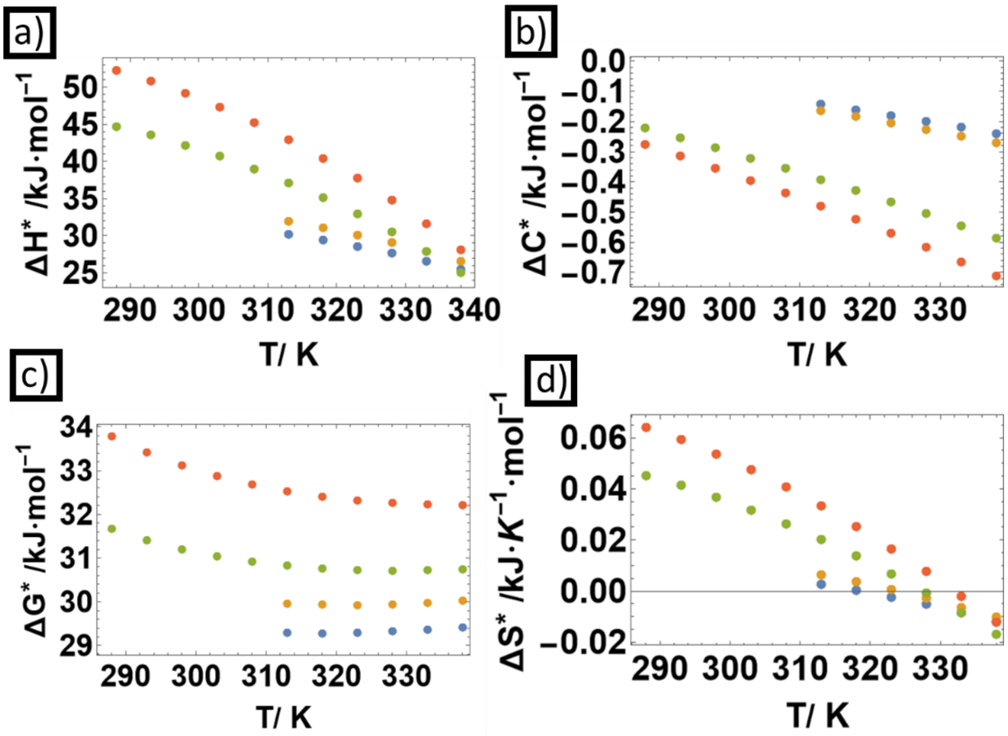

Figure 3.50. Thermodynamic activations parameters for $[C_2Im][NO_3]$ + $Mg(NO_3)_2$. Blue dots represent pure IL, orange dots 0.5 mol·Kg^{-1}, green dots 1 mol·Kg^{-1} and red dots 2 mol·Kg^{-1}.

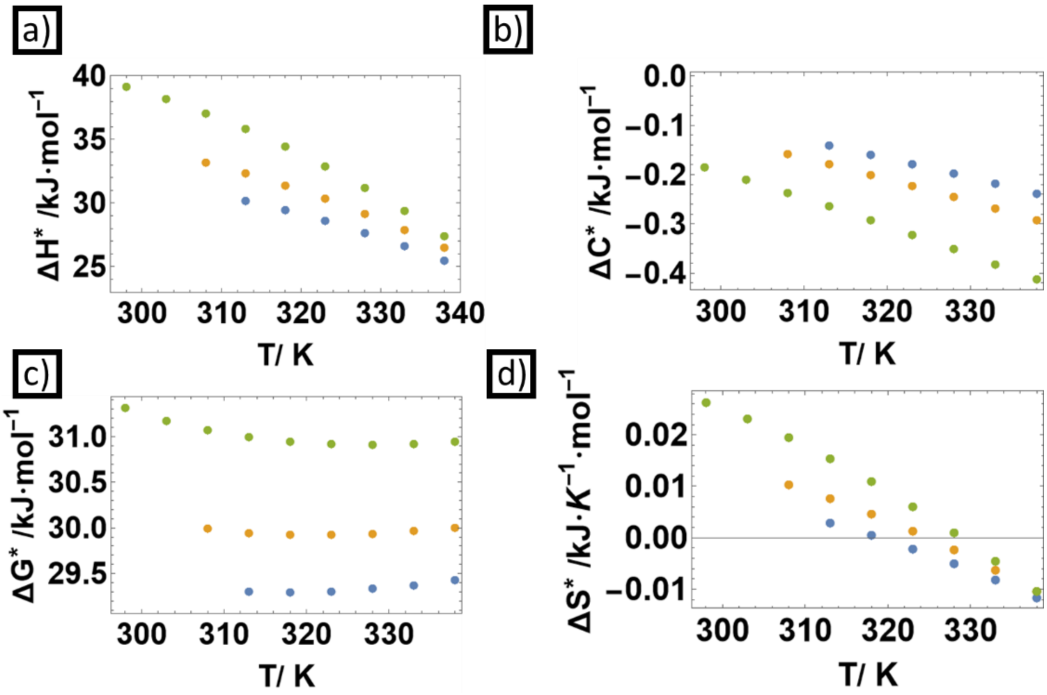

Figure 3.51. Thermodynamic activations parameters for $[C_2Im][NO_3]$ + $Al(NO_3)_3$. Blue dots represent pure IL, orange dots 0.5 mol·Kg^{-1} and green dots 1 mol·Kg^{-1}.

3.5. Electrochemical characterization

In this section the electrochemical characterization of the ILs EAN, [C_2Im][NO_3] and [C_4C_1Pyrr][TFSI] and its mixtures with inorganic salts in liquid and gel states will be studied. This will be done using different techniques, starting with the ionic conductivity measured by a conductimeter and followed with more complete techniques such as broadband dielectric spectroscopy (BBDS), electrochemical impedance spectroscopy (EIS) and galvanostatic charge-discharge with potential limitation (GCPL) studies. The aim of the ionic conductivity and BBDS characterization is to perform a comparative study between the selected ILs to perform further electrochemical studies such as EIS and assay a 2032 charging/discharging experiments (GCPL).This part of the thesis represents a vast amount of data that will be collected hereunder and in the appendix tables at this end of the manuscript.

Manufacturers of Li-ion batteries usually provide the optimal operating temperature range from 0 to 45 °C to charging and from -20 to 60 °C to discharging [108]. The temperature range for the electrochemical measuring conditions was selected according to these specifications.

3.5.1 Ionic conductivity

Using a GLP31 CRISON conductimeter (see chapter 2.- materials and methods) the ionic conductivity of the pure ILs EAN, [C_2Im][NO_3] and [C_4C_1Pyrr][TFSI], and of its mixtures with lithium salts with common cations were determined. Additionally, the effect of the nanoconfinement in this property was also analyzed for all these samples.

3.5.1.1. Pure Ionic Liquids

The conductivity of EAN, [C_2Im][NO_3] and [C_4C_1Pyrr][TFSI] between 243K and 323K was measured in cooling and heating ramps and the results are presented in Fig 3.52 . A clearly visible hysteresis loop in the liquid state, corresponding to first order phase transitions, is the most remarkable observation for protic ILs, which is in agreement, and even expected, with the supercooling effect observed in the DSC results of these ILs, with melting and freezing peaks in the interval of temperatures here studied (EAN T_m = 285 K and [C_2Im][NO_3] T_m = 307 K), but [C_4C_1Pyrr][TFSI] does not show this hysteresis effect owing to the phase transitions during the conductivity determination ([C_4C_1Pyrr][TFSI] T_m = 265 K) being out of the temperature interval, see Chapter 3, thermal characterization. Due to this fact, the values selected in this work correspond to cooling ramp.

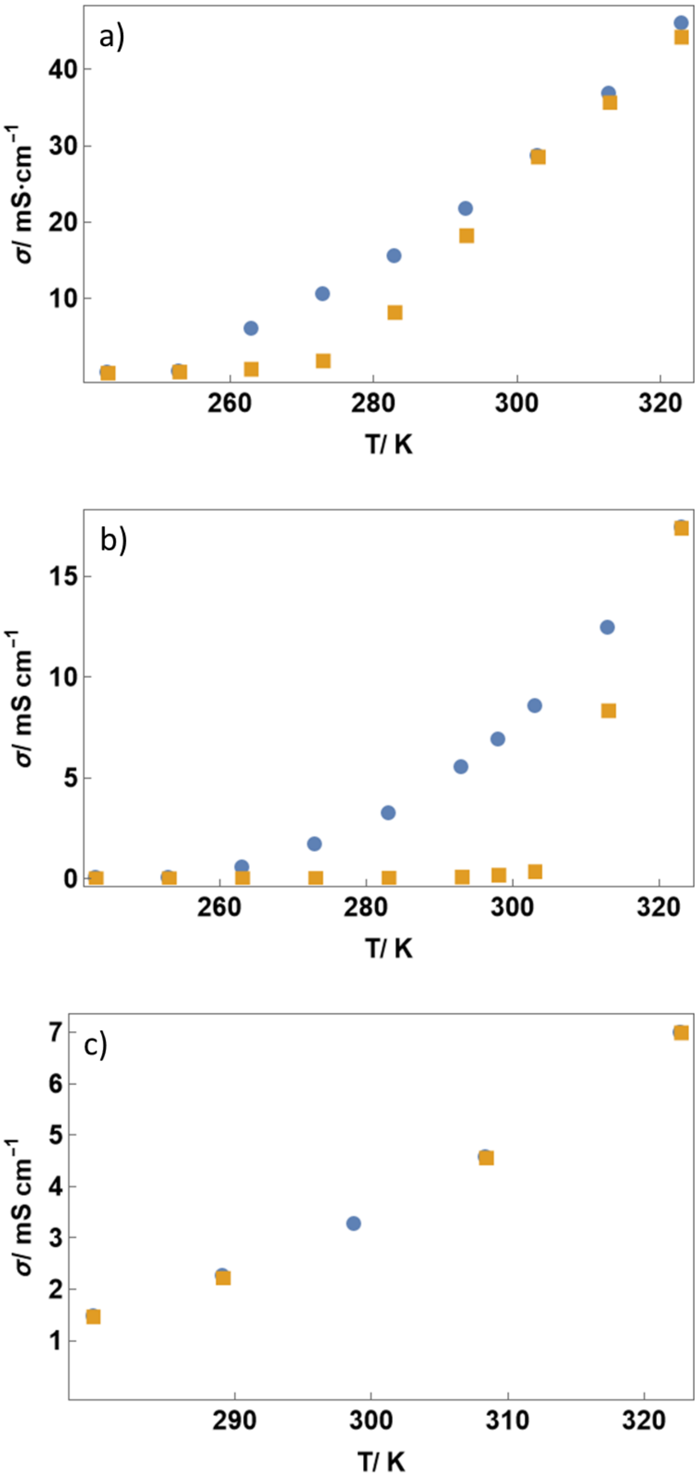

Figure 3.52. Ionic conductivity vs temperature of liquid state of a) pure EAN, b) pure $[C_2Im][NO_3]$ and c)) pure $[C_4C_1Pyrr][TFSI]$. Heating ramp (orange squares) and cooling ramp (blue dots)

Although the values of conductivity of conventional aqueous-carbonate electrolyte solutions applied in electrochemistry are higher than those reported here [109], our values are similar to those of lithium-ion electrolyte solutions conventionally used in lithium-ion batteries, ca. 10 mS/cm.

Fig. 3.53 shows the ionic conductivity in cooling ramp of pure EAN, pure [C_2Im][NO_3] and [C_4C_1Pyrr][TFSI]. Values of conductivity of pure liquid EAN and [C_4C_1Pyrr][TFSI] are in good agreement with the literature [110–112], and no published data were found for [C_2Im][NO_3]. As can be expected, this property increases with temperature, contrary to dynamic viscosity (see the previous section). The temperature dependence of conductivity cannot be described by Arrhenius law, and a Vogel–Tammann–Fulcher equation (Eq. (3.15)) must be applied in a similar way to dynamic viscosity in the previous subsection [98,113,114].

$$\sigma = A \cdot \exp\left(-\frac{B}{T-C}\right) = \sigma_0 \cdot \exp\left(-\frac{E_a}{k_b(T-T_0)}\right) \tag{3.15}$$

where $A = \sigma_0$ is the ionic conductivity at infinite temperature, E_a is the activation energy (in eV per particle) and T_0 is the ideal glass transition (or Vogel temperature). The VFT fitting parameters for the studied ILs are summarized in Table 3.24. The thermal activation of the VFT type is associated with the presence of several relaxation times in the underlying dynamics, characteristic of disordered systems. On the other hand, the Vogel temperature can be related with the glass transition temperature (T_g), verifying $T_0 < T_g$ [109] for slow processes, which is approximately the case in this work.

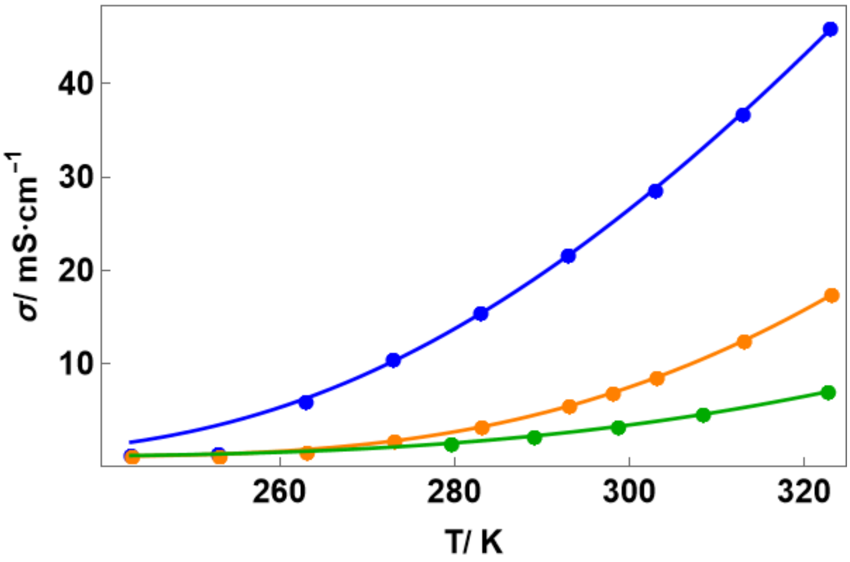

Figure 3.53. Ionic conductivity of pure EAN (blue dots), [C_2Im][NO_3] (orange dots) and [C_4C_1Pyrr][TFSI] (green dots), line represent the VFT fit.

3.5.1.2. Mixtures of ILs and inorganic salts. Effect of salt addition.

The effect of the addition of lithium salt on ionic conductivity of the mixture IL + lithium salt study was analyzed, and the results are summarized in this section. This property was studied as a function of the temperature and lithium salt concentration in bulk liquid state.

Figs. 3.54, 3.55 and 3.56 show the electrical conductivity of liquid mixtures of different concentrations of the lithium salt with common anion for EAN, [C_2Im][NO_3] and [C_4C_1Pyrr][TFSI], respectively. As expected, this property increases with increasing temperature and decreases with salt concentration, the inverse behavior of viscosity with salt concentration (see previous section Thermophysical properties - Viscosity). This trend is widely reported in the literature for different IL families, for example, two different imidazolium cation and TFSI anion with Li TFSI mixtures [115], for pyrrolidinium TFSI with Li TFSI [17], among others [116–119], indicating that the formation of new diffusive lithium ionic species in the solutions can contribute to this decrease. Kim et. al [120] concludes, by means of Raman spectroscopy, that the decrease in ionic conductivity when the $[C_4C_1Pyrr][TFSI]$ is doped with lithium salt is due to a coordination between $[TFSI]^-$ anions with Li^+ cations forming aggregates $[Li(TFSI)_2]^-$, and the formation of these aggregates increases when salt concentration increases. This agrees with the behavior of classical electrolyte solutions and mixtures of other ILs with different metal salts, where the conductivity is proportional to the density of charge carriers and inversely proportional to viscosity, as is widely reported in the literature [17,109,121–123].

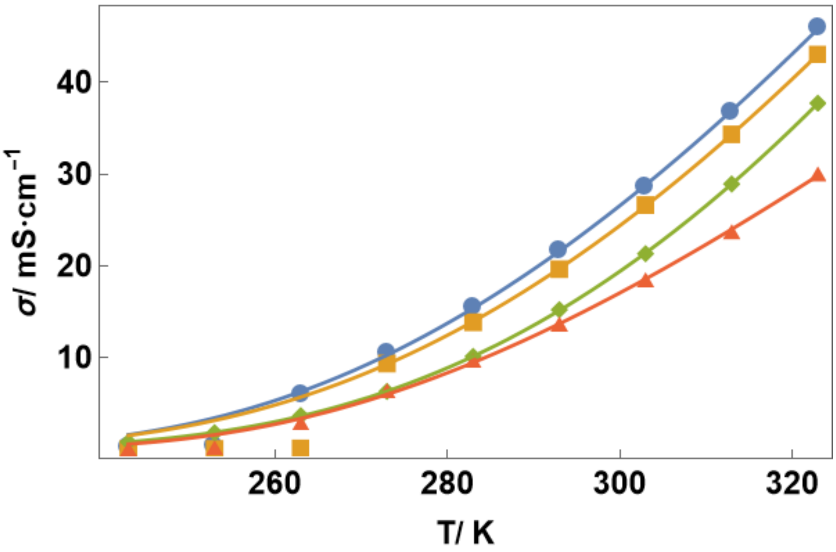

Figure 3.54. Electrical conductivity against temperature of liquid mixtures EAN + Li NO_3. Blue dots represent pure IL, orange squares represent 0.1 mol·kg^{-1}, green diamonds 1 mol·kg^{-1} and red triangles 2 mol·kg^{-1} mixtures. Lines show the corresponding VFT fitting.

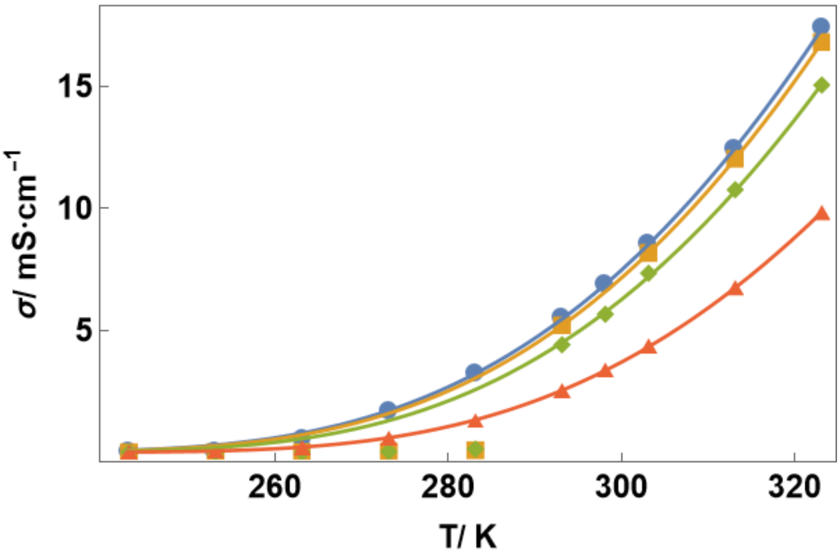

Figure 3.55. Electrical conductivity against temperature of liquid mixtures $[C_2Im][NO_3]$ + Li NO_3. Blue dots represent pure IL, orange squares represent 0.5 mol·kg^{-1}, green diamonds 1 mol·kg^{-1} and red triangles 3 mol·kg^{-1} mixtures. Lines show the corresponding VFT fitting.

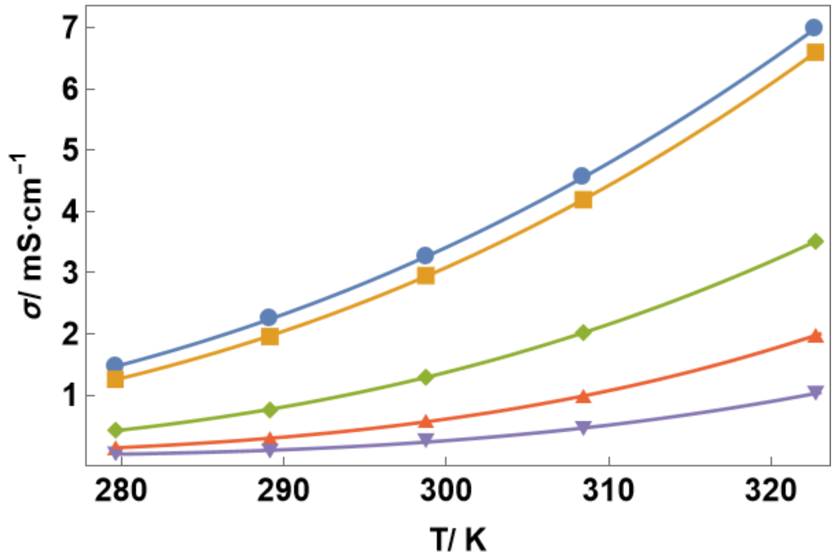

Figure 3.56. Ionic conductivity of $[C_4C_1Pyrr][TFSI]$ mixtures with lithium salt. Blue dots represent pure IL, orange squares represent 0.1 mol·kg^{-1}, green diamonds 0.5 mol·kg^{-1}, red triangles 1 mol·kg^{-1} and purple triangles 1.5 mol·kg^{-1} mixtures. Lines show the corresponding VFT fitting.

As pointed out previously, the ionic conductivity is a transport property, which is linked to the viscosity (η). The viscosity, at the same time, is related with the molecular diffusion (D) of the system through the Stokes-Einstein equation, which for a spherical particle is defined by Eq. (3.16):

$$D \, \alpha \, \frac{k_B T}{6\pi\eta r} \tag{3.16}$$

where k_B is Boltzmann's constant, T is the temperature and r is the radius of the spherical particle. Eq. (3.16) indicates that the larger the viscosity of a fluid, the slower the diffusion of particles, including ions. Therefore, a high viscosity can slow down the motion of ions, reducing the ionic conductivity of the solution. Furthermore, the ionic conductivity can be affected by the type and concentration of ions in the solution. High valency ions generally have a higher charge density and can interact more strongly with the solvent molecules, leading to a higher viscosity [124,125]. This can reduce the mobility of the ions and decrease the ionic conductivity.

The diffusion of the particles in the bulk system is the main relaxation mechanism of the system, making the VFT equation the right one to describe the system.

Similarly to pure ILs, the ionic conductivity vs temperature of all studied electrolyte mixtures were fitted using the VFT equation (Eq. (3.15)), in intervals where phase transition is not observed [98,126,127], and the obtained fitting parameters are shown in Table 3.24.VFT parameters do not follow a clear tendency with salt concentration for EAN + lithium salt mixtures. While for pure ILs the parameters remain nearly constant, for 1 molal salt addition the activation energy (E_a) and the infinite temperature conductivity (σ_∞) suffer a significant increase, and the ideal glass transition (T_0) decreases. This is the opposite behaviour to the saturation concentration (2 molal). For [C_2Im][NO_3] a decrease of σ_∞ with salt addition on liquid samples is observed. The obtained activation energy (Ea) values seem to remain at a constant value with salt concentration. The ideal glass transition temperature (Tg) ranges from 174 to 210 K in the studied samples, which is in relatively good agreement with the thermal analysis results shown in Section 1. With regards to the VFT obtained parameters for [C_4C_1Pyrr][TFSI] + lithium salt mixtures, the activation energy remains constant with lithium salt concentration considering the error bars and the glass transition temperature increases with salt concentration.

Table 3.24. Fitting parameters of the VFT equation for pure EAN and its mixtures with lithium salt in liquid form.

Sample	*A=σ_0 / mS·cm^{-1}*	*E_a · 10^{-3}/eV*	*T_0 /K*
EAN			
Pure EAN	*1000 ± 200*	*41 ± 5*	*169 ± 7*
EAN + LiNO$_3$0.1m	*1330 ± 190*	*48 ± 4*	*161 ± 5*
EAN + LiNO$_3$ 1.0m	*2310 ± 150*	*58.5 ± 1.5*	*157.9 ± 1.8*
EAN + LiNO$_3$ 2.0m	*450 ± 170*	*31 ± 7*	*189 ± 12*
[C$_2$Im][NO$_3$]			
Pure [C$_2$Im][NO$_3$].	*1730 ± 190*	*59 ± 3*	*174 ± 3*
[C$_2$Im][NO$_3$] + LiNO$_3$ 0.5 m.	*1770 ± 100*	*59.9 ± 1.4*	*174 ± 2*
[C$_2$Im][NO$_3$] + LiNO$_3$ 1 m	*500 ± 200*	*34 ± 9*	*210 ± 13*

$[C_2Im][NO_3]$ + $LiNO_3$ 3 m	*740 ± 50*	*46.8 ± 1.4*	*192 ± 2*
$[C_4C_1Pyrr][TFSI]$			
Pure $[C_4C_1Pyrr][TFSI]$	*1000 ± 180*	*77 ± 5*	*142 ± 5*
$[C_4C_1Pyrr][TFSI]$ + Li TFSI 0.1m	*1100 ± 300*	*77 ± 7*	*147 ± 7*
$[C_4C_1Pyrr][TFSI]$ + Li TFSI 0.5m	*620 ± 180*	*66 ± 7*	*175 ± 7*
$[C_4C_1Pyrr][TFSI]$ + Li TFSI 1m	*1400 ± 900*	*84 ± 16*	*173 ± 12*
$[C_4C_1Pyrr][TFSI]$ + Li TFSI 1.5m	*200 ± 400*	*50 ± 30*	*210 ± 30*

3.5.1.3. Effect of nanoconfinement of pure ILs and salt mixtures

The effect of nanoconfinement on the conductivity of the protic ILs (EAN and $[C_2Im][NO_3]$) and their mixtures with salt will be analyzed in this subsection. To our knowledge no values of conductivity of these ionogels have been previously reported. Different behaviors can be observed for both ionogels. Firstly, the disappearance of the thermal hysteresis in pure EAN ionogel (by ethanol route), as can be seen in Fig. 3.57, whereas the $[C_2Im][NO_3]$ ionogel shows this hysteresis phenomenon, similar to its liquid state. These observations are in agreement with the thermal behavior of these ionogels (see section 2.- Thermal Characterization) characterized by a completely amorphous behavior in the temperature interval for the EAN ionogel (no phase transitions), while the imidazolium based ionogel shows melting and freezing transitions at similar temperatures than those obtained by DSC.

Fig. 3.58 shows the ionic conductivity vs temperature in liquid and gel states for EAN and $[C_2Im][NO_3]$. As can be expected, and similarly to the behavior of the liquid phase, this parameter increases with temperature for gel samples, although a different behavior can be observed for both ILs. The EAN ionogel shows higher values of ionic conductivity than those reported for liquid, due to presence of water and ethanol inside the silica matrix, difficult to eliminate during the purifying process. These impurities can act as a cosolvent, reducing the viscosity of the sample (see section 3.- Structural Characterization). In contrast, the conductivities of $[C_2Im][NO_3]$ gel, as is clearly seen, are lower than pure IL in liquid state.

As can be seen, the VFT model (Eq. (3.15)) accurately describes the temperature dependence of the ionic conductivity, and the obtained fitted values are listed in Table 3.25. For EAN gel, it is especially remarkable that the activation energies for liquid and gel samples coincide, which is an indicator that the mechanism behind the conductivity is the same in both states. This conclusion is not so clear for $[C_2Im][NO_3]$, whose activation energy for the gel state is lower than that of the liquid state, but the difference is not important enough to ensure that the ionic conductivity mechanism has changed due to confinement, but could be due mainly to the fitting procedure or to experimental differences in measuring conditions.

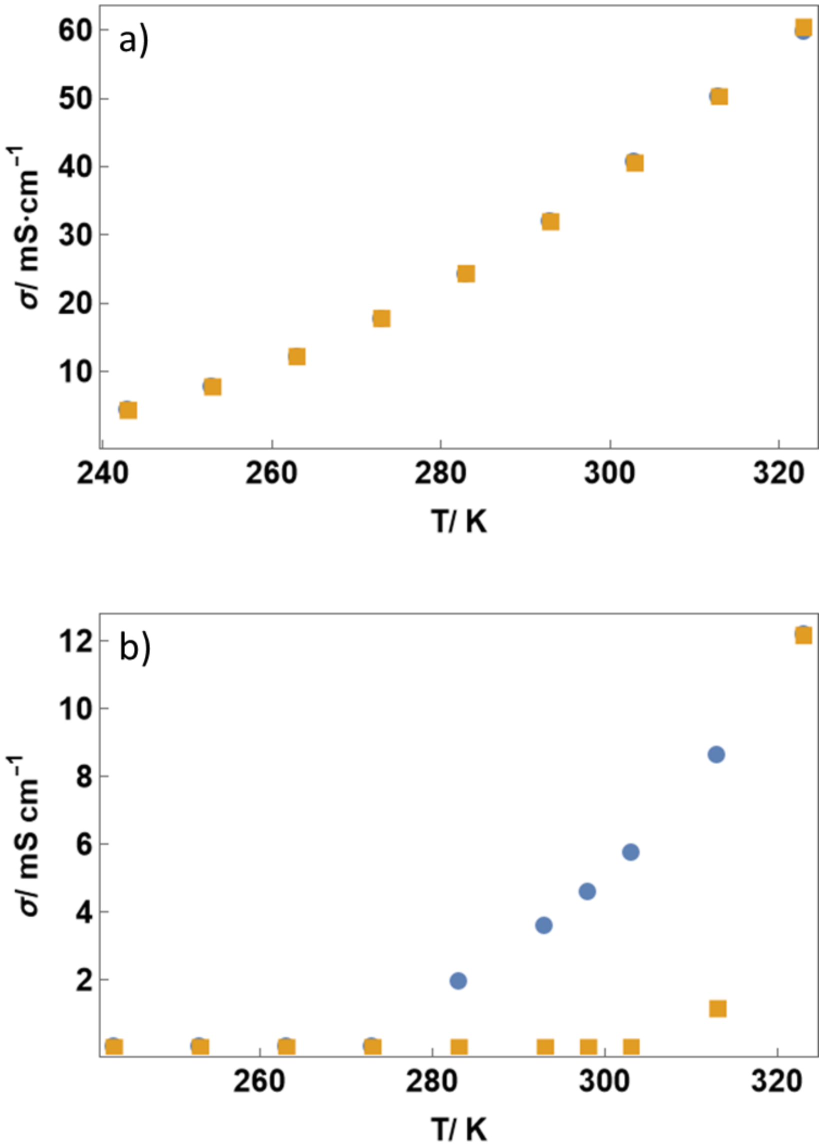

Figure 3.57. Ionic conductivity vs temperature of a) EAN in gel and b) [C_2Im][NO_3] gel. Heating ramp (orange squares) and cooling ramp (blue dots).

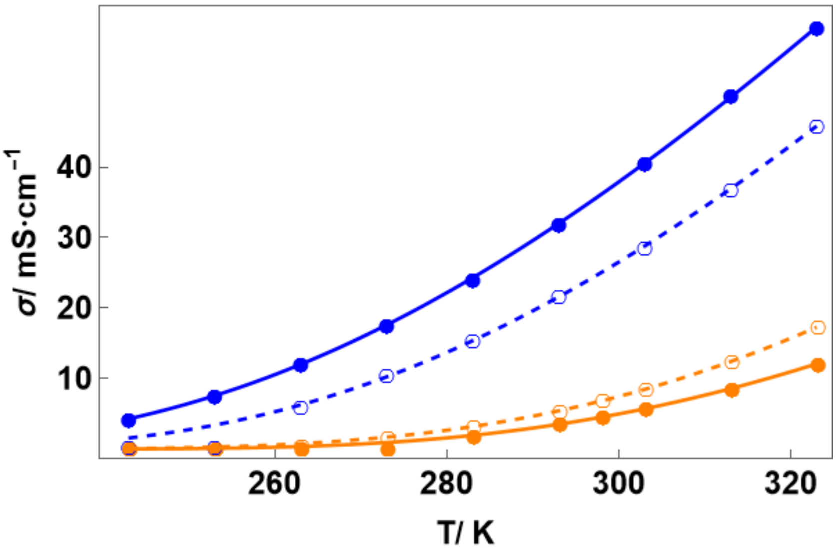

Figure 3.58. Ionic conductivity vs temperature of EAN liquid (empty blue circles), EAN ionogel (filled blue circles), [C$_2$Im][NO$_3$] liquid (empty orange circles) and [C$_2$Im][NO$_3$] ionogel (filled orange circles). Lines represent the corresponding VFT fit (dashed for liquid form and continuous for gel form).

Table 3.25. Fitting parameters of the VFT equation for ionic conductivity of gels EAN and [C$_2$Im][NO$_3$] and its mixtures with lithium salt.

	A /mS·cm^{-1}	*E$_a$ · 10^{-3}/eV*	*T$_0$/ K*
EAN + LiNO$_3$ mixtures (Gel form)			
EAN	*1040 ± 70*	*41.1 ± 1.6*	*156 ± 3*
EAN + LiNO$_3$ 0.1m	*820 ± 30*	*35.3 ± 0.7*	*160.1 ± 1.3*
EAN + LiNO$_3$ 1.0m	*1050 ± 80*	*41.4 ± 1.7*	*155 ± 3*
EAN + LiNO$_3$ 2.0m	*1610 ± 110*	*52.6 ± 1.7*	*146 ± 2*
[C$_2$Im][NO$_3$] + LiNO$_3$ mixtures (Gel form)			
[C$_2$Im][NO$_3$]	*810 ± 100*	*47 ± 3*	*191 ± 3*
[C$_2$Im][NO$_3$] + LiNO$_3$ 0.5m	*1000 ± 200*	*51 ± 5*	*185 ± 6*
[C$_2$Im][NO$_3$] + LiNO$_3$ 1.0m	*1500 ± 300*	*60 ± 4*	*180 ± 5*
[C$_2$Im][NO$_3$] + LiNO$_3$ 3.0m	*1300 ± 200*	*55 ± 3*	*189 ± 4*

The ionic conductivity vs temperature and the ionic conductivity vs salt concentration of the mixtures EAN + Li NO$_3$ and [C$_2$Im][NO$_3$] + Li NO3 in gel shown are shown in Figs. 3.60 and 3.61, respectively. As expected, ionic conductivity increases with temperature for all studied samples. Nevertheless, the trend observed with salt concentration is different for the liquid and gel samples. Ionic conductivity decreases in liquid samples with salt addition. In contrast, this property reaches a maximum at the lowest studied concentration mixture in gel form followed by a decrease with salt concentration (Fig. 3.59 b and 3.60 b). For example, for pure EAN gel the ionic conductivity at 293 K is 31.9

mS·cm^{-1}, EAN + Li NO$_3$ 0.1 mol·kg^{-1} at the same temperature is 37.5 mS·cm^{-1} (which represents an increase of 17.5%). While for [C$_2$Im][NO$_3$] ionogel exhibits a conductivity of 12.16 mS·cm^{-1} and its mixtures with lithium salt at 323 K and 0.5 mol·kg^{-1} with LiNO$_3$ the obtained conductivity is 13.26 mS·cm^{-1} at the same temperature (an increase of conductivity of 9%). Although this behavior agrees with other authors, such as Sajid *et al*. [128], there is no general agreement in the literature, and some controversial conclusions can be found [47]. Although this increase after gelation could be initially related to the presence of water in the sample, the NMR characterization of [C$_2$Im][NO$_3$] shows that no significant amounts of water (or other cosolvents) is contained in the analyzed sample (see section 2.-Structural Characterization).

It is especially interesting to mention that EAN + LiNO$_3$ gel samples exhibit higher ionic conductivity than its equivalent in liquid state for all temperatures and salt concentrations. This behavior is not always reported in the literature and some controversial conclusions can be derived. Noor et al. [47] established that the ionic conductivity of ionogels of 1-butyl-3-methyl imidazolium tetrafluoroborate with different amount of TEOS decreases as the amount of silica increases, being the hydrogen bond networks between [BF$_4$]$^-$ and the hydroxyl group in the silica the mechanism of IL immobilization suggested by these authors. On the contrary, Le Negre et al. [129] and Sajid et al. [130] found similar or even higher values of the ionic conductivity of ionogels of N, N, N triethyl octyl ammonium bromide with regard to neat IL in the temperature interval between 253 K and 333 K, which evidences the relatively small impact of the silica scaffold in this property, as happens here, for the gel of the lowest salt concentration. In this work, the increase in ionic conductivity is attached to the presence of impurities from the gelation reaction. An appropriate assessment of the presence of gel precursor spurious traces or molecular compounds generated during the sol-gel synthesis is fundamental, as well as knowing how these traces affect the results (see Section 3.-Structural Characterization).

The ionic conductivity of the ionogels have been fitted with the VFT model (Eq. (3.15)) and the results can be found in Table 3.25. For EAN mixtures with lithium nitrate, the conductivity at infinite temperature (σ_∞) tends to decrease with gelation for pure IL and its mixtures of 0.1 and 1 m, whereas these parameters increase after gelation for the sample at the highest concentration of salt. The T$_0$ values tend to decrease after gelation, as a thermal analysis study also indicates. In this case, the fragility index increases with the salt concentration for gel samples, which renders to a decrease of the ideal glass transition temperature (T$_0$). For [C$_2$Im][NO$_3$] mixtures with lithium salt, an increase of σ_∞ with salt addition can be seen. The obtained activation energy (E$_a$) values remain approximately constant with salt addition. The ideal glass transition temperature (T_g) ranges from 180 to 191 K in the studied samples, which is in relatively good agreement with the thermal analysis results.

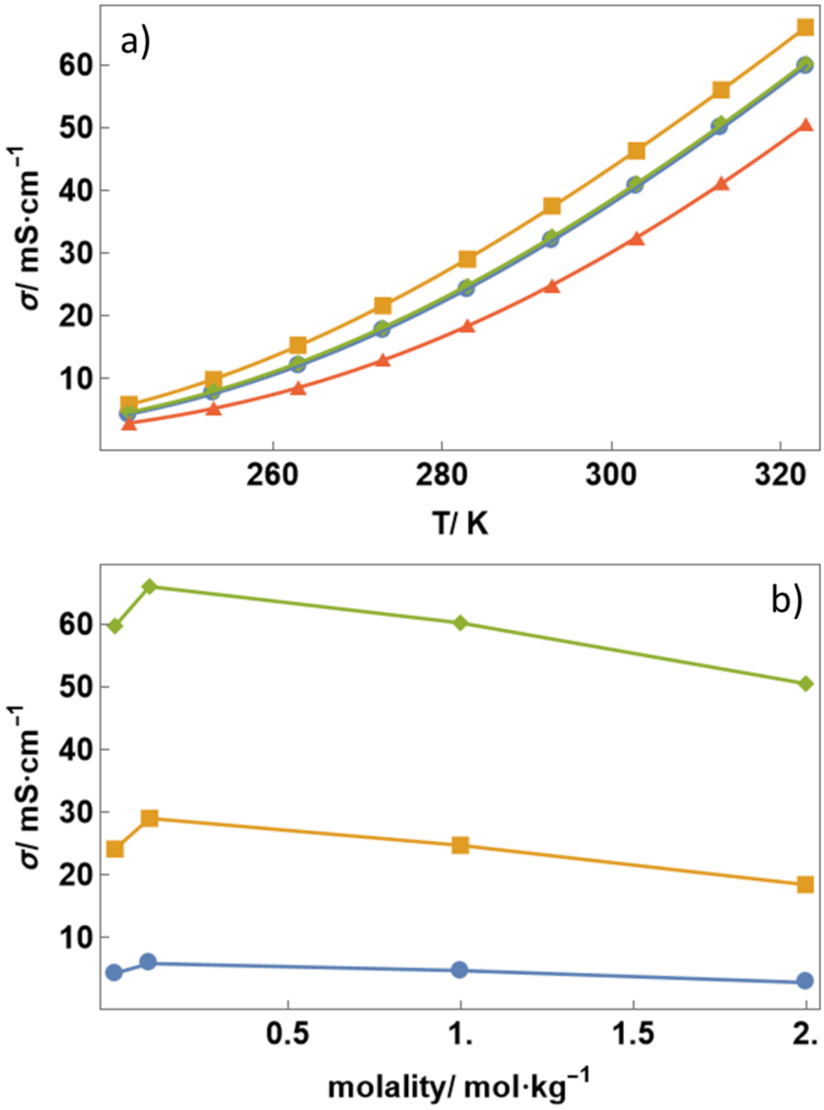

Figure 3.59. a) Ionic conductivity vs temperature of EAN gel (blue dots) and its mixtures of 0.1 mol·kg^{-1} (orange squares), 1 mol·kg^{-1} (green diamonds), 2 mol·kg^{-1} (red triangles). b) Ionic conductivity vs salt concentration at T = 243 K (blue dots), T = 283 K (orange squares) and T = 323 K (green diamonds). Lines are guides to the eye.

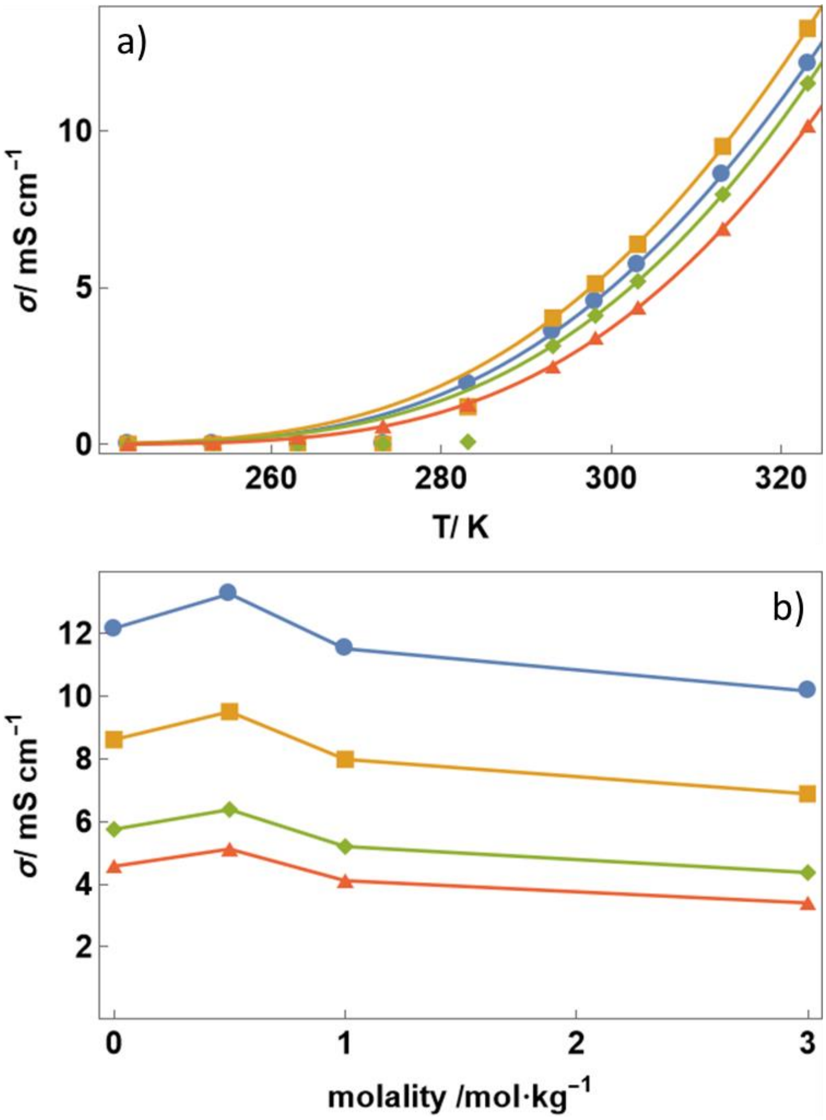

Figure 3.60. a) Comparison of the electrical conductivity versus temperature of ionogels of $[C_2Im][NO_3]$ + $LiNO_3$ mixtures (lines correspond to the fitting to the VFT equation): $[C_2Im][NO_3]$ (blue), $[C_2Im][NO_3]$ + $LiNO_3$ at 0.5 molal (orange), $[C_2Im][NO_3]$ + $LiNO_3$ at 1 molal (green) and $[C_2Im][NO_3]$ + $LiNO_3$ at 3 molal (red). b) Comparison of the electrical conductivity versus concentration (mol kg^{-1}) of salt addition for gel mixtures (0 concentration refers to pure $[C_2Im][NO_3]$) at different temperatures: 323 K (blue dots), 313 K (orange squares), 303 K (green diamonds) and 293 K (red triangles). Lines are guides to the eye.

3.5.2 Broadband Dielectric Relaxation

As was widely exposed in the materials and methods section, broadband dielectric spectroscopy (BBDS) refers to the frequency-dependent response of a material to an applied electric field. This technique involves the measurement of the dielectric response over a wide frequency range, typically extending over several orders of magnitude. This technique is useful for studying both fast and slow processes within materials, as different relaxation mechanisms can be observed at different frequencies. The study of broadband dielectric relaxation can reveal information about the microscopic dynamics and structure of these materials.

There follows a BBDS study of the pure ionic liquids $[C_2Im][NO_3]$ and $[C_4C_1Pyrr][TFSI]$. The changes induced by salt addition and nanoconfinement is studied from the variation of the real and imaginary parts of the electric permeability against frequency and the Cole-Cole plot.

3.5.2.1. Pure Ionic liquids.

Fig. 3.61 a) and b) shows the dielectric spectroscopy of the IL $[C_4C_1Pyrr][TFSI]$ real and imaginary parts, respectively in the liquid state at 298 K. Charge accumulation in the electrodes is produced, due to the charge motion following the electromagnetic applied field [131–133]. There are, to our knowledge, two main criteria to distinguish the different regimes in the interfacial polarization due to charge accumulation in the electrodes. The first one is based on the real part of the dielectric permittivity, and it is proposed by Jan Leys et. al. [126]. The second criterion is based on Eq. (3.17) which is based on a Krammers-Kronig relation obtaining the free-conductivity effect imaginary dielectric permittivity, and is proposed by Ubbenhorst et al. [134]

$$\varepsilon''_{der} = -\frac{\pi}{2}\frac{d\varepsilon'(\omega)}{d\,ln\omega} \qquad (3.17)$$

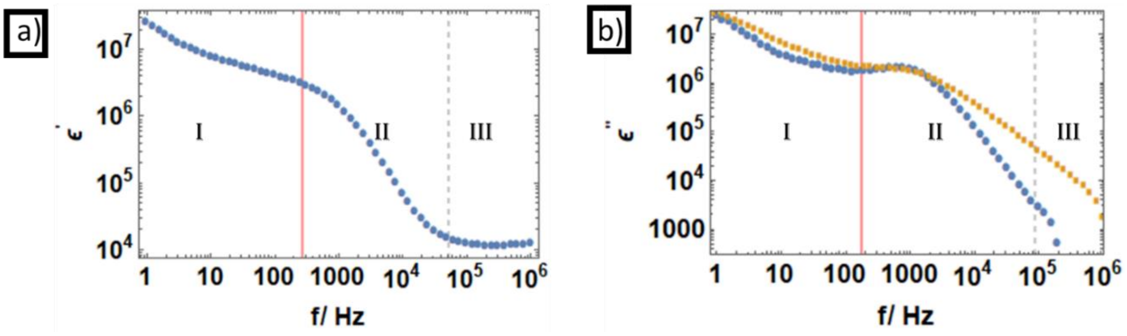

Figure 3.61. Dielectric spectroscopy of the liquid 1-Butyl-1-methylpyrrolidinium bis(trifluoromethylsulfonyl)imide at 298 K, a) real part of the dielectric constant and b) blue dots represent the theoretical model ε''_{der} (Eq. (3.17)) and orange dots represent the measured imaginary part of the dielectric constant.

Electrode polarization (EP) is due to the formation of the electric double layer (EDL) in the neighborhood of the electrodes by accumulation of free ions [131,133,135–137]. According to Leys et al. [126], the EP is given until the high frequency limit of the dielectric constant (ε_∞) is reached. The drastic decrease of the real part of the dielectric constant with frequency is due to the delay in polarization with the electromagnetic field frequency [135][138]. In Fig. 3.61 a) it is clearly seen that the high frequency limit permittivity (high frequency plateau, ε_∞) is reached around $5\cdot10^4$ Hz for 298 K. Another interesting frequency interval is that ranging from 0.5 to 273 Hz for 298 K, where a low frequency plateau is observed (static permittivity, ε_S). In this plateau maximum charge accumulation is produced, and the MWS effect (total charge accumulation in the electrodes) is maximum in this plateau.

Eq. (3.16) is a good approximation to calculate the free-conductivity effect for the imaginary part of the dielectric permittivity [134]. The criterion to distinguish if the EP effect is ruling the sample or not (transition from zone II to zone III) is given by a slope change in ε''_{der} in the ohmic region, as indicated by the dashed vertical grey line in Fig. 3.61 b), and in this representation it occurs around 8·10⁴ Hz. In most of the representations of the dielectric constant, the transition to the nonlinear polarization from the linear polarization (transition from zone I to zone II) is characterized by a subtle kink in both magnitudes, ε''_{der} and ε'' (presented at 172 Hz for [C_4C_1Pyrr][TFSI]), as F. Pabst and co-workers pointed out [139].

Figs. 3.62 and 3.63 show the frequency dependence of ε' and ε'' (real and imaginary parts of dielectric permittivity, respectively) curves recorded at different temperatures in the 20 Hz-10^6 Hz spectroscopic range for pure [C_2Im][NO_3] and [C_4C_1Pyrr][TFSI]. A resonance induced by experimental equipment above 10^5 Hz was detected for the first IL studied, so data corresponding to these frequencies are not considered in this case. The real part, for all studied temperatures (Figs.3.62 a, and 3.63 a), is governed by the EP, defined above, until approximately 10^5 Hz. The corresponding MWS plateau ranges from 20 Hz to 300 Hz for [C_2Im][NO_3] at 288 K and from 1 Hz to 600 Hz for [C_4C_1Pyrr][TFSI] at 298 K, and becomes wider in frequency with temperature for both IL. This can be explained by an increase in ionic mobility.

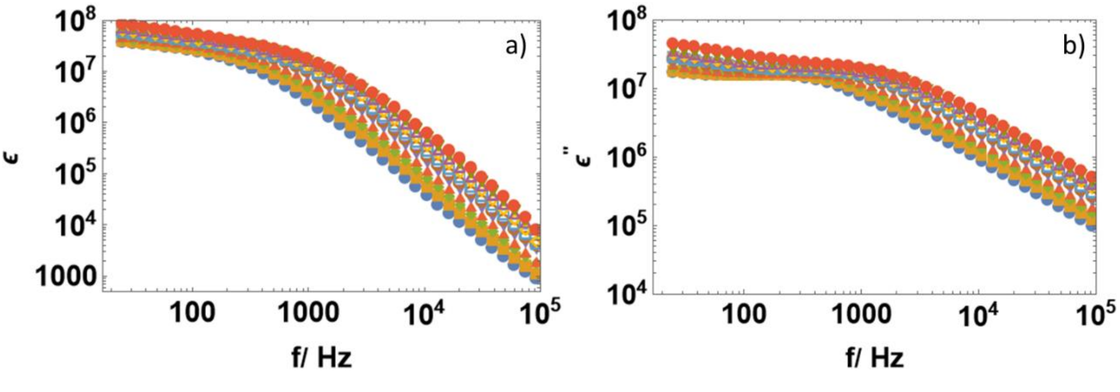

Figure 3.62. Dielectric spectroscopy of [C_2Im][NO_3] liquid, a) is the real part and b) the imaginary part for pure IL. Blue filled dots correspond to 288 K, orange filled squares 293 K, green filled diamonds 298 K, red filled triangles 303 K, purple filled triangle 308 K, brown empty dots 313 K, blue empty squares 318 K, yellow empty diamonds 323 K, purple empty triangles 328 K, green empty triangles 333 K and red filled dots 338 K.

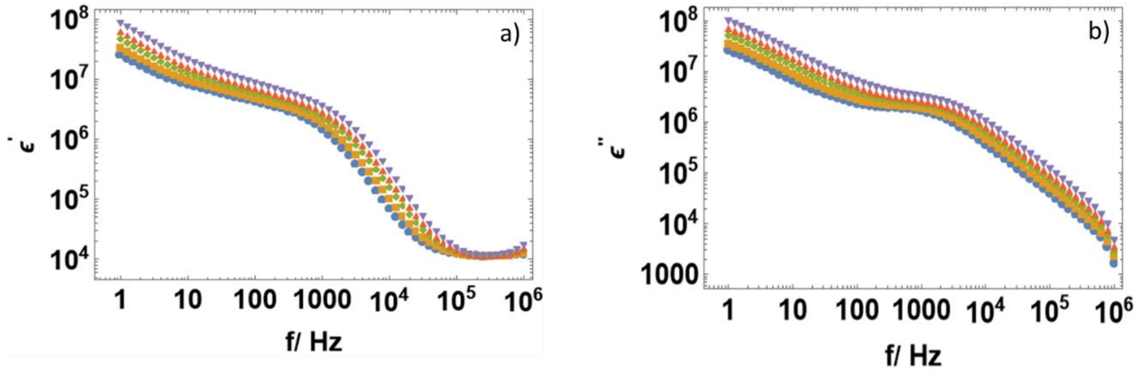

Figure 3.63. Dielectric spectroscopy of 1-Butyl-1-methylpyrrolidinium bis(trifluoromethylsulfonyl)imide liquid form, a) real part of dielectric spectroscopy, b) imaginary part of dielectric spectroscopy. Blue dots correspond to 298K, orange squares 303K, green diamonds 313, red upper triangles 323K and purple down triangles 333K.

The imaginary parts of the dielectric constant (Figs. 3.62 b and 3.63 b), initially show a plateau ending in a maximum that shifts to higher frequencies when increasing the temperature, followed by a linear behavior with slope -1.00 in the log-log representation, indicating that the ohmic region is achieved [126][140][141]. This ohmic regime is achieved in a different spectroscopic window for each temperature since its trigger frequency is shifted upwards with increasing temperature. The plateau like zone is due to the movement of the ions forming the electrolyte which is not aligned with the electric field lines as Wekang Tu and co-workers indicated [142]. This ohmic behaviour followed by the ionic current in the analyzed samples is followed also by dipolar liquids [143], electrolyte solutions [144] and other ionic liquids [145].

Figs. 3.64 and 3.65 show the Cole-Cole plot at different temperatures for [C_2Im][NO_3] and for [C_4C_1Pyrr][TFSI], respectively. In the high-frequency region, a single semicircle is found for all studied samples, corresponding to the interfacial relaxation of the sample. This semicircle is distorted at low frequencies due to the nonaligned movements of the ions with respect to the electrical field lines [142]. At lower frequencies there is straight line that corresponds to the plateau of the EP (MWS effect). This Cole-Cole study shows that the dielectric permittivity module ($|\varepsilon^*|$) increases with temperature (the semicircle becomes broader and higher), as Mazzer and co-workers also found in 2-Hydroxy ethyl ammonium Citrate [146], although they could not find a Debye-like relaxation (see section 2.- materials and methods), as in our case. Figs. 3.64 and 3.65 show an increase of the ionic mobility with increasing temperature [135], which is associated to the broadening of the semicircle as the temperature rises and the motion of charge carriers becomes easier, and then an easier and faster dielectric response to an external electromagnetic perturbation is registered. This assumption is corroborated by the decrease of the fitted relaxation times with increasing temperature (both Debye and Cole-Cole approximation), which means the dielectric excitation/deexcitation becomes easier.

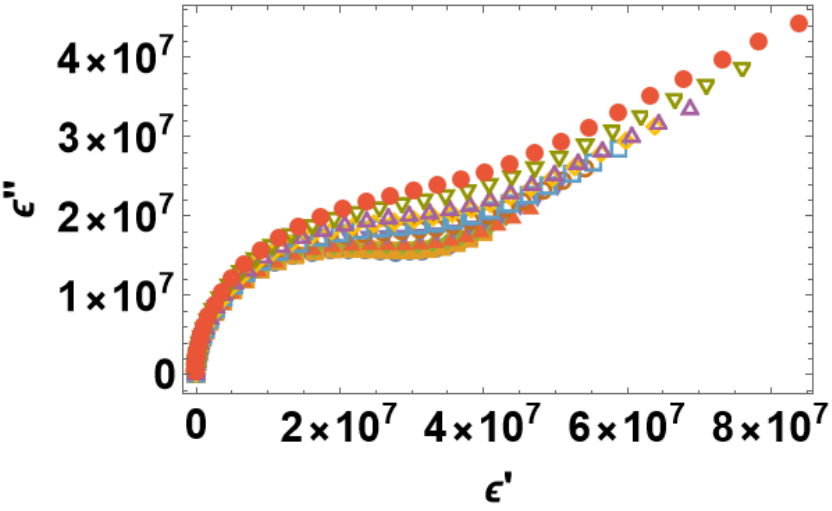

Figure 3.64. Cole-Cole plot for [C_2Im][NO_3]. Blue filled dots correspond to 288 K, orange filled squares 293 K, green filled diamonds 298 K, red filled triangles 303 K, purple filled triangle 308 K, brown empty dots 313 K, blue empty squares 318 K, yellow empty diamonds 323 K, purple empty triangles 328 K, green empty triangles 333 K and red filled dots 338 K.

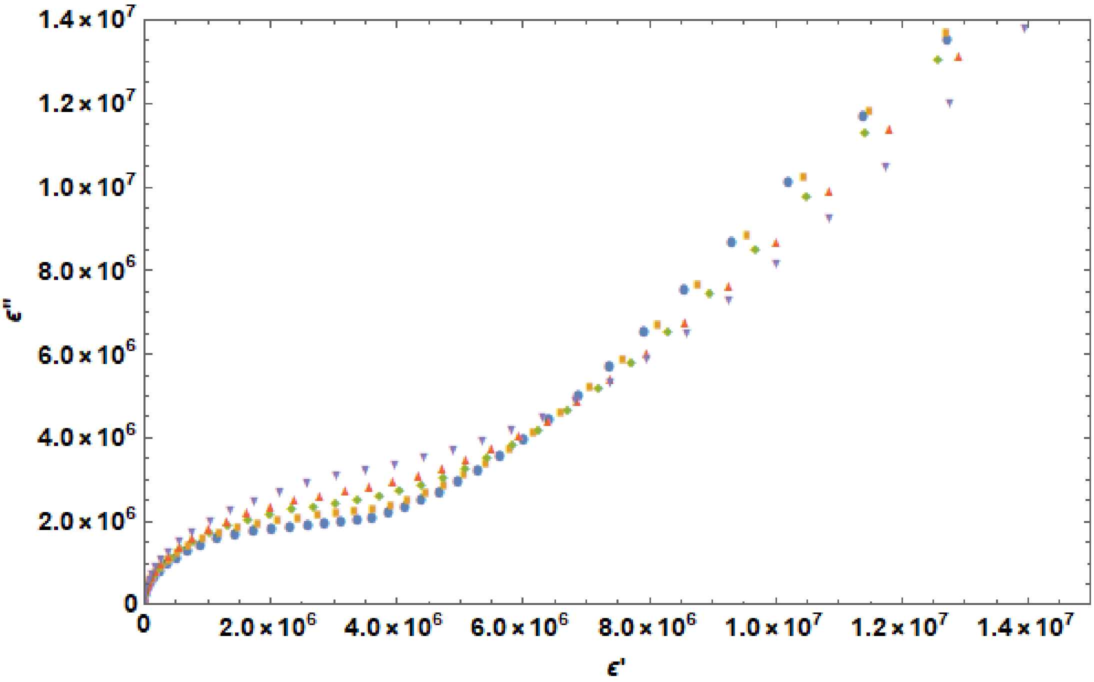

Figure 3.65. Cole-Cole plot of liquid 1-Butyl-1-methylpyrrolidinium bis(trifluoromethylsulfonyl)imide. Blue dots correspond to 298K, orange squares 303K, green diamonds 313, red upper triangles 323K and purple down triangles 333K.

In the linear region of Fig. 3.65 corresponding to the MWS effect a crossover of the data can be observed, probably due to the ion accumulation in the walls of the electrode, increasing the slope of the MWS effect at lower temperatures, indicating that the ions are easily accumulated at lower temperatures.

Table 3.26 lists the fitting parameters for the Debye approximation for the ILs $[C_2Im][NO_3]$ and $[C_4C_1Pyrr][TFSI]$. The relaxation time is in a good agreement, both for real and imaginary fitting, and is decreasing with temperature. This is in good agreement with the previous affirmation of the increasing freedom degrees while increasing temperature.

Table 3.26. Fitting parameters for dielectric spectroscopy on the Debye approximation of liquid $[C_2Im][NO_3]$ and $[C_4C_1Pyrr][TFSI]$.

$[C_2Im][NO_3]$			
Sample	$\boldsymbol{\varepsilon_s \cdot 10^6}$	$\boldsymbol{\varepsilon_\infty}$	$\boldsymbol{\tau \cdot 10^{-4}}$
288	2.52 ± 0.04	680 ± 90	4.71 ± 0.03
293	2.56 ± 0.04	780 ± 130	3.779 ± 0.016
298	2.60 ± 0.04	1200 ± 150	3.107 ± 0.015
303	2.62 ± 0.05	1100 ± 200	2.577 ± 0.013
308	2.66 ± 0.05	2300 ± 300	2.174 ± 0.011
313	2.69 ± 0.06	2500 ± 400	1.852 ± 0.009
318	2.71 ± 0.07	1800 ± 400	1.591 ± 0.008
323	2.71 ± 0.07	1400 ± 600	1.392 ± 0.007
328	2.78 ± 0.08	3500 ± 700	1.260 ± 0.006
333	2.80 ± 0.10	2200 ± 800	1.121 ± 0.005
338	2.81 ± 0.12	1400 ± 900	1.010 ± 0.004
$[C_4C_1Pyrr][TFSI]$			
Sample	$\varepsilon_s \cdot 10^6$	ε_∞	$\tau \cdot 10^{-4}$
298	3.32 ± 0.06	11270 ± 80	1.81 ± 0.06
303	3.59 ± 0.07	11230 ± 100	1.49 ± 0.05
313	4.06 ± 0.09	11210 ± 160	1.22 ± 0.05
323	4.44 ± 0.10	11200 ± 200	1.04 ± 0.04
333	5.18 ± 0.12	11200 ± 300	0.90 ± 0.03

Fig. 3.66 shows the Debye fit for pure $[C_2Im][NO_3]$ at 288 K (a) and 388 K (b), and as can be seen there, the mid-low frequency region in the semicircle is perturbed by the MWS effect.

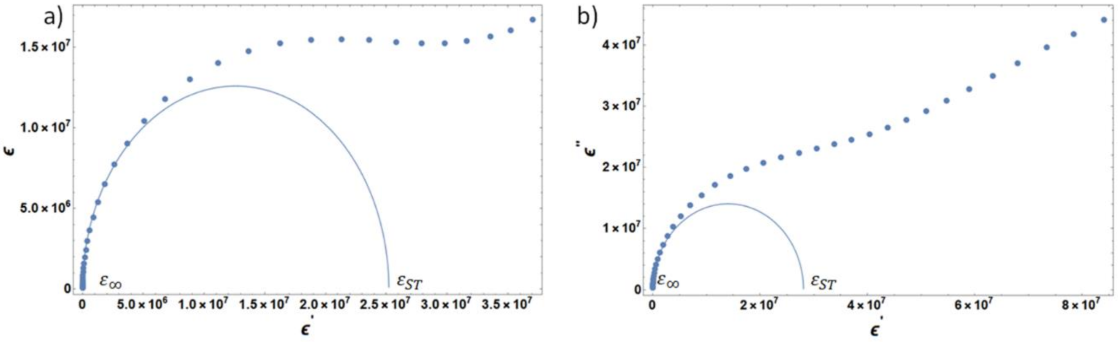

Figure 3.66. Cole-Cole plot of $[C_2Im][NO_3]$ with Debye fitting at a) 288K and b) 388 K

The DC ionic conductivity was obtained by means of BBDS (see section 2.- materials and methods) and is found from the linear fitting of this spectroscopical window as described elsewhere [145]. Fig. 3.67 shows the DC ionic conductivity dependence with temperature of the pure ILs [C_2Im][NO_3] and [C_4C_1Pyrr][TFSI], as can be seen, the electrical conductivity increases with temperature, as expected. The ionic conductivity found by this methodology is in good agreement (lower deviation than 8%) with that found by the CRISON conductimeter (see Table 3.27). DC ionic conductivity has been fitted with the Vogel-Fulcher-Tamman (VFT) model for [C_2Im][NO_3] and the Arrhenius model has been used for [C_4C_1Pyrr][TFSI]. The different used models are related with the glass transition temperature which should be much lower for the pyrrolidinium based IL. The obtained fitting parameters for the conductivity by means of BBDS can be found in Table 3.28.

Fig. 3.68 presents the AC conductivity (real and imaginary part for liquid and gel states) for 1-Butyl-1-methylpyrrolidinium bis(trifluoromethylsulfonyl)imide liquid and gel phase. The AC conductivity is obtained as follows:

$$\sigma^* = j\omega\varepsilon_0\varepsilon^* \tag{3.18}$$

The plateau shown in the real part of the AC conductivity σ' (Fig. 3.68 a) for liquid form) corresponds to DC conductivity [126]. When σ' reaches the high frequency plateau, the imaginary part of the dielectric constant against frequency is ruled by the linear behaviour with slope of -1 in the log-log representation, indicating that the sample is already in the ohmic region [147].

Regarding the imaginary part of AC conductivity (Fig. 3.68 b), we observe a maximum and a minimum corresponding to the maximum charge accumulation (MWS plateau) and the high frequency plateau (high frequency permittivity limit), respectively.

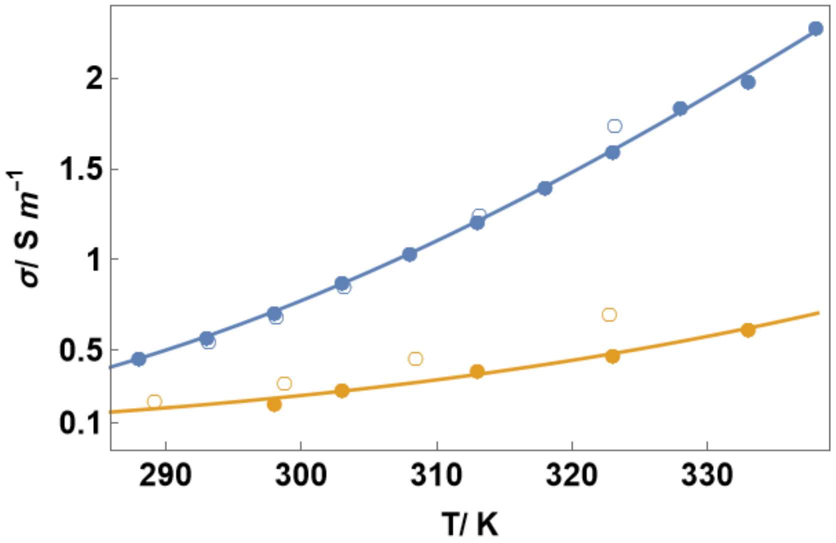

Figure 3.67. Ionic conductivity by BBDS (filed dots) and by conductimeter (empty dots) of $[C_2Im][NO_3]$ (blue dots) and $[C_4C_1Pyrr][TFSI]$ (orange squares). Lines represent VFT fitting.

Table 3.27. Comparison of ionic conductivity of $[C_2Im][NO_3]$ obtained by conductimeter and by BBDS

	$[C_2Im][NO_3]$	
Temperature	*Conductimeter /mS·cm^{-1}*	*BBDS /mS·cm^{-1}*
323	*17.38*	*16.00*
313	*12.44*	*12.13*
303	*8.53*	*8.73*
298	*6.9*	*7.07*
293	*5.48*	*5.75*

Table 3.28. Fitting parameters for pure $[C_2Im][NO_3]$ by bbds means.

	$[C_2Im][NO_3]$		
Sample	*σ_∞ /S·m^{-1}*	*$E_a \cdot 10^{-3}$/ eV*	*T_g/K*
$[C_2Im][NO_3]$	*36 ± 11*	*32 ± 6*	*201 ± 11*
	$[C_4C_1Pyrr][TFSI]$		
Sample	*σ_∞/ S·m^{-1}*	*$E_a \cdot 10^{-3}$/ eV*	
$[C_4C_1Pyrr][TFSI]$	*2300 ± 1400*	*236 ± 16*	

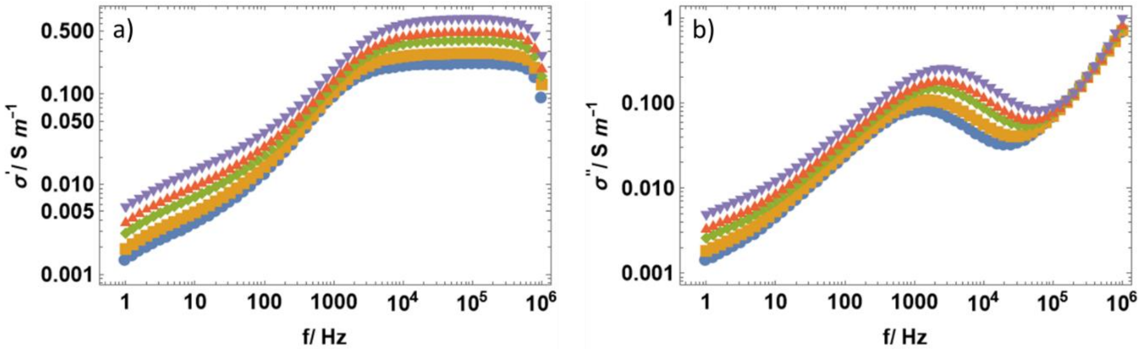

Figure 3.68. Complex AC conductivity, a) real and b) imaginary part of AC conductivity of 1-Butyl-1-methylpyrrolidinium bis(trifluoromethylsulfonyl)imide liquid form respectively.

3.5.2.2. [C_2Im][NO_3] mixtures with different salts (liquid form)

To analyze the effect of the salt addition on electrochemical response, the protic IL [C_2Im][NO_3] was selected for several reasons, mainly its high ionic conductivity and the numerous available salts with the common anion, as well as the affordable price of all these compounds.

For this study, the BBDS analysis of mixtures of [C_2Im][NO_3] + $M(NO_3)_n$ (M=Li, Mg, Al) at different concentrations versus temperature was performed. Fig. 3.69 shows the frequency dependence of ε' and ε'' curves recorded at different temperatures in the 20 Hz-10^5 Hz frequency range for pure [C_2Im][NO_3] (a,b), and its salt saturated mixtures [C_2Im][NO_3] + $LiNO_3$ at 3 molal (c,d), [C_2Im][NO_3] + $Mg(NO_3)_2$ 2 molal (e,f) and finally for [C_2Im][NO_3] + $Al(NO_3)_3$ at 1 molal(g,h). The rest of the figures can be found in the Annex Figs. A1-A13.

The addition of lithium salt induces changes on the low frequency plateau (maximum EP or MWS effect) of the real part [$\varepsilon'(\omega)$], a clear increase in frequency domain, with regards to pure IL, probably due to the mobility of the ions, which is higher when the monovalent lithium salt is added, and are easily accumulated in the electrodes, while the frequency of the applied excitation (electric field) is low. Magnesium and aluminum salt addition did not show significant changes regarding the pure IL. The changes in the spectroscopical window of the different presented regimes do not depend on the added salt concentration, but only in the chosen cation (Li, Mg or Al) at constant frequency range.

As mentioned in the materials and methods section [19], Debye and Cole-Cole approximations are models used to describe the frequency-dependent dielectric properties of materials with relaxation processes. Summarizing the main aspect indicated in materials and methods, while the Debye approximation is appropriate for materials with a narrow distribution of relaxation times, because this model assumes a single relaxation time for the material studied. A Cole-Cole approximation is used in cases where the relaxation time distribution is broad and cannot be modelled by the Debye equation.

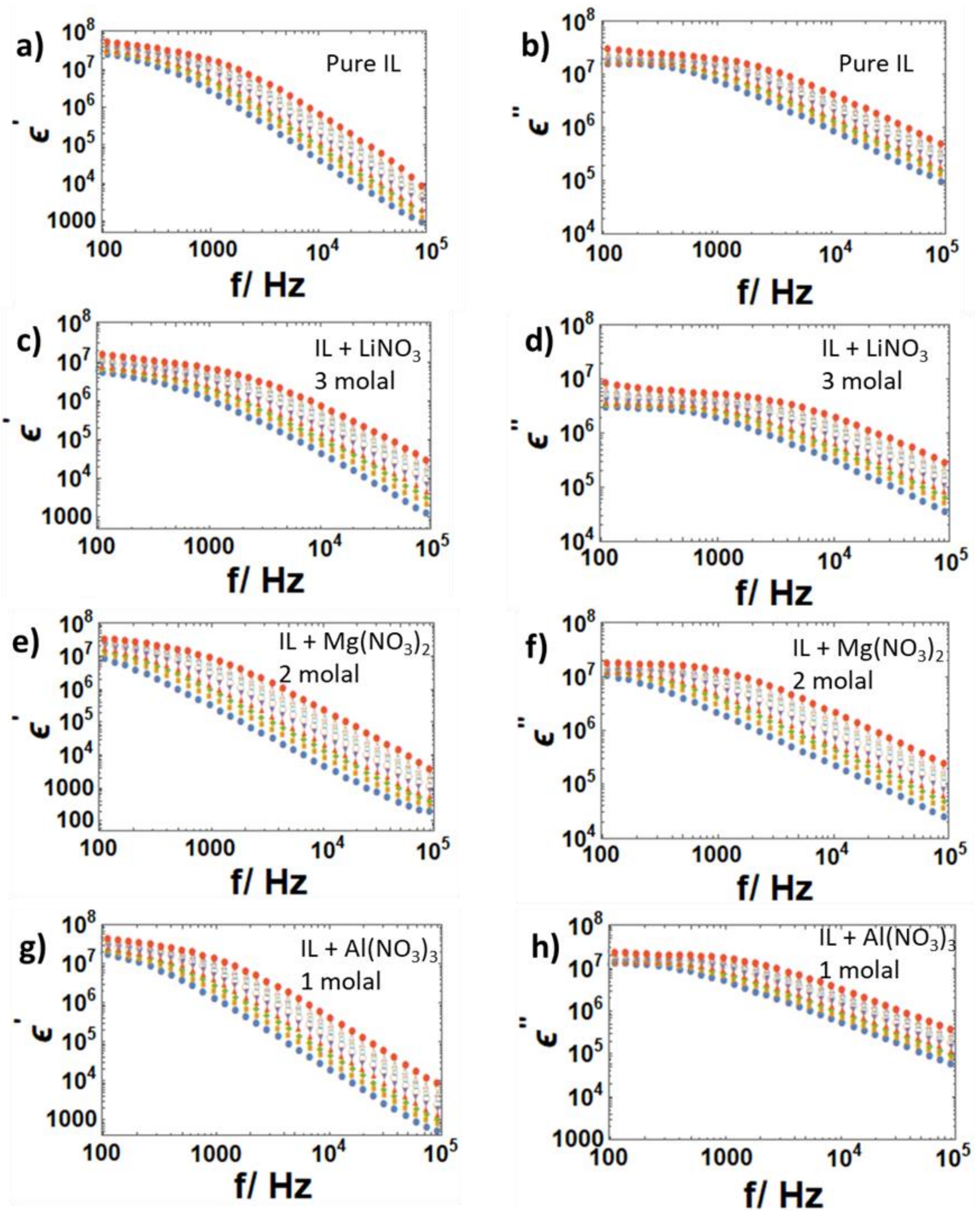

Figure 3.69. Dielectric spectroscopy of liquid $[C_2Im][NO_3]$ with different salts, a) is the real part and b) the imaginary part for pure IL. c) is the real part and d) the imaginary part for IL + $LiNO_3$ at 3 molal. e) is the real part and f) the imaginary part for IL + $Mg(NO_3)_2$ at 2 molal. g) is the real part and h) the imaginary part for IL + $Al(NO_3)_2$·at 1 molal. Blue filled dots correspond to 288 K, orange filled squares 293 K, green filled diamonds 298 K, red filled triangles 303 K, purple filled triangle 308 K, brown empty dots 313 K, blue empty squares 318 K, yellow empty diamonds 323 K, purple empty triangles 328 K, green empty triangles 333 K and red filled dots 338 K.

The Cole-Cole plot of the pure IL and saturated mixtures at different temperatures are shown in Fig. 3.70. Firstly, observation of the Cole-Cole plot is a distorted semicircle in low frequency region as in the case of pure IL, and as mentioned before, this is due to the nonaligned movement of ions with respect to electrical field lines [142]. Table 3.29 shows the fitted parameters such as dielectric permittivity $\omega \rightarrow 0$ (or static permittivity, ε_s), the permittivity at $\omega \rightarrow \infty$ (or high frequency limit of the permittivity, ε_∞) and relaxation times (τ) corresponding to the Debye approximation. As happens with the pure IL, the relaxation time decreases with temperature, which is related to the behavior of the mobility of the ions in the bulk electrolyte. The Debye fit for mixtures does not change significantly with regards to the pure IL.

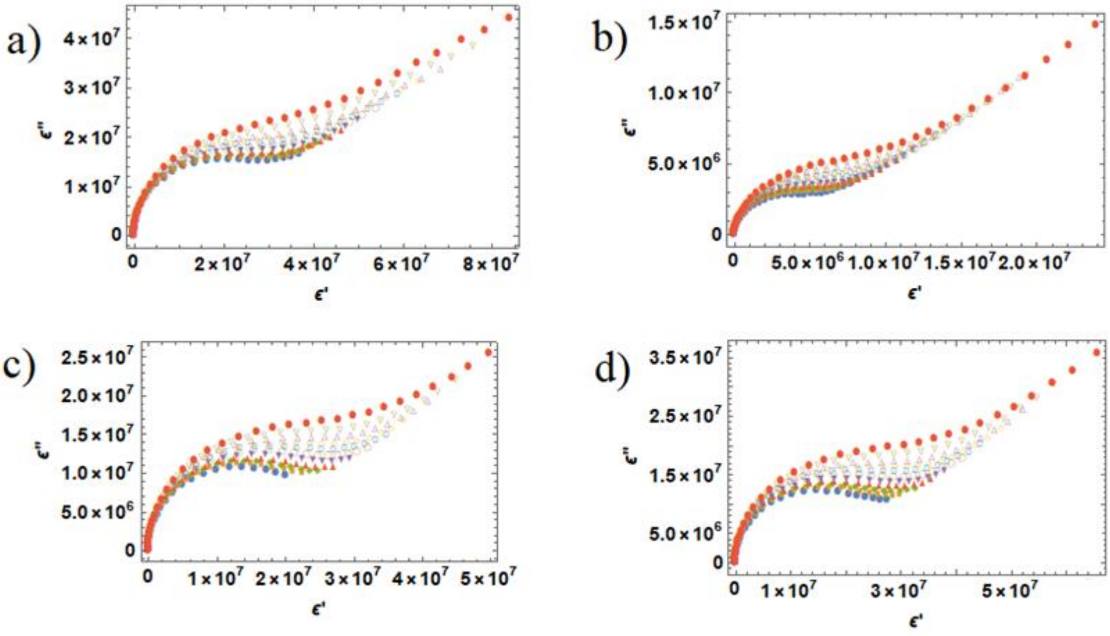

Figure 3.70. Cole-Cole plot for pure ILs and its mixtures at saturated concentrations of $[C_2Im][NO_3]$ and different salts at different temperatures. a) $[C_2Im][NO_3]$ pure, b) $[C_2Im][NO_3] + LiNO_3$ at 3 molal, c) $[C_2Im][NO_3] + Mg(NO_3)_2$ at 2 molal and d) $[C_2Im][NO_3] + Al(NO_3)_3$ at 1 molal. Blue filled dots correspond to 288 K, orange filled squares 293 K, green filled diamonds 298 K, red filled triangles 303 K, purple filled triangle 308 K, brown empty dots 313 K, blue empty squares 318 K, yellow empty diamonds 323 K, purple empty triangles 328 K, green empty triangles 333 K and red filled dots 338 K.

Table 3.29. Fitting parameters of Debye relaxation model for $[C_2Im][NO_3]$ and salts mixtures with studied salts at different concentrations

	Pure $[C_2Im][NO_3]$		
T(K)	ε_s ($\cdot 10^7$)	ε_∞	τ (s) 10^{-4} (s)
288	2.52 ± 0.04	680 ± 90	4.71 ± 0.03
293	2.56 ± 0.04	780 ± 130	3.779 ± 0.016
298	2.60 ± 0.04	1200 ± 150	3.107 ± 0.015
303	2.62 ± 0.05	1100 ± 200	2.577 ± 0.013
308	2.66 ± 0.05	2300 ± 300	2.174 ± 0.011

313	2.69 ± 0.06	2500 ± 400	1.852 ± 0.009
318	2.71 ± 0.07	1800 ± 400	1.591 ± 0.008
323	2.71 ± 0.07	1400 ± 600	1.392 ± 0.007
328	2.78 ± 0.08	3500 ± 700	1.260 ± 0.006
333	2.80 ± 0.10	2200 ± 800	1.121 ± 0.005
338	2.81 ± 0.12	1400 ± 900	1.010 ± 0.004

[C$_2$Im][NO$_3$] + LiNO$_3$ 0.5 m

T(K)	ε_s (·10^6)	ε_∞	τ (s) 10^{-4} (s)
293	3.24 ± 0.11	2300 ± 200	0.685 ± 0.010
298	3.57 ± 0.11	2250 ± 100	0.609 ± 0.010
303	3.80 ± 0.12	2290 ± 120	0.545 ± 0.010
308	4.21 ± 0.12	6600 ± 400	0.494 ± 0.009
313	4.56 ± 0.13	2620 ± 180	0.454 ± 0.009
318	4.89 ± 0.13	2700 ± 200	0.421 ± 0.009
323	5.22 ± 0.15	4300 ± 300	0.382 ± 0.009
328	5.56 ± 0.15	2700 ± 300	0.363 ± 0.009
333	5.90 ± 0.16	2100 ± 400	0.350 ± 0.009
338	6.15 ± 0.17	12300 ± 500	0.325 ± 0.009

[C$_2$Im][NO$_3$] + LiNO$_3$ 1 m

T(K)	ε_s (·10^7)	ε_∞	τ (s) 10^{-4} (s)
288	1.08 ± 0.02	920 ± 130	2.62 ± 0.02
293	1.16 ± 0.03	1260 ± 180	2.24 ± 0.02
298	1.24 ± 0.03	1700 ± 200	1.93 ± 0.02
303	1.27 ± 0.03	2300 ± 300	1.605 ± 0.018
308	1.30 ± 0.03	3000 ± 400	1.341 ± 0.016
313	1.39 ± 0.03	3900 ± 600	1.209 ± 0.016
318	1.48 ± 0.04	4900 ± 700	1.107 ± 0.017
323	1.56 ± 0.04	5900 ± 900	1.034 ± 0.018
328	1.65 ± 0.04	7300 ± 1200	0.965 ± 0.018
333	1.73 ± 0.04	9000 ± 1400	0.815 ± 0.017
338	1.77 ± 0.04	12100 ± 1400	0.794 ± 0.016

[C$_2$Im][NO$_3$] + LiNO$_3$ 2 m

T(K)	ε_s (·10^7)	ε_∞	τ (s) 10^{-4} (s)
288	7.74 ± 0.16	430 ± 70	3.02 ± 0.02
293	8.60 ± 0.18	670 ± 130	2.45 ± 0.03
298	9.19 ± 0.18	920 ± 180	2.09 ± 0.03
303	9.5 ± 0.2	1200 ± 200	1.70 ± 0.02
308	9.8 ± 0.2	1600 ± 300	1.40 ± 0.02
313	10.1 ± 0.2	2200 ± 400	1.166 ± 0.018
318	10.5 ± 0.2	2700 ± 400	1.064 ± 0.017
323	11.0 ± 0.3	3700 ± 600	0.894 ± 0.015
328	11.10 ± 0.03	4200 ± 400	0.774 ± 0.012
333	11.29 ± 0.03	4700 ± 300	0.676 ± 0.011
338	11.58 ± 0.03	5200 ± 300	0.644 ± 0.011

[C_2Im][NO_3] + $LiNO_3$ 3 m

T(K)	ε_s (·10^6)	ε_∞	τ (s) 10^{-4} (s)
288	3.89 ± 0.14	650 ± 70	2.36 ± 0.04
293	4.39 ± 0.15	1100 ± 100	2.01 ± 0.04
298	4.64 ± 0.16	1370 ± 130	1.59 ± 0.03
303	4.86 ± 0.17	1900 ± 170	1.29 ± 0.02
308	5.05 ± 0.18	2800 ± 200	1.063 ± 0.017
313	5.59 ± 0.19	3600 ± 300	0.954 ± 0.017
318	6.1 ± 0.2	4600 ± 400	0.872 ± 0.017
323	6.7 ± 0.2	5900 ± 500	0.804 ± 0.017
328	7.3 ± 0.2	7400 ± 600	0.747 ± 0.017
333	7.4 ± 0.2	8900 ± 700	0.650 ± 0.014
338	7.9 ± 0.2	10500 ± 900	0.622 ± 0.015

[C_2Im][NO_3] + $Mg(NO_3)_2\cdot 6H_2O$ 0.5 m

T(K)	ε_s (·10^7)	ε_∞	τ (s) 10^{-4} (s)
288	1.71 ± 0.03	570 ± 90	5.52 ± 0.04
293	1.77 ± 0.03	810 ± 140	4.37 ± 0.03
298	1.83 ± 0.03	1110 ± 190	3.51 ± 0.02
303	1.89 ± 0.03	1500 ± 200	2.87 ± 0.02
308	2.00 ± 0.03	1800 ± 300	2.49 ± 0.02
313	2.06 ± 0.03	2300 ± 300	2.10 ± 0.03
318	2.10 ± 0.04	2900 ± 400	1.791 ± 0.015
323	2.15 ± 0.04	3500 ± 500	1.542 ± 0.013
328	2.19 ± 0.04	4200 ± 600	1.344 ± 0.011
333	2.21 ± 0.04	3600 ± 300	1.181 ± 0.009
338	2.23 ± 0.04	9000 ± 700	1.052 ± 0.008

[C_2Im][NO_3] + $Mg(NO_3)_2\cdot 6H_2O$ 1 m

T(K)	ε_s (·10^7)	ε_∞	τ (s) 10^{-4} (s)
288	1.83 ± 0.04	590 ± 50	7.78 ± 0.03
293	1.96 ± 0.04	2030 ± 40	6.20 ± 0.02
298	2.08 ± 0.04	860 ± 100	5.00 ± 0.02
303	2.20 ± 0.04	1650 ± 140	4.16 ± 0.02
308	2.31 ± 0.04	1600 ± 200	3.567 ± 0.018
313	2.46 ± 0.04	1500 ± 300	3.001 ± 0.018
318	2.51 ± 0.04	1900 ± 400	2.535 ± 0.017
323	2.64 ± 0.04	2200 ± 400	2.235± 0.017
328	2.76 ± 0.06	2300 ± 600	2.007 ± 0.019
333	2.89 ± 0.05	3500 ± 500	1.827 ± 0.018
338	3.12 ± 0.06	3700 ± 900	1.805 ± 0.018

[C_2Im][NO_3] + $Mg(NO_3)_2\cdot 6H_2O$ 2 m

T(K)	ε_s (·10^7)	ε_∞	τ (s) 10^{-4} (s)
288	1.77 ± 0.03	180 ± 20	13.54 ± 0.06
293	1.84 ± 0.03	250 ± 30	10.16 ± 0.05

298	1.92 ± 0.03	350 ± 50	7.71 ± 0.04
303	1.99 ± 0.03	480 ± 80	6.11 ± 0.03
308	2.06 ± 0.04	660 ± 120	4.85 ± 0.02
313	2.12 ± 0.04	870 ± 170	3.94 ± 0.02
318	2.17 ± 0.04	1100 ± 200	3.253 ± 0.016
323	2.22 ± 0.05	1400 ± 300	2.748 ± 0.015
328	2.26 ± 0.05	1700 ± 400	2.324 ± 0.014
333	2.31 ± 0.06	2100 ± 400	2.034 ± 0.012
338	2.32 ± 0.06	2400 ± 400	1.764 ± 0.010
[C_2Im][NO_3] + Al(NO_3)$_3$·9H_2O 0.5 m			
T(K)	εs (·107)	ε∞	τ (s) 10-4 (s)
288	4.53 ± 0.11	1070 ± 120	1.94 ± 0.05
293	4.84 ± 0.11	1440 ± 90	1.61 ± 0.04
298	4.96 ± 0.12	1730 ± 80	1.31± 0.04
303	5.07 ± 0.13	2240 ± 100	1.09 ± 0.03
308	5.20 ± 0.13	2750 ± 120	0.93 ± 0.03
313	5.29 ± 0.14	3820 ± 160	0.78 ± 0.02
318	5.37 ± 0.16	3130 ± 190	0.67 ± 0.02
323	5.63 ± 0.18	8800 ± 200	0.556 ± 0.012
328	5.75 ± 0.18	4400 ± 300	0.51 ± 0.02
333	5.83 ± 0.19	4000 ± 300	0.44 ± 0.02
338	5.7 ± 0.2	8500 ± 400	0.421 ± 0.015
[C_2Im][NO_3] + Al(NO_3)$_3$·9H_2O 1 m			
T(K)	ε_s (·10^7)	ε_∞	τ (s) 10^{-4} (s)
288	2.29 ± 0.03	460 ± 90	7.48 ± 0.07
293	2.37 ± 0.03	630 ± 130	6.05 ± 0.06
298	2.45 ± 0.03	860 ± 180	4.87 ± 0.05
303	2.54 ± 0.03	1100 ± 300	4.00 ± 0.04
308	2.60 ± 0.04	1500 ± 300	3.38 ± 0.03
313	2.67 ± 0.04	1900 ± 400	2.85 ± 0.03
318	2.73 ± 0.04	2300 ± 500	2.451 ± 0.019
323	2.79 ± 0.04	2800 ± 500	2.122 ± 0.017
328	2.85 ± 0.05	3300 ± 600	1.863 ± 0.015
333	2.92 ± 0.05	4000 ± 700	1.634 ± 0.013
338	2.96 ± 0.05	4400 ± 300	1.497 ± 0.011

The relaxation times obtained from the Debye approximation against temperature for a) pure [C_2Im][NO_3], b) [C_2Im][NO_3] + LiNO_3 at 3 molal, c) [C_2Im][NO_3] + Mg(NO_3)$_2$ at 2 molal and d) [C_2Im][NO_3] + Al(NO_3)$_3$ at 1 molal are presented in Fig 3.71. These results were fitted to Eq. (3.19) and lines in these figures represent the fits. Fitting parameters are presented in Table 3.30.

$$\tau = A \exp\left[\frac{B}{(T-C)}\right] \tag{3.19}$$

A is the high temperature limit relaxation time (τ_∞), $B = E_a/k_B$, where E_a is the activation energy of the dielectric excitation (in eV per particle) and k_B is the Boltzmann constant, finally C is the ideal glass transition temperature (T_g).

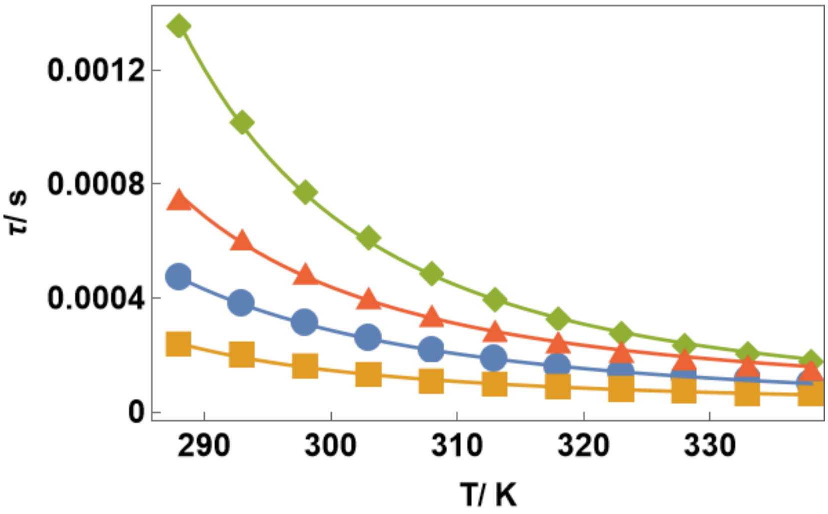

Figure 3.71. Relaxation times vs temperature in the Debye aproximation of a) $[C_2Im][NO_3]$ (blue dots), $[C_2Im][NO_3]$ + $LiNO_3$ at 3 molal (orange squares), $[C_2Im][NO_3]$ + $Mg(NO_3)_2$ at 2 molal (Green diamonds) and $[C_2Im][NO_3]$ + $Al(NO_3)_3$ at 1 molal (red triangles). Lines represent the corresponding VFT fit.

Table 3.30. VFT fitting parameters for the relaxation time against temperature of the $[C_2Im][NO_3]$ mixtures with nitrate salts at different concentrations.

Sample	$\tau_\infty \cdot 10^{-6}$ /s	E_a/ eV ($x10^{-3}$)	T_g/K
Pure IL	*4.3 ± 0.7*	*40 ± 3*	*187 ± 4*
IL + $LiNO_3$ at 0.5m	*5.3 ± 1.9*	*23 ± 8*	*190 ± 20*
IL + $LiNO_3$ at 1m	*10 ± 5*	*24 ± 9*	*203 ± 19*
IL + $LiNO_3$ at 2m	*4 ± 2*	*32 ± 12*	*200 ± 20*
IL + $LiNO_3$ at 3m	*10 ± 5*	*17 ± 6*	*225 ± 15*
IL + $Mg(NO_3)_2 \cdot 6H_2O$ at 0.5m	*6.3 ± 1.9*	*34 ± 5*	*200 ± 8*
IL + $Mg(NO_3)_2 \cdot 6H_2O$ at 1m	*14 ± 4*	*28 ± 5*	*206 ± 9*
IL + $Mg(NO_3)_2 \cdot 6H_2O$ at 2m	*8 ± 3*	*34 ± 5*	*210 ± 6*
IL + $Al(NO_3)_3 \cdot 9H_2O$ at 0.5m	*6 ± 3*	*21 ± 8*	*220 ± 16*
IL + $Al(NO_3)_3 \cdot 9H_2O$ at 1m	*19 ± 8*	*22 ± 6*	*220 ± 11*

The fitted activation energy is in good agreement with that obtained by the VFT fitting of the conductivity results except for lithium salt 1 molal as will be analyzed latter.

As pointed out in the materials and methods (section 2), the Cole-Cole model is mainly used to visualize the deviation of the dielectric behavior of the sample analyzed from the Debye model, which is based on a single relaxation time. In our cases, the deviation is clearly observed and the second proposed model, the Cole-Cole model, was also considered. Fig. 3.72 shows the fitting to the Cole-Cole model (see materials and methods for the description) for the pure IL at 288 K and 338 K, and, as can be seen, the Cole-Cole model excellently describes the dielectric behavior of the analyzed samples. Essentially, Cole-Cole analysis considers a spectrum of the relaxation times through the β parameter (see Eq. (2.15) of the materials and methods section). Regarding this question, β ranges between 1 and 0.83, being 1 the Debye relaxation, and β decreases with temperature, which means that the relaxation times spectrum becomes broader with increasing temperature but is still close to unity ($\beta \approx 1$). Hence, our results are compatible with a narrow spectrum of relaxation time due to the small size of the IL molecule .

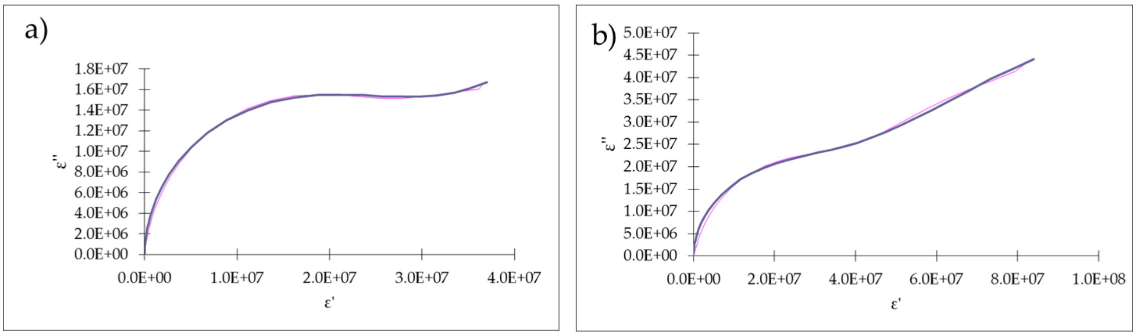

Figure 3.72. Cole-Cole data plot (pink line) and Cole-Cole fitting (blue line) of $[C_2Im][NO_3]$ pure IL at a) 288K and b) 338 K.

On the other hand, the ionic conductivity obtained from the imaginary part of the dielectric permittivity, is shown in Fig. 3.73. A decrease in conductivity with the salt addition is observed for all cases, which can be explained by the increase of viscosity, reported previously, resulting in a reduced mobility of the ions and consequently in a reduction of the transport number [89]. Although, interestingly, room temperature ionic conductivity ranges between 0.7 $S \cdot m^{-1}$ and 0.35 $S \cdot m^{-1}$, for all the samples, allowing the application of these mixtures in potential electrolyte candidates for batteries and energy storage devices. For a given temperature and concentration, the conductivity of the IL-salt mixtures follows the trend $\sigma_{Li} > \sigma_{Al} > \sigma_{Mg}$.

The obtained ionic conductivity, as in the case of pure IL, is well described by the VFT equation. From Table 3.31, one can notice a slight tendency of the activation energy to decrease with the salt addition for activation energy for all studied samples as expected. Despite similar values obtained through VFT fitting, mixtures with aluminum salt seem to have the highest ideal glass transition temperature. The obtained ideal glass transition temperatures are in good agreement with those obtained by the DSC method, considering the uncertainties of the fitting obtained parameters (see thermal characterization).

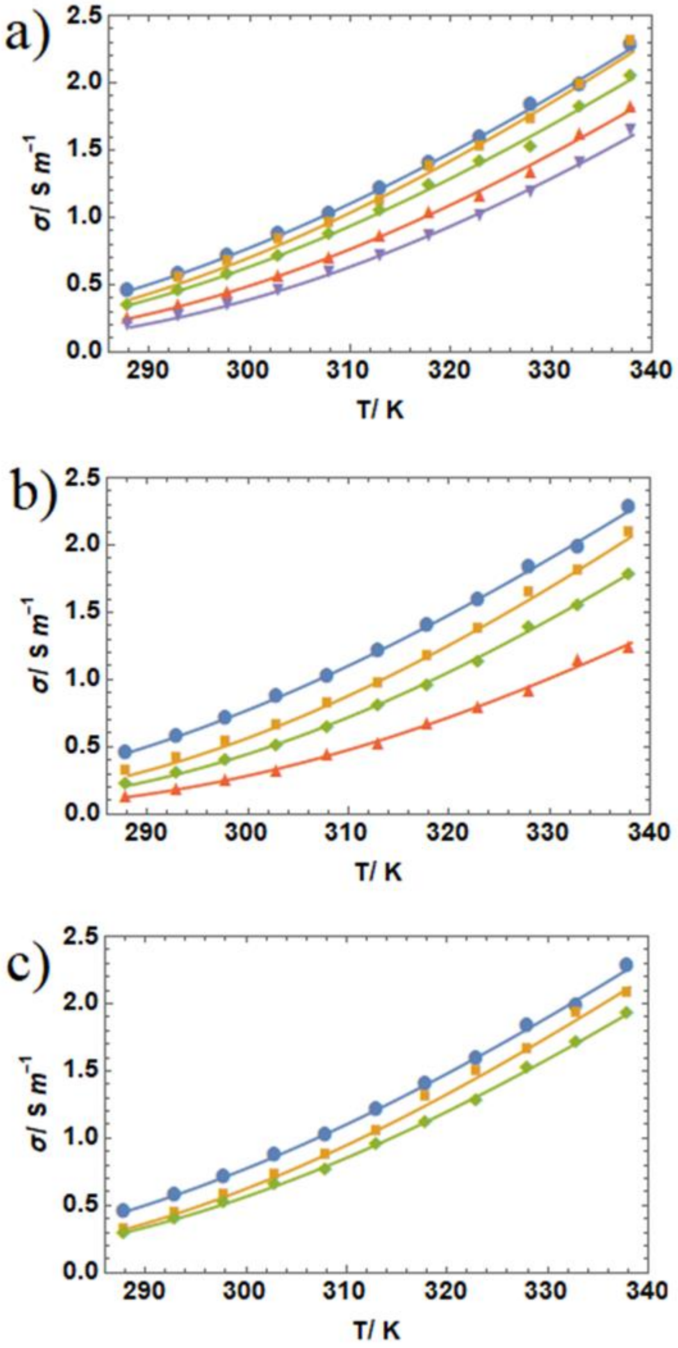

Figure 3.73. a) Ionic conductivity of [C_2Im][NO_3] + $LiNO_3$ mixtures at different concentrations. Blue dots represent pure IL, orange squares IL + salt at 0.5 m, green diamonds IL + salt at 1 m, upward red triangles IL + salt at 2 m and downward purple triangles represent IL + salt at 3 m. b) Ionic conductivity of [C_2Im]$^+$ [NO_3]$^-$ + $Mg(NO_3)_2·6H_2O$ mixtures at different concentrations. Blue dots represent pure IL, orange squares IL + salt at 0.5 m, green diamonds IL + salt at 1 m, upward red triangles IL + salt at 2 m. c) Ionic conductivity of [C_2Im]$^+$ [NO_3]$^-$ + $Al(NO_3)_3·9H_2O$ mixtures at different concentrations. Blue dots represent pure IL, orange squares IL + salt at 0.5 m, green diamonds IL + salt at 1 m. Lines represent the corresponding VFT fitting.

Table 3.31. Obtained fitting parameters and standard error for ionic conductivity data from Fig. 3.73 by applying VFT equation (Eq 3.15) of the $[C_2Im][NO_3]$ with nitrate salts at different concentrations.

Sample	σ_∞ /S·m^{-1}	E_a/ eV ($x10^{-3}$)	T_g/K
Pure IL	*36 ± 11*	*32 ± 6*	*201 ± 11*
IL + $LiNO_3$ at 0.5m	*35 ± 9*	*31 ± 6*	*209 ± 11*
IL + $LiNO_3$ at 1m	*34 ± 11*	*31 ± 9*	*208 ± 15*
IL + $LiNO_3$ at 2m	*35 ± 9*	*32 ± 9*	*213 ± 15*
IL + $LiNO_3$ at 3m	*35 ± 10*	*32 ± 8*	*217 ± 12*
IL + $Mg(NO_3)_2·6H_2O$ at 0.5m	*35 ± 13*	*30 ± 6*	*216 ± 11*
IL + $Mg(NO_3)_2·6H_2O$ at 1m	*35 ± 13*	*31 ± 6*	*219 ± 10*
IL + $Mg(NO_3)_2·6H_2O$ at 2m	*30 ± 18*	*32 ± 10*	*219 ± 16*
IL + $Al(NO_3)_3·9H_2O$ at 0.5m	*30 ± 11*	*28 ± 7*	*217 ± 12*
IL + $Al(NO_3)_3·9H_2O$ at 1m	*35 ± 10*	*32 ± 6*	*210 ± 9*

3.5.2.3. Effect of gelation

The effect on the dielectric permittivity of gelation has been analyzed for the IL $[C_4C_1Pyrr][TFSI]$, because this IL, in pure form (both liquid and gel spectra), has been selected to assay as electrolyte for a functional LIB as will be seen in galvanostatic charge/discharge with potential limitation (GCPL) experiences. The selection of this IL as battery electrolyte is based on different reasons such as their large liquid range, high thermal stability, high ionic conductivity, and, as will be seen in the next sections, large electrochemical window.

In Fig. 3.74 the dielectric permittivity of $[C_4C_1Pyrr][TFSI]$ in the liquid and gel states is shown. Both samples behave similarly, although small differences in the position of the maximum MWS frequency (low frequency plateau) and high frequency dielectric permittivity plateau, as can be seen in Fig. 3.74 a), while the imaginary part shows a similar ohmic regime than its liquid state (Fig. 3.74 b).

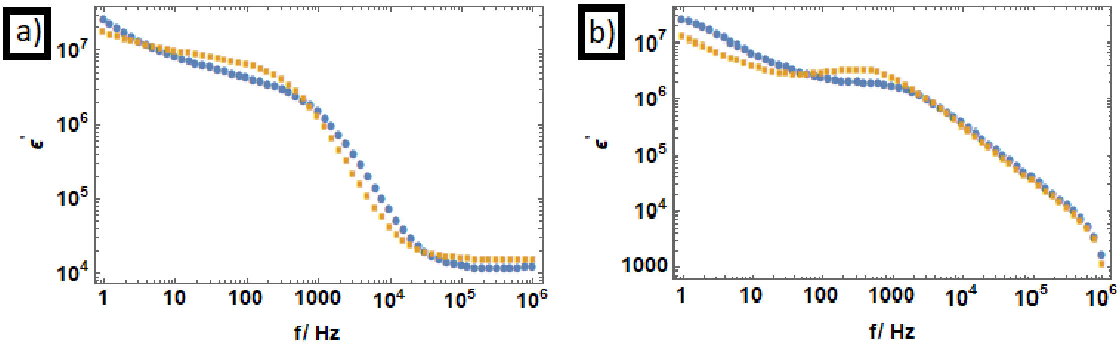

Figure 3.74. Comparison of dielectric permittivity of 1-Butyl-1-methylpyrrolidinium bis(trifluoromethylsulfonyl)imide in liquid (Blue dots) and gel (orange squares) state at 298 K. a) Real part and b) imaginary part

For gel samples, the MWS plateau frequency extends up to 167 Hz, and high frequency permittivity is reached at 3.2·10⁴ Hz for 298 K, while for liquid samples the MWS plateau extends up to 600 Hz, while high frequency permittivity is reached around 5·10⁴ Hz for the same temperature. For a better understanding, Fig 3.75 a) shows the frequency intervals, following the criterion of Jan Leys [126], highlighting that both frequency intervals are shifted down in the gel state relative to its liquid states. This indicates that nanoconfinement reduces ion mobility.

According to the second criterion, defined elsewhere [134], (Fig. 3.75 b), the MWS plateau (maximum EP), or the transition between zone I and zone II is observed at 31 Hz, while transition between zone II and zone III (no EP is presented in the sample, or the reaching of infinitum permittivity) is presented in a similar frequency than the other criterion, around 3.2·10⁴ Hz.

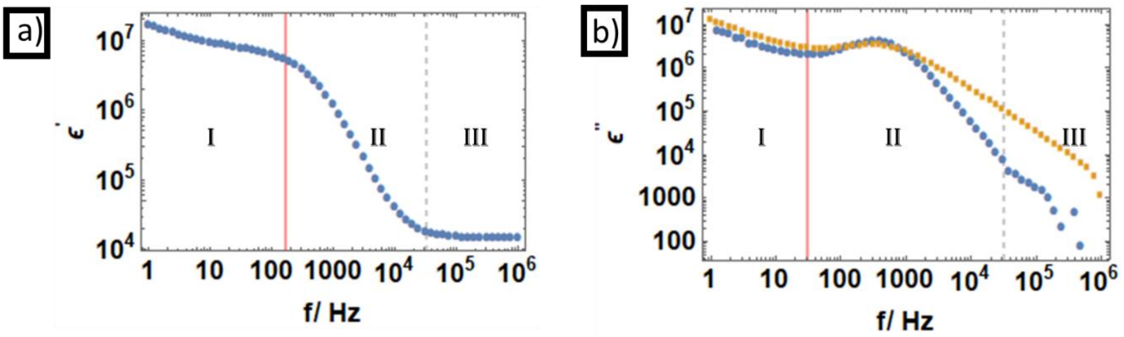

Figure 3.75. Dielectric permittivity of 1-Butyl-1-methylpyrrolidinium bis(trifluoromethylsulfonyl)imide in gel state at 298 K, a) real part and b) blue dots represent the ε''_{der} and orange dots represent the imaginary part of the dielectric constant.

On the other hand, the behavior of dielectric permittivity against temperature (Fig 3.76) is similar to the corresponding liquid state. Increasing temperature both frequencies (MWS plateau and high frequency plateau) shift up, because the ionic mobility of the nanoconfined ionic liquid increases as temperature rises.

As observed in Fig. 3.76 a), the low frequency plateau, which correspond to the maximum EP, widens the spectroscopical window while increasing the temperature, while the ohmic regime (Fig. 3.76 b) moves to higher frequencies while increasing temperature, similar to liquid state, but in the case of the gel state, the ohmic conduction law is reached at lower frequencies than as a liquid.

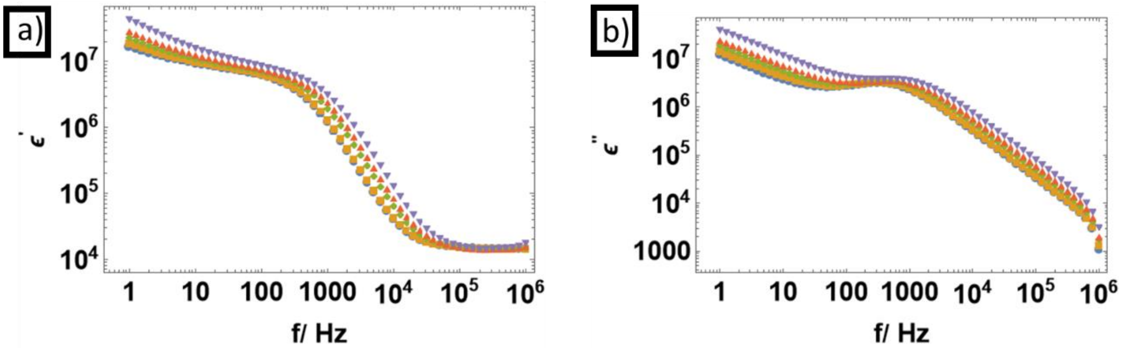

Figure 3.76. Dielectric permittivity of 1-Butyl-1-methylpyrrolidinium bis(trifluoromethylsulfonyl)imide in gel state, a) real part of dielectric spectroscopy, b) imaginary part of dielectric spectroscopy. Blue dots correspond to 298K, orange squares 303K, green diamonds 313, red upper triangles 323K and purple down triangles 333K.

There is visual confirmation that the EDL and EP is stronger in liquid state than in gel state by looking up the straight line (MWS effect) of the Cole- Cole plot (Fig. 3.77), characterized by a lower slope in gel than in liquid state. This renders to a higher charge accumulation in the walls of the electrodes in the liquid sample. Also, a single semicircle is obtained for all studied temperatures, and the increment of ionic mobility when increasing the temperature is observed. The low frequency crossover is not observed in the gel sample, indicating that the accumulations of the ions in the neighborhoods of the electrodes does not depend on the temperature for these samples.

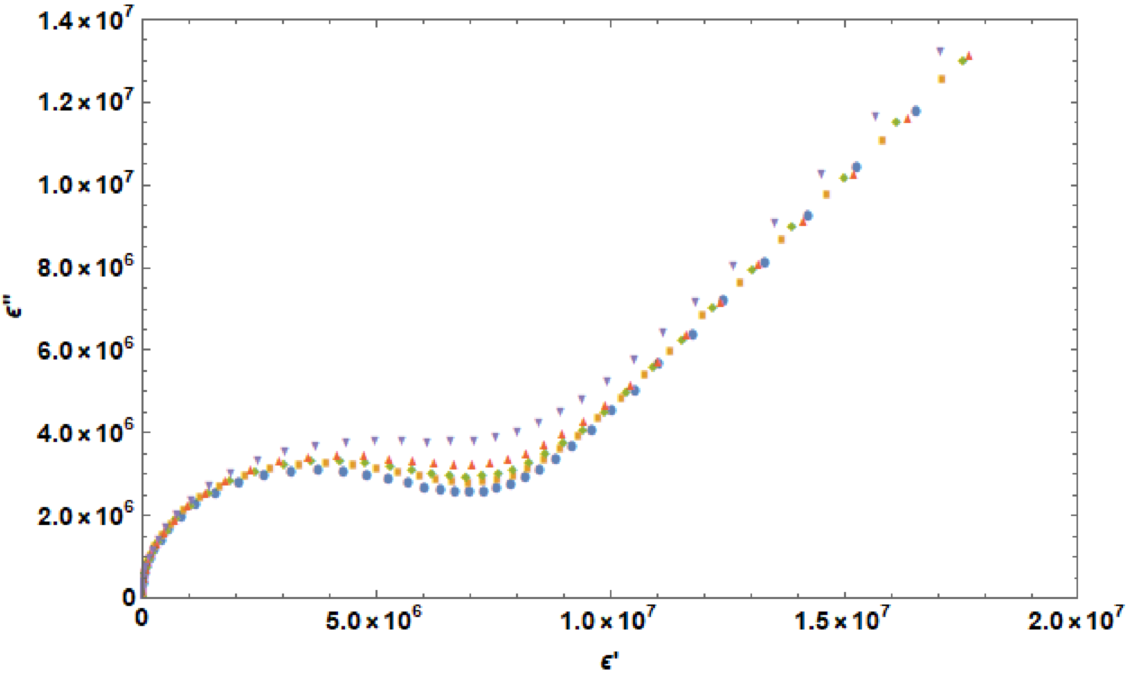

Figure 3.77. Cole-Cole plot of 1-Butyl-1-methylpyrrolidinium bis(trifluoromethylsulfonyl)imide in gel state. Blue dots correspond to 298K, orange squares 303K, green diamonds 313, red upper triangles 323K and purple down triangles 333K.

Table 3.32 summarizes the obtained fitting parameters for the Debye approximation. For liquid samples, static permittivity rises with temperature and high frequency permittivity remains constant for all temperatures. Relaxation time decreases with temperature, and it is more than twice as large as that in liquid state for all temperatures.

Table 3.32. Fitting parameters for dielectric spectroscopy on the Debye approximation of 1-Butyl-1-methylpyrrolidinium bis(trifluoromethylsulfonyl)imide in ionogels.

Sample	$\varepsilon_s \cdot 10^6$	ε_∞	$\tau_{real} \cdot 10^{-4}$	$\tau_{im} \cdot 10^{-4}$
298	6.24 ± 0.07	14223 ± 15	3.76 ± 0.06	3.75 ± 0.07
303	6.50 ± 0.08	14270 ± 30	3.69 ± 0.06	3.69 ± 0.07
313	6.54 ± 0.08	14160 ± 90	2.58 ± 0.04	2.53 ± 0.03
323	6.94 ± 0.09	14130 ± 100	2.30 ± 0.04	2.26 ± 0.04
333	7.48 ± 0.12	14100 ± 200	1.88 ± 0.03	1.83 ± 0.03

Following the methodology exposed in the study of pure ILs, the complex AC ionic conductivity of the gels of [C_4C_1Pyrr][TFSI] is shown in Fig. 3.78 (ionic AC conductivity of pure IL in liquid state is also presented for a better comparison). As can be seen, the sample in the gel phase (Fig. 3.78 a) reaches the characteristic plateau before the liquid one (Fig. 3.78 b), and as pointed out previously, this is probably because the ionic motion aligns easier with the direction of the electromagnetic field in the liquid phase.

The DC conductivity of ionogel obtained with the methodology indicated in the materials and methods section (Eq. (2.8)) is shown in Fig. 3.79. This conductivity is lower than that of the liquid sample for all the studied temperatures, as expected, but the ionic conductivity at 298 K is $\sigma = 1.86 \pm 0.12\ mS \cdot cm^{-1}$, which is a good value to consider the gel sample as a potential electrolyte [148]. Table 3.33 shows the corresponding Arrhenius fitting parameters, and as can be seen, the activation energy is similar for liquid and gel. This is an indicator that the foundations of ionic transport are the same in both systems.

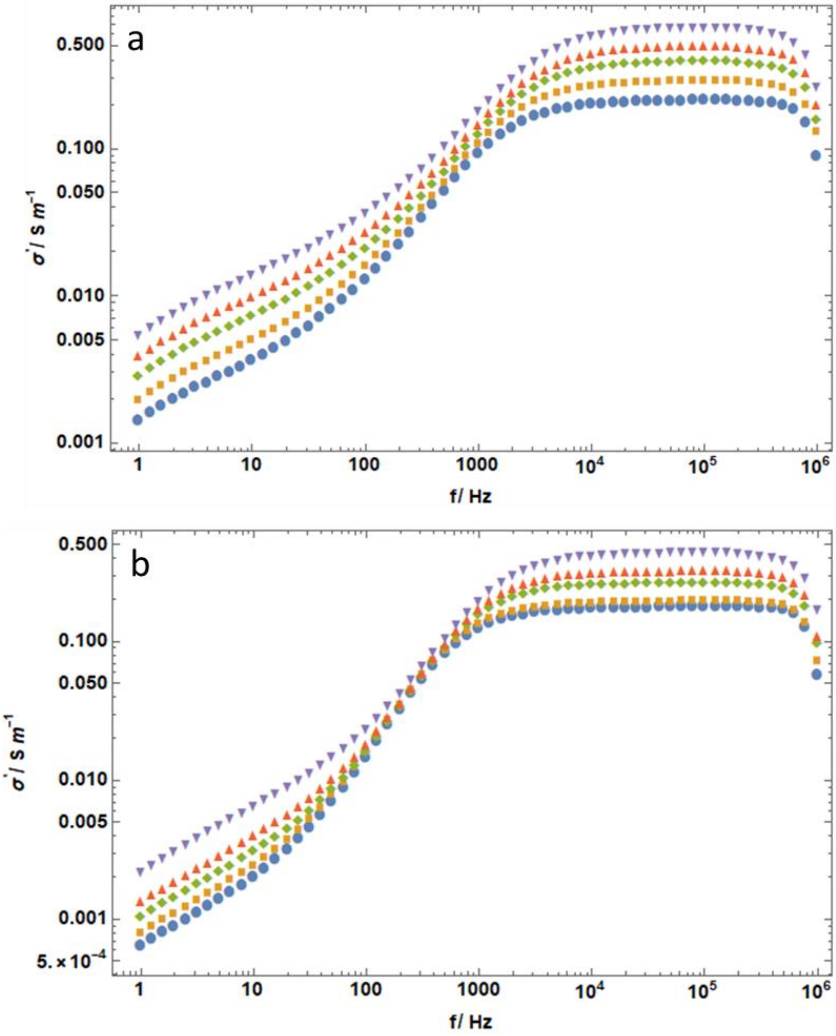

Figure 3.78. Real part of AC conductivity of [C_4C_1Pyrr][TFSI] of a) liquid and b) gel state respectively.

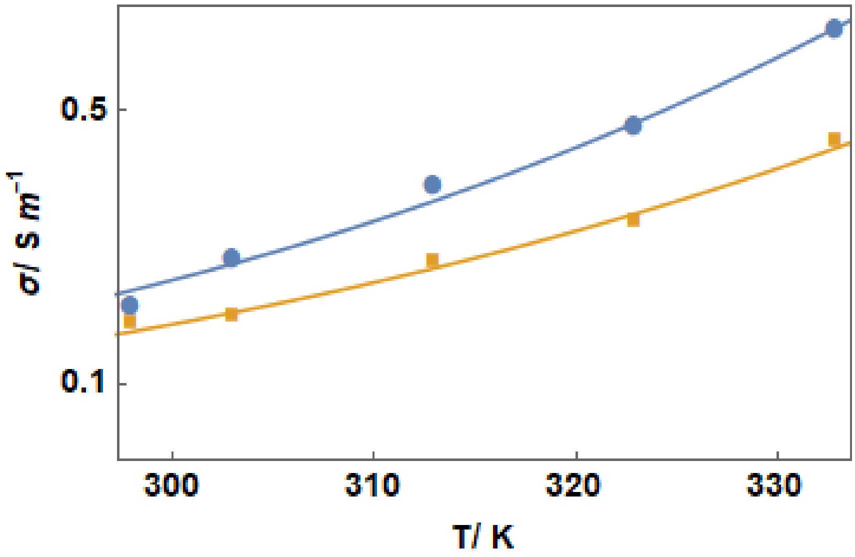

Figure 3.79. DC conductivity of 1-Butyl-1-methylpyrrolidinium bis(trifluoromethylsulfonyl)imide. Blue dots for liquid state and orange squares for gel state. Lines represent the corresponding Arrhenius fittings.

Table 3.33. Arrhenius fitting parameters for Fig. 3.79

Sample	*A/ S·m⁻¹*	*B /K*
Liquid	2300 ± 1400	-2740 ± 190
Gel	1200 ± 600	-2630 ± 150

3.5.3. Electrochemical Impedance Spectroscopy (EIS) of [C_4C_1Pyrr][TFSI]

Due to the suitable characteristics shown by the liquid and gel samples of [C_4C_1Pyrr][TFSI], such as high ionic conductivity, an evident dielectric relaxation, large liquid range, among others, studied during this thesis, the following studies are focused on this IL, in liquid and gel states as a potential candidate for the electrolyte of a fully operating LIB.

Fig. 3.80 shows the Bode Plot, i.e. the impedance module (a and c) and phase (b and d) against frequency, of [C_4C_1Pyrr][TFSI] liquid and gel state. As is recorded in the materials and methods section of this work, this ionogel was prepared following the two silica precursors route (see section 2.- materials and methods). The implantation of this route was performed to improve the mechanical stability of the gel samples to obtain a self-standing semisolid material, which can be handled without breaking or decomposition.

The impedance spectra of liquid sample shows a linear behavior in the low frequency region (between 10 – 1000 Hz), corresponding to the accumulation of charge at a blocking electrode, and another linear behavior beyond $2{\cdot}10^5$ Hz corresponding to the relaxation of the interfacial polarization, as will be remarked in the study of the dielectric constant. Additionally, the Bode plot shows a plateau in the frequency region between 3000 - 10^5 Hz, which was also reported by Zhao et al. [149] studying [C_4C_1Im][PF_6] in platinum blocking electrodes.

The behavior of the ionogel sample is similar to that of the liquid, although it presents a shift to lower frequencies due to the nanoconfinement restricting the mobility of the IL as mentioned before in BBDS section. The impedance module spectra also show a linear behavior in the low frequency region (from 3 to 400 Hz), related to the accumulation of charge at the blocking electrode, as in the case of the liquid sample. In the high frequency region (above 10^5 Hz) there is another linear behavior related to the interfacial polarization relaxation. At intermediate frequencies (1000 - 90000 Hz) the Bode plot shows a plateau.

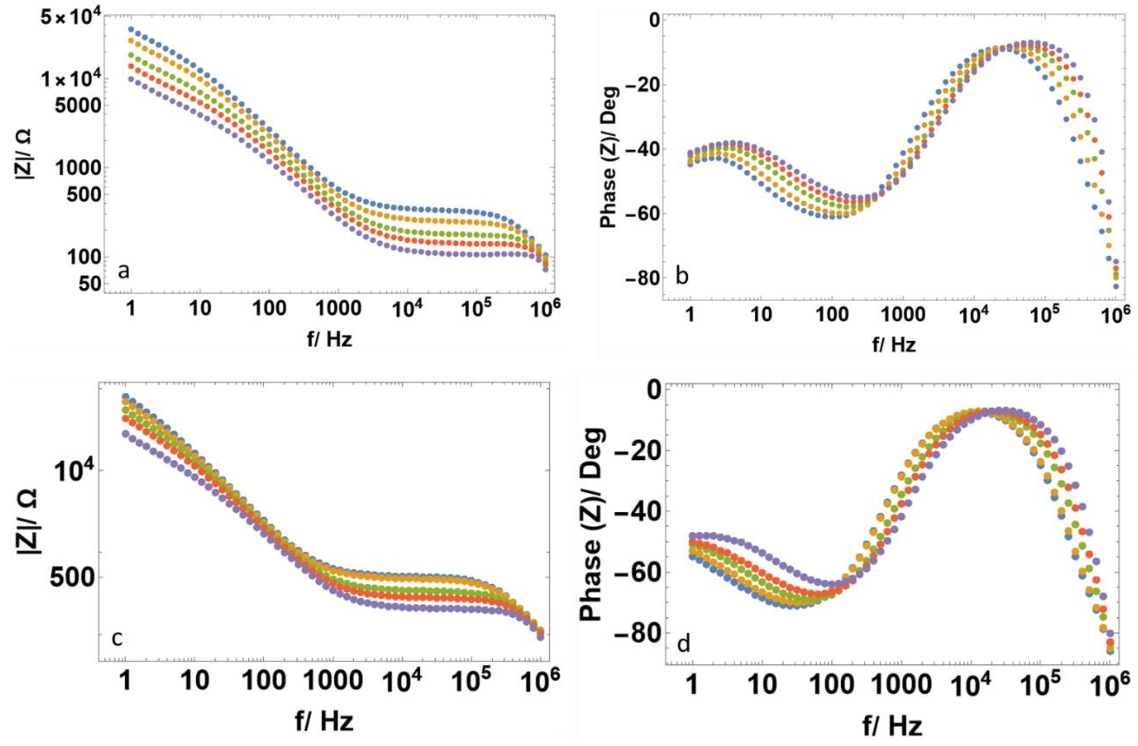

Figure 3.80. Bode Plot for the liquid and gel 1-Butyl-1-methylpyrrolidinium bis(trifluoromethylsulfonyl)imide. a) $|Z|$ vs frequency as a function of temperature in the liquid state and b) Phase between current and voltage vs frequency at different temperatures in the liquid state c) $|Z|$ vs frequency as a function of temperature in gel state and d) Phase between current and voltage vs frequency at different temperatures in the gel state. Blue dots represent 298 K, orange dots 303 K, green dots 313 K, red dots 323 K and purple dots 333 K.

The module of impedance decreases with increasing temperature for a given frequency in both liquid and gel samples, as expected, and the frequency range of charge accumulation and interfacial relaxation shifts to higher frequencies.

A typical Nyquist plot (graphical representation of the complex impedance of a system as a function of frequency) can be observed in Fig. 3.81 for the liquid and gel samples. The real part of the impedance is represented on the x-axis, while the imaginary part is represented on the y-axis, being characterized by a semicircle at high frequencies associated to the effect of the bulk electrolyte resistance (R_b), and a linear region at the low frequencies associated with charge accumulation in the blocking electrodes [150,151]. It is commonly used in control engineering and circuit analysis to analyze the stability of a system.

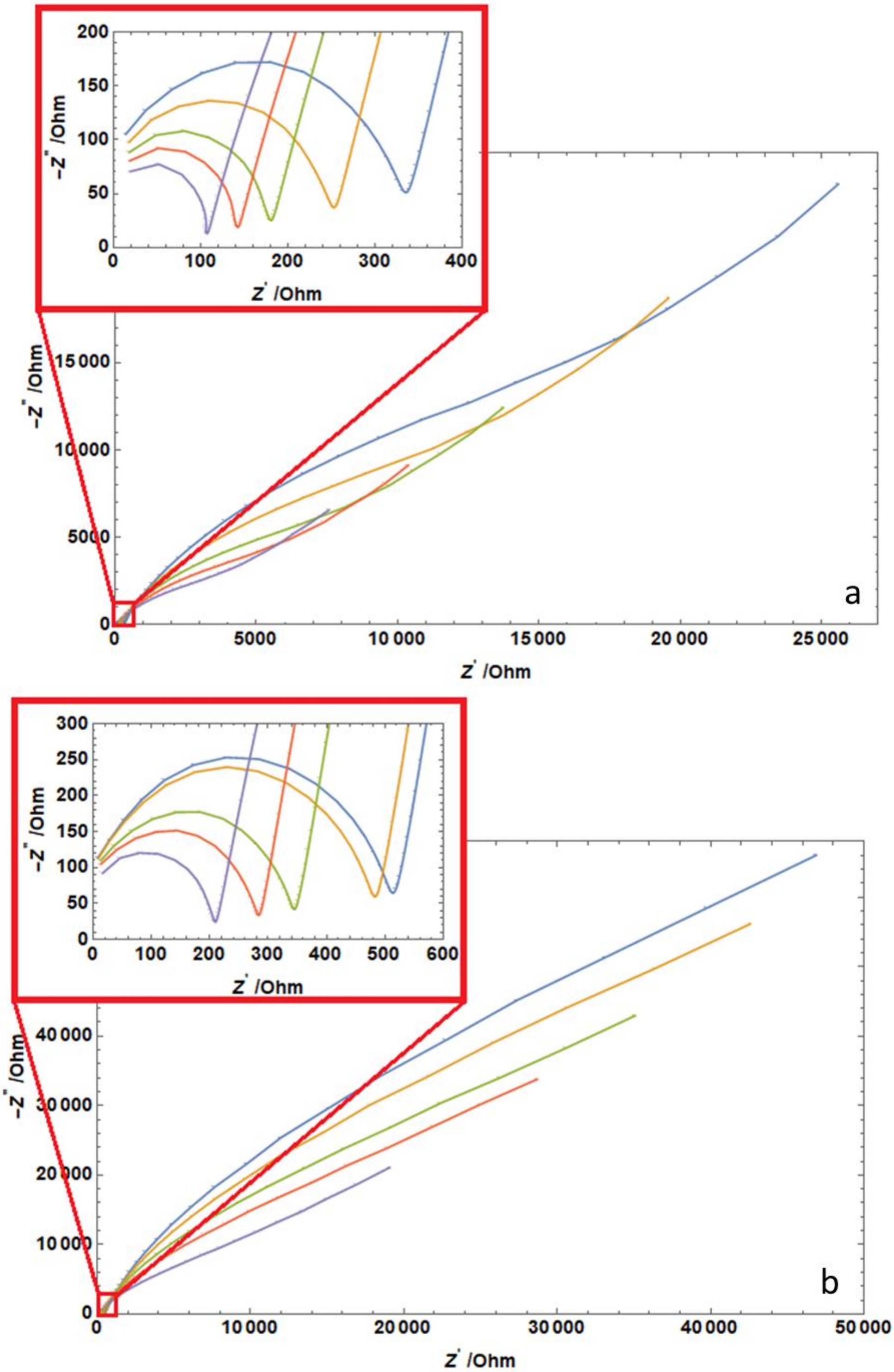

Figure 3.81. Nyquist plot of $[C_4C_1Pyrr][TFSI]$ in a) liquid and b) gel. Blue line corresponds to 298K, orange line 303K, green line 313, red line 323K and purple line 333K.

Likewise, the impedance of the system at the high frequency which leaves in a semicircle (insets in Fig. 3.81), can be attributed, for liquid and gel samples, to a parallel combination of the bulk electrolyte resistance (R_b) and a double layer capacitator (C_{dl}) [152], while at the very low frequency, often related with ion diffusion, this impedance can be associated with a Warburg element or a constant phase element (CPE) [153]. R_b is calculated as the intersection of the straight line of the Nyquist plot, corresponding to intermediate-high frequencies, with Z′ axis [151]. At intermediate frequencies a deviation of the linearity is observed which is basically due to the diffusive layer resistance (EDL formation and ion diffusion in the bulk electrolyte) [154]. The experimental data, at intermediate frequencies, can be fitted to an electrical equivalent circuit consisting of a series combination of resistance solution (R_s) with a CPE (Fig. 3.82 a), or a series combination of R_s with a parallel configuration of charge transfer resistance (R_{ct}) with a CPE element [155] (Fig. 3.82 b).

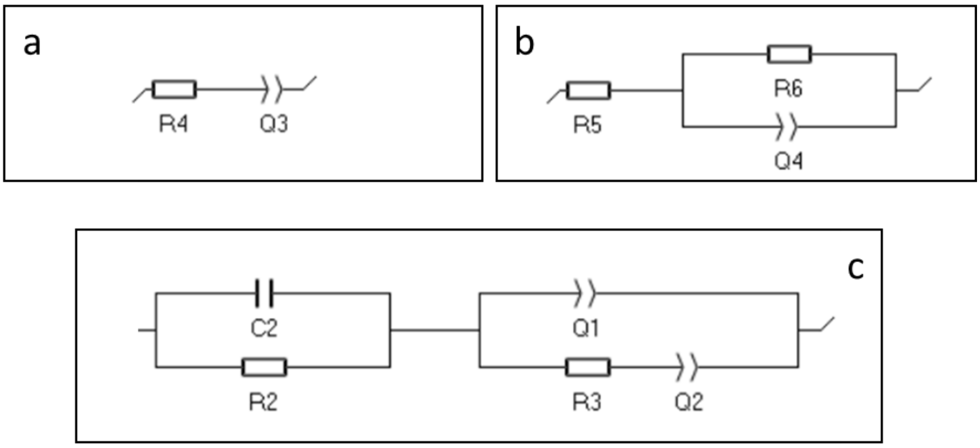

Figure 3.82. a) Series circuit to fit intermediate frequencies, b) parallel circuit to fit medium frequencies and c) Equivalent circuit used to fit the complete spectroscopical data of the obtained Nyquist plot.

Furthermore, to provide a physical interpretation of the complete recorded spectra of the Nyquist plot of this pure IL in liquid and gel states, equivalent RC circuits have been used to fit the impedance values obtained for each temperature. For these fittings in the complete spectroscopical data, a combination of series RC circuits proposed by Gupta et al. and Silva et al. [152,155] is used (figure 3.82 c), where a complex CPE element is described by Eq. (3.19).

$$Q_{CPE} = Q_0(i\omega)^n \tag{3.20}$$

where Q_0 is the CPE module and n is the index of the CPE, both of them are fitting parameters. The fitting parameters of the used equivalent RC circuit are summarized in Table 3.34. As can be seen, all obtained resistances (R_2 and R_3) decrease with increasing temperature, as expected. For Q_1 the obtained potential index lies in 0.8237 - 0.7930 for the liquid samples, and 0.880 - 0.8742 for the gel samples. These values are relatively close to 1, indicating that the behavior of this element is close to that corresponding to a capacitor. Q_2 CPE potential index lies between 0.5623 - 0.4966 for liquid samples and 0.5503 - 0.5000 for gel samples, very close to 0.5, which means that the behavior of this CPE is very close to a Warburg element [156].

The differential capacitance of the sample can be obtained from Eq. (3.20), as proposed by Brug et al. [157], and it is also presented in Table 3.34

$$C = Q_1^n \left(\frac{1}{R_2} + \frac{1}{R_3}\right)^{(n-1)/n} \tag{3.21}$$

where R_2 and R_3 are the resistances in Fig. 3.82 c). These results are also shown in Table 3.34. As can be clearly seen, the obtained differential capacity increases with increasing temperature, as expected, but surprisingly higher values of differential capacity were obtained for the gel samples.

Table 3.34. Equivalent RC circuit (Fig. 3.82 c) fitting obtained parameters for liquid and gel sample.

T /K	*C_2 /F*	*R_2 /Ω*	*Q_1 /F·s$^{(a-1)}$*	*n_1*	*R_3 /Ω*	*Q_2 / F·s$^{(a-1)}$*	*n_2*	C /μF·cm^{-2}
Liquid state								
298	$1.308\cdot10^{-9}$	344	$1.846\cdot10^{-6}$	0.8237	20179	$10.89\cdot10^{-6}$	0.5623	0.74
303	$1.257\cdot10^{-9}$	269.7	$2.145\cdot10^{-6}$	0.8203	13179	$14.98\cdot10^{-6}$	0.5442	0.81
313	$1.164\cdot10^{-9}$	208.6	$2.766\cdot10^{-6}$	0.8103	7941	$22.67\cdot10^{-6}$	0.529	0.93
323	$1.094\cdot10^{-9}$	176.6	$3.27\cdot10^{-6}$	0.8068	5111	$31.39\cdot10^{-6}$	0.5053	1.06
333	$0.983\cdot10^{-9}$	148.5	$4.443\cdot10^{-6}$	0.793	3459	$44.44\cdot10^{-6}$	0.4966	1.25
Gel state								
298	$1.34\cdot10^{-9}$	517.3	$1.485\cdot10^{-6}$	0.8786	79728	$3.964\cdot10^{-6}$	0.5503	1.12
303	$1.344\cdot10^{-9}$	484.5	$1.525\cdot10^{-6}$	0.880	52686	$4.604\cdot10^{-6}$	0.5308	1.17
313	$1.271\cdot10^{-9}$	359.7	$1.674\cdot10^{-6}$	0.8763	32429	$6.213\cdot10^{-6}$	0.5165	1.20
323	$1.231\cdot10^{-9}$	304.5	$1.804\cdot10^{-6}$	0.8742	18724	$7.784\cdot10^{-6}$	0.5033	1.25
333	$1.2\cdot10^{-9}$	237.1	$1.937\cdot10^{-6}$	0.8778	7551	$12.92\cdot10^{-6}$	0.5	1.37

3.5.4. Galvanostatic Charge/Discharge with Potential Limitation

The final study performed during this thesis aims to check the viability of $[C_4C_1Pyrr][TFSI]$ without salt addition, in liquid and ionogel states, as an electrolyte for functional LIB electrolyte. In this framework, a 2032 coin cell in a half cell configuration, using LFP as cathode and metallic lithium as anode, was cycled in a charge/discharge GCPL experiment. The aim of this experiment is to ensure the operativity of the LIB, and is one of the most extensively used experimental assays to check the viability of the battery cell setup.

It is worth noting that in this experiment no lithium salt is added to the electrolyte, demonstrating that the lithium contained in the electrodes is enough to enable the charge/discharge of a LIB.

Prior to this study, the 4th cycle of the cyclic voltammetry, in a Swagelok stainless steel/metallic lithium configuration, of liquid and gel samples of this IL is shown in Fig. 3.83 to discard any chemical degradation of the battery electrolyte and to ensure suitability for LIBs [158]. The four cycles of liquid and gel samples can be seen in the annexed material A (Fig. A15 and A16 respectively).

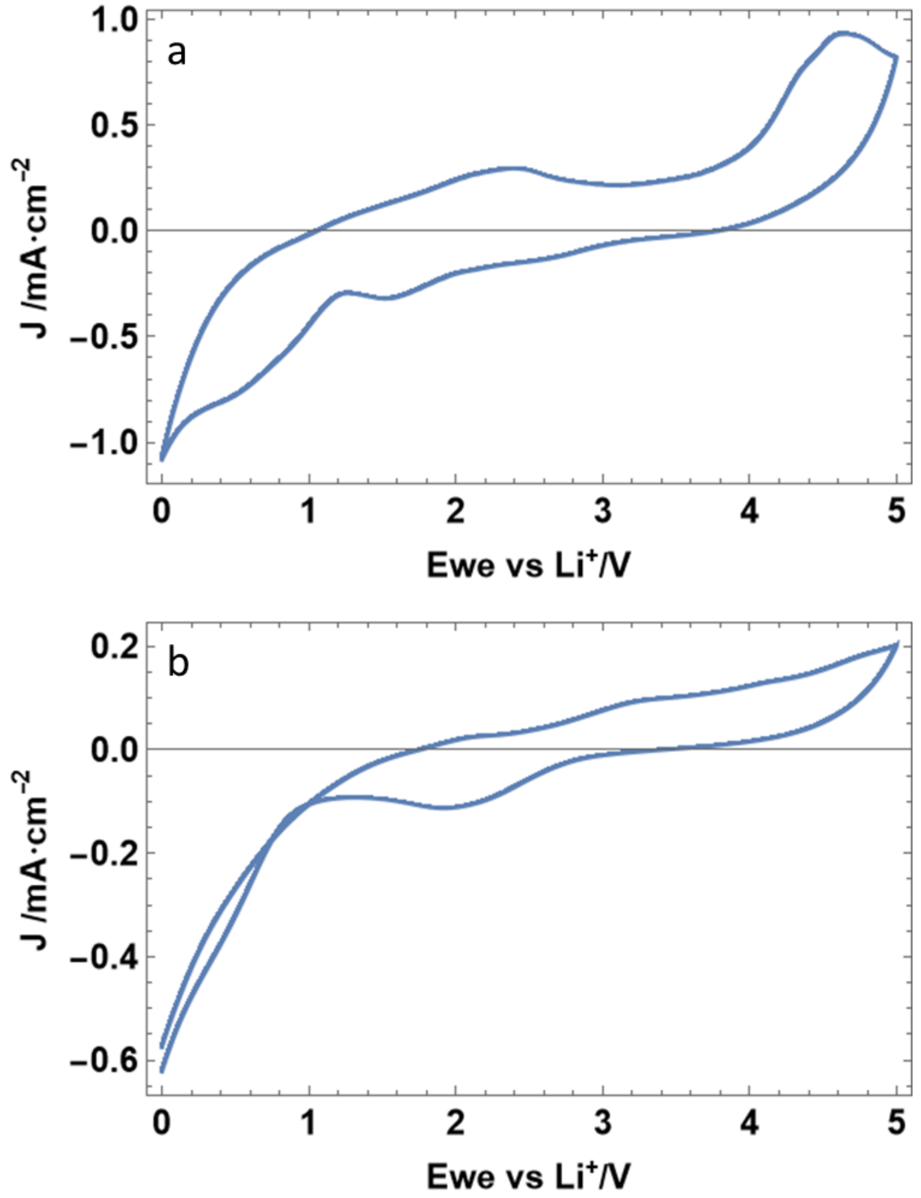

Figure 3.83. 4th cycle of the cyclic voltammetry of [C_4C_1Pyrr][TFSI] a) liquid and b) gel state at 298 K.

Fig. 3.84 shows the charge/discharge curves of [C_4C_1Pyrr][TFSI] in liquid and gel states at C/20 in a 2032 type coin cell with lithium iron phosphate (LFP) as cathode, and metallic lithium as anode. For liquid samples, Fig. 3.84 corresponds to the initial charge/discharge step (or conditioning step). Its first cycle is attributed to the anodic SEI layer formation, with an initial plateau observed at 3.2V. After the first cycle, the charge plateau is observed at 3.5 V vs Li/Li$^+$, which corresponds to the lithium insertion/extraction plateau for LFP [159]. Interestingly, as can be seen in Fig. 3.84 a, this first cycle does not show any apparent discharge, but this appears and becomes more pronounced as the number of cycles increases. This can be due to the IL dissolving lithium from the electrodes, and later inserting it into the cathode during the discharge. Once the electrolyte had adsorbed enough lithium to make the discharge process feasible, as can be seen in Fig. 3.84 b, the charge and discharge cycles progress easily.

For the gel sample (Fig. 3.84 c and d) a similar behavior to that found in a liquid state is observed. In the first cycle of Fig. 3.84 c) (conditioning step), a charge process of around 3.5 V is detected but no significant discharge is observed. The discharge capacity increases by increasing the number of cycles. During the SEI layer formation, some spikes are observed in the conditioning step of GCPL of the ionogel. As with the liquid sample, the charge/discharge becomes stable after some intermediate steps, as illustrated in Fig. 3.84 d, which shows the GCPL behavior after C/10, C/5, C/2 and C/1 cycles.

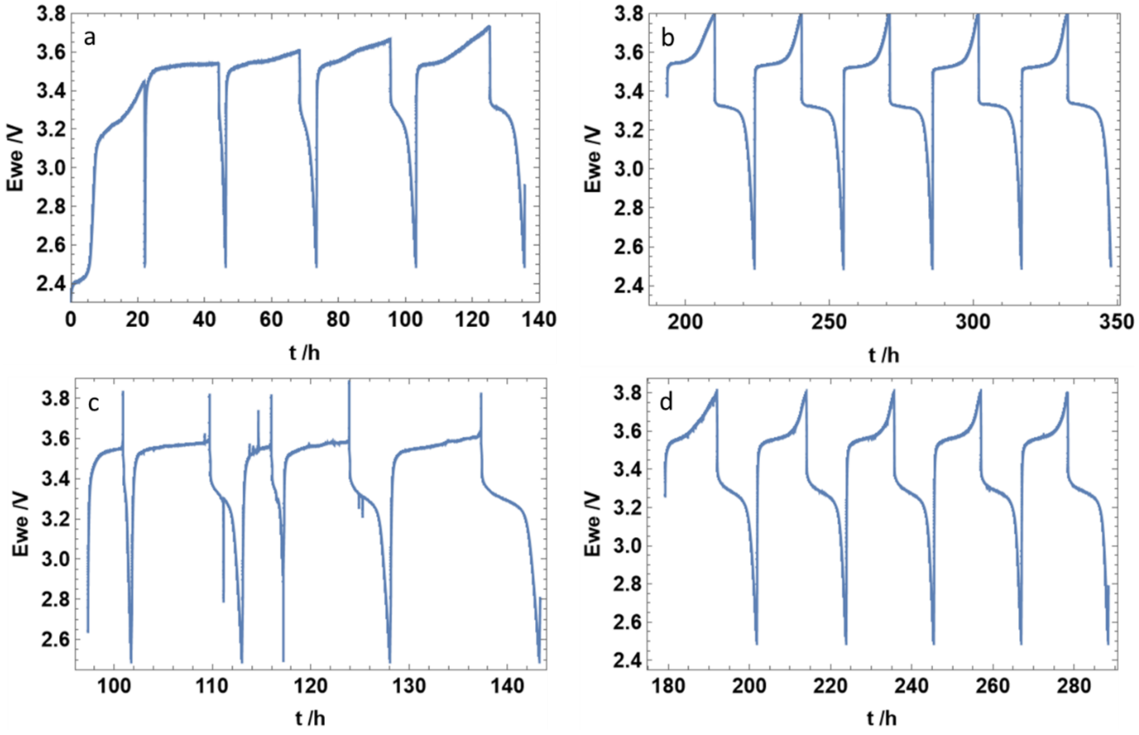

Figure 3.84. GCPL at C/20 of $[C_4C_1Pyrr][TFSI]$ a) initial and b) final of liquid sample and c) initial and d) final of gel sample. Final step was performed after being cycled at C/20, C/10, C/5; C/2 and C/1 five times each step.

Voltage against specific capacity for the last cycle (5th cycle) of conditioning (blue line) and final steps (black line) are shown in Fig. 3.85 for liquid (a) and ionogel (b) samples. The 5th cycle is shown in Fig. 3.85 due to its higher stability. It is important to note that, for the liquid sample, in the 5th cycle of the conditioning step (blue line of Fig. 3.85, see section 2.- materials and methods) the charge capacity reaches 179 mA·h·g^{-1}, while the discharge reaches 82 mA·h·g^{-1} , corresponding to a coulombic efficiency of 45.81%. However, the 5th cycle of the last cycling step (black line) the charge capacity reaches 130 mA·h·g^{-1}, while the discharge capacity reaches 122 mA·h·g^{-1}. This corresponds to a coulombic efficiency of 93.84%. These results are in good agreement with those obtained at C/20 for the ternary mixtures of $[C_1C_1C_6Im][NTf_2]$ + $[Li][NTf_2]$ + vinylene carbonate (5% wt) with LFP cathode and metallic lithium as anode [160]. The theoretical capacity of LFP is 170 mA·h·g^{-1}, which is a closer value to the reached capacity by this configuration, but nevertheless it is high enough to keep studying ILs in their pure form as potential electrolytes for batteries. Additionally, the polarization current is reduced from 230 mV to 185 mV from the conditioning step (Fig. 3.85 a) to the final cycling step.

With regards to the gel sample (Fig. 3.85 b), a similar behavior. Upon conditioning step reaches 81.6 mA·h·g^{-1} while the discharge reaches 52 mA·h·g^{-1}, this corresponds to a coulombic efficiency of 63.72%. The final step charge reaches 101 mA·h·g^{-1} while the discharge reaches 88 mA·h·g^{-1} that corresponds to a Coulombic efficiency of 87.13%. The polarization current for both curves (conditioning and final step) is 250 mV.

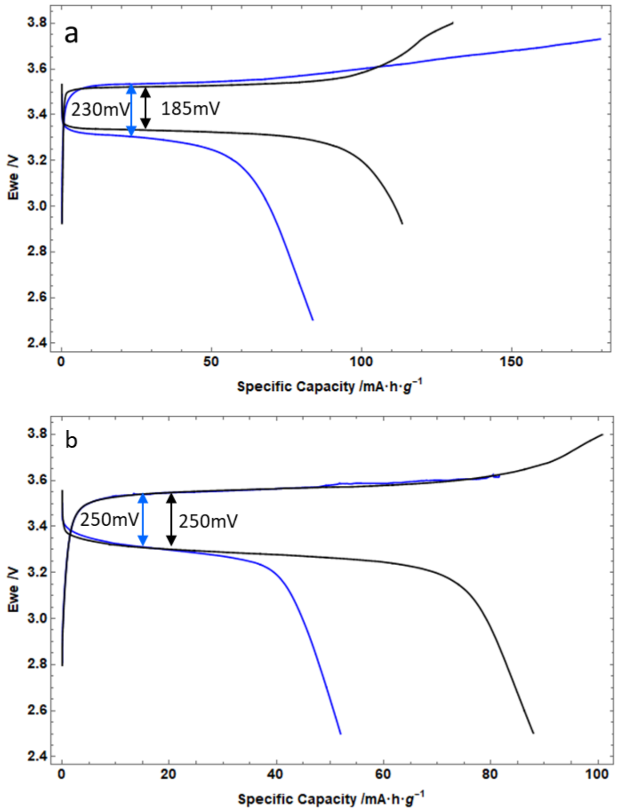

Figure 3.85. Charge/discharge curves of $[C_4C_1Pyrr][TFSI]$ in a) liquid and b) gel state for in 2032 coin cell using LPF as cathode and metallic lithium as anode. Blue line represents the 5th cycle of figure 84 a while black line represents the 5th cycle of figure 84 b.

The voltage vs specific capacity for different C-rates for liquid (a) and gel (b) samples is shown in Fig. 3.86. For the liquid sample, the charge/discharge capacities for C/10 were found as 84/73 mA·h·g^{-1}, which corresponds to a coulombic efficiency of 86%. Higher values of capacity were found by Jun Xia *et. al*. [161] using $LiPF_6$ 1 M on EC:DEC mixture. The differences between the values of these authors and those corresponding to this work can be attributed to the high viscosity of IL, slowing down the diffusion of lithium between the electrodes during the charge/discharge process [159]. The charge/discharge capacities for C/5 obtained were 18.7/16 mA·h·g-1. It can be expected that the specific capacity decreases as the charge/discharge velocity (C-rate) increases. The drastic capacity decrease obtained makes this pure IL unfeasible for industrial implementation with the reported conditions. Nevertheless, it is important to highlight the relevance of the result obtained, since a functional electrolyte was obtained without added lithium salt. A similar behavior to that of the liquid sample was observed for the ionogels (Fig. 3.86 b), C/10 experiments charge/discharge reaches 69.9/55.9 mA·h·g^{-1}, respectively (79.97% Coulombic efficiency), while charge/discharge capacities for C/5 were found as 15.3/14.9 mA·h·g^{-1} (97% Coulombic efficiency).

Fig. 3.87 shows the discharge capacity against cycle number for liquid (a) and gel (b) states. The liquid sample shows that the discharge capacity in the C/20 conditioning step increases while the cycle number increases. In the second step (C/10) the capacity tends to stabilize but still does not remain constant upon cycling. In the C/5 step the capacity is completely constant with the number of cycles, and, in the final step, the discharge capacity reaches the highest value and remains constant upon cycling. As can be seen in Fig. 3.87 b, in the conditioning step, the capacity increases while cycle number increases. For the C/10 step, the capacity is still not stable yet, but when the C/5 step is realized the capacity becomes very stable with cycle number for the gel samples. Again, with the C/20 final step, the reached capacity is the highest and stability is good enough.

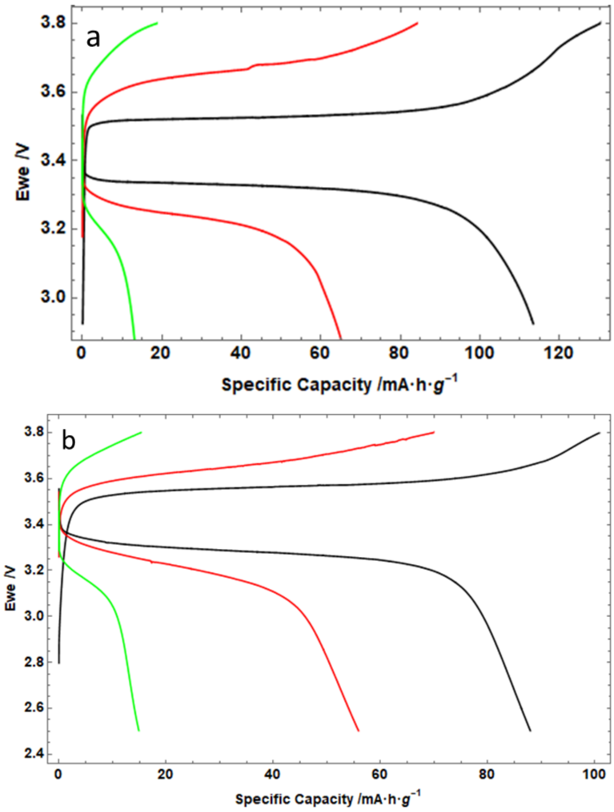

Figure 3.86. Charge/discharge curves of [C_4C_1Pyrr][TFSI] in a) liquid and b) gel samples for different C-rates. Black line represents C/20 rate, red line C/10 and green line C/5 charge/discharge curves.

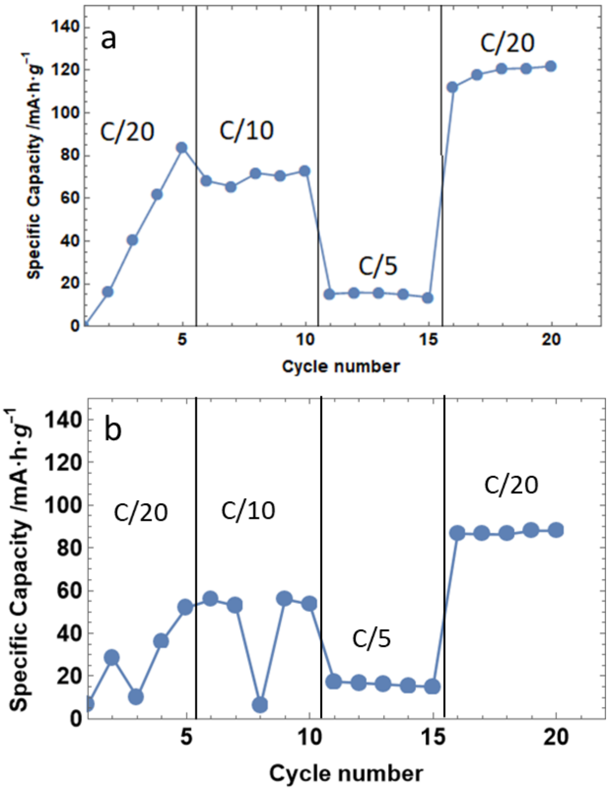

Figure 3.87. Discharge Capacity vs Cycle number at different C-rates for a) liquid and b) gel samples.

During this section, the viability of the pure IL [C$_4$C$_1$Pyrr][TFSI] as potential electrolyte for LIBs has proven by means of GCPL experiments in a 2032 coin cell. The half cell configuration, using LFP as cathode active material and metallic lithium as anode, is shown to be feasible in liquid and in gel state. Despite low C-rates were used to obtain significative capacities, these results show an interesting point of view to a new class of lithium-free electrolytes indirectly proving that the lithium contained in the cathode is enough to enable battery cycling.

References

[1] V.N. Emel'Yanenko, G. Boeck, S.P. Verevkin, R. Ludwig, Volatile times for the very first ionic liquid: Understanding the vapor pressures and enthalpies of vaporization of ethylammonium nitrate, Chemistry - A European Journal 20 (2014) 11640–11645.

[2] N. V. Plechkova, K.R. Seddon, Applications of ionic liquids in the chemical industry, Chem Soc Rev 37 (2008) 123–150.

[3] E. Gómez, N. Calvar, Á. Domínguez, Thermal behaviour of pure Ionic Liquids, in: Scott Handy (Ed.), Ionic Liquids- Current State of the Art, INTECH, 2012: pp. 135–152.

[4] M. Allen, D.F. Evans, R. Lumry, Thermodynamic properties of the ethylammonium nitrate + water system: Partial molar volumes, heat capacities, and expansivities, J Solution Chem 14 (1985) 549–560.

[5] V.N. Emel'Yanenko, G. Boeck, S.P. Verevkin, R. Ludwig, Volatile Times for the Very First Ionic Liquid: Understanding the Vapor Pressures and Enthalpies of Vaporization of Ethylammonium Nitrate, Chemistry – A European Journal 20 (2014) 11640–11645.

[6] N. V. Plechkova, K.R. Seddon, Applications of ionic liquids in the chemical industry, Chem Soc Rev 37 (2007) 123–150.

[7] K.N. Marsh, J.A. Boxall, R. Lichtenthaler, Room temperature ionic liquids and their mixtures—a review, Fluid Phase Equilib 219 (2004) 93–98.

[8] R. Zarrougui, M. Dhahbi, D. Lemordant, Transport and thermodynamic properties of ethylammonium nitrate-water binary mixtures: Effect of temperature and composition, J Solution Chem 44 (2015) 686–702.

[9] T.L. Greaves, A. Weerawardena, C. Fong, I. Krodkiewska, C.J. Drummond, Protic ionic liquids: Solvents with tunable phase behavior and physicochemical properties, Journal of Physical Chemistry B 110 (2006) 22479–22487.

[10] J.J. Parajó, M. Villanueva, J. Troncoso, J. Salgado, Thermophysical properties of choline and pyridinium based ionic liquids as advanced materials for energy applications, Journal of Chemical Thermodynamics 141 (2020) 105947.

[11] C.D.C.D. Rodríguez Fernández, Y. Arosa, E. López Lago, J. Salgado, P. Verdiá, E. Tojo, O. Cabeza, L.M.L.M. Varela, R. De La Fuente, New Insights on the Characterization of the Ionic Liquid Crystal 1-Ethyl-3-Methylimidazolium Decylsulfate, Journal of Physical Chemistry C 123 (2019) 31196–31211.

[12] W. Tu, G. Szklarz, K. Adrjanowicz, K. Grzybowska, J. Knapik-Kowalczuk, M. Paluch, Effect of Cation n-Alkyl Side-Chain Length, Temperature, and Pressure on the Glass-Transition Dynamics and Crystallization Tendency of the

[CnC1Pyrr]+[Tf2N]− Ionic Liquid Family, The Journal of Physical Chemistry C 123 (2019) 12623–12637.

[13] J.J. Parajó, M. Villanueva, J. Troncoso, J. Salgado, Thermophysical properties of choline and pyridinium based ionic liquids as advanced materials for energy applications, Journal of Chemical Thermodynamics 141 (2020).

[14] C.D. Rodríguez Fernández, Y. Arosa, E. López Lago, J. Salgado, P. Verdiá, E. Tojo, O. Cabeza, L.M. Varela, R. De La Fuente, New Insights on the Characterization of the Ionic Liquid Crystal 1-Ethyl-3-Methylimidazolium Decylsulfate, Journal of Physical Chemistry C 123 (2019) 31196–31211.

[15] K. Hayamizu, Y. Aihara, H. Nakagawa, T. Nukuda, W.S. Price, Ionic conduction and ion diffusion in binary room-temperature ionic liquids composed of [emim][BF4] and LiBF4, Journal of Physical Chemistry B 108 (2004) 19527–19532.

[16] A. Martinelli, A. Matic, P. Jacobsson, L. Börjesson, A. Fernicola, B. Scrosati, Phase behavior and ionic conductivity in LiTFSI doped ionic liquids of the pyrrolidinium cation and TFSI anion, J Phys Chem B 113 (2009) 11247–11251.

[17] A. Martinelli, A. Matic, P. Jacobsson, L. Börjesson, A. Fernicola, B. Scrosati, Phase behavior and ionic conductivity in LiTFSI doped ionic liquids of the pyrrolidinium cation and TFSI anion, J Phys Chem B 113 (2009) 11247–11251.

[18] V. Gómez-González, B. Docampo-álvarez, H. Montes-campos, J.C. Otero, E. López Lago, O. Cabeza, L.J. Gallego, L.M. Varela, Solvation of Al3+ cations in bulk and confined protic ionic liquids: a computational study, Physical Chemistry Chemical Physics : Submitted (2018).

[19] A. Martinelli, A. Matic, P. Jacobsson, L. Börjesson, A. Fernicola, B. Scrosati, Phase behavior and ionic conductivity in LiTFSI doped ionic liquids of the pyrrolidinium cation and TFSI anion, J Phys Chem B 113 (2009) 11247–11251.

[20] J.J. Parajó, P. Vallet, L. Fernández-Miguez, M. Villanueva, O. Cabeza, L.M. Varela, J. Salgado, Thermal Behaviour of Ionogels Based on Ionic Liquid Lithium Salt Mixtures, in: J.A. Seijas (Ed.), Chemistry Proceedings, MDPI, 2020: p. 131.

[21] J. Le Bideau, L. Viau, A. Vioux, Ionogels, ionic liquid based hybrid materials, Chem. Soc. Rev. 40 (2011) 907–925.

[22] R. Göbel, A. Friedrich, A. Taubert, Tuning the phase behavior of ionic liquids in organically functionalized silica ionogels, Dalton Transactions 39 (2009) 603–611.

[23] J. Salgado, J.J. Parajó, M. Villanueva, J.R. Rodríguez, O. Cabeza, L.M. Varela, Liquid range of ionic liquid – Metal salt mixtures for electrochemical applications, J Chem Thermodyn 134 (2019) 164–174.

[24] J.J. Parajó, T. Teijeira, J. Fernández, J. Salgado, M. Villanueva, Thermal stability of some imidazolium [NTf2] ionic liquids: isothermal and dynamic kinetic study through thermogravimetric procedures, J Chem Thermodyn 112 (2017) 105–113.

[25] A. Efimova, L. Pfützner, P. Schmidt, Thermal stability and decomposition mechanism of 1-ethyl-3-methylimidazolium halides, Thermochim Acta 604 (2015) 129–136.

[26] M. Villanueva, J.J. Parajó, P.B. Sánchez, J. García, J. Salgado, Liquid range temperature of ionic liquids as potential working fluids for absorption heat pumps, Journal of Chemical Thermodynamics 91 (2015) 127–135.

[27] J.José. Parajó, M. Villanueva, I. Otero, J. Fernández, J. Salgado, Thermal stability of aprotic ionic liquids as potential lubricants. Comparison with synthetic oil bases, Journal of Chemical Thermodynamics 116 (2018) 185–196.

[28] J.J. Parajó, M. Villanueva, J. Salgado, Thermal stability of ionic liquids, in: J. Seijas, P. Vázquez (Eds.), Ionic Liquids Synthesis, Properties, Technologies and Applications, MDPI, Berlin, 2019: pp. 1–16.

[29] S. Zhang, J. Zhang, Y. Zhang, Y. Deng, Nanoconfined Ionic Liquids, Chem Rev 117 (2017) 6755–6833.

[30] J.J. Parajó, M. Villanueva, J. Salgado, Thermal stability of ionic liquids, in: J. Seijas, P. Vázquez (Eds.), Ionic Liquids Synthesis, Properties, Technologies and Applications, MDPI, Berlin, 2019: pp. 1–16.

[31] T.J. Wooster, K.M. Johanson, K.J. Fraser, D.R. MacFarlane, J.L. Scott, Thermal degradation of cyano containing ionic liquids, Green Chemistry 8 (2006) 691–696.

[32] K.J. Baranyai, A.G.B. Deacon, A.D.R. Macfarlane, J.M. Pringle, J.L. Scott, Thermal Degradation of Ionic Liquids at Elevated Temperatures, Aust J Chem 57 (2004) 145–147.

[33] J. Salgado, J.J. Parajó, J. Fernández, M. Villanueva, Long-term thermal stability of some 1-butyl-1-methylpyrrolidinium ionic liquids, J Chem Thermodyn 74 (2014) 51–57.

[34] L. Chancelier, A.O. Diallo, C.C. Santini, G. Marlair, T. Gutel, S. Mailley, C. Len, Targeting adequate thermal stability and fire safety in selecting ionic liquid-based electrolytes for energy storage, Physical Chemistry Chemical Physics 16 (2014) 1967–1976.

[35] Z. Bin Zhou, H. Matsumoto, K. Tatsumi, Cyclic Quaternary Ammonium Ionic Liquids with Perfluoroalkyltrifluoroborates: Synthesis, Characterization, and Properties, Chemistry – A European Journal 12 (2006) 2196–2212.

[36] M. Villanueva, A. Coronas, J. García, J. Salgado, Thermal stability of ionic liquids for their application as new absorbents, Ind Eng Chem Res 52 (2013) 15718–15727.

[37] J.J. Parajó, M. Villanueva, J. Salgado, Thermal Stability of Ionic Liquids, in: Encyclopedia of Ionic Liquids, 2020: pp. 1–10.

[38] J.J. Parajó, T. Teijeira, J. Fernández, J. Salgado, M. Villanueva, Thermal stability of some imidazolium [NTf2] ionic liquids: isothermal and dynamic kinetic study through thermogravimetric procedures, J Chem Thermodyn 112 (2017) 105–113.

[39] B. Zhang, S.H. Liu, J. Liu, Z.H. Zhang, B. Laiwang, C.M. Shu, Thermal stability and flammability assessment of 1-ethyl-2, 3-dimethylimidazolium nitrate, Process Safety and Environmental Protection 135 (2020) 219–227.

[40] V. Gómez-González, B. Docampo-álvarez, H. Montes-campos, J.C. Otero, E. López Lago, O. Cabeza, L.J. Gallego, L.M. Varela, Solvation of Al3+ cations in bulk and confined protic ionic liquids: a computational study, Physical Chemistry Chemical Physics : Submitted (2018).

[41] J. Salgado, J.J. Parajó, M. Villanueva, J.R. Rodríguez, O. Cabeza, L.M. Varela, Liquid range of ionic liquid – Metal salt mixtures for electrochemical applications, J Chem Thermodyn 134 (2019) 164–174.

[42] M. Nádherná, J. Reiter, J. Moškon, R. Dominko, Lithium bis(fluorosulfonyl)imide–PYR14TFSI ionic liquid electrolyte compatible with graphite, J Power Sources 196 (2011) 7700–7706.

[43] V.N. Emel'Yanenko, G. Boeck, S.P. Verevkin, R. Ludwig, Volatile times for the very first ionic liquid: Understanding the vapor pressures and enthalpies of vaporization of ethylammonium nitrate, Chemistry - A European Journal 20 (2014) 11640–11645.

[44] N.I. of Health.U.N.L. of M.- NCBI, PubChem Compounds, Open Chemistry Database (n.d.).

[45] N.I. of Health.U.N.L. of M.- NCBI, PubChem Compounds, Open Chemistry Database (n.d.).

[46] M.N. Garaga, L. Aguilera, N. Yaghini, A. Matic, M. Persson, A. Martinelli, Achieving enhanced ionic mobility in nanoporous silica by controlled surface interactions, Physical Chemistry Chemical Physics 19 (2017) 5727–5736.

[47] S.A.M. Noor, P.M. Bayley, M. Forsyth, D.R. MacFarlane, Ionogels based on ionic liquids as potential highly conductive solid state electrolytes, Electrochim Acta 91 (2013) 219–226.

[48] A. Taubert, R. Löbbicke, B. Kirchner, F. Leroux, First examples of organosilica-based ionogels: Synthesis and electrochemical behavior, Beilstein Journal of Nanotechnology 8 (2017) 736–751.

[49] H. Zhu, R. Vijayaraghavan, D.R. Macfarlane, M. Forsyth, Self-assembled structure and dynamics of imidazolium-based protic salts in water solution, Physical Chemistry Chemical Physics 21 (2019) 2691–2696.

[50] K. Takao, T. Tsubomura, Weakly-basic anion exchange resin scavenges impurities in ionic liquid synthesized from trialkyloxonium salt, J Chem Eng Data 57 (2012) 2497–2502.

[51] F. D'Anna, S. La Marca, R. Noto, Kemp elimination: A probe reaction to study ionic liquids properties, Journal of Organic Chemistry 73 (2008) 3397–3403.

[52] B.P. Thapaliya, C.L. Do-Thanh, C.J. Jafta, R. Tao, H. Lyu, A.Y. Borisevich, S. ze Yang, X.G. Sun, S. Dai, Simultaneously Boosting the Ionic Conductivity and Mechanical Strength of Polymer Gel Electrolyte Membranes by Confining Ionic Liquids into Hollow Silica Nanocavities, Batter Supercaps 2 (2019) 985–991.

[53] C. D'Agostino, M.D. Mantle, C.L. Mullan, C. Hardacre, L.F. Gladden, Diffusion, Ion Pairing and Aggregation in 1-Ethyl-3-Methylimidazolium-Based Ionic Liquids Studied by 1H and 19F PFG NMR: Effect of Temperature, Anion and Glucose Dissolution, ChemPhysChem 19 (2018) 1081–1088.

[54] V. V. Matveev, A. V. Ievlev, M.A. Vovk, O. Cabeza, J. Salgado-Carballo, J.J. Parajó, J.R. Rodríguez, R. de la Fuente, E. Lähderanta, L.M. Varela, NMR investigation of the structure and single-particle dynamics of inorganic salt solutions in a protic ionic liquid, J Mol Liq 278 (2019) 239–246.

[55] S. Zhang, J. Zhang, Y. Zhang, Y. Deng, Nanoconfined Ionic Liquids, Chem Rev 117 (2017) 6755–6833. https://doi.org/10.1021/acs.chemrev.6b00509.

[56] K. Fumino, A. Wulf, R. Ludwig, Hydrogen Bonding in Protic Ionic Liquids: Reminiscent of Water, Angewandte Chemie International Edition 48 (2009) 3184–3186.

[57] T. Zentel, V. Overbeck, D. Michalik, O. Kühn, R. Ludwig, Hydrogen bonding in protic ionic liquids: structural correlations, vibrational spectroscopy, and rotational dynamics of liquid ethylammonium nitrate, Journal of Physics B: Atomic, Molecular and Optical Physics 51 (2018) 034002.

[58] P. Charisiadis, V.G. Kontogianni, C.G. Tsiafoulis, A.G. Tzakos, M. Siskos, I.P. Gerothanassis, 1H-NMR as a structural and analytical tool of intra- and intermolecular hydrogen bonds of phenol-containing natural products and model compounds, Molecules 19 (2014) 13643–13682.

[59] V. Exarchou, A. Troganis, I.P. Gerothanassis, M. Tsimidou, D. Boskou, Do strong intramolecular hydrogen bonds persist in aqueous solution? Variable temperature gradient 1H, 1H–13C GE-HSQC and GE-HMBC NMR studies of flavonols and flavones in organic and aqueous mixtures, Tetrahedron 58 (2002) 7423–7429..

[60] H. Zhu, R. Vijayaraghavan, D.R. Macfarlane, M. Forsyth, Self-assembled structure and dynamics of imidazolium-based protic salts in water solution, Physical Chemistry Chemical Physics 21 (2019) 2691–2696.

[61] M. Hasani, L. Nordstierna, A. Martinelli, Molecular dynamics involving proton exchange of a protic ionic liquid-water mixture studied by NMR spectroscopy, Physical Chemistry Chemical Physics 21 (2019) 22014–22021.

[62] T. Méndez-Morales, J. Carrete, Ó. Cabeza, O. Russina, A. Triolo, L.J. Gallego, L.M. Varela, Solvation of lithium salts in protic ionic liquids: A molecular dynamics study, Journal of Physical Chemistry B 118 (2014) 761–770.

[63] A.G. Palmer, H. Koss, Chapter Six - Chemical Exchange, in: A.J.B.T.-M. in E. Wand (Ed.), Biological NMR Part B, Academic Press, 2019: pp. 177–236.

[64] H. Zhu, R. Vijayaraghavan, D.R. Macfarlane, M. Forsyth, Self-assembled structure and dynamics of imidazolium-based protic salts in water solution, Physical Chemistry Chemical Physics 21 (2019) 2691–2696.

[65] T. Méndez-Morales, J. Carrete, Ó. Cabeza, O. Russina, A. Triolo, L.J. Gallego, L.M. Varela, Solvation of lithium salts in protic ionic liquids: A molecular dynamics study, Journal of Physical Chemistry B 118 (2014) 761–770.

[66] O.D. Pavel, I. Podolean, V.I. Parvulescu, S.F.R. Taylor, H.G. Manyar, K. Ralphs, P. Goodrich, C. Hardacre, Impact of SCILL catalysts for the S-S coupling of thiols to disulfides, Faraday Discuss 206 (2018) 535–547.

[67] D.H. Sutter, W.H. Flygare, The molecular Zeeman effect, Bonding Structure (1976) 89–196.

[68] T. Stettner, S. Gehrke, P. Ray, B. Kirchner, A. Balducci, Water in Protic Ionic Liquids: Properties and Use of a New Class of Electrolytes for Energy-Storage Devices, ChemSusChem 12 (2019) 3827–3836.

[69] R. Zarrougui, M. Dhahbi, D. Lemordant, Transport and Thermodynamic Properties of Ethylammonium Nitrate – Water Binary Mixtures : Effect of Temperature and Composition, J Solution Chem 44 (2015) 686–702.

[70] T.K.N. Tran, A. Guyomard-Lack, C. Cerclier, B. Humbert, G. Colomines, J.F. Pilard, R. Deterre, J. Le Bideau, E. Leroy, Natural rubber-based ionogels, J Renew Mater 6 (2018) 251–258.

[71] J. Le Bideau, P. Gaveau, S. Bellayer, M.A. Néouze, A. Vioux, Effect of confinement on ionic liquids dynamics in monolithic silica ionogels: 1H NMR study, Physical Chemistry Chemical Physics 9 (2007) 5419–5422.

[72] R.V. Pivato, F. Rossi, M. Ferro, F. Castiglione, F. Trotta, A. Mele, β-Cyclodextrin Nanosponge Hydrogels as Drug Delivery Nanoarchitectonics for Multistep Drug Release Kinetics, ACS Appl Polym Mater 3 (2021) 6562–6571.

[73] P.B. Sánchez, M.R. Currás, M.M. Mato, J. Salgado, J. García, Density and viscosity study of pyridinium based ionic liquids as potential absorbents for natural refrigerants: Experimental and modelling, Fluid Phase Equilib 405 (2015) 37–45.

[74] J. Salgado, T. Regueira, L. Lugo, J. Vijande, J. Fernández, J. García, Density and viscosity of three (2,2,2-trifluoroethanol+1-butyl-3-methylimidazolium) ionic liquid binary systems, J Chem Thermodyn 70 (2014) 101–110.

[75] K.R. Seddon, A. Stark, M.J. Torres, Influence of chloride, water, and organic solvents on the physical properties of ionic liquids, Pure and Applied Chemistry 72 (2000) 2275–2287.

[76] P.J. Carvalho, T. Regueira, L.M.N.B.F. Santos, J. Fernandez, J.A.P. Coutinho, Effect of water on the viscosities and densities of 1-butyl-3- methylimidazolium dicyanamide and 1-butyl-3-methylimidazolium tricyanomethane at atmospheric pressure, J Chem Eng Data 55 (2010) 645–652.

[77] R. Zarrougui, M. Dhahbi, D. Lemordant, Transport and Thermodynamic Properties of Ethylammonium Nitrate – Water Binary Mixtures : Effect of Temperature and Composition, J Solution Chem 44 (2015) 686–702.

[78] L. Segade, M. Cabanas, M. Domínguez-Pérez, E. Rilo, S. García-Garabal, M. Turmine, L.M. Varela, V. Gómez-González, B. Docampo-Alvarez, O. Cabeza, Surface and bulk characterisation of mixtures containing alkylammonium nitrates and water or ethanol: Experimental and simulated properties at 298.15 K, J Mol Liq 222 (2016) 663–670.

[79] J.N. Canongia Lopes, J.M.S.S. Esperança, A.M. De Ferro, A.B. Pereiro, N. V. Plechkova, L.P.N. Rebelo, K.R. Seddon, I. Vázquez-Fernández, Protonic Ammonium Nitrate Ionic Liquids and Their Mixtures: Insights into Their Thermophysical Behavior, Journal of Physical Chemistry B 120 (2016) 2397–2406.

[80] R. Zarrougui, M. Dhahbi, D. Lemordant, Transport and thermodynamic properties of ethylammonium nitrate-water binary mixtures: Effect of temperature and composition, J Solution Chem 44 (2015) 686–702.

[81] A.S.M.C. Rodrigues, M.A.A. Rocha, H.F.D. Almeida, C.M.S.S. Neves, J.A. Lopes-Da-Silva, M.G. Freire, J.A.P. Coutinho, L.M.N.B.F. Santos, Effect of the Methylation and N-H Acidic Group on the Physicochemical Properties of Imidazolium-Based Ionic Liquids, Journal of Physical Chemistry B 119 (2015) 8781–8792.

[82] Z. Chen, O. Morales-Collazo, J.F. Brennecke, Protic Imidazolium Cation-Based Ionic Liquids Show Unexpected Interfacial Properties, Langmuir 36 (2020) 8904–8913.

[83] A.S. Khan, Z. Man, M.A. Bustam, G. Gonfa, F.K. Chong, Z. Ullah, A. Nasrullah, A. Sarwono, P. Ahmad, N. Muhammad, Effect of Structural Variations on the Thermophysical Properties of Protic Ionic Liquids: Insights from Experimental and Computational Studies, J Chem Eng Data 62 (2017) 2993–3003.

[84] Y.A. Fadeeva, M.S. Gruzdev, N.O. Kudryakova, L.E. Shmukler, L.P. Safonova, Physico-chemical characterization of alkyl-imidazolium protic ionic liquids, J Mol Liq 297 (2020) 111305.

[85] T. Regueira, L. Lugo, J. Fernández, Influence of the pressure, temperature, cation and anion on the volumetric properties of ionic liquids: New experimental values for two salts, J Chem Thermodyn 58 (2013) 440–448.

[86] F.M. Gaciño, T. Regueira, L. Lugo, M.J.P. Comuñas, J. Fernández, Influence of molecular structure on densities and viscosities of several ionic liquids, J Chem Eng Data 56 (2011) 4984–4999.

[87] M. Součková, J. Klomfar, J. Pátek, Measurements and group contribution analysis of 0.1 MPa densities for still poorly studied ionic liquids with the [PF6] and [NTf2] anions, J Chem Thermodyn 77 (2014) 31–39.

[88] P. Vallet, J.J. Parajó, O. Cabeza, L.M. Varela, J. Salgado, M. Villanueva, Determination of Thermophysical Properties of the Protic Ionic Liquid EIM NO3, Pure and Doped with Lithium Nitrate Salt, (2021) 126.

[89] P. Vallet, S. Bouzón-Capelo, T. Méndez-Morales, V. Gómez-González, Y. Arosa, R. de la Fuente, E. López-Lago, J.R. Rodríguez, L.J. Gallego, J.J. Parajó, J. Salgado, M. Turmine, L. Segade, O. Cabeza, L.M. Varela, On the physical properties of mixtures of nitrate salts and protic ionic liquids, J Mol Liq 350 (2022) 118483.

[90] T.Y. Wu, Y.H. Wang, S.G. Su, Y.C. Lin, C.W. Kuo, J.K. Chang, I.W. Sun, Influence of LiTFSI addition on conductivity, diffusion coefficient, Spin-lattice relaxation times, and chemical shift of one-dimensional NMR spectroscopy in LiTFSI -doped dual-functionalized imidazolium-based ionic liquids, J Chem Eng Data 60 (2015) 471–483.

[91] Q. Huang, Y.Y. Lee, B. Gurkan, Pyrrolidinium Ionic Liquid Electrolyte with Bis(trifluoromethylsulfonyl)imide and Bis(fluorosulfonyl)imide Anions: Lithium Solvation and Mobility, and Performance in Lithium Metal-Lithium Iron Phosphate Batteries, Ind Eng Chem Res 58 (2019) 22587–22597.

[92] K. Matsumoto, E. Nishiwaki, T. Hosokawa, S. Tawa, T. Nohira, R. Hagiwara, Thermal, Physical, and Electrochemical Properties of Li[N(SO2F)2]-[1-Ethyl-3-methylimidazolium][N(SO2F)2] Ionic Liquid Electrolytes for Li Secondary Batteries Operated at Room and Intermediate Temperatures, Journal of Physical Chemistry C 121 (2017) 9209–9219.

[93] A. Kadyan, S. Pandey, Lithium bis(trifluoromethylsulfonyl)imide-added ionic liquid 1-ethyl-3-methylimidazolium bis(trifluoromethylsulfonyl)imide mixture: Densities and dynamic viscosities in the temperature range (298.15–358.15) K, J Chem Thermodyn 116 (2018) 159–165.

[94] V. Gómez-González, B. Docampo-Álvarez, O. Cabeza, M. Fedorov, R.M. Lynden-Bell, L.J. Gallego, L.M. Varela, Molecular dynamics simulations of the structure and single-particle dynamics of mixtures of divalent salts and ionic liquids, J Chem Phys 143 (2015) 124507.

[95] V. Gómez-González, B. Docampo-Álvarez, O. Cabeza, M. Fedorov, R.M. Lynden-Bell, L.J. Gallego, L.M. Varela, Molecular dynamics simulations of the structure and single-particle dynamics of mixtures of divalent salts and ionic liquids, J Chem Phys 143 (2015) 124507.

[96] J. Jacquemin, P. Husson, A.A.H. Padua, V. Majer, Density and viscosity of several pure and water-saturated ionic liquids, Green Chemistry 8 (2006) 172.

[97] T. Stettner, S. Gehrke, P. Ray, B. Kirchner, A. Balducci, Water in Protic Ionic Liquids: Properties and Use of a New Class of Electrolytes for Energy-Storage Devices, ChemSusChem 12 (2019) 3827–3836.

[98] J. Vila, P. Ginés, J.M. Pico, C. Franjo, E. Jiménez, L.M. Varela, O. Cabeza, Temperature dependence of the electrical conductivity in EMIM-based ionic liquids: Evidence of Vogel-Tamman-Fulcher behavior, Fluid Phase Equilib 242 (2006) 141–146.

[99] J.N. Canongia Lopes, J.M.S.S. Esperança, A.M. De Ferro, A.B. Pereiro, N. V. Plechkova, L.P.N. Rebelo, K.R. Seddon, I. Vázquez-Fernández, Protonic Ammonium Nitrate Ionic Liquids and Their Mixtures: Insights into Their Thermophysical Behavior, Journal of Physical Chemistry B 120 (2016) 2397–2406.

[100] K.R. Seddon, A. Stark, M.J. Torres, Viscosity and density of 1-alkyl-3-methylimidazolium ionic liquids, ACS Symposium Series 819 (2002) 34–49.

[101] R. Zarrougui, M. Dhahbi, D. Lemordant, Volumetric and transport properties of N-Butyl-N-methylpyrrolidinium bis(Trifluoromethanesulfonyl)imide-methanol binary mixtures, Ionics (Kiel) 17 (2011) 343–352.

[102] D. Warmińska, I. Cichowska-Kopczyńska, Thermodynamic study of binary mixtures of toluene with ionic liquids, 1-butyl-1-methylpyrrolidinium bis(trifluoromethylsulfonyl)imide, 1-hexyl-1-methylpyrrolidinium bis(trifluoromethylsulfonyl)imide and 1-butylpyridinium bis(trifluoromethylsulfonyl)imide, J Mol Liq 304 (2020) 112754.

[103] M. Tariq, P.J. Carvalho, J.A.P. Coutinho, I.M. Marrucho, J.N.C. Lopes, L.P.N. Rebelo, Viscosity of (C2–C14) 1-alkyl-3-methylimidazolium bis(trifluoromethylsulfonyl)amide ionic liquids in an extended temperature range, Fluid Phase Equilib 301 (2011) 22–32.

[104] S. Seki, T. Kobayashi, Y. Kobayashi, K. Takei, H. Miyashiro, K. Hayamizu, S. Tsuzuki, T. Mitsugi, Y. Umebayashi, Effects of cation and anion on physical properties of room-temperature ionic liquids, J Mol Liq 152 (2010) 9–13.

[105] J. Jacquemin, P. Husson, A.A.H. Padua, V. Majer, Density and viscosity of several pure and water-saturated ionic liquids, Green Chemistry 8 (2006) 172–180.

[106] A.J.L. Costa, J.M.S.S. Esperança, I.M. Marrucho, L.P.N. Rebelo, Densities and viscosities of 1-ethyl-3-methylimidazolium n -alkyl sulfates, J Chem Eng Data 56 (2011) 3433–3441.

[107] I. Mukherjee, K. Manna, G. Dinda, S. Ghosh, S.P. Moulik, Shear- and temperature-dependent viscosity behavior of two phosphonium-based ionic liquids and surfactant triton X-100 and their biocidal activities, J Chem Eng Data 57 (2012) 1376–1386.

[108] D. David Agwu, F. Opara, D. Dike, A.D. Daberechi, O.F. K, D.D. O, Review Of Comparative Battery Energy Storage Systems (Bess) For Energy Storage Applications In Tropical Enviroments, 2018.

[109] M. Galiński, A. Lewandowski, I. Stepniak, Ionic liquids as electrolytes, Electrochim Acta 51 (2006) 5567–5580.

[110] A. Oleinikova, M. Bonetti, Critical behavior of the electrical conductivity of concentrated electrolytes: Ethylammonium nitrate in n-octanol binary mixture, J Solution Chem 31 (2002) 397–413.

[111] T.L. Greaves, A. Weerawardena, C. Fong, I. Krodkiewska, C.J. Drummond, Protic Ionic Liquids : Solvents with Tunable Phase Behavior and Physicochemical Properties, J. Phys. Chem. B 110 (2006) 22479–22487.

[112] T. Vogl, P. Goodrich, J. Jacquemin, S. Passerini, A. Balducci, The Influence of Cation Structure on the Chemical-Physical Properties of Protic Ionic Liquids, Journal of Physical Chemistry C 120 (2016) 8525–8533.

[113] S. Bouzón- Capelo, T. Méndez-Morales, J. Carrete, E. López Lago, J. Vila, O. Cabeza, J.R. Rodríguez, M. Turmine, L.M. Varela, Effect of temperature and cationic chain length on the physical properties of ammonium nitrate-based protic ionic liquids, Journal of Physical Chemistry B 116 (2012) 11302–11312.

[114] J. Vila, P. Ginés, E. Rilo, O. Cabeza, L.M. Varela, Great increase of the electrical conductivity of ionic liquids in aqueous solutions, Fluid Phase Equilib 247 (2006) 32–39.

[115] S. Seki, Y. Ohno, Y. Kobayashi, H. Miyashiro, A. Usami, Y. Mita, H. Tokuda, M. Watanabe, K. Hayamizu, S. Tsuzuki, M. Hattori, N. Terada, Imidazolium-Based Room-Temperature Ionic Liquid for Lithium Secondary Batteries, J Electrochem Soc 154 (2007) A173.

[116] K. Hayamizu, Y. Aihara, H. Nakagawa, T. Nukuda, W.S. Price, Ionic conduction and ion diffusion in binary room-temperature ionic liquids composed of [emim][BF4] and LiBF4, Journal of Physical Chemistry B 108 (2004) 19527–19532.

[117] S. Tsuzuki, K. Hayamizu, S. Seki, Origin of the low-viscosity of [emim][(FSO2)2N] ionic liquid and its lithium salt mixture: Experimental and theoretical study of self-diffusion coefficients, conductivities, and intermolecular interactions, Journal of Physical Chemistry B 114 (2010) 16329–16336.

[118] T.Y. Wu, Y.H. Wang, S.G. Su, Y.C. Lin, C.W. Kuo, J.K. Chang, I.W. Sun, Influence of LiTFSI addition on conductivity, diffusion coefficient, Spin-lattice relaxation times, and chemical shift of one-dimensional NMR spectroscopy in LiTFSI -doped dual-functionalized imidazolium-based ionic liquids, J Chem Eng Data 60 (2015) 471–483.

[119] K. Matsumoto, E. Nishiwaki, T. Hosokawa, S. Tawa, T. Nohira, R. Hagiwara, Thermal, Physical, and Electrochemical Properties of Li[N(SO2F)2]-[1-Ethyl-3-methylimidazolium][N(SO2F)2] Ionic Liquid Electrolytes for Li Secondary Batteries Operated at Room and Intermediate Temperatures, Journal of Physical Chemistry C 121 (2017) 9209–9219.

[120] J.-K. Kim, D.-H. Lim, J. Scheers, J. Pitawala, S. Wilken, P. Johansson, J.-H. Ahn, A. Matic, P. Jacobsson, Properties of N-butyl-N-methyl-pyrrolidinium Bis(trifluoromethanesulfonyl) Imide Based Electrolytes as a Function of Lithium Bis(trifluoromethanesulfonyl) Imide Doping, Journal of the Korean Electrochemical Society 14 (2011) 92–97.

[121] T. Vogl, S. Passerini, A. Balducci, The impact of mixtures of protic ionic liquids on the operative temperature range of use of battery systems, Electrochemisty Communications 78 (2017) 47–50.

[122] K. Hayamizu, Y. Aihara, H. Nakagawa, T. Nukuda, W.S. Price, Ionic conduction and ion diffusion in binary room-temperature ionic liquids composed of [emim][BF4] and LiBF4, Journal of Physical Chemistry B 108 (2004) 19527–19532.

[123] J. Vila, E. Rilo, L. Segade, O. Cabeza, L.M. Varela, Electrical conductivity of aqueous solutions of aluminum salts, Phys Rev E Stat Nonlin Soft Matter Phys 71 (2005) 1–8. https://doi.org/10.1103/PhysRevE.71.031201.

[124] N.S. Schauser, R. Seshadri, R.A. Segalman, Multivalent ion conduction in solid polymer systems, Mol Syst Des Eng 4 (2019) 263–279.

[125] H. Zhang, L. Qiao, H. Kühnle, E. Figgemeier, M. Armand, G.G. Eshetu, From lithium to emerging mono- and multivalent-cation-based rechargeable batteries: non-aqueous organic electrolyte and interphase perspectives, Energy Environ Sci 16 (2023) 11–52.

[126] J. Leys, M. Wübbenhorst, C. Preethy Menon, R. Rajesh, J. Thoen, C. Glorieux, P. Nockemann, B. Thijs, K. Binnemans, S. Longuemart, Temperature dependence of the electrical conductivity of imidazolium ionic liquids, Journal of Chemical Physics 128 (2008).

[127] J. Vila, L.M. Varela, O. Cabeza, Cation and anion sizes influence in the temperature dependence of the electrical conductivity in nine imidazolium based ionic liquids, Electrochim Acta 52 (2007) 7413–7417.

[128] I.H. Sajid, M.F.M. Sabri, S.M. Said, M.F.M. Salleh, N.N.N. Ghazali, R. Saidur, B. Subramaniam, S.W. Hasan, H.A. Jaffery, Crosslinked thermoelectric hydro-ionogels: A new class of highly conductive thermoelectric materials, Energy Convers Manag 198 (2019).

[129] L. Negre, B. Daffos, V. Turq, P.L. Taberna, P. Simon, Ionogel-based solid-state supercapacitor operating over a wide range of temperature, Electrochim Acta 206 (2016) 490–495.

[130] I.H. Sajid, M.F.M. Sabri, S.M. Said, M.F.M. Salleh, N.N.N. Ghazali, R. Saidur, B. Subramaniam, S.W. Hasan, H.A. Jaffery, Crosslinked thermoelectric hydro-ionogels: A new class of highly conductive thermoelectric materials, Energy Convers Manag 198 (2019).

[131] V.A. Rana, D.K. Barot, H.P. Vankar, T.R. Pandit, J.B. Karakthala, AC/DC conductivity and dielectric relaxation behavior of ionic solutions of 1-butyl-3-methylimidazolium chloride in methanol, J Mol Liq 296 (2019) 111804.

[132] R.J. Sengwa, S. Choudhary, S. Sankhla, Dielectric behaviour and relaxation processes of montmorillonite clay nano-platelet colloidal suspensions in poly(vinyl pyrrolidone)-ethylene glycol oligomer blends, Polym Int 58 (2009) 781–789.

[133] R.J. Sengwa, S. Choudhary, S. Sankhla, Low frequency dielectric relaxation processes and ionic conductivity of montmorillonite clay nanoparticles colloidal suspension in poly(vinyl pyrrolidone)-ethylene glycol blends, Express Polym Lett 2 (2008) 800–809.

[134] M. W. U Ubbenhorst, J. Van Turnhout, Analysis of complex dielectric spectra. I. One-dimensional derivative techniques and three-dimensional modelling, (n.d.).

[135] A.L. Saroj, R.K. Singh, Thermal, dielectric and conductivity studies on PVA/Ionic liquid [EMIM][EtSO4] based polymer electrolytes, Journal of Physics and Chemistry of Solids 73 (2012) 162–168.

[136] C. Chassagne, E. Dubois, M.L. Jiménez, J.P.M. van der Ploeg, J. van Turnhout, Compensating for electrode polarization in dielectric spectroscopy studies of colloidal suspensions: Theoretical assessment of existing methods, Front Chem 4 (2016) 30.

[137] P. Vadhva, J. Hu, M.J. Johnson, R. Stocker, M. Braglia, D.J.L. Brett, A.J.E. Rettie, Electrochemical Impedance Spectroscopy for All-Solid-State Batteries: Theory, Methods and Future Outlook, ChemElectroChem 8 (2021) 1930–1947.

[138] S. Ramesh, A.H. Yahaya, A.K. Arof, Dielectric behaviour of PVC-based polymer electrolytes, Solid State Ion 152–153 (2002) 291–294..

[139] F. Pabst, J. Gabriel, P. Weigl, T. Blochowicz, Molecular dynamics of supercooled ionic liquids studied by light scattering and dielectric spectroscopy, Chem Phys 494 (2017) 103–110.

[140] R.J. Sengwa, S. Choudhary, P. Dhatarwal, Characterization of relaxation processes over static permittivity frequency regime and compliance of the Stokes-Einstein-Nernst relation in propylene carbonate, J Mol Liq 225 (2017) 42–49.

[141] R.J. Sengwa, S. Choudhary, P. Dhatarwal, Characterization of relaxation processes over static permittivity frequency regime and compliance of the Stokes-Einstein-Nernst relation in propylene carbonate, J Mol Liq 225 (2017) 42–49.

[142] W. Tu, R. Richert, K. Adrjanowicz, Dynamics of Pyrrolidinium-Based Ionic Liquids under Confinement. I. Analysis of Dielectric Permittivity, Journal of Physical Chemistry C 124 (2020) 5389–5394.

[143] J. Świergiel, L. Bouteiller, J. Jadzyn, Interpretation of the electric impedance spectra recorded for liquids in the presence of ionic and displacement currents, Ind Eng Chem Res 52 (2013) 11974–11979.

[144] J.S.´Wiergiel, I.P. Płowaś, J. Grembowski, J. Jadż, Stokes−Einstein−Nernst Relation in Dilute Electrolyte Solutions of Lithium Perchlorate in Polyethylene Glycols (200, 300, 400, and 600), (2015).

[145] P. Vallet, J.J. Parajó, F. Sotuela, A. Morcillo, M. Villanueva, O. Cabeza, L.M. Varela, Electrical Conductivity and Nyquist Plot of C 4 C 1 Im BF 4 at Room Temperature by Impedance Spectroscopy, (n.d.) 1–8.

[146] H. Mazzer, L. Cardozo-Filho, P.R.G. Fernandes, Broadband dielectric spectroscopy of protic ethylammonium-based ionic liquids synthetized with different anions, J Mol Liq 269 (2018) 556–563.

[147] R.J. Sengwa, S. Choudhary, P. Dhatarwal, Characterization of relaxation processes over static permittivity frequency regime and compliance of the Stokes-Einstein-Nernst relation in propylene carbonate, J Mol Liq 225 (2017) 42–49.

[148] G.P. Pandey, S.A. Hashmi, Solid-state supercapacitors with ionic liquid based gel polymer electrolyte: Effect of lithium salt addition, J Power Sources 243 (2013) 211–218.

[149] F. Zhao, X. Wu, M. Wang, Y. Liu, L. Gao, S. Dong, Electrochemical and bioelectrochemistry properties of room-temperature ionic liquids and carbon composite materials, Anal Chem 76 (2004) 4960–4967.

[150] J.P. Tafur, A.J. Fernández Romero, Electrical and spectroscopic characterization of PVdF-HFP and TFSI-ionic liquids-based gel polymer electrolyte membranes. Influence of ZnTf2 salt, J Memb Sci 469 (2014) 499–506.

[151] R. Baskaran, S. Selvasekarapandian, G. Hirankumar, M.S. Bhuvaneswari, Vibrational, ac impedance and dielectric spectroscopic studies of poly(vinylacetate)-N,N-dimethylformamide-LiClO4 polymer gel electrolytes, J Power Sources 134 (2004) 235–240.

[152] H. Gupta, L. Balo, V.K. Singh, K. Singh, A.K. Tripathi, Y. Lal Verma, R.K. Singh, Effect of temperature on electrochemical performance of ionic liquid based polymer electrolyte with Li/LiFePO 4 electrodes, (2017).

[153] M.R. Shoar Abouzari, F. Berkemeier, G. Schmitz, D. Wilmer, On the physical interpretation of constant phase elements, Solid State Ion 180 (2009) 922–927.

[154] B.A. Mei, O. Munteshari, J. Lau, B. Dunn, L. Pilon, Physical Interpretations of Nyquist Plots for EDLC Electrodes and Devices, Journal of Physical Chemistry C 122 (2018) 194–206.

[155] F. Silva, C. Gomes, M. Figueiredo, R. Costa, A. Martins, C.M. Pereira, The electrical double layer at the [BMIM][PF6] ionic liquid/electrode interface - Effect of temperature on the differential capacitance, Journal of Electroanalytical Chemistry 622 (2008) 153–160.

[156] S.R. Taylor, E. Gileadi, Physical Interpretation of the Warburg Impedance, Corrosion 51 (1995).

[157] G.J. Brug, A. Van Den Eeden, M. Sluyters-Rehbach, J.H. Sluyters, The analysis of electrode impedances complicated by the presence of a constant phase element, Journal of Electroanalytical Chemistry 176 (1984) 275–295.

[158] Y.S. Zhu, S.Y. Xiao, M.X. Li, Z. Chang, F.X. Wang, J. Gao, Y.P. Wu, Natural macromolecule based carboxymethyl cellulose as a gel polymer electrolyte with adjustable porosity for lithium ion batteries, J Power Sources 288 (2015) 368–375..

[159] S. Menne, J. Pires, M. Anouti, A. Balducci, Protic ionic liquids as electrolytes for lithium-ion batteries, Electrochem Commun 31 (2013) 39–41..

[160] H. Srour, L. Chancelier, E. Bolimowska, T. Gutel, S. Mailley, H. Rouault, C.C. Santini, C. gr, Ionic liquid-based electrolytes for lithium-ion batteries: review of performances of various electrode systems, J Appl Electrochem 46 (n.d.).

[161] J. Xia, F. Zhu, G. Wang, L. Wang, Y. Meng, Y. Zhang, Synthesis of LiFePO4/C using ionic liquid as carbon source for lithium ion batteries, Solid State Ion 308 (2017) 133–138.

4. Conclusions

The main aim of this thesis was to verify the viability of liquid and semisolid electrolytes (ionogel) based on the mixtures IL + salt of electrochemical interest (Li, Mg, Ca and Al), with common anion, for the use in energy storage. This work introduces the provision of stable synthesis routes of the ionogels and the systematic characterization of their most relevant physicochemical properties (thermal, structural, physical and electrochemical).

Specifically, the main conclusions of this thesis are listed below:

- The solubility limits of IL-salt mixtures in liquid state have been determined, being dependent of both compounds (IL and salt), ranging between 1.5 (for [C_4C_1Pyrr][TFSI] with LiTFSI salt) and 3 (for [C_2Im][NO_3] with $LiNO_3$) mol of salt/litre of IL.
- The IL and IL + salt mixtures can be confined inside a silica matrix obtaining a semisolid self-standing and easy-to-handle electrolytic material. The confinement synthesis route has been modified and improved during the development of the thesis, concluding that the use of two silane compounds as precursors is the most suitable.
- Phase transitions of the pure ILs in liquid state for EAN, [C_2Im][NO_3], [C_4C_1Pyrr][TFSI], [C_2C_1Im][TFSI] have been reported, observing a crystalline behaviour in all the pure ILs. The melting temperature follow the trend: [C_2C_1Im][TFSI] (-17 °C) < [C_4C_1Pyr][TFSI] (-6 °C) < EAN (17 °C) < [C_2Im][NO_3] (40 °C). But important differences have been found in the thermal behavoir of the pure ionogels. The nanoconfinement of EAN tends to a complete vanishing of the phase transitions, whereas [C_2Im][NO_3] and [C_4C_1Pyrr][TFSI] show similar, but wider melting peaks, shifted to lower temperatures, after confinement. This different behaviour is related with the pore size of the matrix, and the order reduction of the polar nanoregions of the sample.
- The addition of salts to protic ILs (EAN, [C_2Im][NO_3]) and aprotic IL ([C_4C_1Pyrr][TFSI]) showed different thermal behavior against the salt concentration. Whereas, the lowest concentration provokes a decrease in melting temperature and a broadening of the melting peaks for both, PILs and APIL, the highest salt concentrations frustrate the crystallization for the PILs + salt mixtures, increasing the amorphous phase, but for APILs + salt mixtures different metastable complexes with different melting point have been observed.
- Thermal degradation by means of TGA of the ILs EAN, [C_2Im][NO_3], [C_4C_1Pyrr][TFSI], [C_2C_1Im][TFSI] have been reported following the trend: [C_2C_1Im][TFSI] > [C_4C_1Pyrr][TFSI] > EAN > [C_2Im][NO_3], highlighting the greater importance of the anion in this property.
- Neither salt addition nor nanoconfinement affect significantly the thermal stability of the samples.
- Despite of a shifting of the donor protons of the PILs to higher energetic magnetic fields with salt addition, and a broadening of the peaks due to nanoconfinement,

neither salt addition nor nanoconfinement change significantly the structural arrangement of the ionic liquid.

- The density of the IL and IL + salt mixtures in liquid state decrease linearly with increasing temperature, whereas viscosity decrease with increasing temperature, and this behavior is well described by VFT model. Salt addition increases the density and the viscosity.
- Broad Band Dielectric Spectroscopy (BBDS) shows that the ionic mobility increases with temperature and decreases with the salt addition for both, liquid and gel, samples. The BBDS shows that the nanoconfinement, in general, reduces the ionic mobility which is traduced in a shift to lower frequencies of the different presented regimes in the interfacial relaxation. Relaxation time decreases with increasing temperature and its dependency with temperature is, also, well described by VFT model.
- The ionic conductivity decreases with lithium salt addition in liquid samples. For EAN, multivalent salt addition effect was studied being the highest reduction corresponding to saturated mixtures of the multivalent salts (Mg^{2+}, Ca^{2+} and Al^{3+}). This means that higher charge surface density give rise to significantly more viscous solutions.
- The ionic conductivity of the ionogels is lower than the analogous liquid sample, although, this property is highly dependent on the selected gelation route. The ionic conductivity increase for EAN gels with respect to its liquid state is presumably due to the presence of water which is a subproduct of the gelation route. Nevertheless, for the ionogels based in PILs (EAN and $[C_2Im][NO_3]$) for the lowest salt concentration studied an increase of the ionic conductivity with salt addition is observed with respect to the pure ionogel. This fact indicates that the disorder associated to the nanoconfinement favours the ionic transport, but the salt concentration and the scaffold seems to be important influence. Further studies must be performed to understand the mechanism behind this facts.
- The temperature dependence of the conductivity was studied in the Vogel-Fulcher-Tammann (VFT) framework. Good agreement is observed in the activation energies obtained from VFT fitting of the ionic conductivity and relaxation times (obtained by BBDS) against temperature.
- Pure $[C_4C_1Pyrr][TFSI]$, in liquid and gel states, is the most suitable compound, among those here studied, to be proposed as electrolyte in a functional Li-ion battery. Then, this IL, in liquid and gel states, was selected for a deeper electrochemical and cyclability studies.
- Electrochemical Impedance Spectroscopy (EIS) of the pure IL $[C_4C_1Pyrr][TFSI]$ in liquid and gel states shows that the impedance module is decreasing with increasing temperature, as expected. The impedance module of the gel sample is higher that of the liquid state.
- A new equivalent circuit and its physical meaning is proposed to fit the complete spectroscopical range of the EIS of the pure IL $[C_4C_1Pyrr][TFSI]$ in liquid and gel states throughout the frequency range of the interfacial relaxation, and the

differential capacity is obtained, which increases with increasing temperature. Surprisingly, the obtained differential capacity of the gel sample is higher than that of the liquid state, indicating that the energy stored in the gel sample is higher than in the liquid sample.

- A half-cell experiment is performed for the pure IL [C_4C_1Pyrr][TFSI] in liquid and gel, demonstrating that the lithium contained in the electrodes is enough to enable the charge-discharge process for a galvanostatic half-cell Li-ion battery.

Final remarks and future work

The main purpose of this thesis was to progress in the propose of a flexible ionogel based in ILs as potential electrolytes for LIBs. Results have been proved that the pure IL [C_4C_1Pyrr][TFSI] is an optimal candidate, allowing the charge/discharge process. This preliminary, but promising result has several implications, such as a decrease of the necessary lithium for the battery assembly, and therefore, a high-cost reduction in the battery manufacturing.

Beyond the results of this thesis, the experimental frontiers of the battery electrolytes have been widened in LIBs and also for post-lithium devices by the extensive and systematic characterization of several IL and IL + salt.

For future work, collecting the knowledge acquired during the development of this thesis, in order to improve the electrolytic characteristics of ILs, a decrease on the viscosity of the electrolytic mixtures (IL + salt) and an increase of the metal cation transport numbers can be proposed by the addition of a molecular cosolvent. Numerous studies are still pending to the final implementation of a LIB based on an electrolyte composed by IL, by this frame, ternary mixtures based on IL + Lithium salt + Carbonate are proposed. The main aim to introduce a non-polar solvent (such carbonates) is to reduce the formation of solvation complexes by the metal salt with the anion, which leads to a negatively charged complexes, that transports the cation toward the positively charged electrode during charge (cathode) and discharge (anode), making impossible their insertion/disinsertion in the charge/discharge process of the battery. Additionally, the nanoconfinement of the ternary mixtures in gel matrices could be a great advance in the implementation of 4th generation LIB.

Annexed Material A

1. Density

Table A1. Density of pure EAN (Figure 32).

Dry EAN	
T /K	**ρ /g·cm^{-3}**
288	1.2162
293	1.2132
298	1.2101
303	1.2071
308	1.2041
313	1.2012
318	1.1982
323	1.1953
328	1.1924
333	1.1895
338	1.1866
343	1.1837
348	1.1809
353	1.1780
358	1.1751
363	1.1723
368	1.1695

Table A2. Density of EAN saturated water content (Figure 32).

Water content saturated EAN	
T /K	**ρ /g·cm^{-3}**
278	1.1874
283	1.1840
288	1.1807
293	1.1775
298	1.1742
303	1.1710
308	1.1678
313	1.1646
318	1.1614
323	1.1582
328	1.1550
333	1.1518
338	1.1486
343	1.1454
348	1.1421
353	1.1389
358	1.1357
363	1.1325

368	1.1293
373	1.1259

Table A3. Density of pure $[C_2Im][NO_3]$ (Figure 34).

Pure $[C_2Im][NO_3]$	
T /K	**ρ /g·cm^{-3}**
313	1.2521
318	1.2486
323	1.2451
328	1.2417
333	1.2382
338	1.2348

Table A4. Density of pure $[C_4C_1Pyrr][TFSI]$ (Figure 34).

Pure $[C_4C_1Pyrr][TFSI]$	
T /K	**ρ /g·cm^{-3}**
283	1.4062
288	1.4018
293	1.3974
298	1.3930
303	1.3886
308	1.3842
313	1.3798
318	1.3754
323	1.3711
328	1.3667
333	1.3623
338	1.3578

Table A5. Density of pure $[C_2C_1Im][TFSI]$ (Figure 34).

Pure $[C_2C_1Im][TFSI]$	
T /K	**ρ /g·cm^{-3}**
283	1.5332
288	1.5281
293	1.5230
298	1.5180
303	1.5130
308	1.5080
313	1.5030
318	1.4980
323	1.4930

328	1.4880
333	1.4830
338	1.4780

Table A6. Density of $[C_2Im][NO_3]$ + $LiNO_3$

$[C_2Im][NO_3]$ + $LiNO_3$ 0.5 mol·kg^{-1}

T /K	ρ /g·cm^{-3}
308	1.2700
313	1.2664
318	1.2629
323	1.2594
328	1.2553
333	1.2524
338	1.2489

$[C_2Im][NO_3]$ + $LiNO_3$ 1 mol·kg^{-1}

T /K	ρ /g·cm^{-3}
298	1.2917
303	1.2881
308	1.2845
313	1.2810
318	1.2774
323	1.2739
328	1.2703
333	1.2668
338	1.2633

$[C_2Im][NO_3]$ + $LiNO_3$ 2 mol·kg^{-1}

T /K	ρ /g·cm^{-3}
298	1.3180
303	1.3144
308	1.3107
313	1.3071
318	1.3035
323	1.2999
328	1.2963
333	1.2927
338	1.2891

$[C_2Im][NO_3]$ + $LiNO_3$ 3 mol·kg^{-1}

T /K	ρ /g·cm^{-3}
288	1.3512
293	1.3474
298	1.3436
303	1.3399
308	1.3363
313	1.3326
318	1.3290
323	1.3253
328	1.3217

333	1.3180
338	1.3144

Table A7. Density of $[C_2Im][NO_3]$ + $Mg(NO_3)_2$

$[C_2Im][NO_3]$ + $Mg(NO_3)_2$ 0.5 mol·kg^{-1}

T /K	ρ /g·cm^{-3}
313	1.2836
318	1.2798
323	1.2761
328	1.2724
333	1.2687
338	1.2651

$[C_2Im][NO_3]$ + $Mg(NO_3)_2$ 1 mol·kg^{-1}

T /K	ρ /g·cm^{-3}
288	1.3333
293	1.3294
298	1.3255
303	1.3217
308	1.3179
313	1.3141
318	1.3103
323	1.3066
328	1.3029
333	1.2991
338	1.2954

$[C_2Im][NO_3]$ + $Mg(NO_3)_2$ 2 mol·kg^{-1}

T /K	ρ /g·cm^{-3}
288	1.3913
293	1.3868
298	1.3824
303	1.3782
308	1.3741
313	1.3700
318	1.3660
323	1.3620
328	1.3580
333	1.3539
338	1.3500

Table A8. Density of $[C_2Im][NO_3]$ + $Al(NO_3)_3$

$[C_2Im][NO_3]$ + $Al(NO_3)_3$ 0.5 mol·kg^{-1}

T /K	ρ /g·cm^{-3}
308	1.3002
313	1.2965

318	1.2927
323	1.2890
328	1.2853
333	1.2816
338	1.2778

$[C_2Im][NO_3] + Al(NO_3)_3$ 1 mol·kg^{-1}	
T /K	**ρ /g·cm^{-3}**
298	1.3428
303	1.3388
308	1.3349
313	1.3310
318	1.3271
323	1.3232
328	1.3193
333	1.3154
338	1.3115

Table A9. Density of $[C_4C_1Pyrr][TFSI]$ + Li TFSI 0.1 mol·kg^{-1}

$[C_4C_1Pyrr][TFSI]$ + Li TFSI 0.1 mol·kg^{-1}	
T /K	**ρ /g·cm^{-3}**
283	1.4180
288	1.4135
293	1.4091
298	1.4047
303	1.4003
308	1.3959
313	1.3915
318	1.3871
323	1.3827
328	1.3783
333	1.3739
338	1.3694

Table A10. Density of $[C_4C_1Pyrr][TFSI]$ + Li TFSI 0.5 mol·kg^{-1}

$[C_4C_1Pyrr][TFSI]$ + Li TFSI 0.5 mol·kg^{-1}	
T /K	**ρ /g·cm^{-3}**
283	1.4635
288	1.4585
293	1.4537
298	1.4490
303	1.4443
308	1.4397
313	1.4351
318	1.4305

323	1.4260
328	1.4214
333	1.4167
338	1.4120

Table A11. Density of [C$_4$C$_1$Pyrr][TFSI] + Li TFSI 1 mol·kg^{-1}

[C$_4$C$_1$Pyrr][TFSI] + Li TFSI 1 mol·kg^{-1}

T /K	ρ /g·cm^{-3}
283	1.4960
288	1.4910
293	1.4858
298	1.4807
303	1.4757
308	1.4709
313	1.4661
318	1.4614
323	1.4567
328	1.4520
333	1.4473
338	1.4425

Table A12. Density of EAN dopped with X(NO$_3$)$_n$ (X=Li, Mg, Ca and Al) at different concentrations (T = 298 K)

EAN + Li(NO$_3$)

χ	ρ /g·cm^{-3}
0.031	1.21938
0.0609	1.23072
0.08866	1.23961
0.1148	1.24599
0.1395	1.25576
0.1629	1.26598
0.1850	1.27565
0.2060	1.28341

EAN + Mg(NO$_3$)$_2$

χ	ρ /g·cm^{-3}
0.0513	1.24893
0.0976	1.28829
0.1395	1.30939
0.1778	1.34071
0.2127	1.35838

EAN + Ca(NO$_3$)$_2$

χ	ρ /g·cm^{-3}
0.0212	1.23047
0.0513	1.25481

0.0703	1.2765
0.0976	1.28933

EAN + Al(NO$_3$)$_3$

χ	ρ /g·cm^{-3}
0.0513	1.26545
0.0976	1.31084
0.1395	1.33849
0.1778	1.37961
0.2127	1.3990

2. Dynamic Viscosity

Table A13. Dynamic Viscosity vs Temperature of EAN, (pure and water content saturated) measured in the rheometer (TA Instruments AR2000) and with the stabinger.

EAN water content saturated (rheometer)

T /K	η /mPa·s
283	11.46
288	10.17
293	8.99
298	8.047
303	7.256
308	6.646
313	6.110
318	5.715
323	5.203
328	4.829
333	4.130
338	4.102

EAN water content saturated (stabinger)

T /K	η /mPa·s
278	7.9387
283	6.9542
288	6.1432
293	5.4606
298	4.941
303	4.3996
308	3.9816
313	3.6117
318	3.2844
323	2.9913
328	2.7374
333	2.5111
338	2.3108
343	2.1329

348	1.9772
353	1.8419
358	1.725
363	1.6261
368	1.6294
373	1.6849

Pure EAN (rheometer)

T /K	η /mPa·s
283	65.30
288	53.67
293	44.82
298	37.78
303	32.21
308	27.72
313	24.26
318	21.23
323	18.7
328	16.56
333	14.91
338	13.47

Pure EAN (stabinger)

T /K	η /mPa·s
288	55.61
293	45.826
298	38.48
303	32.337
308	27.611
313	23.802
318	20.70
323	18.144
328	16.019
333	14.25
338	12.742
343	11.465
348	10.373
353	9.434
358	8.6239
363	7.9203
368	7.3058

Table A14. Dynamic Viscosity vs Temperature of [C_2Im][NO_3].

[C_2Im][NO_3]

T /K	η /mPa·s
313	38.848
318	32.358

323	27.332
328	23.316
333	20.061
338	17.436

Table A15. Dynamic Viscosity vs Temperature of $[C_4C_1Pyrr][TFSI]$.

$[C_4C_1Pyrr][TFSI]$	
T /K	**η /mPa·s**
283	149.02
288	113.56
293	88.163
298	69.74
303	56.123
308	45.836
313	37.971
318	31.857
323	27.033
328	23.179
333	20.053
338	17.497

Table A16. Dynamic Viscosity vs Temperature of $[C_2C_1Im][TFSI]$.

$[C_2C_1Im][TFSI]$	
T /K	**η /mPa·s**
283	59.058
288	47.575
293	38.989
298	32.423
303	27.328
308	23.282
313	20.08
318	17.466
323	15.324
328	13.55
333	12.068
338	10.818

Table A17. Dynamic viscosity of EAN dopped with $X(NO_3)_n$ (X=Li, Mg, Ca and Al).

EAN + $LiNO_3$ 1 mol·kg^{-1}	
T /K	**η /mPa·s**
283	48.066
293	33.044

298	28.423
303	23.819
313	17.955

EAN + LiNO$_3$ 2 mol·kg^{-1}

T /K	*η* /mPa·s
283	87.185
293	55.305
298	45.627
303	38.148
313	27.714

EAN + Mg(NO$_3$)$_2$ 1.5 mol·kg^{-1}

T /K	*η* /mPa·s
283	176.182
293	137.713
298	112.266
303	91.535
313	77.449

EAN + Mg(NO$_3$)$_2$ 2.5 mol·kg^{-1}

T /K	*η* /mPa·s
283	351.493
293	246.921
298	195.469
303	151.578
313	119.223

EAN + Ca(NO$_3$)$_2$ 0.5 mol·kg^{-1}

T /K	*η* /mPa·s
283	134.169
293	107.013
298	87.171
303	71.997
313	60.237

EAN + Ca(NO$_3$)$_2$ 1 mol·kg^{-1}

T /K	*η* /mPa·s
283	162.803
293	125.873
298	103.629
303	81.965
313	68.692

EAN + Al(NO$_3$)$_3$ 1.5 mol·kg^{-1}

T /K	*η* /mPa·s
283	274.308
293	210.671
298	154.495
303	117.156
313	90.692

EAN + Al(NO$_3$)$_3$ 2.5 mol·kg^{-1}

T /K	η /mPa·s
298	389.179
303	285.799
313	182.482

Table A18. Dynamic Viscosity vs Temperature of $[C_4C_1Pyrr][TFSI]$ with Li TFSI.

$[C_4C_1Pyrr][TFSI]$ + Li TFSI 0.1 mol·kg^{-1}

T /K	η /mPa·s
283	205.93
288	153.22
293	116.88
298	90.868
303	72.048
308	58.041
313	47.477
318	39.364
323	33.048
328	28.056
333	24.054
338	20.802

$[C_4C_1Pyrr][TFSI]$ + Li TFSI 0.5 mol·kg^{-1}

T /K	η /mPa·s
283	623.38
288	430.27
293	306.25
298	223.77
303	167.24
308	128
313	99.857
318	79.456
323	64.025
328	52.447
333	43.595
338	36.581

$[C_4C_1Pyrr][TFSI]$ + Li TFSI 1 mol·kg^{-1}

T /K	η /mPa·s
283	1159.3
288	763.77
293	520.13
298	365.41
303	264.2
308	195.78
313	148.48
318	114.97
323	90.629

328	72.554
333	59.064
338	48.636

Table A19. Dynamic viscosity of $[C_2Im][NO_3]$ dopped with $X(NO_3)_n$ (X=Li, Mg and Al).

$[C_2Im][NO_3]$ + $LiNO_3$ 0.5 mol·kg^{-1}

T /K	η /mPa·s
308	50.547
313	41.596
318	34.464
323	28.945
328	24.590
333	21.110
338	18.297

$[C_2Im][NO_3]$ + $LiNO_3$ 1 mol·kg^{-1}

T /K	η /mPa·s
298	95.942
303	74.518
308	59.097
313	47.773
318	39.252
323	32.734
328	27.643
333	23.623
338	20.396

$[C_2Im][NO_3]$ + $LiNO_3$ 2 mol·kg^{-1}

T /K	η /mPa·s
298	137.23
303	104.62
308	81.561
313	64.796
318	52.342
323	43.126
328	36.023
333	30.567
338	26.169

$[C_2Im][NO_3]$ + $LiNO_3$ 3 mol·kg^{-1}

T /K	η /mPa·s
288	390.38
293	272.43
298	196.60
303	146.09
308	111.45
313	87.108
318	69.518

323	56.504
328	46.544
333	38.893
338	32.868

[C_2Im][NO_3] + $Mg(NO_3)_2$ 0.5 mol·kg^{-1}

T /K	η /mPa·s
313	47.880
318	39.522
323	33.023
328	27.923
333	23.864
338	20.600

[C_2Im][NO_3] + $Mg(NO_3)_2$ 1 mol·kg^{-1}

T /K	η /mPa·s
288	259.23
293	185.45
298	136.84
303	103.82
308	80.671
313	64.017
318	51.754
323	42.530
328	35.458
333	29.945
338	25.585

[C_2Im][NO_3] + $Mg(NO_3)_2$ 2 mol·kg^{-1}

T /K	η /mPa·s
288	578.67
293	390.64
298	274.01
303	198.74
308	148.39
313	113.66
318	89.007
323	71.048
328	57.701
333	47.580
338	39.770

[C_2Im][NO_3] + $Al(NO_3)_3$ 0.5 mol·kg^{-1}

T /K	η /mPa·s
308	57.471
313	46.609
318	38.457
323	32.168
328	27.213
333	23.248

338	20.017
$[C_2Im][NO_3] + Al(NO_3)_3$ 2 mol·kg^{-1}	
T /K	**η /mPa·s**
298	136.58
303	104.52
308	81.815
313	65.300
318	52.993
323	43.668
328	36.435
333	30.740
338	26.195

3. BBDS

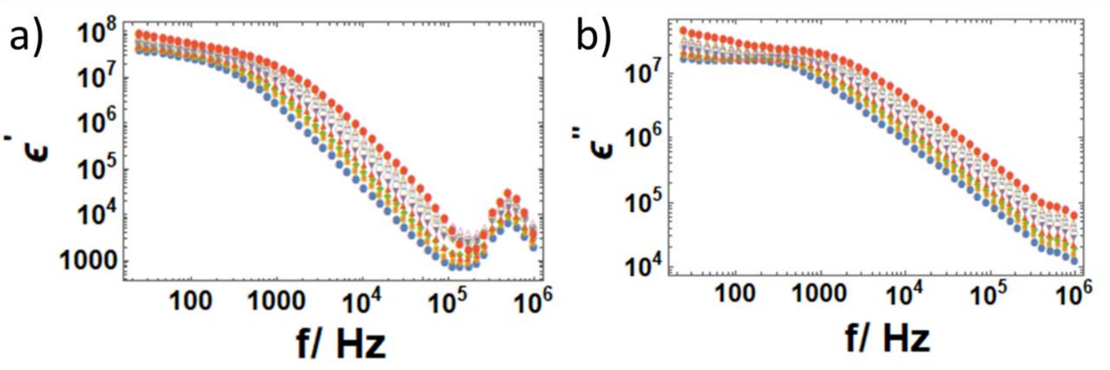

Figure A1. Dielectric spectroscopy from 20-10^6 Hz of $[C_2Im]^+$ $[NO_3]^-$, a) real part, b) imaginary part. Blue filled dots correspond to 288K, orange filled squares 293K, green filled diamonds 298K, red filled triangles 303K, purple filled triangle 308K, brown empty dots 313K, blue empty squares 318K, yellow empty diamonds 323K, purple empty triangles 328K, green empty triangles 333K and red filled dots 338K.

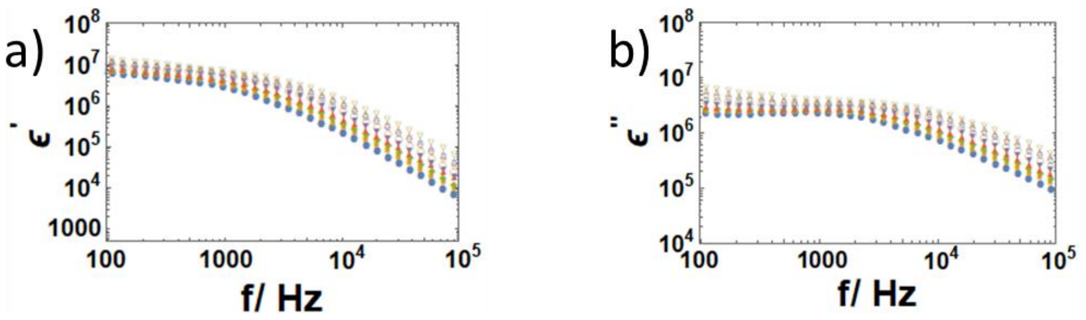

Figure A2. Dielectric spectroscopy of $[C_2Im]^+$ $[NO_3]^-$ + $LiNO_3$ 0.5 m, a) real part, b) imaginary part. Blue filled dots correspond to 293K, orange filled squares 298K, green filled diamonds 303K, red filled triangles 308K, purple filled triangle 313K, brown empty dots 318K, blue empty squares 323K, yellow empty diamonds 328K, purple empty triangles 333K and green empty triangles 338K.

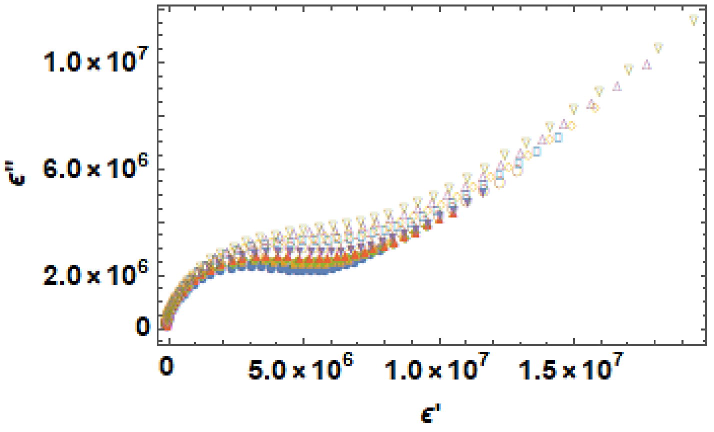

Figure A3. Cole-Cole plot of $[C_2Im]^+$ $[NO_3]^-$ + $LiNO_3$ 0.5 m. Blue filled dots correspond to 293K, orange filled squares 298K, green filled diamonds 303K, red filled triangles 308K, purple filled triangle 313K, brown empty dots 318K, blue empty squares 323K, yellow empty diamonds 328K, purple empty triangles 333K and green empty triangles 338K.

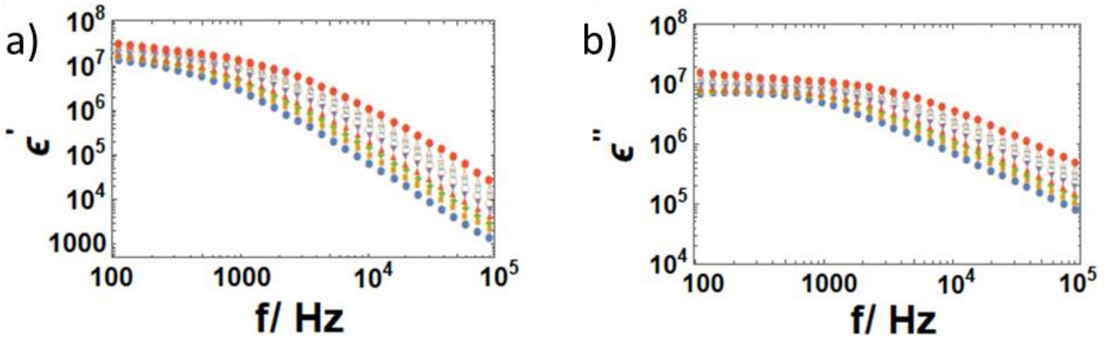

Figure A4. Dielectric spectroscopy of $[C_2Im]^+$ $[NO_3]^-$ + $LiNO_3$ 1 m, a) real part, b) imaginary part. Blue filled dots correspond to 288K, orange filled squares 293K, green filled diamonds 298K, red filled triangles 303K, purple filled triangle 308K, brown empty dots 313K, blue empty squares 318K, yellow empty diamonds 323K, purple empty triangles 328K, green empty triangles 333K and red filled dots 338K.

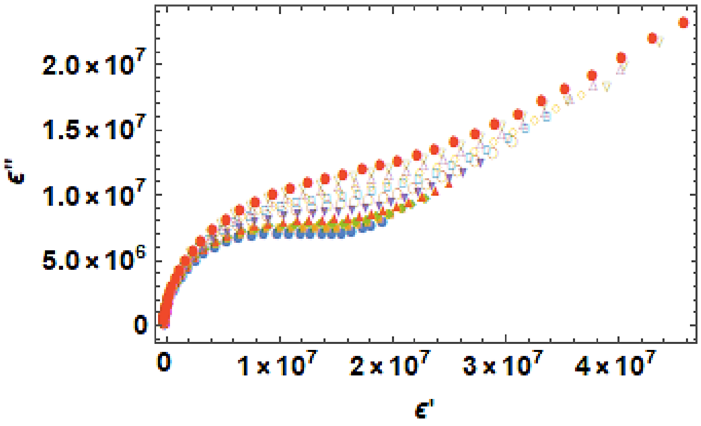

Figure A5. Cole-Cole plot of $[C_2Im]^+$ $[NO_3]^-$ + $LiNO_3$ 1 m, a) real part, b) imaginary part. Blue filled dots correspond to 288K, orange filled squares 293K, green filled diamonds 298K, red filled triangles 303K, purple filled triangle 308K, brown empty dots 313K, blue empty squares 318K, yellow empty diamonds 323K, purple empty triangles 328K, green empty triangles 333K and red filled dots 338K.

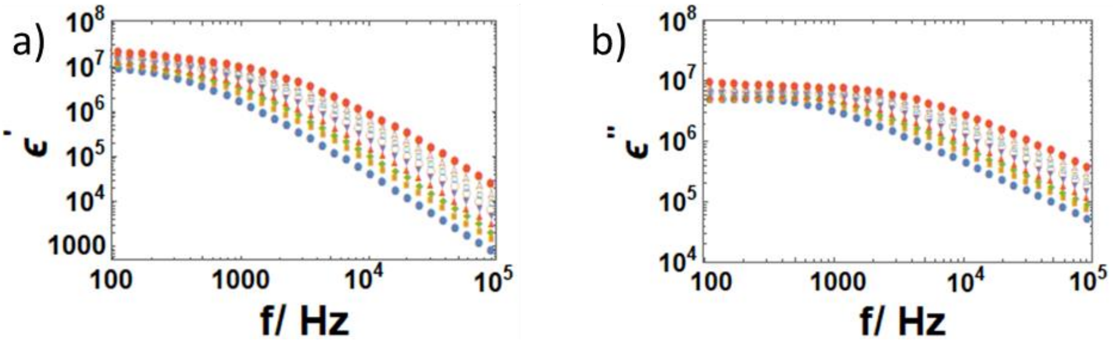

Figure A6. Dielectric spectroscopy of $[C_2Im]^+ [NO_3]^- + LiNO_3$ 2 m, a) real part, b) imaginary part. Blue filled dots correspond to 288K, orange filled squares 293K, green filled diamonds 298K, red filled triangles 303K, purple filled triangle 308K, brown empty dots 313K, blue empty squares 318K, yellow empty diamonds 323K, purple empty triangles 328K, green empty triangles 333K and red filled dots 338K.

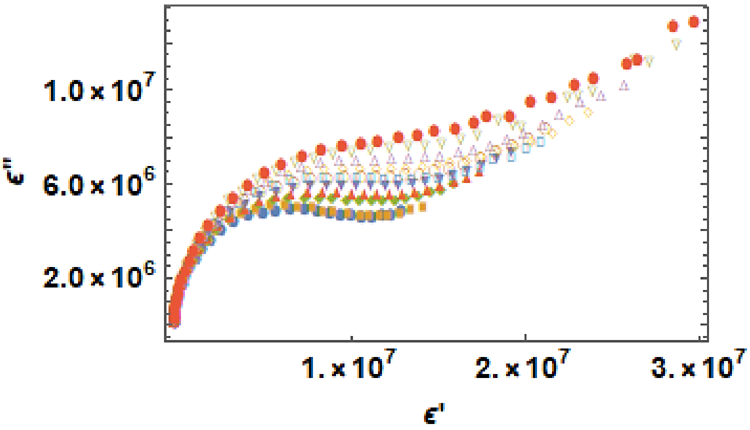

Figure A7. Cole-Cole plot of $[C_2Im]^+ [NO_3]^- + LiNO_3$ 2 m. Blue filled dots correspond to 288K, orange filled squares 293K, green filled diamonds 298K, red filled triangles 303K, purple filled triangle 308K, brown empty dots 313K, blue empty squares 318K, yellow empty diamonds 323K, purple empty triangles 328K, green empty triangles 333K and red filled dots 338K.

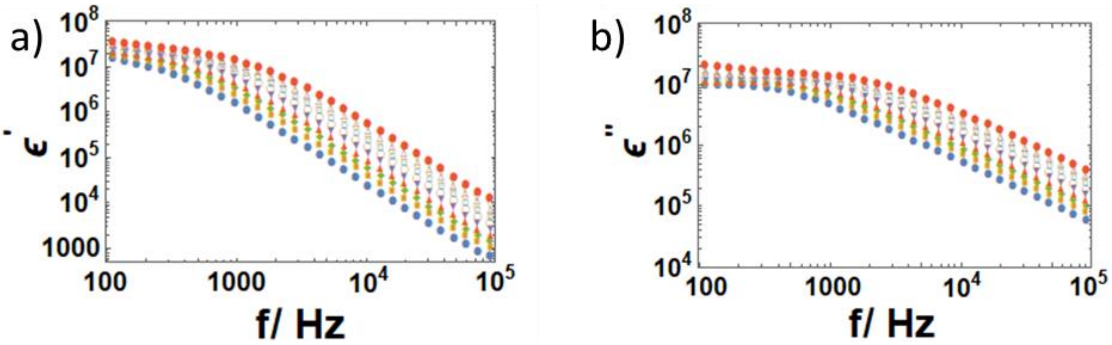

Figure A8. Dielectric spectroscopy of $[C_2Im]^+$ $[NO_3]^-$ + $Mg(NO_3)_2$ 0.5 m, a) real part, b) imaginary part. Blue filled dots correspond to 288K, orange filled squares 293K, green filled diamonds 298K, red filled triangles 303K, purple filled triangle 308K, brown empty dots 313K, blue empty squares 318K, yellow empty diamonds 323K, purple empty triangles 328K, green empty triangles 333K and red filled dots 338K.

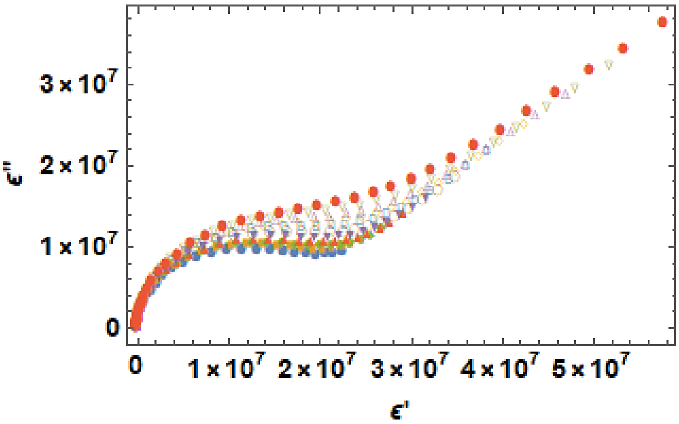

Figure A9. Cole-Cole plot of $[C_2Im]^+$ $[NO_3]^-$ + $Mg(NO_3)_2$ 0.5 m. Blue filled dots correspond to 288K, orange filled squares 293K, green filled diamonds 298K, red filled triangles 303K, purple filled triangle 308K, brown empty dots 313K, blue empty squares 318K, yellow empty diamonds 323K, purple empty triangles 328K, green empty triangles 333K and red filled dots 338K.

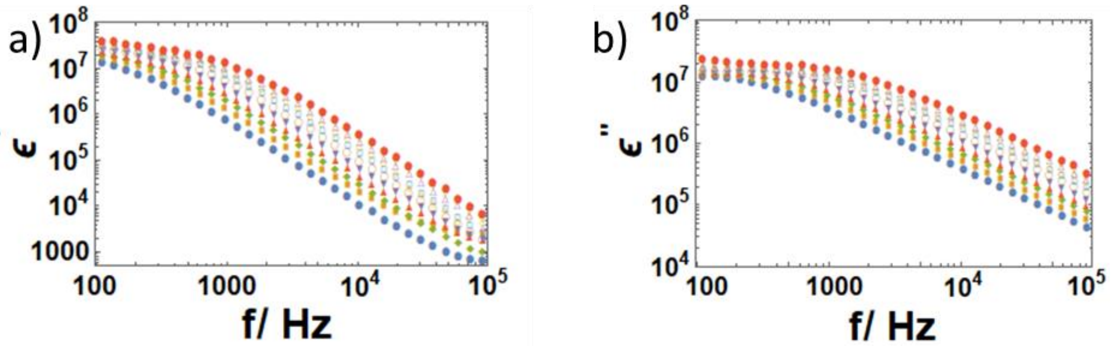

Figure A10. Dielectric spectroscopy of $[C_2Im]^+ [NO_3]^- + Mg(NO_3)_2$ 1 m, a) real part, b) imaginary part. Blue filled dots correspond to 288K, orange filled squares 293K, green filled diamonds 298K, red filled triangles 303K, purple filled triangle 308K, brown empty dots 313K, blue empty squares 318K, yellow empty diamonds 323K, purple empty triangles 328K, green empty triangles 333K and red filled dots 338K.

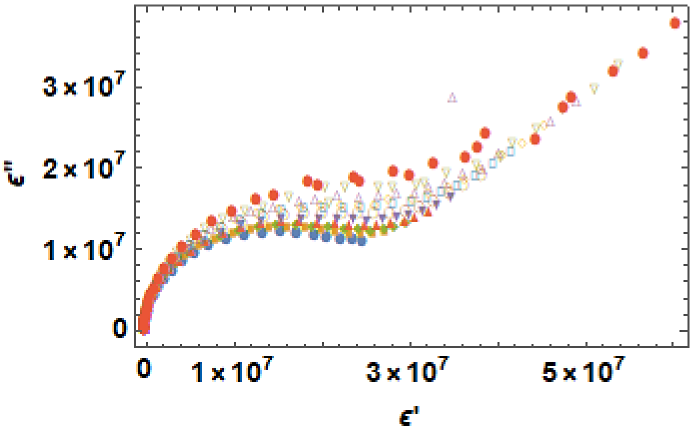

Figure A11. Cole-Cole plot of $[C_2Im]^+ [NO_3]^- + Mg(NO_3)_2$ 1 m. Blue filled dots correspond to 288K, orange filled squares 293K, green filled diamonds 298K, red filled triangles 303K, purple filled triangle 308K, brown empty dots 313K, blue empty squares 318K, yellow empty diamonds 323K, purple empty triangles 328K, green empty triangles 333K and red filled dots 338K.

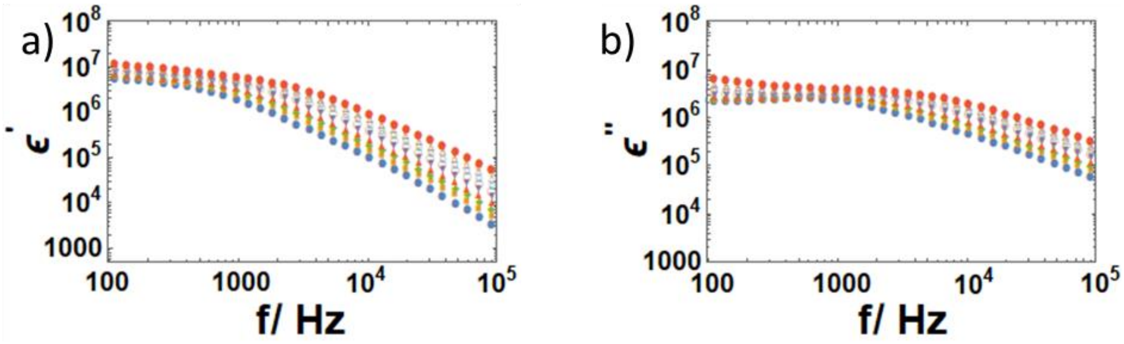

Figure A12. Dielectric spectroscopy of $[C_2Im]^+$ $[NO_3]^-$ + $Al(NO_3)_3$ 0.5 m, a) real part, b) imaginary part. Blue filled dots correspond to 288K, orange filled squares 293K, green filled diamonds 298K, red filled triangles 303K, purple filled triangle 308K, brown empty dots 313K, blue empty squares 318K, yellow empty diamonds 323K, purple empty triangles 328K, green empty triangles 333K and red filled dots 338K.

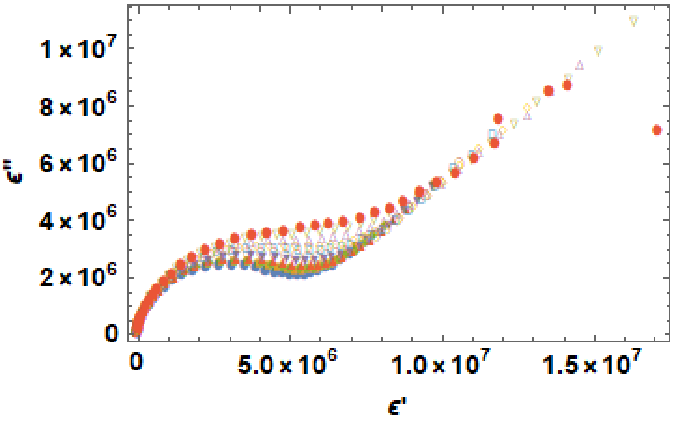

Figure A13. Cole-Cole plot of $[C_2Im]^+$ $[NO_3]^-$ + $Al(NO_3)_3$ 0.5 m. Blue filled dots correspond to 288K, orange filled squares 293K, green filled diamonds 298K, red filled triangles 303K, purple filled triangle 308K, brown empty dots 313K, blue empty squares 318K, yellow empty diamonds 323K, purple empty triangles 328K, green empty triangles 333K and red filled dots 338K.

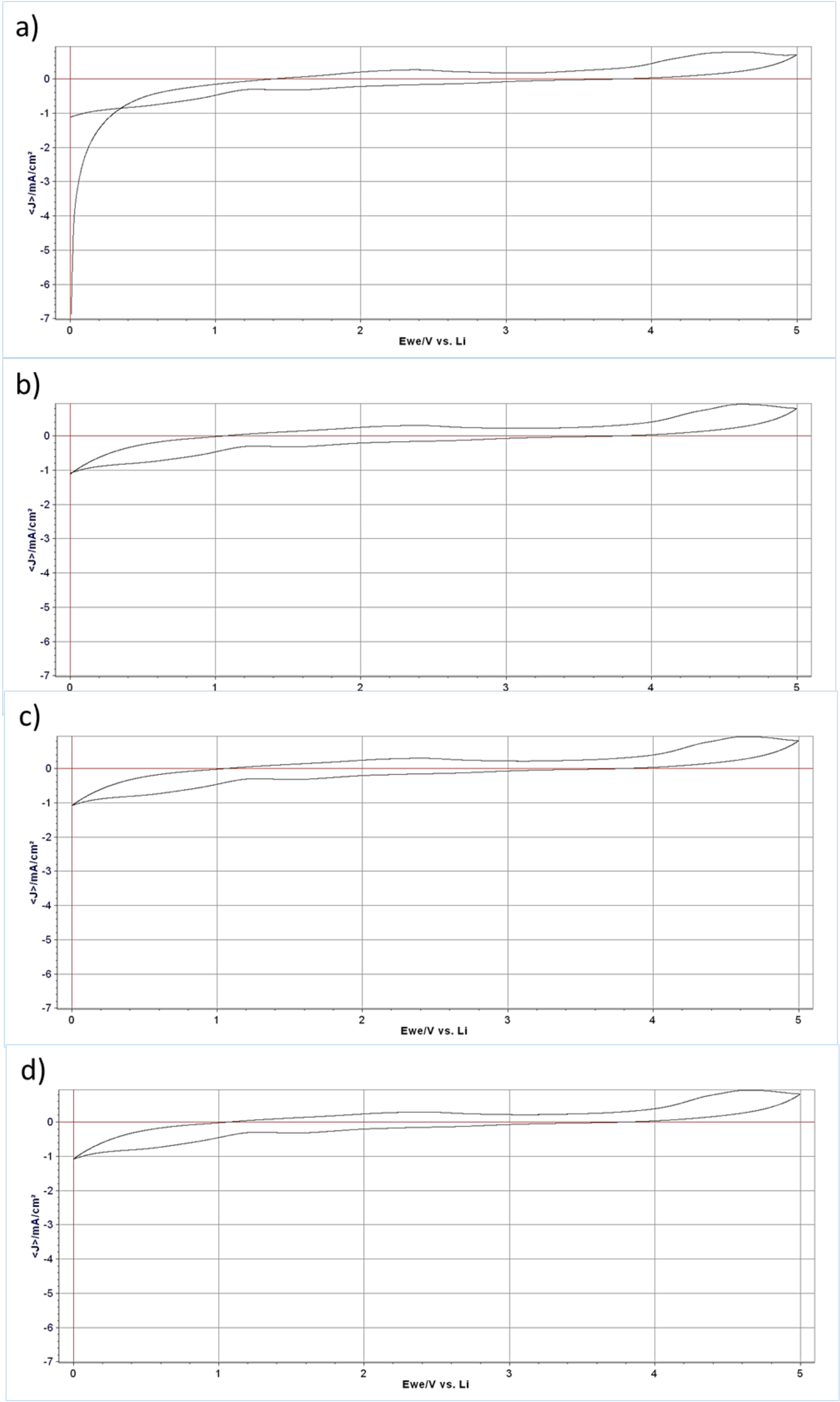

Figure A14. Cyclic voltammetry of [C_4C_1Pyrr][TFSI] in liquid state at 298 K. 1st cycle a), 2nd cycle b), 3rd cycle c) and 4th cycle d).

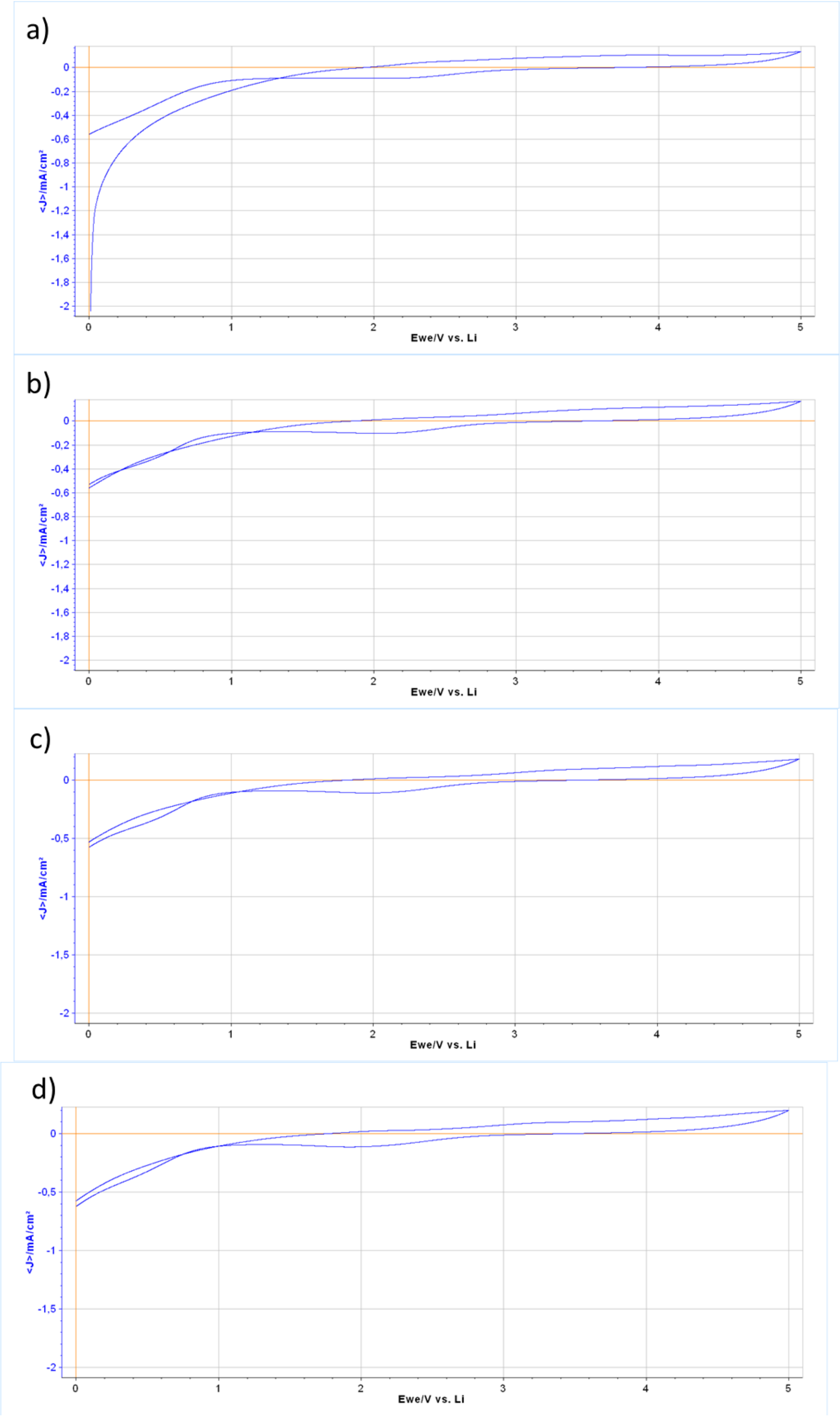

Figure A15. Cyclic voltammetry of [C$_4$C$_1$Pyrr][TFSI] in gel state at 298 K. 1st cycle a), 2nd cycle b), 3rd cycle c) and 4th cycle d).

Annexed Material B

List of publications used in this thesis and publication rights:

1.- J. J. Parajó, P. Vallet, M. J. G. Guimarey, A. Santiago, T. Teijera, A. Amigo, L. M. Varela,J. Salgado & M. Villanueva. “Thermophysical properties of n-alkyl-ammonium nitrate ionic liquids (n = 2,3,4) pure and water saturated for energy applications”. Journal of Thermal Analysis and Calorimetry volume 148, pages6699–6714 (2023). DOI:10.1007/s10973-023-12194-1.

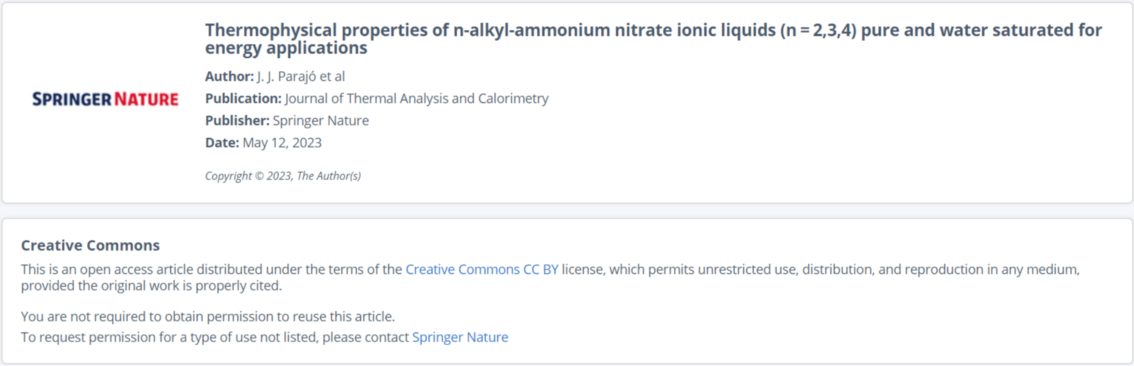

Thermophysical properties of n-alkyl-ammonium nitrate ionic liquids (n = 2,3,4) pure and water saturated for energy applications

SPRINGER NATURE

Author: J. J. Parajó et al
Publication: Journal of Thermal Analysis and Calorimetry
Publisher: Springer Nature
Date: May 12, 2023

Copyright © 2023, The Author(s)

Creative Commons

This is an open access article distributed under the terms of the Creative Commons CC BY license, which permits unrestricted use, distribution, and reproduction in any medium, provided the original work is properly cited.

You are not required to obtain permission to reuse this article.
To request permission for a type of use not listed, please contact Springer Nature

Authorship contribution statement:

P. Vallet: Data curation, Formal analysis, Methodology, Validation, Writing original draft.

Journal rank:

Q1 in Thermodinamics (position: 13/63).

Impact factor: 4.4.

Pablo Vallet, Silvia Bouzón-Capelo, Trinidad Méndez-Morales, Víctor Gómez-González, Yago Arosa, Raúl de la Fuente, Elena López-Lago, Julio R. Rodríguez, Luis J. Gallego, Juan J. Parajó, b, Josefa Salgado, Mireille Turmine, Luisa Segade, Oscar Cabeza, Luis M. Varela. "On the physical properties of mixtures of nitrate salts and protic ionic liquids". Journal of Molecular Liquids. Volume 350, 15 March 2022, 118483. DOI: 10.1016/j.molliq.2022.118483.

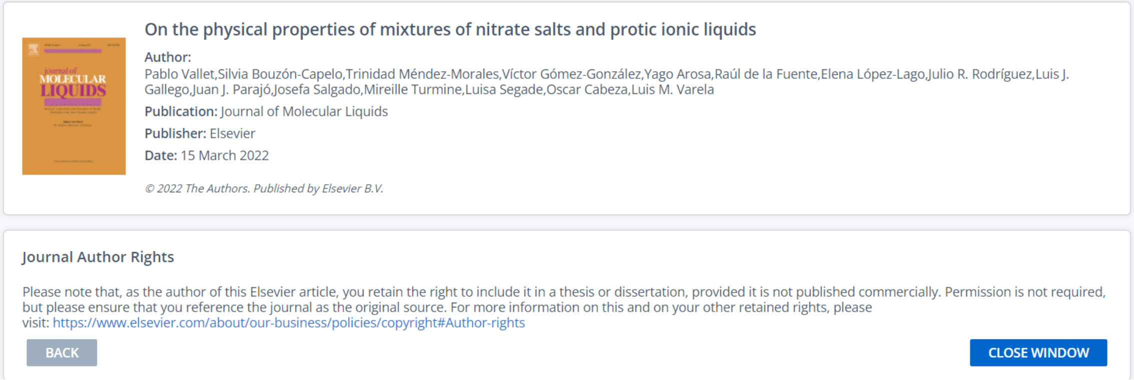

On the physical properties of mixtures of nitrate salts and protic ionic liquids

Author:
Pablo Vallet,Silvia Bouzón-Capelo,Trinidad Méndez-Morales,Víctor Gómez-González,Yago Arosa,Raúl de la Fuente,Elena López-Lago,Julio R. Rodríguez,Luis J. Gallego,Juan J. Parajó,Josefa Salgado,Mireille Turmine,Luisa Segade,Oscar Cabeza,Luis M. Varela

Publication: Journal of Molecular Liquids

Publisher: Elsevier

Date: 15 March 2022

© 2022 The Authors. Published by Elsevier B.V.

Journal Author Rights

Please note that, as the author of this Elsevier article, you retain the right to include it in a thesis or dissertation, provided it is not published commercially. Permission is not required, but please ensure that you reference the journal as the original source. For more information on this and on your other retained rights, please visit: https://www.elsevier.com/about/our-business/policies/copyright#Author-rights

Authorship contribution statement:

P. Vallet: Investigation, Validation, Formal analysis, Data curation, Visualization.

Journal rank:

Q1 in PHYSICS, ATOMIC, MOLECULAR & CHEMICAL (Position 13/63)

Impact factor of the journal: 6.0.

J.J. Parajó, P. Vallet, M. Villanueva, O. Cabeza, F. Fernández-Carretero, A. García Luis, M.E. Di Pietro, A. Mele, F. Castiglione, J. Salgado, L.M. Varela. "Ionogels based on protic ionic liquid - lithium salt mixtures". Journal of Molecular Liquids. Volume 397, 1 March 2024, 124093. DOI: 10.1016/j.molliq.2024.124093

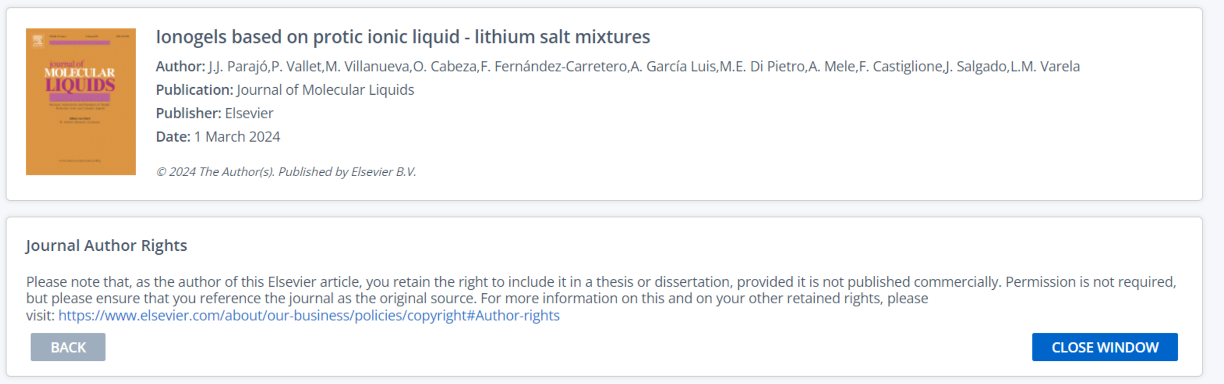

Ionogels based on protic ionic liquid - lithium salt mixtures

Author: J.J. Parajó,P. Vallet,M. Villanueva,O. Cabeza,F. Fernández-Carretero,A. García Luis,M.E. Di Pietro,A. Mele,F. Castiglione,J. Salgado,L.M. Varela

Publication: Journal of Molecular Liquids

Publisher: Elsevier

Date: 1 March 2024

© 2024 The Author(s). Published by Elsevier B.V.

Journal Author Rights

Please note that, as the author of this Elsevier article, you retain the right to include it in a thesis or dissertation, provided it is not published commercially. Permission is not required, but please ensure that you reference the journal as the original source. For more information on this and on your other retained rights, please visit: https://www.elsevier.com/about/our-business/policies/copyright#Author-rights

Authorship contribution statement:

P. Vallet: Data curation, Formal analysis, Methodology, Validation, Writing original draft.

Journal rank:

Q1 in PHYSICS, ATOMIC, MOLECULAR & CHEMICAL (Position 13/63)

Impact factor of the journal: 6.0.

P. Vallet, J.J. Parajó, A. Santiago-Alonso, M. Villanueva, Ó. Cabeza, L.M. Varela, J. Salgado. "Anomalous behaviour of the ionic conductivity of nanoconfined IL -lithium salt mixtures". Journal of Molecular Liquids. In Press, Journal Pre-proof. DOI: 10.1016/j.molliq.2024.124630

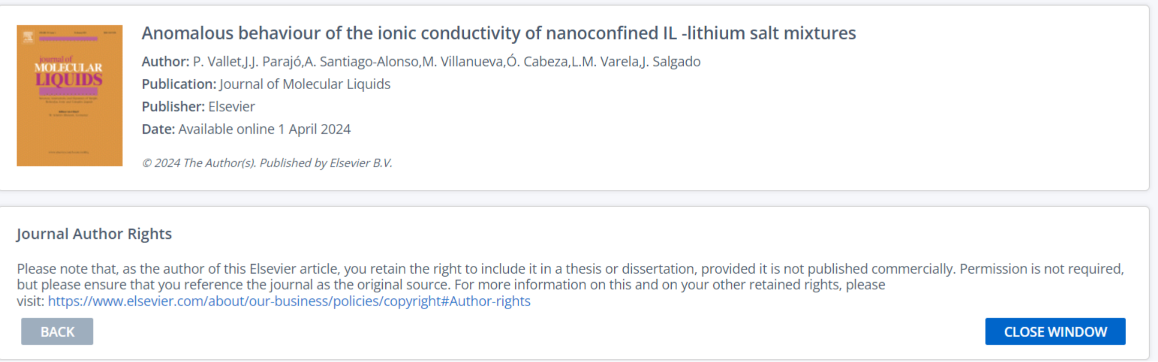

Anomalous behaviour of the ionic conductivity of nanoconfined IL -lithium salt mixtures

Author: P. Vallet,J.J. Parajó,A. Santiago-Alonso,M. Villanueva,Ó. Cabeza,L.M. Varela,J. Salgado

Publication: Journal of Molecular Liquids

Publisher: Elsevier

Date: Available online 1 April 2024

© 2024 The Author(s). Published by Elsevier B.V.

Journal Author Rights

Please note that, as the author of this Elsevier article, you retain the right to include it in a thesis or dissertation, provided it is not published commercially. Permission is not required, but please ensure that you reference the journal as the original source. For more information on this and on your other retained rights, please visit: https://www.elsevier.com/about/our-business/policies/copyright#Author-rights

Authorship contribution statement:

P. Vallet: Conceptualization, Data curation, Writing original draft.

Journal rank:

Q1 in PHYSICS, ATOMIC, MOLECULAR & CHEMICAL (Position 13/63)

Impact factor of the journal: 6.0.

RESUMO

Os novos acordos alcanzados na unión europea para reducir as emisións de dióxido de carbono (CO_2) entre outros gases de efecto invernadoiro son un feito, para iso desenvolveuse un ambicioso plan chamado "*fit for 55*", cuxo obxectivo é reducir en, polo menos, un 55% as emisións dos devanditos gases comparado cos niveis emitidos no 1990 para o 2030 e chegar a cero emisións para o 2050. Isto supón un gran desafío para a poboación europea, e en xeral, para toda a humanidade. O plan "*fit for 55*" consiste nunha serie de propostas para asegurar que os países membros están aliñados nas súas políticas climáticas a través do concilio europeo. Para levar a cabo este plan, apostouse por unha transición cara ás enerxías renovables, pero estas presentan picos de produción que normalmente non coinciden cos picos de demanda da rede eléctrica dificultando a substitución completa das fontes de enerxía tradicionais. Por este motivo, o almacenamento de enerxía convértese en crucial para poder levar a cabo este ambicioso plan e a electrificación dos vectores industriais, móbiles e económicos da sociedade. Adicionalmente, e debido ás últimas inestabilidades xeopolíticas, a unión europea para facer fronte á crise enerxética ha lanzado a iniciativa REPowerEU, que, entre outras, está a axudar a que os países membros aforren enerxía, produzan enerxía limpa e diversifiquen o seu abastecemento enerxético. Grazas a esta iniciativa, conseguiuse reducir nun 20% o consumo de enerxía en territorio europeo, reducir a dependencia de combustibles fósiles, introducido un tope aos prezos do gas e tope aos prezos mundiais do petróleo e duplicouse o despregamento adicional de enerxías renovables.

Ata a data, a demanda enerxética social era cuberta, en gran medida, polo petróleo e os seus derivados, debido á súa alta densidade enerxética (35-45 $GJ\cdot m^3$ para a gasolina), pero é ben sabido que a situación actual de cambio climático foi provocada pola liberación de gases de efecto invernadoiro que se producen durante a queima de combustibles fósiles. Esta situación provocou que os gobernos de todo o mundo mobilícense para tomar medidas e paliar, en medida do posible, a situación de emerxencia climática e realizar unha transición cara a fontes de enerxías limpas e verdes non contaminantes.

Na presente tese analízase desde o punto de vista experimental, a viabilidade de novos electrólitos para baterías de Ión-Litio, compostos por mesturas de Líquidos Iónicos (IL polas súas siglas en inglés) e sales inorgánicos de interese electroquímico de catión Litio, Magnesio, Calcio e Aluminio e anión común ao do líquido iónico. Estas mesturas electroquímicas serán confinadas en matrices de sílice (baseadas en ligazóns silicio-osíxeno) co obxectivo de obter un material semisólido electrolítico, coñecido como ionogel, para novas baterías, co fin de obter un material interesante para a industria que impida derramamentos na ensamblaxe das baterías de ión litio, ademais de ampliar o coñecemento en baterías da era post-litio.

Os ILs son compostos heteroxéneos formados por un catión orgánico e un anión orgánico ou inorgánico unidos por interaccións electrostáticas. Tecnicamente, os ILs son sales, pero coa peculiaridade de ter o punto de fusión por baixo dos 100 °C. En 1914, Paul

Walden sintetizou o primeiro Líquido Iónico, o $[C_2NH_3][NO_3]$ (posteriormente coñecido como o EAN), aínda que na actualidade segue sendo material de estudo na primeira liña de investigación. Particularmente, distínguense os ILs a temperatura ambiente (RTILs polas súas siglas en inglés), que son ILs co punto de fusión por baixo da temperatura ambiente. Durante as últimas décadas os ILs suscitaron un gran interese tanto no mundo académico como entre os máis diversos sectores tecnolóxicos e industriais, debido á infinidade de aplicacións na que poden ser usados. Algunhas das súas asombrosas características son presión de vapor case nula, baixa toxicidade (comparados cos cosolventes electrolíticos tradicionais), alta condutividade iónica, ampla xanela electroquímica, non inflamables, alta estabilidade térmica entre outras. Debido a estas propiedades destácase a súa alta potencialidade de uso en diversas aplicacións industriais; enxeñería de materiais, no sector enerxético (por exemplo electrólitos para células solares, pilas de combustible, baterías de ión litio, fluídos de transferencia de calor, lubricantes ou aditivos de lubricantes), na industria farmacéutica e como alternativa "verde" para evitar/reducir a produción de substancias perigosas para o medioambiente. Dependendo do seu método de síntese, os ILs poden ser divididos en dous grandes grupos, os próticos (PILs polas súas siglas en inglés) e os apróticos (APILs). Os PILs son sintetizados vía transferencia protónica mentres que os APILs teñen diferentes métodos de sínteses.

Estúdanse catro ILs comerciais diferentes, próticos e apróticos, das familias de cationes máis comúns, como son o amonio, o imidazolio e o pirrolidinio. Os aniones correspondentes foron dous, nitrato (NO_3) e bis(trifluorometilsulfonil)imida (TFSI), establecendo así as catro combinacións catión-anión dos ILs usados, concretamente nitrato de etilamonio (EAN) e nitrato de 1-etilimidazolio ($[C_2Im][NO_3]$) como líquidos iónicos próticos e 1-butil-1-metilpirrolidinio bis(trifluorometilsulfonil)imida ($[C_4C_1Pyrr][TFSI]$) e 1-etil-3-metilimidazolio bis(trifluorometilsulfonil)imida ($[C_2C_1Im][TFSI]$) como líquidos iónicos apróticos. Como se dixo anteriormente, a sal de interese electroquímica utilizada para a síntese das mesturas electrolíticas é seleccionada con anión común co IL, sendo nitrato de Litio, nitrato de Magnesio, nitrato de Calcio e nitrato de Aluminio as usadas para as combinacións con EAN e $[C_2Im][NO_3]$ e Litio Bis(trifluorometilsulfonil)imida para as mesturas con $[C_4C_1Pyrr][TFSI]$ e con $[C_2C_1Im][TFSI]$.

Unha das partes máis innovadoras deste traballo foi a procura do método de xelificación máis adecuada para obter un electrólito semisólido manipulable. Os métodos de sínteses de xelificación das mesturas electrolíticas usadas teñen como precursores compostos baseados en silicio e están descritas completamente neste manuscrito. Principalmente, estúdanse tres métodos de xelificación diferentes, dous delas usan un único precursor de silicio con dous catalizadores diferentes, ácido fórmico e etanol e a terceira fai uso de dous precursores de sílice con ácido fórmico como catalizador. As dous primeiros métodos, denominadas como a ruta do ácido fórmico e a ruta do etanol respectivamente, xa eran coñecidas no grupo de investigación NaFoMat, mentres que a terceira, denominada como a ruta de dous precursores, desenvolveuse durante unha estancia de investigación no instituto de materiais Jean Rouxel da Universidade de Nantes baixo a supervisión do profesor Jean Le Bideau. Cada unha destes métodos ten unhas características e proporcións propias para crear o Ionogel e como resultado obtéñense propiedades diferentes. O método de síntese de ionogeles asume que o IL permaneza inalterable durante a reacción de xelificación, non reaccionando quimicamente con ningún dos compoñentes usados para formar a matriz de sílice, dando como resultado un material electrolítico semisólido mantendo as propiedades do IL o máis inalteradas posibles, noutras palabras, a matriz de sílice confina o IL o cal mantén as propiedades da súa forma líquida. Estas afirmacións veranse confirmadas ao longo desta tese mediante as diferentes técnicas de caracterización experimental utilizadas.

Estúdase o comportamento térmico, os cambios estruturais, propiedades termo-físicas como a densidade e a viscosidade e comportamento electroquímico en función da concentración de sal, do tipo de sal e da temperatura no caso das mesturas en estado líquido. Analízanse tamén os cambios destas propiedades e comportamentos como consecuencia do nanoconfinamiento das mesturas anteriores.

O estudo térmico realízase polas técnicas como calorimetría diferencial de varrido (DSC) e análise termo-gravimétrico (TGA). As principais observacións para a DSC foron que a adición de sal tradúcese nunha redución da cristalinidade para os IL próticos, é dicir, os picos de cristalización e fusión característicos dos ILs puros tenden a desaparecer ou perder definición a medida que se aumenta a concentración de sal. Con respecto ás mesturas en forma líquida dos ILs apróticos obsérvase un desprazamento dos picos de transición de fase cara a temperaturas maiores. O efecto do confinamento das mesturas electrolíticas en matrices de sílice non segue un patrón definido, dependendo do método de xelificación e do IL, aínda que si se observa unha tendencia ao aumento do comportamento amorfo nas mostras. Concretamente, EAN e [C_2Im][NO_3], que foron xelificados usando os métodos dun único precursor (a ruta do ácido fórmico e a do etanol), mostran resultados diferentes, no primeiro caso obsérvase una completa desaparición dos picos de transición de fase, mentres que para o segundo temos un desdobramento do pico de fusión e un desprazamento cara a temperaturas menores do pico de cristalización. Por último, co nanoconfinamiento do IL [C_4C_1Pyrr][TFSI], realizado pola ruta de dous precursores, non se obtén un cambio significativo das transicións de fase. Estes resultados indican que o tamaño de poro da rede de sílice depende do método seguido e do IL.

A estabilidade térmica das mostras estudadas non depende de adición de sal nin do nanoconfinamiento, vén determinada pola estabilidade do propio IL, que como é ben sabido depende maioritariamente do seu anión, outorgando maior estabilidade térmica o TFSI que o NO_3.

Analízanse os cambios na estrutura das mesturas electrolíticas por medio de Resonancia Magnética Nuclear (RMN) atopando que esta permanece inalterada pola adición de sal, pero atópase un desprazamento dos protóns doantes (teoría ácido-base de Lewis) cara a campos magnéticos de maior enerxía (up-field), sendo os protóns lábiles dos ILs próticos os máis afectados pola adición de sal. O confinamento en matrices de sílice non provoca cambios estruturais significativos na mestura electrolítica, aínda que se observa unha retardación da dinámica molecular e un contorno químico diferente entre as moléculas do centro do poro e as próximas ás paredes da matriz de sílice.

As propiedades termofísicas, densidade e viscosidade, das mesturas líquidas caracterízanse usando as técnicas de denso-viscometría e reometría. Os resultados obtidos mostran dependencias polinómicas da densidade con respecto á concentración de sal (incremento seguindo un polinomio grao 2 ou tendencia cuadrática) e á temperatura (diminución lineal). No caso da viscosidade das mesturas electrolíticas observouse un aumento desta coa concentración de sal, como se esperaba, e unha diminución coa temperatura seguindo un comportamento descrito polo modelo Vogel–Fulcher–Tammann (VFT).

Como parte fundamental deste traballo, realízanse medicións electroquímicas usando Espectroscopía Dieléctrica de Banda Ancha (BBDS), a condutividade iónica, espectroscopía de impedancia (EIS), voltametría cíclica (CV) e cargas e descargas galvanostáticas con limitación de potencial (GCPL).

A Espectroscopía Dieléctrica de Banda Ancha (BBDS) analízase no réxime interfacial para estudar a Dobre Capa Eléctrica (EDL). O aprendizaxe da BBDS desenvolveuse durante unha estancia de investigación na Universidade de Porto, no Departamento de Física, baixo a supervisión do profesor Agostinho e, posteriormente, implantouse esta técnica experimental e o seu posterior desenvolvemento e tratamento de datos no grupo de investigación de NaFoMat da USC. A través de medicións espectroscópicas da impedancia obtense a constante dielectrica (magnitude complexa) en función da frecuencia e analizouse a xanela frecuencial dos distintos réximes presentes, en especial a saturación de ións nas veciñanzas das paredes ou interfase dos eléctrodos (efecto coñecido como Maxwell-Wagner-Sillars, MWS), así como o fenómeno de relaxación interfacial. A través da parte imaxinaria da constante dieléctrica pódese obter o réxime óhmico da mostra, derivando de leste, con gran exactitude, o rango de frecuencias en que este fenómeno prodúcese, e con ela determinar a condutividade iónica da mostra analizada cun alto grao de fiabilidade. Estes estudos realízanse en función da temperatura, a adición de sal e do nanoconfinamiento. Obsérvase que tanto a adición de sal como o nanoconfinamiento desprazan a xanela espectroscópica dos diferentes réximes presentes a frecuencias menores. Isto tradúcese nunha redución da mobilidade iónica do "*bulk*" da mostra analizada. O efecto da temperatura é o esperado, a mobilidade iónica aumenta cando a temperatura aumenta. A relaxación dieléctrica foi un estudo crítico para a selección dun IL para a implantación nunha batería funcional de IL, a cal é analizada mediante o diagrama Cole-Cole. Este diagrama representa a parte imaxinaria da constante dieléctrica fronte ao seu parte real, obtendo un indicativo da relevancia desta relaxación e, por tanto, convértese nunha cuantificación crucial no estudo de electrólitos.

A condutividade iónica é un dos parámetros críticos a determinar cando se estuda o comportamento electroquímico dos electrólitos en dispositivos de almacenamento de enerxía, como son as baterías. A condutividade iónica das mesturas electrolíticas estudadas obtense por dous métodos diferentes, unha medida directa desta propiedade por medio dun conductímetro comercial, e por medio da parte imaxinaria da BBDS cando se alcanza o réxime óhmico da mostra, como xa se indicou. É ben sabido que a condutividade iónica é unha propiedade de transporte, do mesmo xeito que a viscosidade (tamén estudada neste manuscrito) e ambas as propiedades teñen un comportamento oposto, así, a condutividade redúcese con adición de sal en todos os casos, mentres que a viscosidade aumenta. Ao contrario que a viscosidade, a condutividade iónica das mesturas electrolíticas aumenta coa temperatura, como se espera, e pode ser ben descrita polo modelo VFT (tamén utilizado para describir a variación da viscosidade coa temperatura). Co confinamento en matrices de sílice esta propiedade diminúe o seu valor, aínda que a condutividade iónica pode ser modificada dependendo do método de síntese de ionogeles utilizada, sendo así unha propiedade tuneable para os ionogeles, aínda que esta sempre será menor que o seu homólogo en forma líquida.

Tras o estudo da BBDS e da condutividade iónica, selecciónase o IL $[C_4C_1Pyrr][TFSI]$ como potencial candidato para unha cela electroquímica de acumulación de enerxía funcional (batería de ión litio) baseada no devandito IL debido á súa evidente relaxación dieléctrica interfacial e a súa alta condutividade iónica, ademais dos resultados obtidos anteriormente como alto rango líquido e unha gran estabilidade térmica, tanto en forma líquida como xel. Polo que se fai un estudo de voltametría cíclica deste IL co fin de obter a xanela electroquímica, e estudar os posibles procesos de descomposición do electrólito e a que potenciais ocorren estes. Isto é determinante para a selección dos eléctrodos que se van a usar na implantación da devandita cela, xa que o potencial de carga-descarga desta cela vai depender exclusivamente dos eléctrodos seleccionados. O potencial de carga e descarga debe de estar dentro da xanela electroquímica para evitar a deterioración da batería, e desta maneira, comprometer a seguridade do operador e do equipo experimental. Os seguintes estudos realizáronse durante unha estancia de investigación no centro tecnolóxico privado TECNALIA baixo a supervisión do doutor Francisco Fernández Carretero.

Antes da implantación do $[C_4C_1Pyrr][TFSI]$ na cela electroquímica, analízase a Espectroscopia de Impedancia Electroquímica (EIS) do IL para coñecer o comportamento desta en función da temperatura. A impedancia estúdase desde dúas representacións, o Bode Plot e o Nyquist Plot, ambas amplamente coñecidas na bibliografía. Como é de esperar, o módulo da impedancia decrece coa temperatura e o comportamento en xeral das impedancias concorda perfectamente co da BBDS. O Nyquist Plot foi axustado cun circuíto equivalente para poder dar un significado físico e á súa vez, a capacidade diferencial da mostra tamén foi obtida e obtense a tendencia de aumentar coa temperatura, sorprendentemente, a capacidade diferencial de mostra xel é maior que a da forma líquida.

O estudo final desta tese céntrase na implantación do IL puro [C_4C_1Pyrr][TFSI], é dicir, sen sal de litio engadida, como electrólito funcional dunha cela electroquímica. Para iso hase ensamblado unha cela tipo "coin cell" 2032, unha das máis usadas pola bibliografía. A montaxe experimental que se seleccionou é unha configuración de media cela usando Litio-Ferro-Fosfato (LiFePO4 ou a súa forma abreviada LFP) como cátodo e litio metálico como ánodo para o electrólito seleccionado nas formas líquido e xel. O cátodo LFP é un eléctrodo amplamente coñecido na bibliografía, o cal posúe unha capacidade teórica de 170 $mA \cdot h \cdot g^{-1}$, presenta un estudio de carga-descarga entorno a 3.5 V moi estable, o LFP é un cátodo comercial e unha gran parte das baterías de ión litio actuais utilízano, aínda que na actualidade é motivo de investigación por parte de moitos investigadores. O litio metálico posúe unha alta capacidade teórica de 3860 $mA \cdot h \cdot g^{-1}$, e normalmente, é usado como ánodo debido á súa alta capacidade, pero cabe mencionar que o litio metálico conleva grandes problemas de seguridade debido a que é altamente reactivo coa auga, chegando a provocar incendios ao contacto con esta. O litio metálico é usado en experimentos de media cela (ou "*half-cell*" en inglés) debido a que este presenta unha capacidade moito maior que os cátodos usados actualmente (caso coñecido como eléctrodo de exceso na bibliografía), podendo medir o comportamento do eléctrodo enfrontado, neste caso, o LFP. Para a montaxe en forma líquida como separador usouse celgar 2500, mentres que en forma xel ningún separador foi usado xa que a propia matriz de sílice cumpre o rol de confinar o líquido iónico e á súa vez impedir o contacto entre ánodo e cátodo, actuando así como separador. Como método experimental usouse a carga e descarga galvanostática con limitación de potencial (GCPL) a diferentes velocidades. Como velocidades de carga e descarga seleccionáronse C/20, C/10, C/5 e outra vez C/20 para estudar a reversibilidade e estabilidade da pila. A pesar de seleccionar un IL en estado puro sen a adición de sal, comprobouse que as cargas e descargas producíanse de forma estable tras un período de, o que denominamos "litiación" do electrólito, e obtense unha alta eficiencia coulómbica, ademais de alcanzar unha capacidade próxima á teórica presentada polo LFP, aínda que esta alta capacidade prodúcese a baixas velocidades de carga/descarga, diminuíndo rapidamente ao aumentala. Cabe resaltar que para fórmaa xel, un paso previo ao primeiro ciclado a velocidade moi baixa, C/50, foi necesario para habilitar as cargas e descargas da pila en cuestión. É importante resaltar que a pesar de utilizar un electrólito sen sal de litio engadida para unha batería de ión litio, as cargas e descargas foron posibles. Este interesante resultado, que supón un importante avance na proposta de novos *Smart-electrolytes*, xa que demostra que o litio contido nos eléctrodos, concretamente no cátodo LFP, é suficiente para que a batería almacene carga e libérea nos seus ciclos de carga e descarga dunha batería de ións litio funcional, a pesar de que as cargas e descargas prodúzanse a baixa velocidade para obter capacidades competitivas. Con todo, antes dunha proposta definitiva e escalable é necesario mellorar as velocidades de carga mantendo altas capacidades, diminuír a viscosidade e así lograr un aumento da difusión dos ións de litio. Isto podería conseguirse a partir de mesturas ternarias IL + sal de litio + carbonato, por exemplo.

A modo de conclusión deste resumo inicial, pódese dicir que esta tese que se centra na análise de novos electrólitos cumpre cos seus obxectivos de ampliar as fronteiras das baterías de Ión-Litio, así como ampliar o coñecemento das baterías da era post-litio. Demostrouse que as mesturas electrolíticas baseadas en líquidos iónicos cun sal de interese electroquímico pódense nanoconfinar en matrices de sílice, mantendo propiedades da súa forma líquida, para obter un material manipulable que evite derrames durante a súa implantación a escala industrial. Estudáronse as transicións de fase e a estabilidade térmica destas mesturas electrolíticas, tanto en forma líquida como xel, comprobando que estas presentan un amplo rango da fase líquida. Comprobouse por medio de técnicas de caracterización estrutural, como RMN, que a adición de sal, así como o confinamento, non afectan á estrutura do IL. Propiedades termofísicas, como son a densidade e viscosidade da forma líquida das devanditas mesturas foron estudadas en profundidade. Finalmente, unha ampla gama de estudos electroquímicos foi realizada co fin de seleccionar un candidato a unha pila de ión litio, obtendo como resultado un electrólito funcional sen sal de litio engadida.

USC
UNIVERSIDADE
DE SANTIAGO
DE COMPOSTELA

CAMPUS VIDA
CAMPUS DE EXCELENCIA INTERNACIONAL

This thesis is about the experimental characterization of new electrolytes for electrochemical devices for energy storage, particularly, for lithium ion batteries and beyon lithium era.

New smart electrolytes based on ionic liquids (ILs) and dopped with electrochemical interest salt and then nanoconfined inside silica matrix to obtain a semisolid, self-standing and handable electrolytic matherial, known as ionogel, keeping the liquid properties desirable for battery electrolytes.

The ILs and the ionogels are characterized by means of DSC, TGA, NMR, density, viscosity and electrochemically by different techniques such as BBDS, ionic conductivity, EIS, CV and GCPL.